UNIVERSITÀ DEGLI STUDI DI PARMA

Dottorato di ricerca in Ingegneria Civile e Architettura

Ciclo 29°

Implementation of PARC_CL 2.0 crack model for reinforced concrete members subjected to cyclic and dynamic loading

Coordinatore:
Chiar.mo Prof. Andrea Carpinteri

Tutor:
Chiar.ma Prof.ssa Beatrice Belletti

Dottorando: Matteo Scolari

Abstract

Nonlinear finite element analysis (NLFEA) are nowadays strongly used both in research and in design practices. The [*fib*-Model Code 2010] introduced the concept of Levels of Approximations (LoA) to estimate a reinforced concrete (RC) structural member's behaviour. The LoA approach is a design strategy, based on the assumption that the structural member's response can be progressively refined through a better estimate of the physical parameters. By increasing the level of approximation, a better accuracy in the estimate of the structural response can be obtained; however, more time and resources have to be devoted to the analyses. In particular, the higher level of approximation is associated with the NLFEA. In the last years the rapid increase of computer power contributed to the development of this numerical tool for both the design of new structures and the assessment of existing ones. For the latter, a proper modelling of the nonlinear behaviour is fundamental for the prediction of the structural response.

The behaviour of thin RC structural members (e.g. walls and slabs) subjected to monotonic, cyclic and dynamic loading, both in-plane and out-of-plane, has been investigated, by means of NLFEA.

In particular, the cyclic response of RC walls has been analysed in detail. RC walls are commonly used as lateral load resisting elements in buildings in seismic region thanks to the high stiffness and resistance they can give to the building. Their principal function is to carry in-plane forces but, as a consequence of particular forces and boundary conditions, they could be subjected also to out-of-plane actions. RC walls can be modelled with different approaches: 1-D models considering lumped or distributed plasticity using *beam elements*, 2-D models using *shell elements* and 3-D models using *solid elements*. In particular, in the present research the behaviour of RC walls was investigated by means of "multi-layer shell" elements (MS) using ABAQUS code.

The MS approach, defined within the ABAQUS code, consists in discretizing the thickness of the element in several layers assuming a plane–stress hypothesis. The aim of this research was to assess the capability of the proposed approach to reproduce the monotonic, cyclic and dynamic behaviour of RC members subjected to in-plane and out-of-plane actions.

Since the adopted MS elements are defined in ABAQUS code in plane-stress condition, they do not include the nonlinear behaviour due to shear along the thickness; it is, therefore, not possible to capture shear or punching shear out-of-plane failure. Within this research a post-processing of the NLFEA results is conducted based on Critical Shear Crack Theory (CSCT). CTCT, as reported in [Muttoni, 2008] and [Muttoni and Fernandez, 2008[a]], allows to calculate shear and punching shear resistance based on few fundamental parameters, such as respectively the axial strain at mid-depth and the out-of-plane rotation of the element. In this context, NLFEA are carried out on several RC slabs experimentally tested in literature. The outcomes highlighted that NLFEA, post-processed according to CSCT, leads to good results when compared with the experimental ones, proving itself able to capture both the bending and shear out-of-plane failure. Moreover,

by comparing with simplified analytical formulations, it was underlined that NLFEA allows considering phenomena like redistribution of stresses and membrane effect due to cracking and boundary conditions.

The main aim of this research was to investigate the capability of MS elements to predict the cyclic and dynamic response of RC walls. The cyclic response of RC structures was widely investigated in literature associated to 1-D elements (e.g. plastic hinge models to study the nonlinear flexural behaviour). On the other hand, concerning 2-D shell and 3-D solid modelling, recent developments in seismic engineering underlined the lack of cyclic crack models for reinforced concrete, while the monotonic behaviour was widely studied in the past.

A cyclic crack model for RC members, defined PARC_CL 2.0 and implemented as a user subroutine UMAT.for within the ABAQUS code, allows, differently from the previous PARC_CL 1.0 crack model, to account for plastic and irreversible deformation in the unloading phase. As a consequence of this it permits to consider the hysteretic cycles both in concrete and steel. Moreover, within the PARC_CL 2.0 crack model, was implemented a formulation able to account for stiffness proportional damping in dynamic analyses.

The implemented PARC_CL 2.0 crack model was primarily validated by means of comparison with experimental tests run on simple RC panels carried out at the University of Houston [Mansour and Hsu, 2005] and in a second phase it was applied to more complex structural members, such as RC walls, with the aim to assess the capability of the implemented model to predict the cyclic and dynamic behaviour and to underline the improvement with respect to the previous PARC_CL 1.0 crack model. In order to evaluate the generalizability of the implemented model, different walls, characterized by different layouts were analysed: squat walls tested at ISPRA laboratory [Pegon, 1998] and slender walls with different cross sections tested at EPFL in Lausanne (two “T-shaped” walls [Rosso et al., 2016] and a “U-shaped” wall [Constantin and Beyer, 2016]).

The results obtained by means of NLFEA with PARC_CL 2.0 crack model was in good agreement with the experimental tests, demonstrating its ability to capture not only cyclic in-plane behaviour but also phenomena associated to the out-of-plane instability.

Sommario

Le analisi non lineari ad elementi finiti (NLFEA) sono uno strumento sempre più utilizzato al giorno d'oggi sia in ambito scientifico che nella prassi progettuale. Il [*fib*-Model Code 2010] introduce, per il calcolo della capacità portante di un elemento strutturale in calcestruzzo armato (CA), il concetto di livelli di approssimazione (LoA). Questo approccio si basa sull'idea che in ambito progettuale la resistenza di un elemento strutturale non sia definibile con una formulazione univoca, ma per mezzo di diversi livelli di approssimazione. All'aumentare del livello di approssimazione aumenta progressivamente la raffinatezza del modello fisico utilizzato e quindi è possibile ottenere una miglior stima del comportamento e della capacità ultima della struttura a discapito di maggiori oneri computazionali richiesti in fase di calcolo. In particolare utilizzando il livello di approssimazione più elevato, la capacità portante di un elemento strutturale può essere desunta da NLFEA. Il rapido incremento delle prestazioni dei calcolatori negli ultimi anni ha contribuito al rapido sviluppo di questa tipologia di analisi, sia nella progettazione di strutture nuove, ma soprattutto nella verifica di strutture esistenti, dove una accurata modellazione del comportamento non lineare diventa fondamentale per prevedere adeguatamente la risposta della struttura.

Nella presente tesi è stata indagata, per mezzo di NLFEA, la risposta di elementi strutturali sottili in CA, come pareti e piastre, soggetti ad azioni monotone, cicliche e dinamiche sia nel piano che fuori dal piano.

In particolare è stata dettagliatamente analizzata la risposta ciclica di pareti in CA, comunemente utilizzate come sistemi sismoresistenti in virtù della elevata rigidezza e resistenza che possono conferire alla struttura. La principale funzione di questa tipologia di elemento strutturale è quindi quella di trasferire azioni nel piano ma, in conseguenza di particolari forze esterne o condizioni vincolari, gli stessi potrebbero trovarsi soggetti ad azioni fuori piano. Le pareti in CA si prestano ad essere modellate con diversi approcci: dai più semplici e meno raffinati modelli monodimensionali a plasticità concentrata e diffusa con elementi finiti *beam*, fino ai modelli bidimensionali con elementi finiti *shell* e modelli tridimensionali con elementi finiti *brick*. In particolare, nella presente ricerca il comportamento delle pareti in CA verrà analizzato per mezzo di elementi finiti *shell multi-layer* (MS) utilizzando il software ABAQUS.

L'approccio MS utilizzato, definito all'interno del software ABAQUS, consiste nella discretizzazione dello spessore dell'elemento finito in un certo numero di layer assunti in stato piano di sforzo. L'obiettivo del presente studio ha riguardato principalmente la valutazione della capacità della tipologia di modellazione proposta di prevedere il comportamento monotono, ciclico e dinamico di strutture in CA soggette ad azioni non solo nel proprio piano ma anche fuori dal piano.

Inizialmente, in ambito monotono, è stata indagata una delle maggiori problematiche associate all'approccio MS adottato, legata all'assunzione di linearità della rigidezza trasversale fuori piano che non consente di considerare la rottura a taglio o punzonamento lungo lo spessore. Nel presente studio è stata proposta una procedura di post-processing dei risultati delle analisi ad elementi finiti, condotta in accordo alla

Critical Shear Crack Theory (CSCT), teoria presentata in [Muttoni, 2008] e [Muttoni and Fernandez, 2008[a]] che permette di stimare la resistenza a taglio o punzonamento di un elemento strutturale sulla base di pochi parametri fondamentali, quali rispettivamente la deformazione assiale a metà spessore o la rotazione fuori piano. In quest'ambito le analisi sono state condotte su una serie di piastre in CA testate in letteratura. I risultati hanno evidenziato come le analisi non lineari, rielaborate in accordo alla CSCT forniscono buoni risultati riuscendo a cogliere sia le rotture flessionali che le rotture a taglio fuori dal piano. Inoltre, è stato evidenziato come, rispetto a formulazioni analitiche semplificate, le NLFEA consentano di tenere in considerazione fenomeni come la ridistribuzione degli sforzi o gli effetti membranali dovuti a fessurazione e a particolari condizioni vincolari esterne.

Le ricerche non si sono limitate all'ambito delle azioni monotone ma anzi, l'obiettivo principale della presente tesi è stato quello di valutare la capacità degli elementi MS di predire il comportamento ciclico e dinamico di sistemi sismoresistenti a pareti in CA. Il comportamento ciclico di strutture in CA è stato ampiamente trattato in letteratura per elementi monodimensionali *beam*, basti pensare al modello di cerniera plastica sviluppato per tenere in considerazione le non linearità flessionali. I recenti sviluppi dell'ingegneria sismica hanno invece evidenziato le carenze di modelli costitutivi ciclici per il calcestruzzo armato, associate ad approcci con elementi bidimensionali *shell* e tridimensionali *brick*, rispetto invece ad una ampia trattazione in letteratura relativamente alle sollecitazioni monotone.

L'obiettivo principale del presente lavoro è stato quindi l'implementazione di un modello fessurativo ciclico per il calcestruzzo armato, definito PARC_CL 2.0. Il modello fessurativo PARC_CL 2.0, implementato come user subroutine all'interno del software ABAQUS consente, a differenza del precedente modello PARC_CL 1.0, di tenere in considerazione le deformazioni plastiche ed irreversibili in fase di scarico e quindi fornisce una realistica modellazione dei cicli isteretici di calcestruzzo ed acciaio. Inoltre, all'interno del modello PARC_CL 2.0 è stata implementata una formulazione che consente di tenere in considerazione lo smorzamento viscoso proporzionale alle rigidezze.

Il modello implementato PARC_CL 2.0 è stato in un primo momento validato per mezzo di confronti con risultati sperimentali su semplici pannelli in calcestruzzo armato testati presso l'Università di Houston [Mansour and Hsu, 2005] e successivamente applicato a elementi strutturali più complessi, nella fattispecie pareti in CA, con l'obiettivo di valutare la sua capacità di predire il comportamento ciclico e dinamico e di evidenziare i miglioramenti apportati rispetto alla precedente versione. Per valutare la generalità del modello proposto sono state analizzate pareti con diverse configurazioni geometriche e meccaniche: pareti tozze testate presso i laboratori di ISPRA [Pegon, 1998] e pareti snelle con differenti sezioni trasversali testate presso EPFL di Losanna (sezione a "T" [Rosso et al., 2016] e sezione a "U" [Constantin e Beyer, 2016]).

Il modello PARC_CL 2.0 si è mostrato in buon accordo con le evidenze sperimentali dimostrandosi in grado di cogliere sia il comportamento ciclico nel piano degli elementi che fenomeni legati all'instabilità fuori dal piano degli stessi.

Contents

Notations

Roman lower case letters

d_{max}	maximum aggregate size;
a_m	average crack spacing;
b	strain hardening ratio of steel reinforcement according to [Menegotto and Pinto, 1973];
b_0	length of the shear resisting control perimeter for the evaluation of punching shear;
d	effective depth;
h	equivalent length, also known as crack band width of the finite element;
$l_{s,max}$	length over which the slip between concrete and steel occurs;
f	frequency;
f_c	cylinder compressive strength of concrete;
f_{cm}	mean value of cylinder compressive strength of concrete;
f_{ck}	characteristic value of cylinder compressive strength of concrete;
f_t	axial tensile strength of concrete;
f_{tm}	mean value of axial tensile strength of concrete;
f_y	yield strength of reinforcing steel in tension;
f_{yi}	yield strength of *i*th order of steel reinforcement in tension;
f_{yd}	design yield strength of of reinforcing steel in tension;
f_{ym}	mean value of yield strength of reinforcing steel in tension;
f_u	ultimate strength of reinforcing steel in tension;
s	space between different reinforcing bar;
w	crack opening;
v	crack sliding;
l_x,l_y	dimensions of finite element in the x,y-directions

t	finite element thickness;

Roman capital letters

C_n	generalized damping factor related to the *n*th vibration mode;
E'	tangent stiffness modulus;
E_c	modulus of elasticity for concrete;
E_{cr}	Secant modulus from the origin to the peak compressive stress;
E'_{c1}	tangent stiffness modulus of concrete in *1*-direction;
E'_{c2}	tangent stiffness modulus of concrete in *2*-direction;
E_h	hardening modulus of reinforcing steel;
E_{hi}	hardening modulus of the *i*th order of steel reinforcement;
E_s	modulus of elasticity of reinforcing steel;
E_{si}	modulus of elasticity of the *i*th order of steel reinforcement;
E'_{si}	tangent stiffness modulus of the *i*th order of steel reinforcement;
G	elastic shear modulus of concrete in the un-cracked phase;
G'_{12}	tangent shear modulus of concrete in the *1,2*- coordinate system;
G_C	fracture energy of concrete in compression;
G_{cr}	secant shear modulus of concrete in the cracked phase;
G^*_{cr}	secant shear modulus of concrete in the cracked phase related to the first linear branch of the bilinear formulation proposed by [Gambarova, 1983];
G_{eq}	secant overall shear modulus of concrete calculated as the equivalent modulus between un-cracked and cracked phase;
G_F	fracture energy of plain concrete in tension;
G^{RC}_F	fracture energy of reinforced concrete in tension;
K_n	generalized stiffness related to the *n*th vibration mode;
M_n	generalized mass related to the *n*th vibration mode;

R parameter which influence the shape of the hysteretic behaviour of steel reinforcement according to [Menegotto and Pinto, 1973];

Greek lower case letters

α mass-proportional damping coefficient for Rayleigh damping;

α_i angle between the *1*-direction and the direction of the *i*th order of steel reinforcement;

β stiffness-proportional damping coefficient for Rayleigh damping;

$\dot{\varepsilon}$ increment of strain in time;

$\dot{\varepsilon}_1$ strain increment, with respect to the time, of concrete along *1*-direction;

$\dot{\varepsilon}_2$ uniaxial strain increment, with respect to the time, of concrete along *2*-direction;

ε_1 biaxial strain of concrete along *1*-direction;

$\bar{\varepsilon}_1$ uniaxial strain of concrete along *1*-direction;

ε_2 biaxial strain of concrete along *2*-direction;

$\bar{\varepsilon}_2$ uniaxial strain of concrete along *2*-direction;

$\varepsilon_{c,cr}$ concrete strain at maximum compressive stress;

$\varepsilon_{c,pl}$ plastic compressive strain of concrete;

$\varepsilon_{c,re}$ minimum compressive strain experienced on the envelope curve of compressive concrete;

$\varepsilon_{c,u}$ ultimate strain of concrete in compression;

$\varepsilon_{t,cr}$ concrete strain at maximum tensile stress;

$\varepsilon_{t,u}$ ultimate strain of concrete in tension;

ε_x normal strain of concrete along *x*-direction;

ε_{xi} strain of the *i*th order of steel reinforcement along x_i-direction;

$\dot{\bar{\varepsilon}}_{xi}$ uniaxial strain increment, with respect to the time, of the *i*th order of steel reinforcement along x_i-direction;

$\bar{\varepsilon}_{xi}$ uniaxial strain of the *i*th order of steel reinforcement along x_i-direction;

ε_y normal strain of concrete along *y*-direction;

ε_{sy} yielding strain of reinforcing steel;

ε_{su} ultimate strain of reinforcing steel;

ϕ diameter of reinforcement bar;

$\dot{\gamma}_{12}$ uniaxial shear strain increment, with respect to the time, of concrete in the *1*,*2*-coordinate system;

γ_{12} biaxial shear strain of concrete in the *1*,*2*-coordinate system;

$\gamma_{12,el}$ biaxial shear strain of concrete in the un-cracked phase in the *1*,*2*-coordinate system;

$\gamma_{12,cr}$ biaxial shear strain of concrete in the cracked phase in the *1*,*2*-coordinate system;

$\bar{\gamma}_{12}$ uniaxial shear strain of concrete in the *1*,*2*-coordinate system;

γ_f shear strain of concrete in the *1*,*2*-coordinate system at the onset of concrete cracking;

γ_{xy} shear strain in the *x*,*y*-coordinate system;

θ inclination angle of the compressive strut;

θ_i angle between the direction of the *i*th order of the bar and the *x*-direction;

ρ_i reinforcement ratio related to the *i*th order of the bar;

σ_1 concrete stress along direction *1*-direction;

σ_2 concrete stress along direction *2*-direction;

$\sigma_{c,re}$ stress related to minimum compressive strain experienced on the envelope curve of compressive concrete;

σ_{damp} stress contribution due to stiffness-proportional damping;

σ_{xi} stress of the *i*th order of steel reinforcement along x_i-direction;

τ_{12} shear stress of concrete in the *1*,*2*-coordinate system;

υ Poisson's ratio;

ω natural frequency;

ω_n natural frequency of the *n*th vibration mode;

ξ damping ratio;

ξ_n damping ratio of the *n*th vibration mode;

Ψ angle between the *1*-direction and the *x*-direction;

ζ softening coefficient of concrete;

Matrices and vectors

$\{\varepsilon_{1,2}\}$ biaxial strain vector for concrete in *1,2*- coordinate system;

$\{\bar{\varepsilon}_{1,2}\}$ uniaxial strain vector for concrete in *1,2*- coordinate system;

$\{\varepsilon_{x,y}\}$ biaxial strain vector for concrete in *x,y*- coordinate system;

$\{\varepsilon_{x_i,y_i}\}$ biaxial strain vector along each steel bars axes;

$\{\bar{\varepsilon}_{x_i,y_i}\}$ uniaxial strain vector along each steel bars axes;

$\{F\}$ external forces vector;

$\{\sigma_{x_i,y_i}\}_{damp}$ damping contribute on the stress vector for the *i*th order of steel reinforcement in x_i,y_i- coordinate system;

$\{\sigma_{x_i,y_i}\}_{dyn}$ dynamic stress vector for the *i*th order of steel reinforcement in x_i,y_i- coordinate system, calculated as the sum of the static and the damping contribution;

$\{\sigma_{x,y}\}_c$ stress vector for concrete in *x,y*-coordinate system;

$\{\sigma_{x,y}\}_{c,dyn}$ dynamic stress vector for concrete in *x,y*-coordinate system, calculated as the sum of the static and the damping contribution;

$\{\sigma_{x,y}\}_{s,i}$ stress vector for the *i*th order of steel reinforcement in *x,y*-coordinate system;

$\{\sigma_{x,y}\}_{s,i,dyn}$ dynamic stress vector for the *i*th order of steel reinforcement in *x,y*-coordinate system, calculated as the sum of the static and the damping contribution;

$\{\sigma_{x,y}\}$ overall stress vector, considering the contribution of both concrete and steel reinforcement, in *x,y*-coordinate system;

$\{\sigma_{x,y}\}_{dyn}$ overall dynamic stress vector, considering the contribution of both concrete and steel reinforcement, in *x,y*-coordinate system;

$\{u(t)\}$ displacement degrees of freedom vector;

$\{\dot{u}(t)\}$ velocity vector;

$\{\ddot{u}(t)\}$ acceleration vector;

$[C]$ damping matrix;

$[D_{1,2}]$ Jacobian matrix of concrete in *1,2*- coordinate system;

$[D_{1,2}]_{damp}$ Jacobian matrix of concrete, related to damping contribution, in *1,2*- coordinate system;

$[D_{1,2}]_{dyn}$ dynamic Jacobian matrix of concrete in *1,2*- coordinate system , calculated as the sum of static and damping contribution;

$[D_{x_i,y_i}]$ Jacobian matrix of the *i*th order of steel reinforcement in x_i,y_i- coordinate system;

$[D_{x_i,y_i}]_{damp}$ dynamic Jacobian matrix of the *i*th order of steel reinforcement in x_i,y_i- coordinate system, calculated as the sum of static and damping contribution;

$[D_{x_i,y_i}]_{dyn}$ Jacobian matrix of the *i*th order of steel reinforcement, related to damping contribution, in x_i,y_i- coordinate system;

$[D_{x,y}]$ overall Jacobian matrix, considering the contribution of both concrete and steel reinforcement, in *x*,*y*-coordinate system;

$[M]$ mass matrix;

$[K]$ stiffness matrix;

$[T_\psi]$, $[T_{\vartheta_i}]$ transformation matrices;

$[T_\psi]^t$ transpose of the transformation matrix;

PART I

INTRODUCTION

1 Introduction

"un libro (io credo) è qualcosa con un principio e una fine, è uno spazio in cui il lettore deve entrare, girare, magari perdersi, ma a un certo punto trovare un'uscita, o magari parecchie uscite, la possibilità di aprirsi una strada per venirne fuori."

Italo Calvino – Le città invisibili

1.1 Definition of the research field

In the last decades reinforced concrete (RC) has become one of the most important building materials and is widely used in many types of engineering structures. The economy, the efficiency, the strength and the stiffness of reinforced concrete make it an attractive material for a wide range of structural applications.

Reinforced concrete structures are commonly designed to satisfy criteria of serviceability and safety. In order to ensure the serviceability requirement it is necessary to predict the cracking and the deflections of RC structures under service loads. In order to assess the margin of safety of RC structures against failure an accurate estimation of the ultimate load is essential and the prediction of the load-deformation behaviour of the structure throughout the range of elastic and inelastic response is desirable.

Within the framework of achieving a wider understanding of all mechanical phenomena associated with the elastic and, particularly, inelastic behaviour of RC members, experimental research still plays a very important role. Moreover, experimental research supplies the information needed for the development of advanced design methods, such as finite element analysis (FEA).

The FEA procedure, as widely explained in **Chapter 2**, is a technique based on the assumption that a structure can be discretized by means of several finite elements. The assembling of all these elements to form the whole structure result in a large set of equations, which are suited to be solved by computers.

Finite element analysis of RC structures is a highly nonlinear problem due to the material nonlinearity of both concrete and reinforcement. The nonlinear problem can be solved, as shown in §2.4, using specific iterative solution algorithms which required high computational efforts. Nowadays, the refinement of knowledge on nonlinear constitutive material laws, which reduced the uncertainties related to the modeling, and the increasing of computers powers, which reduced the time required to run analyses, make it possible to perform nonlinear finite element analysis of RC complex structures subjected to several loading conditions.

Therefore, nonlinear finite element analysis (NLFEA), which was initially used in research studies to support experimental investigations and explain observed structural behaviour; has recently become a powerful design tool. In the design process, NLFEA provides the engineer with a refined verification of a structural solution by simulating structural response under different kinds of design actions. For these reasons, in design practices NLFEA can be used as an alternative to simplified traditional linear analysis. In traditional design, distribution of internal forces is carried out by linear analysis and safety is checked locally in sections. There are two important discrepancies worth mentioning in this approach. First, the elastic force distribution is one of the many possible states of equilibrium, which can be realistic at low load levels only. A significant force redistribution can occur due to inelastic response (e.g. compressive membrane action phenomenon in deck slabs, as discussed in this document). Second, the local section safety check of limit states is made under the assumption of nonlinear material behaviour (cracking, reinforcement yielding, etc.), which is not consistent with the elastic analysis of internal forces. Furthermore, the local safety check does not provide any information about overall structural safety. Nevertheless, this approach represents a very robust design method verified through many years of experience.

For all these reasons nonlinear finite element analysis (NLFEA) is becoming a useful tool for the design of new structures as well as for the assessment of existing ones. Furthermore, in new standard codes and guidelines, this type of analysis is proposed as an alternative, and more powerful, method of verification to the analytical calculation [Hendriks et al., 2012] and [*fib*-Model Code 2010]. In particular, the [*fib*-Model Code 2010] introduced the concept of levels of approximation (LoA) approach as a design strategy to estimate the response of structural members. LoA approach is based on the idea that all the analyses performed for the design of structural members, whether based on analytical calculation or NLFEA, are approximations of reality and these approximations can be done with different levels of accuracy: the higher the level of approximation, the higher the accuracy of the prediction, as well as the complexity and the time devoted to analysis. Particularly related to the topic of this thesis is the highest level of approximation, which is associated to numerical procedures such as NLFEA.

1.2 Objectives

The objective of this research is to provide tools that can help to improving the knowledge about NLFEA of reinforced concrete structures. In particular, the focus is pointed on the analysis of thin RC members (shear and slender walls, deep girders, deck slabs, nuclear containment vessels and offshore platforms).

A thin RC member can be analysed, by means of NLFEA, following several approaches, as widely explained in §2.2. From the simplified 1-D *beam elements* approach to the most complex 3-D *solid elements* approach. The first one is characterized by the discretization of the structural member into several beam elements and allows to capture only the flexural behaviour. For this reason, is suitable for modelling only simple slender members. On the other hand, the second one consists in using of continuum three-dimensional *solid elements* (as known as brick elements), defined in the global 3-D space and it is suitable for the modelling

of structures which present complex geometry and loading conditions (e.g. out-of-plane imposing load); nevertheless, this approach presents high computational costs and several uncertainties related to the modelling choices. In between this two approaches, the *shell elements* approach is suitable for modeling structures subjected to plane stress conditions since shell elements neglect the nonlinear behaviour due to shear along the thickness. However, compared to solid element models, a shell element model can provide more stable results and, furthermore, NLFEA carried out using shell elements enable to save time and computational efforts. The latter can prove to be an important advantage in case of meshes of full-scale structures or/and a lot load combinations and in general for the probabilistic assessment, which requires a lot of NLFEA.

In this research, several monotonic, cyclic and dynamic problems, solved by means of NLFEA, using multi-layer shell (MS) elements, are presented. The *multi-layer shell elements* approach, as widely discuss in §2.2.1, includes all the advantages related to the shell elements modelling, presented above, and furthermore it allows to subdivide the thickness of each element into several layers that can have different nonlinear properties (e.g. different reinforcement ratio).

The aim of this research is to assess that NLFEA carried out by means of MS elements, using a proper material nonlinear model, are able to predict the monotonic, cyclic and dynamic behavior of RC members subjected not only to in-plane load, but also to out-of-plane actions.

1.3 Methodology and personal contributions

A literature review of finite element formulation is included in **Chapter 2** in order to make the reader familiar with the topic of this research. In §2.2 a brief review of the different modelling approaches suitable for modelling RC thin structural members is presented, focusing on the multi-layer shell (MS) element approach which is the one adopted within this work. In §2.2.1 the multi-layer shell element approach is widely presented in order to highlight not only its potential, but also its deficiencies. In §2.3 the focus is pointed on different constitutive laws, presented in literature, able to model the cyclic response of reinforced concrete. Finally, in §2.4 a brief review of the different methods used by the finite element codes to solve the nonlinear equations in static and dynamic fields is presented.

In **Chapter 3** the capability of NLFEA, using multi-layer shell elements, to predict the nonlinear behaviour of RC members under monotonic loading is assessed. For the analysis presented in Chapter 3 the nonlinear material behaviour in employed using the *PARC_CL 1.0* (Physical Approach for Reinforced Concrete under Cyclic Load) crack model. The *PARC_CL 1.0* crack model, developed at the University of Parma in 2013 [Belletti et al., 2013[a]], is a fixed crack model which allows to consider the nonlinear behaviour of both concrete and steel reinforcement under cyclic condition; however, the cyclic condition is obtained considering an unloading-reloading branch secant to the origin as discussed in §3.2. The *PARC_CL 1.0* crack model is not implemented by the author of this research, however, some of its applications are presented in Chapter 3 since they are considered quite important for the overall aim of the work.

In particular in §3.3 the simulation of the **out-of-plane monotonic behaviour of RC slabs** is presented. As already stated, the MS element approach does not allow to capture the out-of-plane shear failure modes because the nonlinear behaviour due to shear along the thickness of the element is not considered. To overcome this problem in §3.3 a post-processing of the NLFEA results is conducted based on the Critical Shear Crack Theory (CSCT). CTCT, as reported in [Muttoni, 2008] and [Muttoni and Fernandez, 2008[a]], allows to calculate shear and punching shear resistance based on few fundamental parameters, such as respectively the axial strain at mid-depth and the out-of-plane rotation of the element. The results reported in §3.3 highlighted the capability of such kind of modelling, post-processed according to the CSCT, to predict the shear out-of-plane failure of slabs; moreover, using NLFEA the effect of compressive membrane action (CMA) on structural resistance assessment can also be taken in consideration, from the compressive actions automatically arising from the boundary and loading conditions of the model, as shown in §3.3.4.

In §3.4 the simulation of the **in-plane cyclic behaviour of a RC squat walls** is presented. The results presented in §3.4 highlighted the capability of *PARC_CL 1.0* crack model to predict the envelope behaviour of the experimental pseudo-dynamic tests. On the other hand the results presented in §3.4 showed that the secant unloading behaviour of such crack model is not able to realistically reproduce the cyclic response.

In order to properly model the cyclic behaviour of RC members a new crack model has been implemented within this research, the *PARC_CL 2.0* crack model, as discussed in **Chapter 4**. The *PARC_CL 2.0* crack model, widely described in §4.2, allows to take into account the plastic and irreversible deformation that occurs during the unloading phase and to consider, this way, the hysteretic cycles of both concrete and steel reinforcement. Moreover, in order to take into account the energy dissipation mechanism that characterises structural vibrations, the Rayleigh stiffness proportional damping is implemented in the model. The new implemented model was primarily validated by means of comparison with experimental outcomes on simple RC panels subjected to cyclic load. In order to highlight the improvement produced by the *PARC_CL 2.0* crack model in the prediction of the **cyclic in-plane behaviour** of a RC members, the same **squat walls** analysed with the *PARC_CL 1.0* crack model in §3.4, are analysed in §4.3 using the PARC_CL 2.0 crack model.

Finally in §4.4, the PARC_CL 2.0 crack model was adopted to analyse the **out-of-plane instability of RC slender walls** subjected to cyclic horizontal loading. RC walls are commonly used as the primary lateral force-resisting system for medium to high-rise buildings. Nevertheless, despite many years of research and subsequent evolution of code provisions, several RC walls still underperform when subjected to seismic actions. The observation of the damages occurred in some recent seismic events (Chile, 2010 and New Zealand, 2011) highlighted that many walls, in their failed configuration, were characterized by large out-of-plane displacements. The failure of these structural walls was, hence, caused or highly influenced by out-of-plane buckling (also defined as out-of-plane instability), which is triggered in the end region of the wall. It is to be pointed out that this deformation mode may be the result of the application of pure in-plane cyclic loading. As shown in §4.4 this phenomenon is strictly related to the opening and closing crack phenomenon and to the

hysteretic cycles of steel. For these reasons the PARC_CL 2.0 crack model, which considers the cyclic behaviour of concrete and steel reinforcement, seems to be suitable to model this particular failure mode.

Three different specimens were analysed: in §4.4.1 two “T shaped” walls were studied, subjected respectively to in-plane horizontal cyclic loading (TW1 specimen) and a combination of in-plane and out-of-plane horizontal cyclic load (TW4 specimen); in §4.4.2 a “U shaped” wall subjected to cyclic load was analysed.

In short, the main personal contributions of this thesis on the topic of nonlinear finite element analysis of RC members can be resumed as follow:

- Assessment of the capability of NLFEA to model in a sound manner several mechanisms not straightforward to capture analytically, especially associated to strong nonlinear behaviour;
- Demonstrate that MS elements are able to predict not only the in-plane behaviour of RC members but also, using a post-processing method according to the CSCT, to capture the out-of-plane shear failure. Moreover, the MS element approach, with respect to the common solid element approach, allows to reduce computational time and uncertainties;
- Implementation of the *PARC_CL 2.0* crack model, which allows to properly model the cyclic hysteretic behaviour of concrete and steel reinforcement and, also, to account for the energy dissipation on material level, due to stiffness-proportional damping;
- Validation of the implemented *PARC_CL 2.0* crack model by means of comparison with experimental tests and demonstration that using the PARC_CL 2.0 crack model, associated to MS elements, it is possible to capture not only the in-plane cyclic behaviour of RC members but also the out-of-plane instability, strictly related to the opening and closing of cracks.

Finally, in order to make the reader comfortable with this document, in Figure 1.1 is graphically reported the scheme of the document, with underlined the main topics covered in each chapter.

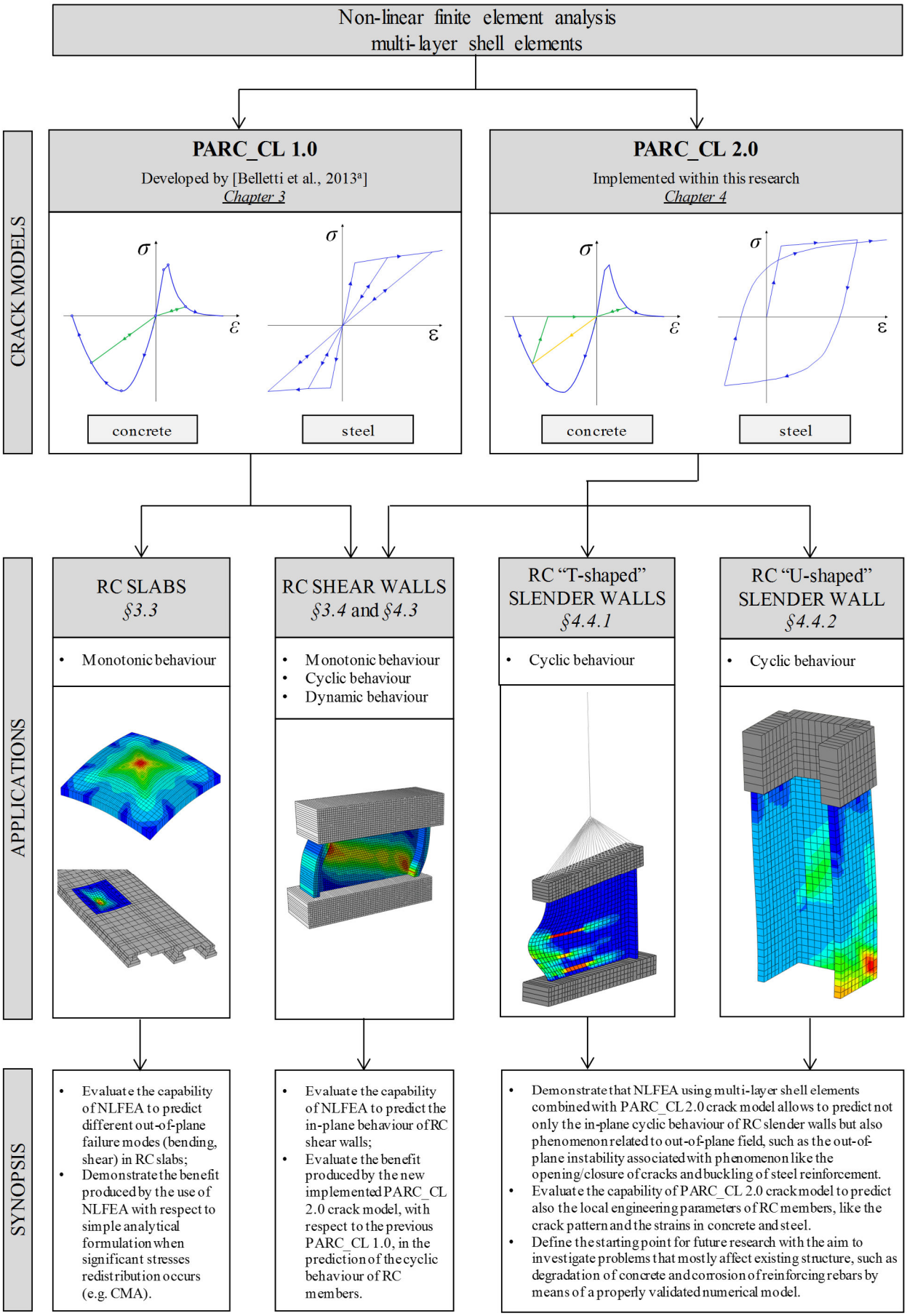

Figure 1.1 – Scheme of the document.

2 State of art

"Le doute n'est pas un état bien agréable,
mais l'assurance est un état ridicule."

Letter to Frederick William, Prince of Prussia
Voltaire, 28 November 1770

2.1 Finite element formulation

The rapid development of computers has completely "revolutionized" research and practice in every scientific and engineering field. The finite element method has long been a fertile research field. It has also been increasingly used as a research tool for numerical experiment. Most importantly, the finite element method has become an analysis and design tool used routinely by structural engineers. The finite element method in structural analysis is a technique that first divides a structure into a set, or different sets, of structural components. These components would share some similar geometric pattern and physical assumption and are defined with a specific kind of finite element which has a specific type of structural shape and is interconnected with the adjacent elements by nodal points. Acting at each node point are nodal forces, and the node is subjected to displacements (degrees of freedom). Thus for each element, a standard set of simultaneous equations can be formulated to relate these physical quantities. Physically assembling these elements to form the whole structure is equivalent to mathematically superimposing these element equations. The result is a large set of simultaneous equations, which are suited for solution by computer. Upon implementing the loading cases and boundary conditions for structural problems, the assembled set of equations can be solved and the unknown parameter can be found. The substitution of these values to the element formulation provides the distributions of stress and displacement. This solution procedure is called 'Finite Element Analysis' (FEA).

FEA can be applied to different structural members in structural engineering: in particular, for the purpose of this thesis, the focus is pointed on thin reinforced concrete (RC) members, such as shear walls, deck slabs, deep girders, nuclear containment vessels and offshore platforms, as shown in Figure 2.1.

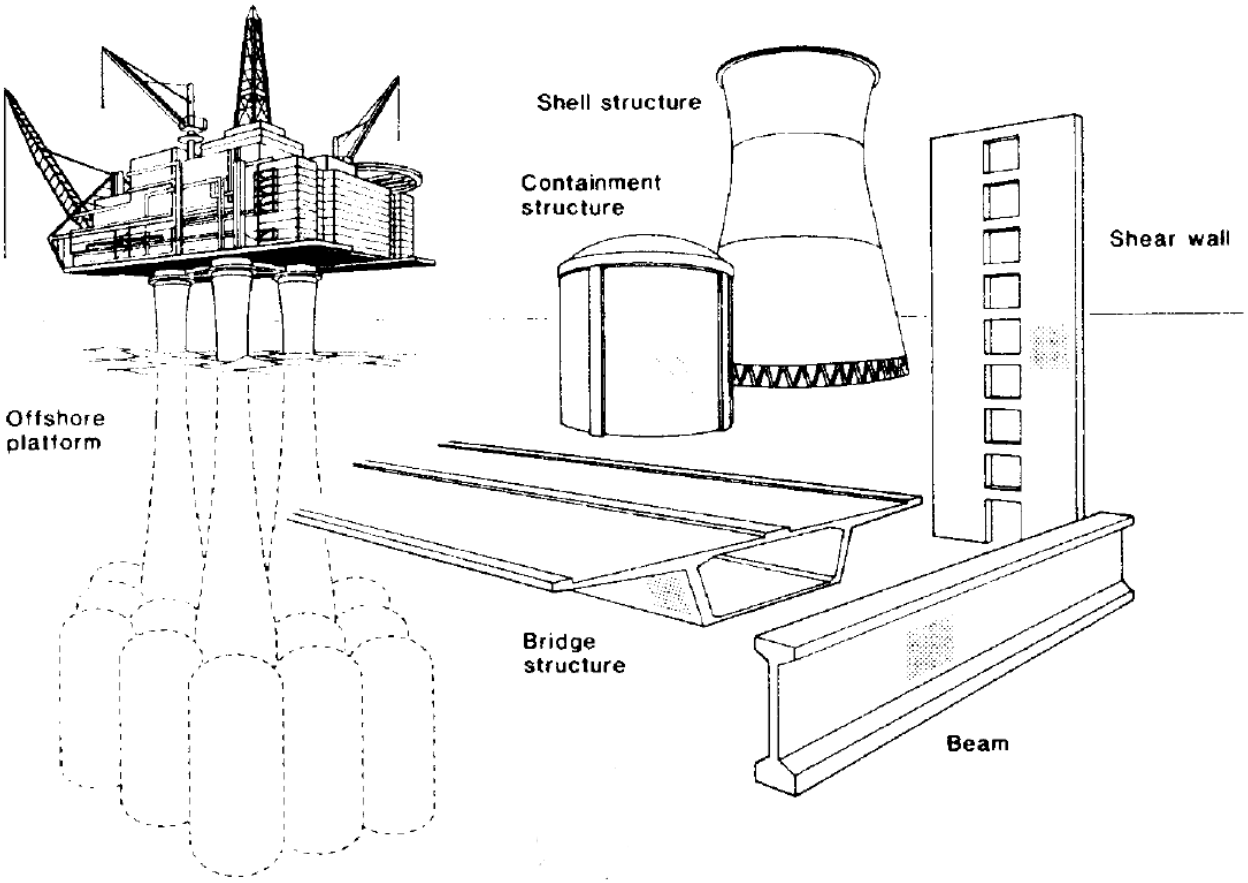

Figure 2.1 – Examples of thin RC members [Vecchio and Collins, 1986].

The behaviour of such whole structures, that is usually a highly nonlinear problem because of the nonlinear constitutive relationships of reinforcement and concrete, can be predicted by performing FEA.

2.2 Different modelling approaches

The nonlinear behaviour thin reinforced concrete (RC) members can be simulated with several different approaches: a frame approach using *beam elements* (considering lumped or distributed plasticity), a *shell elements* approach, a *solid elements* approach and a *discrete* approach. All these different approaches are briefly described in the following, highlighting the advantages and the disadvantages associated to each one.

The *beam elements* approach is widely used in structural engineering: in particular, such approach has proved to be very suitable for modelling frame structures [Yazgan and Dazio, 2011]. The main advantages associated to this modelling approach are related to the accuracy in the global response prediction and to the computational efficiency. On the other hand, while slender frame structures tend to exhibit a response dominated by flexural behaviour, other kind of structures (e.g. wall structures) combine different mechanisms which are not easy to capture with *beam elements*. In particular, it is difficult to capture the shear contribution (associated to the development of inclined crack), the interaction between the element and the foundation or the interaction with other adjacent elements, (associated to torsional effects). The nonlinear flexural behaviour

can be assessed using two different models. The *lumped plasticity* models allow to concentrate the nonlinearity in some limited part of the element. This approach is simpler and computationally lighter but, on the other hand, it requires a lot of experience by the operator to establish the nonlinear behaviour and the characteristic length of the nonlinear parts. On the contrary, the *distributed plasticity* models (also known as fibre models) allow to capture the spread of nonlinearity through the whole member. To obtain this, the cross section of the element is discretized in several fibres with a nonlinear behaviour. As already stated, using *beam elements* it is not possible to account for shear deformation; to solve this lack, several authors such as [Beyer et al., 2008[a]], [Oesterle et al., 1984], introduce zero-length shear spring at mid-height of each wall with an average stiffness between cracked and uncracked condition. Nevertheless, this approach can not capture the shear failure modes and so its applications are limited to particular case studies.

A completely different approach is the *solid elements* approach, in which the structural member is subdivided into several three dimensional finite elements characterized at each node by translational degrees of freedom. Typical applications of solid elements are the analysis of voluminous structures like concrete foundations and off-shore structures, thick walls and floors, soil masses. This approach can describe the geometry of the structure, especially the connection of adjacent members (e.g. walls and slabs), more accurately than *beam* or *shell* element models. Moreover, due to the fact that these elements are defined in the 3-D space, they can capture different failure modes, related to flexural and shear behaviour both in-plane and out-of-plane. However, because of their tendency to produce large systems of equations, this approach is usually applied only when other approaches are unsuitable or would produce inaccurate analysis results.

A further accurate approach to model the nonlinear behaviour of RC members is the *discrete* approach, in which a structure is idealized as an assemblage of rigid bodies connected by normal and tangential springs. The Rigid-Body-Spring Model (RBSM), developed by [Kawai, 1977], is one of the discrete-type methods, in which concrete is partitioned into an assemblage of regular cells. Since cracks are constrained to follow cell boundaries, regularity in the mesh design may strongly influence crack directions. To minimize this influence and to automate the meshing process, [Bolander et Satio, 1998] introduced a random geometry to the RBSM mesh using Voronoi tessellation. Discrete-type numerical methods have advantages in modeling localized phenomena until failure stage, such as cracking, its propagation, frictional shear slip, compressive failure and so on.

The last numerical approach, introduced above, was characterized by *shell elements*, which is the approach adopted in this thesis and hence it is widely described in the following.

2.2.1 Shell elements and multi-layer shell elements

Shell elements can be considered as a simplification, with respect to solid element, based on two main hypotheses.

The first one is the well-known assumption that a plane section remains a plane before and after deformation. For thick shell elements the shear deformation may became significant and this fact has to be

taken into account. It can be considered by allowing the cross-section to be non-perpendicular to the mid surface but still a plane after deformation. This is known as Reissner-Mindlin assumption and it is schematically reported in Figure 2.2.

The second consideration is that stresses, acting normal to the mid-surface of the shell elements, are negligible.

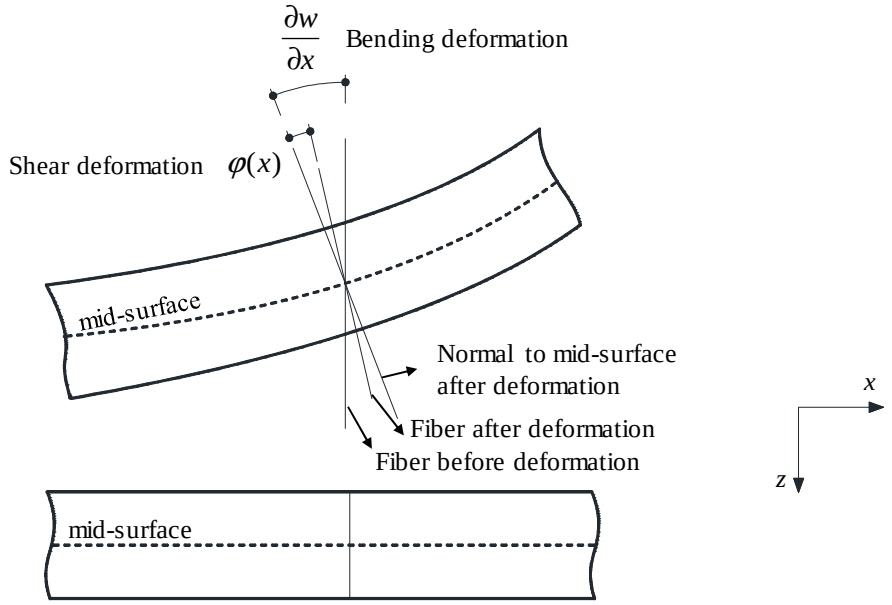

Figure 2.2 – Reissner-Mindlin assumption for out-of-plane deformation of shell elements.

Based on these assumptions a solid element (e.g. 20 nodes quadratic element) can degenerate to a shell element (e.g. 8 node shell element), as shown in Figure 2.3.

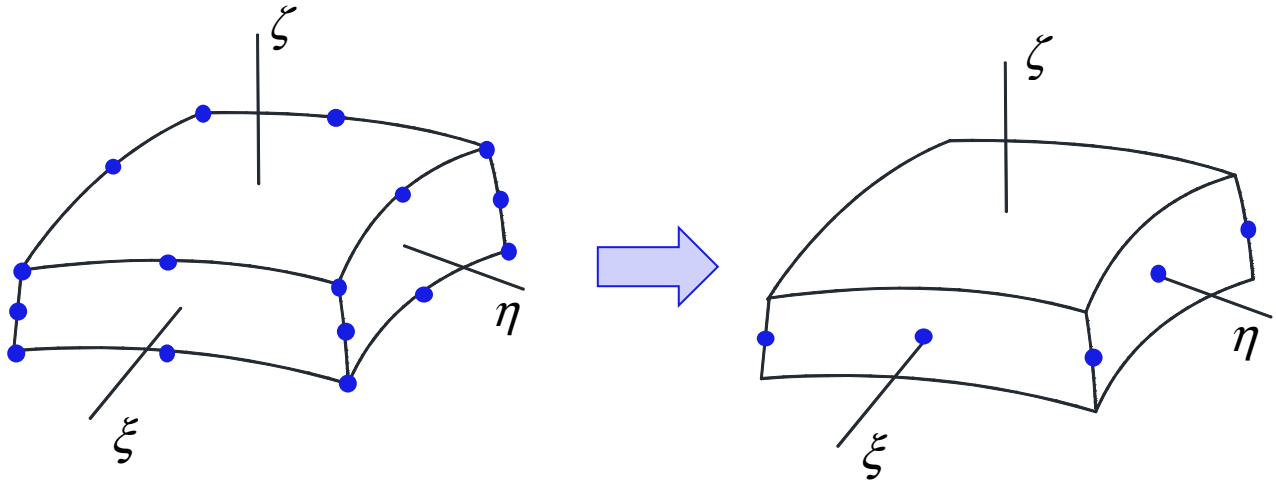

20 nodes three dimensional *solid element*

8 nodes three dimensional *shell element*

Figure 2.3 – Degeneration for solid element to shell element.

The resulting element has five degrees of freedom for node: three translations (u, v, w) and two rotations (θ_x, θ_y), hence the displacement field can be expressed as in Eq.(2.1).

$$\{u\} = \begin{Bmatrix} u \\ v \\ w \\ \theta_x \\ \theta_y \end{Bmatrix} \tag{2.1}$$

The degrees of freedom are defined at the mid-surface of the element thickness. Based on the Reissner-Mindlin assumption, the displacement at each node of the shell element can be decomposed into membrane and bending terms and expressed as:

$$u(x, y, z) = u_0(x, y) - z \cdot \theta_x(x, y) \tag{2.2}$$

$$v(x, y, z) = v_0(x, y) - z \cdot \theta_y(x, y) \tag{2.3}$$

$$w(x, y, z) = w_0(x, y) \tag{2.4}$$

where $u_0(x,y)$ and $v_0(x,y)$ are in-plane membrane displacements in x- and y- directions respectively, $w_0(x,y)$ is the transverse out-of-plane displacement in z-direction and $\theta_x(x,y)$ and $\theta_y(x,y)$ are rotations about y- and x- axes respectively.

The strain field can be computed by differentiating the displacement field. The generalized strain and related forces can by subdivided into in-plane and out-of-plane.

The generalized in-plane strains in the mid-surface can be written as:

$$\varepsilon_x = \frac{\partial u}{\partial x} = \frac{\partial u_0}{\partial x} - z \cdot \frac{\partial \theta_x}{\partial x} \tag{2.5}$$

$$\varepsilon_y = \frac{\partial v}{\partial y} = \frac{\partial v_0}{\partial y} - z \cdot \frac{\partial \theta_y}{\partial y} \tag{2.6}$$

$$\gamma_{xy} = \frac{\partial u}{\partial y} + \frac{\partial v}{\partial x} = -z \cdot \left(\frac{\partial \theta_x}{\partial y} + \frac{\partial \theta_y}{\partial x} \right) \tag{2.7}$$

The generalized out-of-plane strains in the mid-surface can be written as:

$$\varepsilon_z = \frac{\partial w}{\partial z} = 0 \tag{2.8}$$

$$\gamma_{xz} = \frac{\partial u}{\partial z} + \frac{\partial w}{\partial x} = \frac{\partial w_0}{\partial x} - \theta_x \tag{2.9}$$

$$\gamma_{yz} = \frac{\partial v}{\partial z} + \frac{\partial w}{\partial y} = \frac{\partial w_0}{\partial y} - \theta_y \tag{2.10}$$

For numerical integration, the stress profile along the thickness must be known at a reasonable number of points (defined integration point) in order to reproduce the variation of in-plane strains in the depth of the element.

The layered approach, based on the definition of the so called multi-layer shell elements, allows to subdivide the shell element into several layers along its depth. In each layer, the equations just reported remains valid and they can be applied to the mid-depth of each layer. It is important to consider that each layer of the element can have different thickness and the number of layers can be different in each element. Moreover, different constitutive laws can be applied to each layer in order, for example, to locate the reinforcement along the element thickness in the exact position.

The just introduced constitutive laws is used to obtain the internal stresses from the generalized strains. Finally, by integrating the internal stresses along the thickness of the element, the internal forces, shown in Figure 2.4, can be calculated.

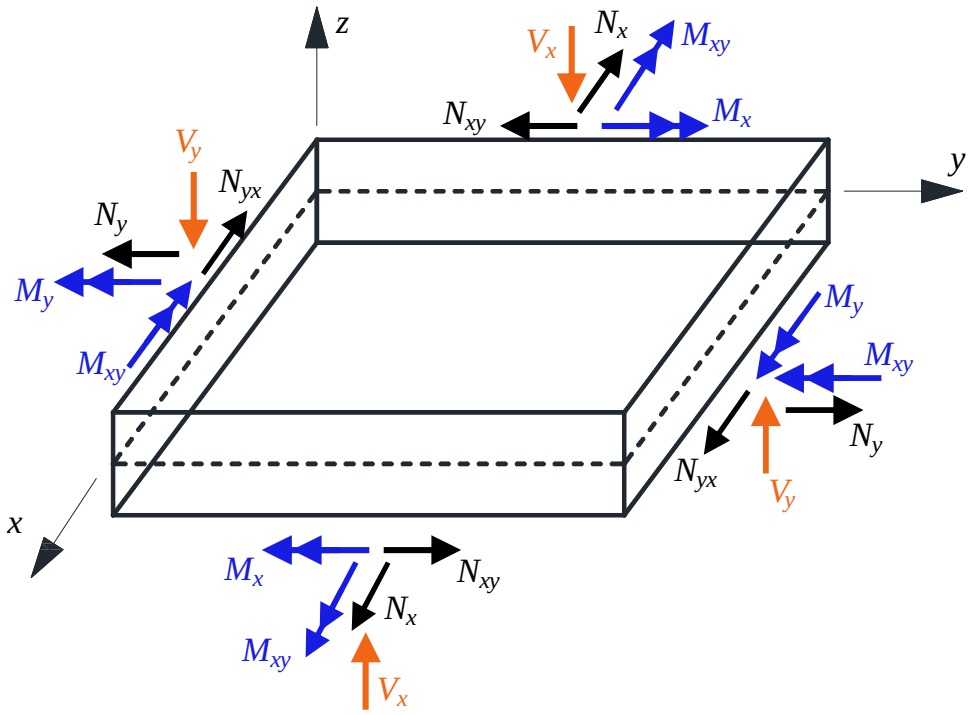

Figure 2.4 – Internal forces acting on the element.

The in-plane stresses vector, can be written as follow:

$$\begin{Bmatrix} \sigma_x \\ \sigma_y \\ \tau_{xy} \end{Bmatrix} = [D] \cdot \begin{Bmatrix} \varepsilon_x \\ \varepsilon_y \\ \gamma_{xy} \end{Bmatrix} \tag{2.11}$$

where [*D*] represents the stiffness in-plane constitutive matrix.

The internal in-plane forces, including membrane forces (*N*) and bending moments (*M*) can be computed by integrating the internal in-plane stresses of Eq.(2.11)

$$N_x = \int_{-t/2}^{+t/2} \sigma_x dz \tag{2.12}$$

$$N_y = \int_{-t/2}^{+t/2} \sigma_y dz \tag{2.13}$$

$$N_{xy} = \int_{-t/2}^{+t/2} \tau_{xy} dz \tag{2.14}$$

$$M_x = \int_{-t/2}^{+t/2} z \cdot \sigma_x dz \tag{2.15}$$

$$M_y = \int_{-t/2}^{+t/2} z \cdot \sigma_y dz \tag{2.16}$$

$$M_{xy} = \int_{-t/2}^{+t/2} z \cdot \tau_{xy} dz \tag{2.17}$$

where t is the thickness of the element, or the thickness of each layer if multi-layered approach is adopted.

On the other hand, the out-of-plane stresses vector, can be written as follow:

$$\begin{Bmatrix} \tau_{xz} \\ \tau_{yz} \end{Bmatrix} = [G] \cdot \begin{Bmatrix} \gamma_{xz} \\ \gamma_{yz} \end{Bmatrix} = \begin{bmatrix} G_C & 0 \\ 0 & G_C \end{bmatrix} \cdot \begin{Bmatrix} \gamma_{xz} \\ \gamma_{yz} \end{Bmatrix} \tag{2.18}$$

where [G] represents the stiffness out-of-plane constitutive matrix.

As just shown for the in-plane forces, the internal out-of-plane forces (also defined transverse shear forces, V), can be computed by integrating the internal out-of-plane stresses of Eq.(2.18):

$$V_x = \int_{-t/2}^{+t/2} \tau_{xz} dz \tag{2.19}$$

$$V_y = \int_{-t/2}^{+t/2} \tau_{yz} dz \tag{2.20}$$

In order to simplify, several finite element codes assume linear relations between out-of-plane strains and out-of-plane stresses (it means to assume G_C as constant in Eq.(2.18), where G_C is the out-of-plane shear modulus of concrete). For thin shells, the shear deformation is relatively small compared with the flexural deformation, hence the linear relationship defined above is considered sufficient. On the other hand, due to the fact that such approach do not consider the nonlinear shear behaviour along the thickness, it is not able to capture shear or punching shear out-of-plane failure.

The multi-layer shell element provided by ABAQUS code [Abaqus 6.12, 2012] and adopted for FEA in this thesis is based on the presented approach.

In order to overcome the deficiencies related to the adopted approach and associated to the impossibility to predict out-of-plane shear failure, in this work it is proposed a post-processing procedure of the FEA results. This procedure, as widely explained §3.3, allows to predict shear failure and punching shear failure in RC slabs by post-processing the FEA using a proper failure criterion.

Nevertheless, the main topic of this research regards the definition of a proper in-plane constitutive law, as shown in Eq.(2.11), that is able to reproduce the nonlinear behaviour of reinforced concrete members subjected to cyclic loading. In order to make the reader familiar with this topic, in the following section a brief review of constitutive laws for the in-plane behaviour of reinforced concrete structures is presented.

2.3 Constitutive laws for reinforced concrete members

The analyses of RC structures subjected to general loading conditions require realistic constitutive laws and analytical procedures to produce accurate simulations of behaviour. In literature, different approaches have been used for material modelling. These include *plasticity models*, *damage mechanics models*, and *nonlinear elastic models*. In the latter case, it can be distinguishing between *discrete crack models* to *smeared crack models* and from fixed crack models to rotating crack models.

Commonly used frameworks are *plasticity*, *damage mechanics* and combinations of plasticity and damage mechanics. Stress-based *plasticity models* are useful for the modelling of concrete subjected to triaxial stress states, since the yield surface corresponds at a certain stage of hardening to the strength envelope of concrete ([Grassl et al., 2002] and [Cervenka and Papanikolaou, 2008]). Furthermore, the strain split into elastic and plastic parts represents realistically the observed deformations in confined compression, so that unloading and path dependency can be described well. However, plasticity models are not able to describe the reduction of the unloading stiffness that is observed in experiments. Conversely, *damage mechanics* models are based on the concept of a gradual reduction of the elastic stiffness [Mazars and Pijaudier-Cabot, 1989]. Furthermore, the stiffness degradation in tensile and low confined compressive loading observed in experiments can be described. However, isotropic damage mechanics models are often unable to describe irreversible deformations observed in experiments and are mainly limited to tensile and low confined compression stress states. On the other hand, combinations of isotropic damage and plasticity are widely used to model both tensile and compressive failure and many different models have been proposed in the literature [Grassl and Jirasek, 2006]. These kinds of constitutive laws allow a physical description of crack initiation and growth but remain delicate to use for severe loadings.

A different approach is based on *nonlinear elastic models*, range from *discrete crack models* to *smeared crack models.* The *smeared crack* approach tends to be the procedure most commonly employed. All the smeared models are based on the assumption that the first crack is developed perpendicular to the principal tensile direction. After cracking, the material loses his isotropic behavior and can be described with

an orthotropic model, defined along the orthotropic directions *1-2*. The smeared crack models can be divided into two categories: *fixed crack models* and *rotating crack models*. The fixed crack approach is based on the hypothesis that after cracking the crack inclination and so the *1,2* coordinate system is fixed; on the other hand, the rotating crack approach allows the crack rotation after first cracking.

Researchers working in each of these areas generally have been successful in producing models that yield results of acceptable accuracy for conditions of monotonic loading. Models that provide accurate simulations of behaviour under general loading conditions, and specifically under reversed cyclic loading, are less common. For such formulations, the *smeared crack* approach can be the most favourite. [Okamura and Maekawa, 1991] have documented models assuming *fixed cracks* directions and have demonstrated good correlation to experimental results. [Stevens, 1987] used a more comprehensive constitutive modelling approach for concrete in *rotating smeared crack* content, however the tangent stiffness approach used by [Stevens, 1987] gave numerical difficulties under cyclic conditions. For the same reason, in order to design reinforced concrete (RC) structures in earthquake regions, a cyclic softened membrane model (CSMM) is presented by [Hsu and Mo, 2010] as an extension of the softened membrane model for monotonic shear behaviour. The cyclic crack model, proposed by [Hsu and Mo, 2010] seems to be in good agreement with experimental outcomes. On the other hand, associated to nonlinear finite element analysis, it presented the disadvantages that some branches, defining the unloading-reloading path, are not defined with an explicit formulation as a function of strains, increasing the computational efforts.

2.4 Computational resolution of nonlinear finite element problems

Defined the constitutive laws, in §2.3, and the modelling approaches, in §2.2, in this section a brief review of the numerical solution adopted by finite element codes to solve the nonlinear equations of equilibrium is reported.

As stated above, many real problems, related to the modelling of RC structural response, involve nonlinear behaviour, which is characterized by a not proportional relationship of cause and effect unlike linear systems.

Compared to linear problem, nonlinear ones are not well developed and understood. According to the finite element modelling, the well-known equation of equilibrium reported in Eq.(2.21), obtained in the linear solution, is no longer valid for nonlinear problems because of stiffness matrix [*K*] does not necessarily remain constant.

$$[K]\cdot\{u\}=\{F\} \tag{2.21}$$

Depending on the type of nonlinearity, stiffness matrix will have to be updated many times during the solution procedure. This process of updating will produce a significant increase in time needed to obtain the results. So, a numerical approximation of the exact solution can be obtained using two different approaches divided in *explicit* and *implicit* methods.

The *explicit* methods allow obtaining explicitly the state of the system at a certain time *t*, as a function of the parameters calculated at the previous time step, *t-1*.

On the other hand, the *implicit* methods find a solution of the system by solving equations involving both the current step time, *t*, and the previous one, *t-1*. This approach, also called "Euler time integration scheme", is unconditionally stable instead of *explicit* methods. The disadvantage related to this type of formulation is that the algorithm requires higher computational efforts due to the calculation of the inverse of stiffness matrix.

Today, thanks to the establishment of the material constitutive relationships, the improvement of the finite element method, and the rapidly increasing of computer power, it is possible to perform nonlinear FEA on reinforced concrete structures subjected to reversed cyclic static or dynamic loading.

2.4.1 Cyclic static nonlinear problems

The aim of nonlinear analysis is to solve the set of equations presented in Eq.(2.21), considering that, as just pointed out, the stiffness matrix [*K*] itself is a function of displacement, and so can be written as [*K(u)*].

The solution of Eq.(2.21) can be obtained following two main different approaches: an "incremental predictor" method and an "iterative corrector" method.

According to the "incremental predictor" solution method, shown in Figure 2.5, each solution step is approximated with a line segment.

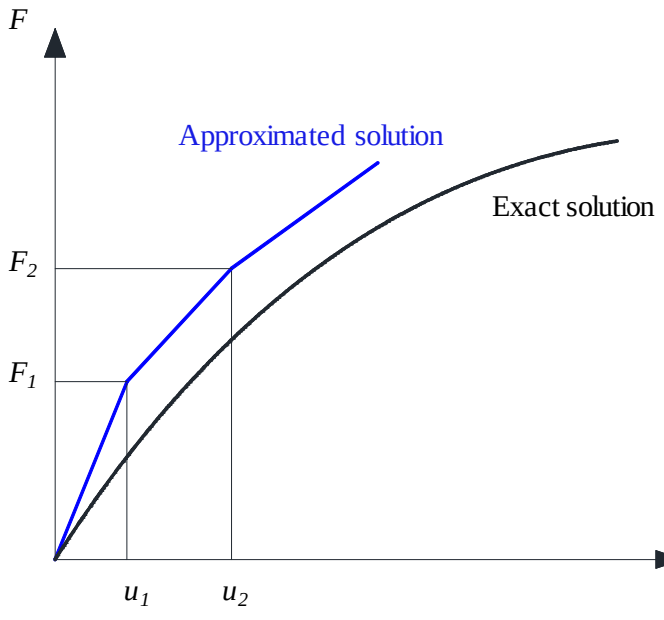

Figure 2.5 – "incremental predictor" method for resolution of nonlinear problems.

Figure 2.5 shows how at each step the approximated solution of the nonlinear system diverges from the exact solution. To correct this problem, the so called "iterative corrector" method was employed.

Two different variations of the "iterative corrector" method can be defined:

- Newton-Raphson method;
- Modified Newton-Raphson method;

The most common implementation of the Newton-Raphson approach combines the incremental and the iterative solutions. In the case shown in Figure 2.6, the tangential solution can be used as a starting point (predictor) for the solution process, followed by subsequent iterations based on newly computed stiffness matrices. In this approach, a load vector "imbalance" is calculated upon completion of each iteration step. This imbalance vector, represents the difference between the forces corresponding to the element stresses and the applied external load. The computer program performs a linear solution based on the imbalance load vector, and checks for convergence. If the convergence is not achieved, the imbalance vector is recomputed, followed by the updating of the stiffness matrix and the FE set of equations are solved again to obtain a new solution. Until convergence has been achieved, this iterative process is continued, otherwise the problem cannot be adequately solved.

The Newton-Raphson approach can become very expensive in large DOF problems due to the fact the tangent stiffness matrix [*K*] must be computed for each iteration step.

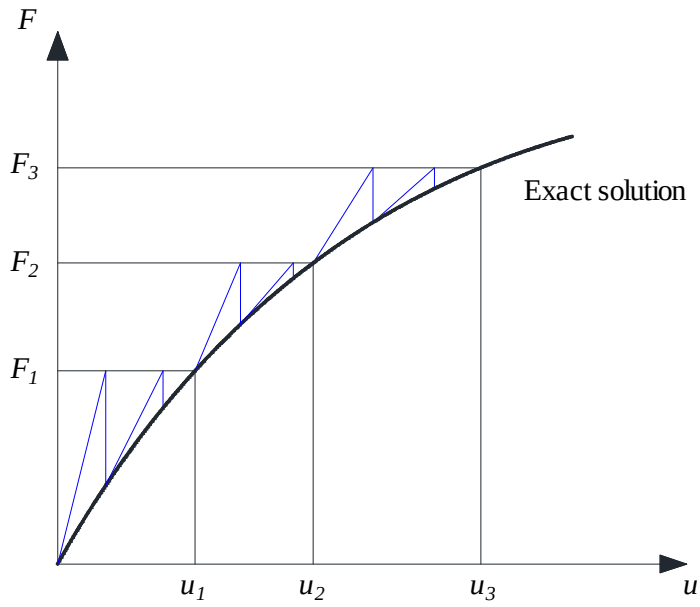

Figure 2.6 – Newton-Raphson method for resolution of nonlinear problems.

An alternative method is known as the Modified Newton-Raphson approach (shown in Figure 2.7). In this method the tangent stiffness matrix is not updated, and iterations at each load step are performed using the same initial stiffness matrix. While this reduces the number of stiffness matrix computations, the number of equilibrium iterations to achieve convergence increases considerably. The equilibrium iteration and the choice of initial tangent stiffness are more critical for hardening structure. A wrong first choice may lead to a divergent solution irrespective of subsequent attempt.

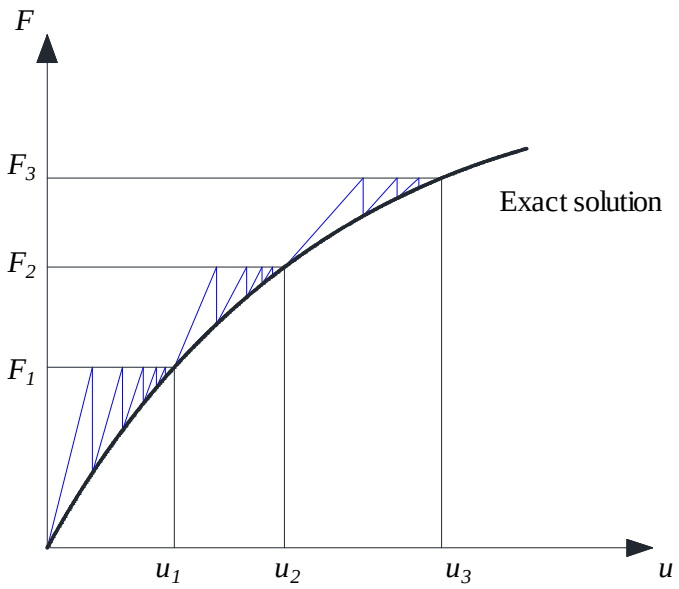

Figure 2.7 – Modified Newton-Raphson method for resolution of nonlinear problems.

In some nonlinear static analyses, the use of the Newton-Raphson method alone causes a non-unique tangent stiffness matrix (i.e the stiffness matrix may become singular) and a severe convergence difficulty. Such occurrences include nonlinear buckling analyses in which the structure either collapses completely or "snaps through" to another stable configuration. For such situations, it is possible to activate an alternative iteration scheme, the “arc-length method”, to help avoid bifurcation points and track unloading, Figure 2.8. The arc-length method causes the Newton-Raphson equilibrium iterations to converge along an arc, thereby often preventing divergence, even when the slope of the load vs. deflection curve becomes zero or negative. Therefore, this method (or some variation of it) is commonly employed in the nonlinear post-buckling analysis.

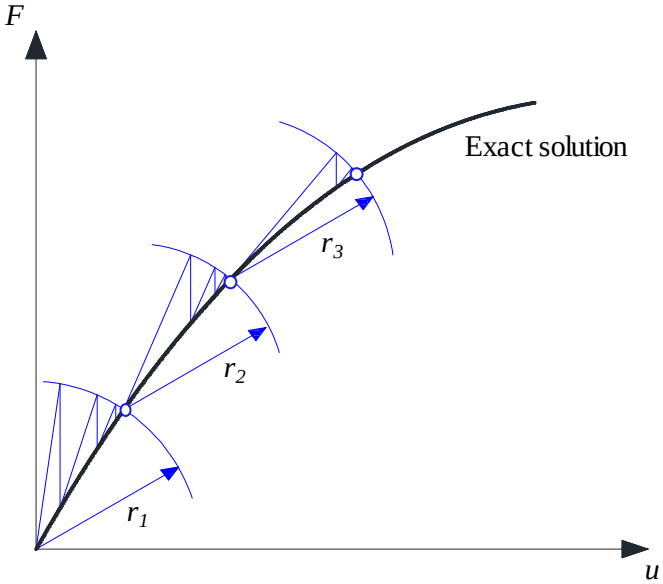

Figure 2.8 – “Arc-length” method for resolution of nonlinear problems.

For all the three different solution methods proposed above, at each load step, the equilibrium iterations are said to converge when the numerical solution is deemed to be "close enough" to the exact solution. This convergence can be addressed using different convergence criteria. A typical convergence criterion is based on the Euclidean norm error defined as:

$$error = \frac{\left\| e_f \right\|}{\left\| R_i \right\|} \tag{2.22}$$

where $\left\| e_f \right\|$ is the SRSS (square root of the sum of the squares) of the current iteration load imbalances for all DOF's of the system and $\left\| R_i \right\|$ is the SRSS of the current external load applied to all DOF's. When the error drop under a certain imposed tolerance the iteration may be terminated and the current iteration is said to have converged. The same ratio can be defined for quantities such as displacements, strain energy norms, etc.

2.4.2 Dynamics problems

The aim of nonlinear dynamics analysis is to solve the equation of motion proposed in the following form:

$$[M]\cdot\{\ddot{u}\}+[C]\cdot\{\dot{u}\}+[K(u)]\cdot\{u\}=\{F\} \tag{2.23}$$

To solve Eq.(2.23) Newmark's method [Newmark, 1959] is well-known implicit methods.

The relationships of displacements, velocities and accelerations from step *i* to step *i+1* can be written as:

$$\dot{u}_{i+1} = \dot{u}_i + (\Delta t)\cdot\ddot{u}_i \tag{2.24}$$

$$u_{i+1} = u_i + (\Delta t)\cdot\dot{u}_i + 0.5\cdot(\Delta t)\cdot\ddot{u}_i \tag{2.25}$$

where u_i , $\dot{u}_i$ and $\ddot{u}_i$ represent the displacement, velocity and acceleration at step *i* respectively and Δt is the time interval.

For the solution of this system, Newmark [Newmark, 1959] proposed an algorithm based on the following interpolations of displacements, velocities and accelerations from step *i* to step *i+1*.

$$\dot{u}_{i+1} = \dot{u}_i + \left[(1-\gamma)\cdot\Delta t\right]\cdot\ddot{u}_i + (\gamma\cdot\Delta t)\cdot\ddot{u}_{i+1} \tag{2.26}$$

$$u_{i+1} = u_i + (\Delta t)\cdot\dot{u}_i + \left[(0.5-\beta)\cdot(\Delta t)^2\right]\cdot\ddot{u}_i + \left[\beta\cdot(\Delta t)^2\right]\cdot\ddot{u}_{i+1} \tag{2.27}$$

where β and γ are parameters defining the variation of displacement velocity and acceleration in the Newmark's method.

Typical values of γ and β are $\gamma = 1/2$ and $1/6 \le \beta \le 1/4$. Changing these values two special cases can be defined: the 'average acceleration method', which is unconditionally stable, is characterized by $\gamma = 1/2$ and

$\beta = 1/4$. On the other hand, the 'linear acceleration method' is characterized by $\gamma = 1/2$ and this method is stable if $\Delta t / T_n \leq 0.551$, where T_n is the shortest natural period of the structure.

The incremental formulation, required by the nonlinear system, can be derived from Eq.(2.26) and Eq.(2.27) and written as:

$$\Delta \dot{u}_i = (\Delta t) \cdot \ddot{u}_i + (\gamma \cdot \Delta t) \cdot \Delta \ddot{u}_i \tag{2.28}$$

$$\Delta u_i = (\Delta t) \cdot \dot{u}_i + \frac{(\Delta t)^2}{2} \ddot{u}_i + \beta \cdot (\Delta t)^2 \cdot \Delta \ddot{u}_i \tag{2.29}$$

where Eq.(2.29) can be solved as:

$$\Delta \ddot{u}_i = \frac{1}{\beta \cdot (\Delta t)^2} \cdot \Delta u_i - \frac{1}{\beta \cdot (\Delta t)} \dot{u}_i - \frac{1}{2 \cdot \beta} \ddot{u}_i \tag{2.30}$$

Substituting Eq.(2.30) into Eq.(2.28) it can be obtain:

$$\Delta \dot{u}_i = \frac{\gamma}{\beta \cdot \Delta t} \cdot \Delta u_i - \frac{\gamma}{\beta} \dot{u}_i + \Delta t \cdot \left(1 - \frac{\gamma}{2 \cdot \beta}\right) \ddot{u}_i \tag{2.31}$$

Finally the equation of motion, reported in Eq.(2.23), can be written in incremental form:

$$M \cdot \Delta \ddot{u}_i + C \cdot \Delta \dot{u}_i + K \Delta u_i = \Delta F \tag{2.32}$$

Eq.(2.32) can be solved, using Eq.(2.30) and Eq.(2.31), by means of an iterative procedure based on the Newton-Raphson method explained above.

PART II

THE PARC_CL 1.0

3 Description of PARC_CL 1.0 crack model and its applications

"Car ce sont les hommes, et non pas l'homme, qui inventent; chacun arrive à son tour et à son heure, s'empare des choses connues de ses pères, les met en œuvre par des combinaisons nouvelles, puis meurt après avoir ajouté quelques parcelles à la somme des connaissances humaines, qu'il lègue à ses fils ; une étoile à la voie lactée. Quant à la création complète d'une chose, je la crois impossible."

Alexandre Dumas

3.1 Introduction

In this section the PARC_CL 1.0 crack model is described and some its applications are presented. The PARC_CL 1.0 crack model (Physical Approach for Reinforced Concrete subjected to Cyclic Loading), implemented at the University of Parma in the user subroutine UMAT.for for ABAQUS code [Belletti et al. 2013[a]], describes the behaviour up to failure of reinforced concrete membrane elements under cyclic loadings. As described in §3.2 the cyclic behaviour, in the PARC_CL 1.0 crack model, is defined with an unloading-reloading branch secant to the origin; for this reason it is suitable especially for the prediction of the monotonic behaviour of RC members, while the cyclic behaviour can not be properly model due to the unrealistic modelling of the unloading branch.

In §3.3 the PARC_CL 1.0 crack model is used to assess the capability of multi-layer shell elements to predict the out-of-plane behaviour of slabs. Indeed, as stated in §2.2.1, the multi-layer shell element approach does not allow to consider the nonlinear shear behaviour along the thickness of the element. To solve this lack, in §3.3 a post-processing of the NLFEA results is conducted on the base of the Critical Shear Crack Theory (CSCT). CTCT, as reported in [Muttoni, 2008] and [Muttoni and Fernandez, 2008[a]], allows to calculate shear and punching shear resistance based on few fundamental parameters, such as respectively the axial strain at mid-depth and the out-of-plane rotation of the element. Related to the evaluation of the shear strength of RC slabs in §3.3.4 the PARC_CL 1.0 crack model is also used to demonstrate that NLFEA is an important tool since it permits us to model in a sound manner several mechanisms not straightforward to capture analytically (e.g. the compressive membrane action effect).

Finally in §3.4 the PARC_CL 1.0 crack model is used to simulate the monotonic and cyclic in-plane behaviour of a RC squat walls with the aim to assess the capability in the prediction of the monotonic behaviour and to underline the influence of the unrealistic unloading-reloading branch on the global hysteretic response.

3.2 Description of PARC_CL 1.0 model

PARC_CL 1.0 crack model, as described in [Belletti et al., 2013[a]] is a fixed crack model, in which at each integration point two reference systems are defined: the local *x*,*y* coordinate system, parallel to the global *X*,*Y* coordinate system, and the *1*,*2* coordinate system along the principal stress directions . The angle between the *1*-direction and the *x*-direction is denoted as ψ, whereas $\alpha_i = \theta_i - \psi$ is the angle between the direction of the *i*th order of the bar and the *1*-direction, where θ_i is the angle between the direction of the *i*th order of the bar and the *x*-direction, Figure 3.1-a. When the maximum tensile principal stress reaches the concrete tensile strength f_t, cracking starts to develop, and the *1*,*2* coordinate system is fixed. The concrete behaviour is assumed to be orthotropic, both before and after cracking; softening in tension and compression, a multiaxial state of stress and the effect of aggregate interlock are taken into account. The reinforcement is modelled through a smeared approach; dowel action and tension stiffening phenomena are considered.

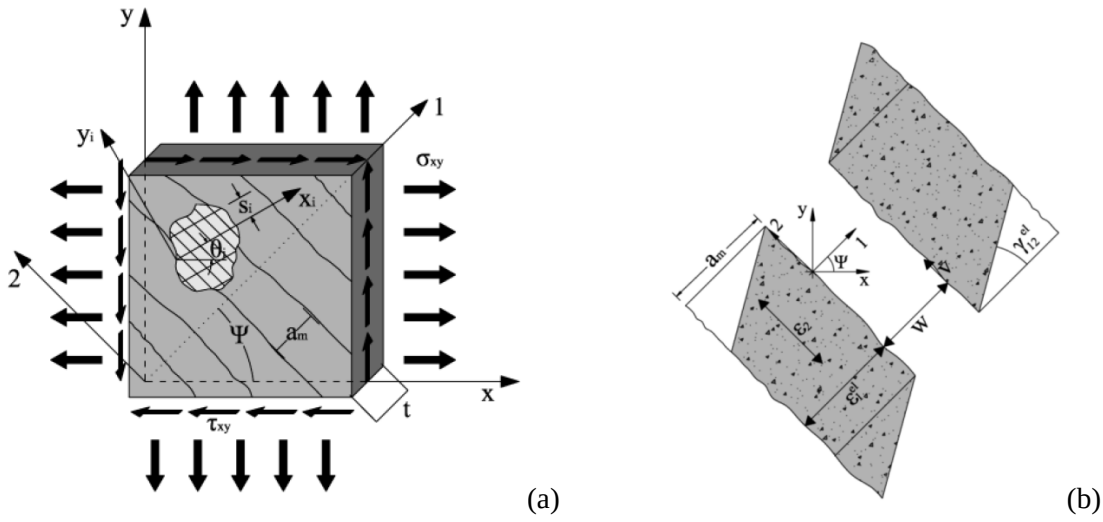

Figure 3.1 – (a) Reinforced concrete member subjected to plane stress state; (b) kinematic quantities of PARC_CL 1.0 model.

The total strains at each integration point are calculated, in the *1*,*2* coordinate system, as the sum of the elastic (subscript *el*) and the inelastic (subscript *cr*) strains, Figure 3.1-b.

$$\varepsilon_1 = \varepsilon_{1,el} + \varepsilon_{1,cr} = \varepsilon_{1,el} + \frac{w}{a_m} \tag{3.1}$$

$$\varepsilon_2 = \varepsilon_{2,el} + \varepsilon_{2.cr} \tag{3.2}$$

$$\gamma_{12} = \gamma_{12,el} + \gamma_{12,cr} = \gamma_{12,el} + \frac{v}{a_m} \tag{3.3}$$

where *w*=crack opening, *v*=crack sliding and *am*= crack spacing calculated trough an a priori method based on the transmission length of bond between concrete and steel according to the formulation proposed in [*fib*-Model Code 2010].

The overall stiffness matrix in the *x,y* coordinate system, $[D^{(x,y)}]$, is obtained by assuming that concrete and reinforcement behave like two springs placed in parallel:

$$\left[D^{(x,y)}\right]=\left[D_c^{(x,y)}\right]+\left[D_s^{(x,y)}\right]=\left[T_\psi\right]^T\cdot\left[D_c^{(1,2)}\right]\cdot\left[T_\psi\right]+\left[T_{\vartheta i}\right]^T\cdot\left[D_s^{(x_i,y_i)}\right]\cdot\left[T_{\vartheta i}\right]=$$

$$=\left[T_\psi\right]^T\cdot\begin{bmatrix}E_{c1}&0&0\\0&E_{c2}&0\\0&0&\beta G\end{bmatrix}\cdot\left[T_\psi\right]+\left[T_{\vartheta i}\right]^T\cdot\begin{bmatrix}\rho_i\cdot E_{si}\cdot g_i&0\\0&0\end{bmatrix}\cdot\left[T_{\vartheta i}\right] \tag{3.4}$$

In Eq. (3.4), the concrete stiffness matrix, $[D_c^{(1,2)}]$ is defined in the *1,2* coordinate system as a function of the concrete contribution in tension and in compression (E_{c1} and E_{c2}) and of the aggregate interlock effect (βG). The steel stiffness matrix $[D_s^{(xi,yi)}]$ is defined in the x_i,y_i coordinate system, as a function of a reinforcement contribution (E_{si}) and tension stiffening (g_i). The transformation matrixes $[T_\psi]$ and $[T_{\vartheta i}]$ are used to rotate the concrete matrix from the *1,2* to the *x,y* coordinate system and the steel matrix from the x_i,y_i to the *x,y* coordinate system, respectively. The stresses $\{\sigma^{(x,y)}\}$,in the *x,y* coordinate system are defined by multiplying the stiffness matrix $[D^{(x,y)}]$ and the strain vector $\{\varepsilon^{(x,y)}\}$.

3.2.1 Cyclic constitutive relationship of concrete

The stress-strain relationship for concrete in tension is described by Eq.(3.5):

$$\sigma=\begin{cases}E_c\cdot\varepsilon & 0\le\varepsilon<\varepsilon_{t,cr}\\ f_t\left[1+0.85\dfrac{(\varepsilon-\varepsilon_{t,cr})}{(\varepsilon_{t,cr}-\varepsilon_{t1})}\right] & \varepsilon_{t,cr}\le\varepsilon<\varepsilon_{t1}\\ 0.15\cdot f_t\left[1+\dfrac{(\varepsilon-\varepsilon_{t1})}{(\varepsilon_{t1}-\varepsilon_{t,u})}\right] & \varepsilon_{t1}\le\varepsilon<\varepsilon_{t,u}\end{cases} \tag{3.5}$$

where the strain ε_{t1} and ε_{tu}, corresponding to residual stress equal to $0.15f_t$ and zero respectively, can be calculated as follow:

$$\varepsilon_{t1}=0.15\cdot\varepsilon_{t,cr}+\frac{G_f\left(2-0.15\cdot\alpha_f\right)}{a_m\cdot f_t} \tag{3.6}$$

$$\varepsilon_{t,u}=\frac{\alpha_f\cdot G_f}{a_m\cdot f_t} \tag{3.7}$$

where G_f represents the fracture energy in tension and α_f is a coefficient calculated according to [*fib*-Model code 1990].

The stress-strain relationship for concrete in compression is described by Eq.(3.8):

$$\sigma = \begin{cases} \dfrac{E_c / E_{cr} - \varepsilon / \varepsilon_{c,cr}}{1 + \left(E_c / E_{cr} - 2 \right) \cdot \varepsilon / \varepsilon_{c,cr}} & \varepsilon_{c,cr} \le \varepsilon < 0 \\ f_c \left[1 - \dfrac{\left(\varepsilon - \varepsilon_{c,cr} \right)^2}{\left(\varepsilon_{c,u} - \varepsilon_{c,cr} \right)^2} \right] & \varepsilon_{c,u} \le \varepsilon < \varepsilon_{c,cr} \end{cases} \tag{3.8}$$

In Eq.(3.8) the compressive branch before reaching the peak is defined in agreement with Sargin's relation [*fib*-Model code 1990] and after the peak with Feenstra's relation [Feenstra 1993], as a function of the concrete compressive strength f_c and concrete fracture energy in compression G_c. the ultimate concrete strain in compression is given by Eq.(3.9):

$$\varepsilon_{c,u} = \varepsilon_{c,cr} + \frac{3 \cdot G_c}{2 \cdot a_m \cdot f_c} \tag{3.9}$$

Multi-axial state of stress is considered by reducing the compressive strength and the corresponding peak strain due to lateral cracking, as given in Eq.(3.10), according to [Vecchio and Collins, 1993]:

$$\zeta = 1 / \left(0.85 - 0.27 \varepsilon_1 / \varepsilon_{c,cr} \right) \tag{3.10}$$

According to the formulation proposed herein the stress-strain relationship obtained for concrete is reported in Figure 3.2, remembering that the unloading-reloading path is defined as secant to the origin.

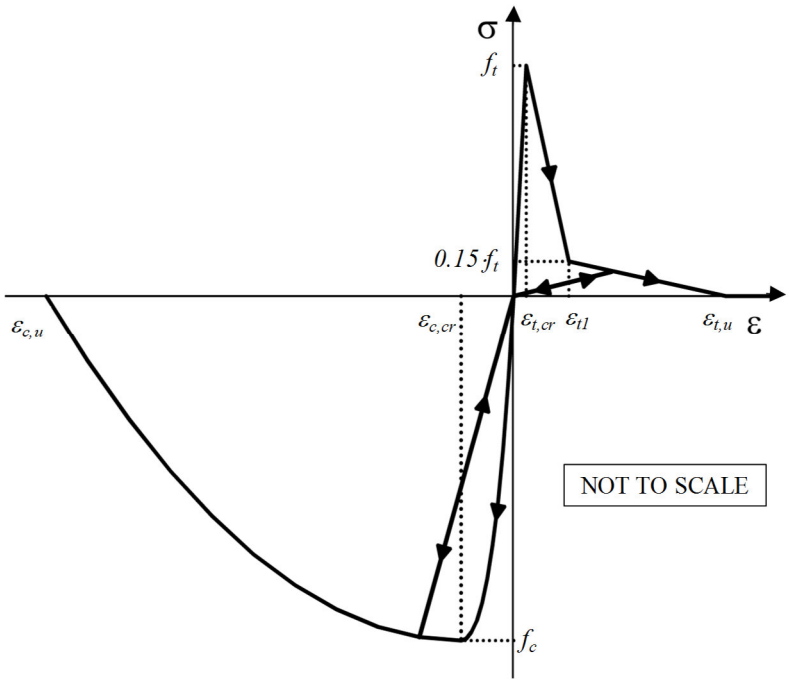

Figure 3.2 – PARC_CL 1.0, cyclic stress-strain relationship for concrete.

3.2.2 Aggregate interlock effect

The shear stress caused by the effect of aggregate interlock is evaluated on the basis of the crack opening, *w*, and the crack sliding, *v*, according to the formulation proposed by [Gambarova, 1983] and is calculated following Eq.(3.11), Figure 3.3-a:

$$\tau_{12} = \bar{\tau}\left(1-\sqrt{\frac{2\,w}{d_{\max}}}\right)\frac{a_3 + a_4\left|\frac{v}{w}\right|^3}{1+a_4\left(\frac{v}{w}\right)^4}\frac{1}{w}v \tag{3.11}$$

where $\bar{\tau} = 0.27\ f_c$; $a_3 = \frac{2.45}{\bar{\tau}}$; $a_4 = 2.44\left(1-\frac{4}{\bar{\tau}}\right)$.

The Gambarova's law can be schematized with a bilinear curve characterised by a first linear relation and the second constant relation (Figure 3.3-b) where the intersection point between the two different relations has coordinates v^*, τ^*, calculated using Eq.(3.12) and Eq.(3.13):

$$v^* = \frac{f_c}{a_5}w + a_6 \tag{3.12}$$

$$\tau^* = \bar{\tau}\left(1-\sqrt{\frac{2\,w}{D_{\max}}}\right)\frac{a_3 + a_4\left|\frac{v^*}{w}\right|^3}{1+a_4\left(\frac{v^*}{w}\right)^4}\frac{1}{w}v^* = c^*\,v^* \tag{3.13}$$

where $a_5 = 0.366\ f_c + 3.333$ and $a_6 = f_c/110$.

The proposed bilinear curve is used to define the stress-strain relationship between the shear stress, τ_{12}, and the shear strain in the cracked phase, $\gamma_{12,cr}$, of the concrete. In this phase, the shear modulus, G_{cr}, is equal to:

$$G_{cr} = \begin{cases} c^*\,a_m & \gamma_{12,cr} < \gamma_{cr}^* \\ \dfrac{c^*\,a_m}{\gamma_{12,cr}} & \gamma_{12,cr} \geq \gamma_{cr}^* \end{cases} \tag{3.14}$$

where c^* is defined with Eq.(3.13) and γ_{cr}^* (Figure 3.3-c) is equal to:

$$\gamma_{cr}^* = \frac{v^*}{a_m} \tag{3.15}$$

According to the total strain concept, it is assumed that the uncracked concrete, characterized by the elastic deformation $\gamma_{12,el}$, and the cracked concrete, characterized by the cracking deformation $\gamma_{12,cr}$, behave like two spring in series. Therefore, the overall shear modulus can be defined by multiplying its initial elastic shear modulus, *G*, for the shear retention factor β, equal to:

$$\beta = \begin{cases} 1 & un-cracked\ \ phase \\ \dfrac{G}{G_{cr}+G} & cracked\ \ phase \end{cases} \tag{3.16}$$

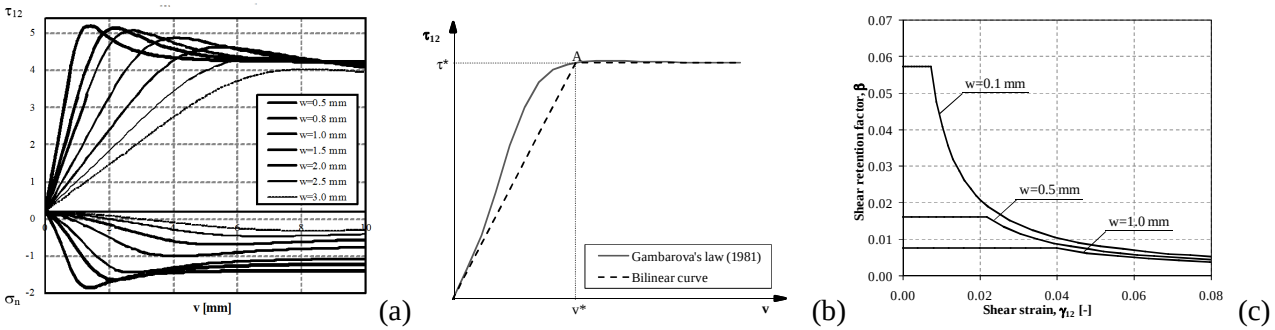

Figure 3.3 – Gambarova's law: (a) shear (τ_{12}) and normal (σ_n) stress due to aggregate interlock for different crack opening values w; (b) bi-linear relation for a given crack opening w and (c) shear retention factor β as a function of total shear strain γ_{12} for different value of crack opening w [Gambarova, 1983].

In the unloading phase the shear- crack sliding behaviour follow the same relationship as for the loading phase.

3.2.3 Cyclic constitutive relationship of steel

The stress-strain relationship for reinforcing steel is represented by an idealized elastic-hardening plastic bilinear curve, identical in tension and compression, Figure 3.4.

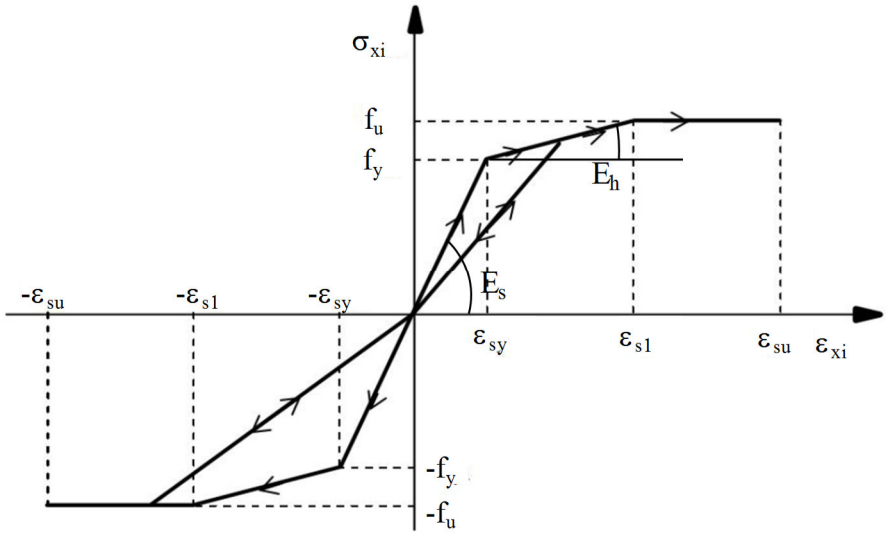

Figure 3.4 – PARC_CL 1.0, cyclic stress-strain relationship for reinforcing steel.

The stress σ_{xi} in the *i*th steel bar is obtained by:

$$\sigma_{xi} = E_{si} \cdot \varepsilon_{xi} \tag{3.17}$$

where the secant modulus assumes the following expression:

$$E_{si} = \begin{cases} \dfrac{f_y}{\varepsilon_{sy}} & \varepsilon_{xi} < \varepsilon_{sy} \\ \dfrac{f_y + (\varepsilon_{xi} - \varepsilon_{sy}) E_{hi}}{\varepsilon_{xi}} & \varepsilon_{sy} \le \varepsilon_{xi} \le \varepsilon_{s1} \\ \dfrac{f_u}{\varepsilon_{xi}} & \varepsilon_{s1} \le \varepsilon_{xi} \le \varepsilon_{su} \end{cases} \tag{3.18}$$

3.2.4 Tension stiffening

In the PARC_CL 1.0 model the tension stiffening is considered according to the formulation proposed by [Giuriani, 1981]. According to the model proposed by Giuriani, the stiffening effect due to the presence of concrete between two cracks, is considered by means of an appropriate increment of the steel bar average strain and is expressed by Eq.(3.19):

$$\sigma_{xi}^{*} = E_{si}(\varepsilon_{xi} + \Delta\varepsilon_{xi}) = E_{si} \cdot \left(1 + \frac{\Delta\varepsilon_{xi}}{\varepsilon_{xi}}\right) \cdot \varepsilon_{xi} = E_{si} \cdot g_i \cdot \varepsilon_{xi} \tag{3.19}$$

where

$$\Delta\varepsilon_{xi} = \varepsilon_{xi}^{*} \cdot g_{0i} \tag{3.20}$$

$$\varepsilon_{xi}^{*} = \frac{w}{a_m} \cdot \cos^2 \alpha_i + \frac{v}{a_m} \cdot \sin \alpha_i \cdot \cos \alpha_i \tag{3.21}$$

$$g_{0i} = g_{1i} + k_1 \cdot g_{2i} \cdot \left(\varepsilon_{xi}^{*}\right)^{k_2 - 1} \tag{3.22}$$

$$g_{1i} = \lambda_i \frac{\cosh \lambda_i}{\sinh \lambda_i} - 1 \tag{3.23}$$

$$g_{2i} = \frac{2\tau_0}{\tau_1 \cdot a_m} \lambda_i \frac{\cosh \lambda_i - 1}{\sinh \lambda_i} \tag{3.24}$$

with

$$\lambda_i = \sqrt{\frac{\tau_1 \cdot a_m^{\,2}}{0.5 \cdot E_{si} \cdot \phi_i}}; \qquad \tau_0 = 3MPa; \qquad \tau_1 \cdot \phi_i = 75MPa; \qquad k_1 = 4.0; \qquad k_2 = 0.2$$

where ϕ_i represents the diameter of the ith order of steel reinforcement.

3.3 Simulation of monotonic out-of-plane behaviour

In this section the monotonic out-of-plane behaviour of RC slabs is investigated by means of NLFEA. NLFEA are carried out using multi-layer shell elements and the in-plane nonlinear behaviour is assigned by means of the just described PARC_CL 1.0 crack model.

Reinforced concrete slabs, often supported on columns, are common structural solutions in practice. The capacity of such slabs in the vicinity of columns is governed either by flexural or punching shear failures. Provisions for most codes of practice are still mainly empirical, calibrated on the basis of experiments on isolated specimens meaning to model just the region of a slab inside the region of hogging moment. However, the shear behaviour of actual continuous slabs may be influenced by mechanisms that cannot be described with standard isolated members, such as moment redistributions which change the location of the line of moment contraflexure and compressive membrane action. This is not just in the case of continuous slabs but also for linearly supported bridge decks subjected to concentrated loads, as shown by several researchers. In general, it has to be remarked that strength enhancement in bending and shear is, up to date, overlooked by codes of practice.

The shear capacity of a slab can be assessed with two different approaches: by evaluating the beam shear resistance over a prescribed effective width b_w (shear failure, Figure 3.5-a) or by checking the punching shear resistance on a control perimeter around the loading area (punching shear failure, Figure 3.5-b).

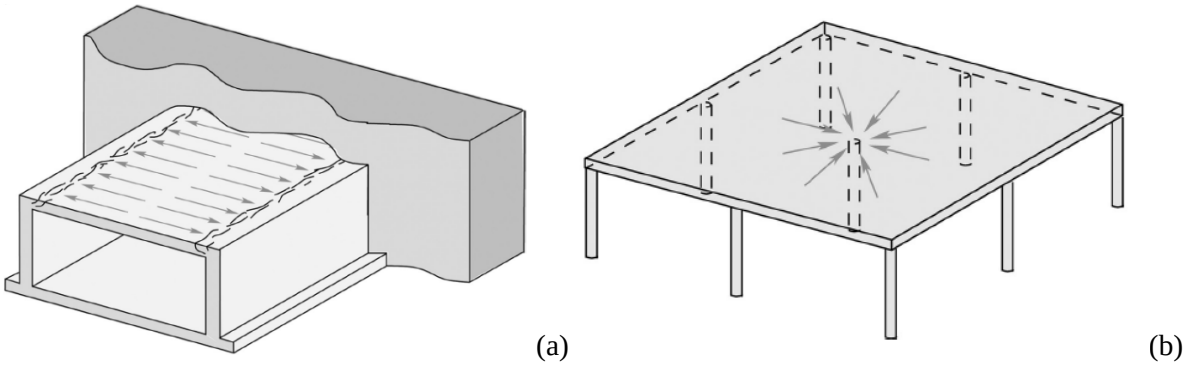

Figure 3.5 – Shear capacity in RC slabs: (a) shear and (b) punching shear [Muttoni and Fernandez 2008[b]].

As stated in §2.2.1 the adopted multi-layer shell elements approach were defined in plane stress condition and so it does not include the nonlinear behaviour due to shear along the thickness. As a consequence of this it is not possible to capture neither shear nor punching shear out-of-plane failure.

In this section a post-processing of the NLFEA results is conducted based on Critical Shear Crack Theory (CSCT). CTCT, as reported in [Muttoni, 2008] and [Muttoni and Fernandez 2008[a]], is a failure criterion which allows to calculate shear and punching shear resistance based on few fundamental parameters, such as respectively the axial strain at mid-depth and the out-of-plane rotation of the slab.

In particular, the proposed post-processing procedure allows to evaluate the shear and the punching shear resistance as the intersection between the nonlinear curve obtained by means of NLFEA and the failure

criterion based on the CSCT. This procedure is schematically reported in Figure 3.6 and widely described in the following of this section.

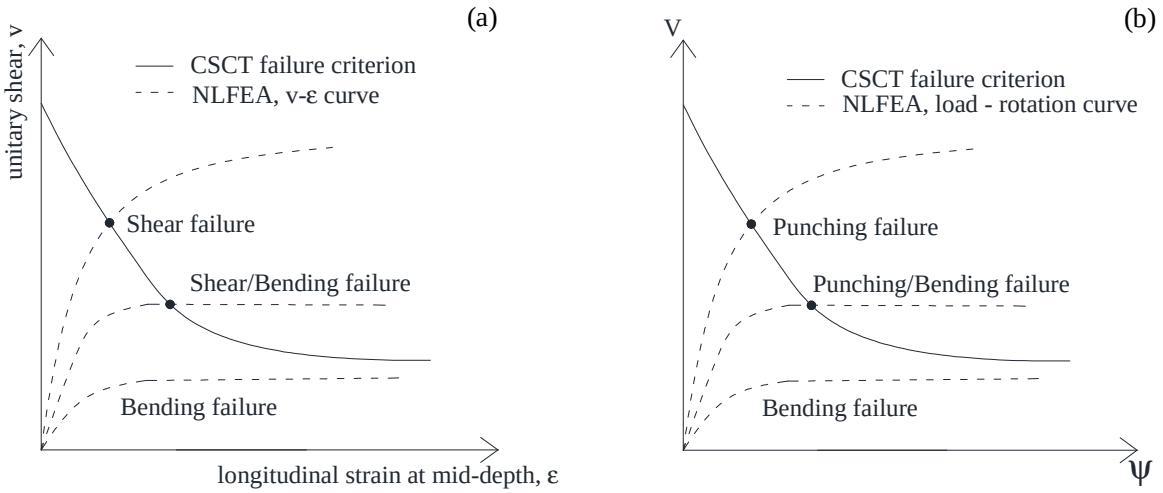

Figure 3.6 – Post-processing procedure of NLFEA for the evaluation of (a) shear resistance and (b) punching shear resistance.

The proposed method was validated by comparison with several experimental outcomes on different RC slabs tested in literature.

In §3.3.1 the CSCT failure criterion is described for the two different failure modes analysed: shear and punching shear. Moreover in §3.3.2 and §3.3.3 the results obtained by means of NLFEA post-processed according to CSCT are compared with the experimental outcomes on simply supported RC slabs tested in literature, in order to highlight the capability of the model to capture different failure modes associated to different mechanical and geometrical conditions.

Finally, the proposed procedure was applied to more complex case studies, such as real deck slabs, in §3.3.4. The aim of this studies is to evaluate the capability of NLFEA to consider phenomena like redistribution of stresses and membrane effect due to cracking and boundary conditions, also called compressive membrane action (CMA), which cannot be taken into account using simplified analytical formulations.

3.3.1 Critical Shear Crack Theory (CSCT)

The Critical Shear Crack Theory is a theory that allows determining the shear strength of slender slabs for both shear and punching shear failure on the basis of the opening of the critical shear crack. This formulation points out that failure in shear occurs when the critical crack propagates through the inclined compression strut, limiting its strength and not allowing the member to reach the flexural capacity. As shown in Figure 3.5 two different approaches can be followed in the evaluation of the out-of-plane shear resistance of RC slabs: shear and punching shear, described in the following.

3.3.1.1 Shear failure

[Muttoni and Fernandez 2008[a]] proposed a failure criterion in terms of one–way shear that estimates the maximum shear force for a given critical crack width. Such parameter can be assumed proportional to the product of a reference longitudinal strain ε times the effective depth *d*. CSCT formulation evaluates the shear strength in the critical section at *0.5d* from the point of maximum acting moment. The reference longitudinal strain is assessed at *0.6d* from the outer compressive fibre considering a linear elastic behaviour for concrete in compression, neglecting concrete tensile strength, Figure 3.7.

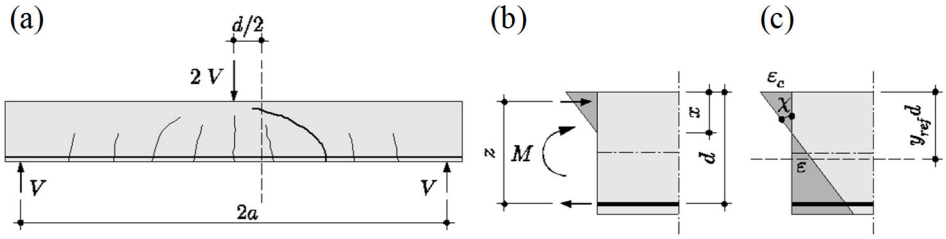

Figure 3.7 - (a) Critical section for point loading; (b)–(c) Evaluation of longitudinal strain in control depth 0.6d [Muttoni and Fernandez 2008[a]].

Hence, taking into account of the effects of the critical shear crack width, the failure criterion is described by Eq. (3.25) and shown in Figure 3.6-a.

$$v_c(\varepsilon) = \frac{d\sqrt{f_c}}{3}\frac{1}{1+\frac{120\cdot\varepsilon\cdot d}{16+d_g}} \tag{3.25}$$

where the longitudinal strain ε and the c_{flex} are defined by Eq. (3.26) and (3.27):

$$\varepsilon = \frac{m}{d\rho E_s\left(d-\frac{c_{flex}}{3}\right)}\frac{0.6d-c_{flex}}{d-c_{flex}} \tag{3.26}$$

$$c_{flex} = d\rho\frac{E_s}{E_c}\left(\sqrt{1+\frac{2E_c}{\rho E_s}}-1\right) \tag{3.27}$$

3.3.1.2 Punching shear failure

[Muttoni, 2008] proposed a failure criterion for the evaluation of punching shear strength of RC slabs based on the assumption that the width of the critical shear crack (*w*) governing the punching shear strength is related to the product of the rotation of the slab (ψ) around the force application area by the average effective depth of the slab (*d*), see Figure 3.8-a for the notation. The roughness of the crack is correlated to the maximum aggregate size (d_g). These assumptions led to the formulation of the failure criterion given by Eq.(3.28) and shown in Figure 3.6-b, which allows determining the punching shear resistance V_{Rm}:

$$\frac{V_{Rm}}{b_0 \cdot d_v \cdot \sqrt{f_c}} = \frac{3/4}{1+15\dfrac{\psi \cdot d}{d_{g0}+d_g}} \tag{3.28}$$

where d_v is the shear-resisting effective depth (assumed equal to d), d_{g0} = 16mm the reference aggregate size, d the effective slab depth and b_0 the length of the shear resisting control perimeter.

The design punching shear resistance, V_{Rd}, is obtained using the characteristic failure criterion reported in Eq.(3.29):

$$\frac{V_{Rd}}{b_0 \cdot d_v \cdot \dfrac{\sqrt{f_{ck}}}{\gamma_c}} = \frac{1}{1.5+0.9 \cdot \psi \cdot d \cdot k_{dg}} \tag{3.29}$$

where k_{dg}=32/(16+d_g).

The mean and the characteristic failure criteria calculated using Eq.(3.28) and Eq.(3.29) are represented in Figure 3.8 where the dots represent the experimental outcomes obtained by [Guadalini et al., 2009] analysing the punching shear resistance of several RC slabs.

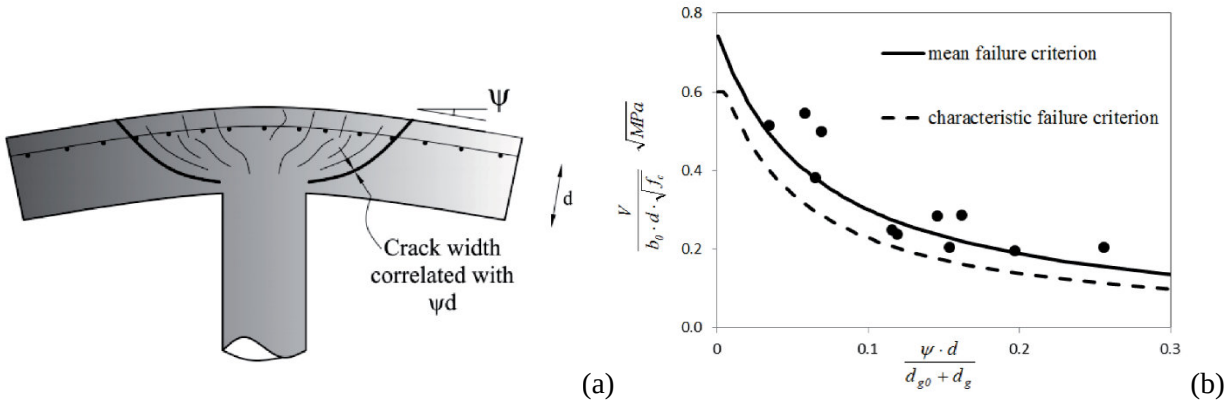

Figure 3.8 – (a) Critical inclined crack developing from the loaded area into the slab [Muttoni 2008] and (b) Comparison of mean and characteristic failure criteria of RC slabs tested by Guadalini [Guadalini et al. 2009].

3.3.2 RC slabs subjected to shear

The shear capacity of linearly supported RC slabs with load applied close to the linear support, can be evaluated as the beam shear resistance over a prescribed effective width b_w (shear failure, Figure 3.5-a). In these cases the failure criterion is defined as reported in §3.3.1.1. The shear resistance occurs at the intersection between the unitary shear v – longitudinal reference strain at mid-depth ε and the failure criterion, as shown in Figure 3.6-a. To enable the calculation, the relationship between unitary shear and longitudinal strain has to be known. This relationship can be obtained using simplified analytical formulation or NLFEA.

In this section two different experimental campaign, characterized by linearly supported RC slabs without shear reinforcement and subjected to concentrated load, were analysed. The details of these two

experimental campaigns can be found in publications by [Natario et al. 2014] and [Rombach and Latte, 2009]. The experimental setup and test results will be pointed out in the following in order to compare them, firstly, to analytical formulations and, consequently, to NLFEA with PARC_CL 1.0 crack model results.

3.3.2.1 Analytical formulation

Several experimental outcomes, carried out for linearly supported slabs under concentrated loads, show clear and rather significant redistributions of the reactions, see for example [Natario et al. 2014]. Redistributions occur not only due to bending cracks but also for the development of the inclined shear crack. Indeed, as the level of applied load increases, the reaction in the region close to the load enhances at a slower rate because load starts to be transferred to the adjacent regions which are less affected by the shear crack. To account for this distribution of internal forces, an average shear stress $v_{avg,4d}$, is calculated along a distance 4d from unitary shear stresses obtained by linear finite element (LFE) analysis.

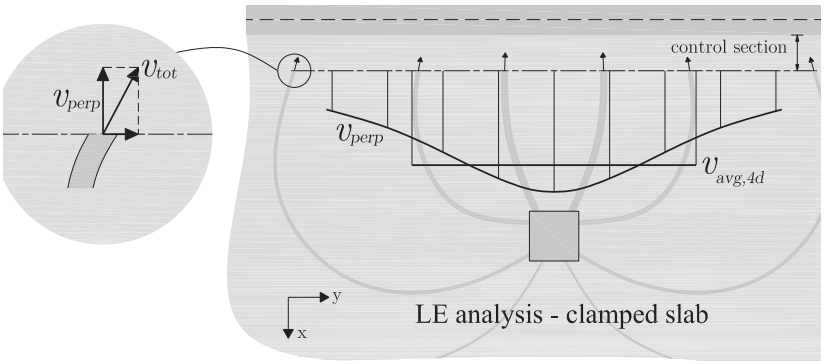

Figure 3.9 – Definition of the averaged shear force $v_{avg,4d}$ [Natario et al., 2014].

The flowchart, illustrated in Figure 3.10 shows that the reference longitudinal strain ε_i is calculated in correspondence of the maximum unitary acting moment m_i. Then, it is calculated the parameter k, as the ratio of the acting moment m_i to the average unitary shear $v_{avg,4d}$ (both of them evaluated in the critical section). Hence, the ultimate shear failure value V_R is evaluated following an iterative procedure, as it is shown in the flowchart of Figure 3.10, at the intersection with the failure criterion of Eq. (3.25).

In order to take into account the arching action that can occur in case of shear spans ranging from *2d* to *3d*, a factor β is applied to increase the shear resistance, according to Eq.(3.30):

$$V_R = \frac{v_{c,n}}{\beta} b \tag{3.30}$$

being b a length evaluated from LFE analysis results as the ratio $F_{hypothesis}/v_{avg,4d}$. The factor β is given by Eq.(3.31):

$$\beta = \frac{a_v}{2.75d} \leq 1 \tag{3.31}$$

where a_v represents the shear span and d represents the effective depth.

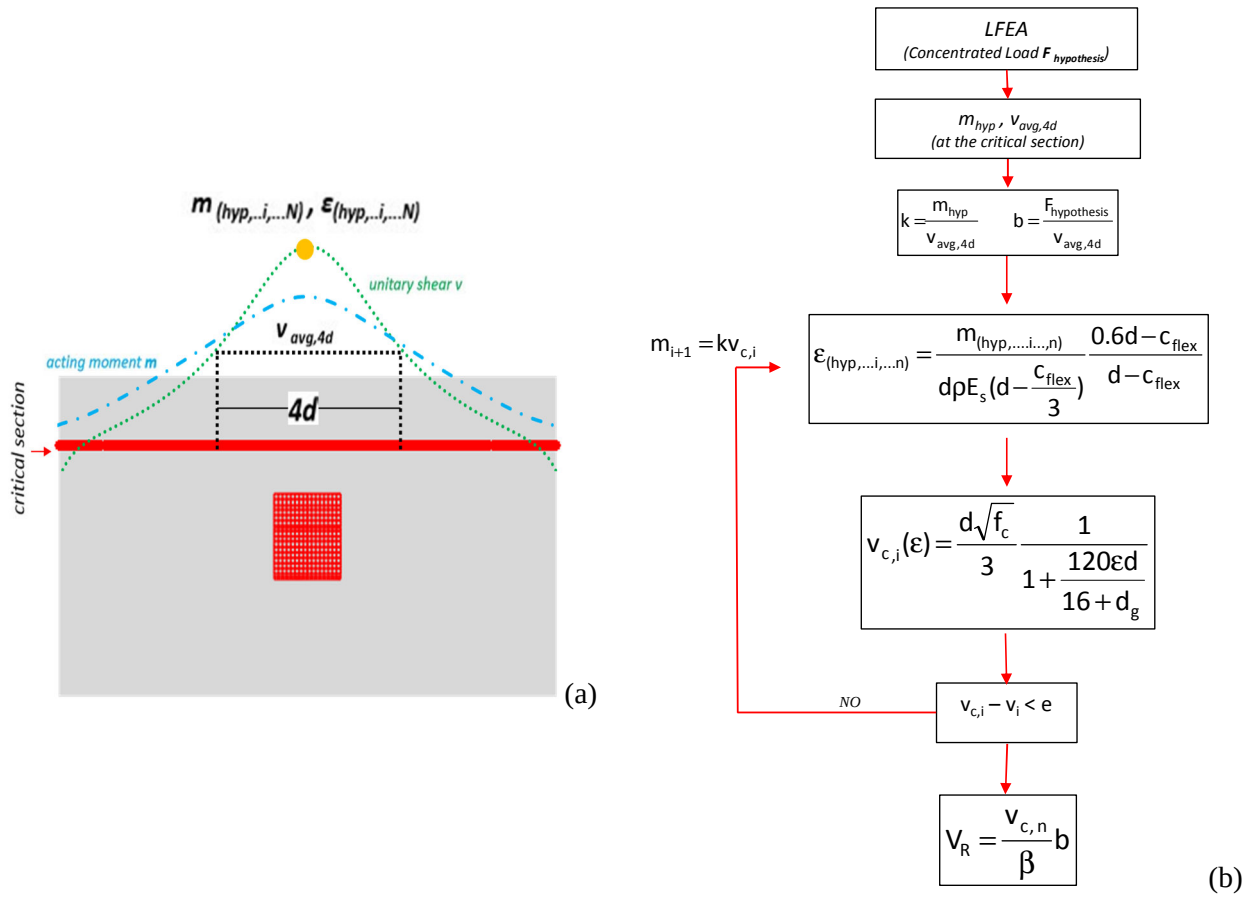

Figure 3.10 – Analytical calculation of the one-way shear resistance: (a) parameters used and (b) Flowchart of the main steps [Belletti et al., 2015].

3.3.2.2 Experimental campaigns by [Natario et al., 2014] and [Rombach and Latte, 2009]

The aim of this section is to assess the capability of NLFEA to predict the shear resistance with respect to the analytical calculation. Two different experimental campaigns were analysed: [Natario et al., 2014] and [Rombach and Latte, 2009] in order to make the comparison between experimental outcomes, NLFEA results and analytical calculation.

3.3.2.2.1 [Natario et al., 2014] experimental campaign

The experimental campaign carried out by [Natario et al., 2014] consists in twelve tests, performed on six RC square slabs (3000 x 3000 x 180 mm) at the Ecole Polytechnique Fédérale de Lausanne. All the slabs have a 180 mm nominal thickness with a thickening at the gusset in the central region (280 mm). The flexural nominal depth *d* is 152 mm for each specimen. Three tests have been performed on slabs without ducts, three on slabs with empty ducts, three on slabs with injected steel ducts and three on injected polypropylene ducts (cross sections in Figure 3.11-e) to simulate a situation which typically occurs in bridges erected with the free cantilever method (where longitudinal tendons are placed in the deck slabs). Each slab is centrally supported by means of an I–shaped aluminium profile equipped with strain gauges to mesure reaction's distribution and is loaded by two hydraulic actuators with a concentrated load distant a_v from the end of the gusset. Figure 3.11-

a shows schematically the test setup while Figure 3.11-b exhibits the reinforcement layout of top and bottom layer.

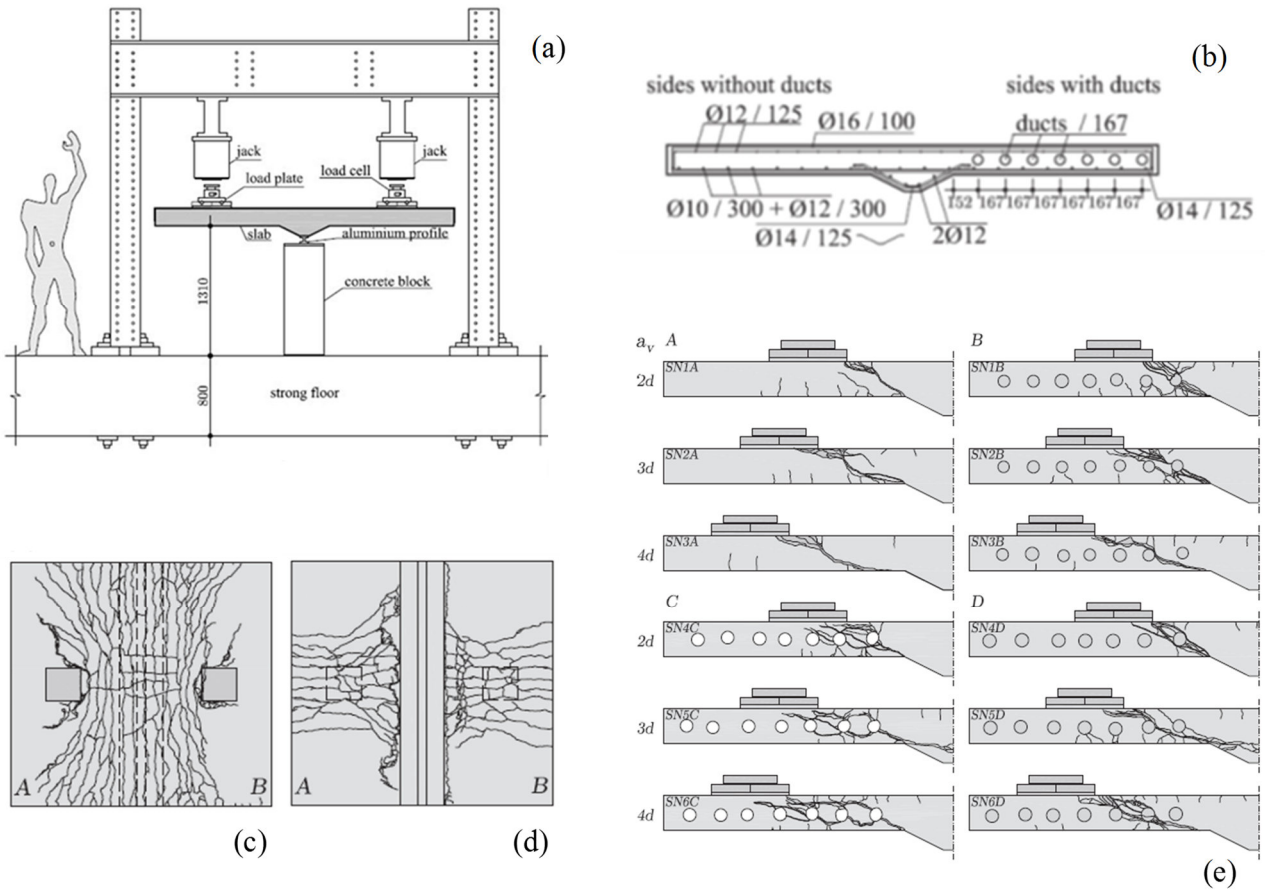

Figure 3.11 – (a) Test set-up for Natario's experimental campaign; (b) reinforcement layout (measure in mm); (c) crack pattern in the top face of slab SN2A after failure; (d) crack pattern in the bottom face of slab SN2A after failure and (e) cross section of all the specimens [Natario et al., 2014].

In Table 3.1 are listed the mechanical properties of reinforcement, while the main mechanical properties for concrete and mortar are reported in Table 3.2.

Table 3.1 – Mechanical properties of the reinforcement of Natario's experimental campaign

ϕ_{rebar} [mm]	f_y [MPa]	f_u [MPa]	Type
16	547	601	Hot-Rolled
14	550	602	Cold-worked
12	548	604	Cold-worked
10	570	640	Cold-worked

Table 3.2 – Main mechanical properties for concrete of Natario's experimental campaign

							Concrete			Injection mortar	
Specimen	Slab	Side	a_v [mm]	a_v/d [-]	Ducts	ϕ_{ducts} [mm]	Age [days]	f_c [Mpa]	E_c [Mpa]	Age [days]	f_m [Mpa]
SN1A	SN1	A	304	2	No ducts		250	30.3	27500		
SN2A	SN2	A	304	2	No ducts		220	30.1	27400		
SN3A	SN3	A	304	2	No ducts		286	30.4	27600		
SN1B	SN1	B	304	2	Injected, polypropylene	63	81	28.3	26600	62	50.3
SN2B	SN2	B	456	3	Injected, polypropylene	63	150	29.5	27100	131	67.1
SN3B	SN3	B	456	3	Injected, polypropylene	63	164	29.7	27200	145	67.8
SN4D	SN4	D	456	3	Injected, steel	72	270	28.8	26900	249	53.6
SN5D	SN5	D	456	3	Injected, steel	72	234	28.7	26700	213	48.8
SN6D	SN6	D	608	4	Injected, steel	72	291	28.9	27000	270	54.2
SN4C	SN4	C	608	4	Non-injected, steel	72	182	28.4	26200		
SN5C	SN5	C	608	4	Non-injected, steel	72	199	28.5	26400		
SN6C	SN6	C	608	4	Non-injected, steel	72	171	28.3	26100		

3.3.2.2.2 [Rombach and Latte, 2009] experimental campaign

The experimental campaign carried out by [Rombach and Latte, 2009] consists in twelve tests on four full–scale specimens of RC deck slabs. Geometrically, each slab is 2.4 m in width, ranging from 5.68 m to 6.58 m in length. Two specimens had a constant thickness, respectively, of 250 mm and 200 mm while the other ones were tapered slabs with variable thickness, Figure 3.12. Each test specimen consists in two cantilever slabs of 1.65 m span and a central slab supported by two web beams. Hence, two cantilever tests (V1 and V2) and a centre slab test (V3) have been carried out for each specimen. In this section the analysis is limited to the cantilever tests, focusing on those ones without shear reinforcement (V1). The main mechanical properties of concrete and the loading details are summarized in Table 3.3; while for reinforcement the BSt 500 S steel with a yield strength of 550 MPa was used. For further detail regarding the mechanical properties please refers to [Rombach and Latte, 2009].

Table 3.3 – Mechanical properties of concrete and loading details of Rombach's experimental campaign

Specimen	ρ	Concrete*		Line load		Concentrated load	
		f_c [Mpa]	$f_{t,split}$ [Mpa]	f_q [kN/m]	e [m]	a^{**} [m]	a/d [-]
VK1	0.81	35	2.85	32.1	1.5	0.71	2.88
VK2	1.16	46	3.42	22.5	1.5	0.71	3.27
VK3	1.16	46.5	3.34	22.5	1.5	0.71	3.27
VK4	1.2	42.5	3.23	-	-	0.71	4.25

* tests on cylinder ϕ=150mm h=300mm

** Distance between load center and edge of the web beam

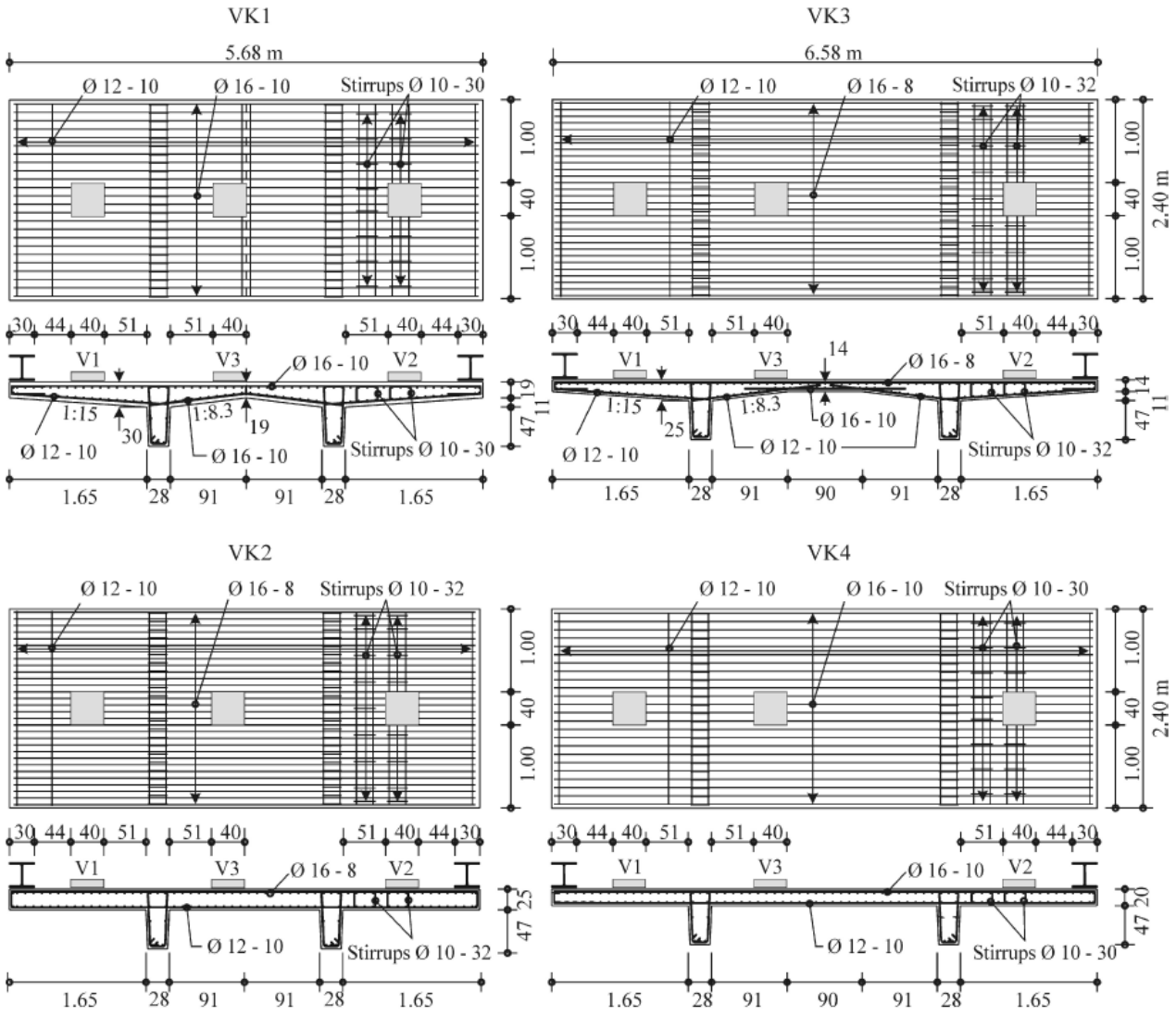

Figure 3.12 – Dimensions and reinforcement layout of the test specimen VK1 to VK4 [Rombach and Latte, 2009].

As regards loading, a constant line load f_q has been applied over the full width of the cantilever tests. In a second step, a point load F_Q has been enforced on a square loading plate until failure. Figure 3.13 describes the test setup and load arrangement.

The cantilever deck slabs without shear reinforcement (V1) failed in a brittle manner before the onset of rebar yielding. As regards the cracking pattern of tests V1 (Figure 3.14), on the top surface of each slab, cracks developed almost parallel to the support while for bottom surface, cracking was mostly concentrated close to the loading area, perpendicularly to the linear support

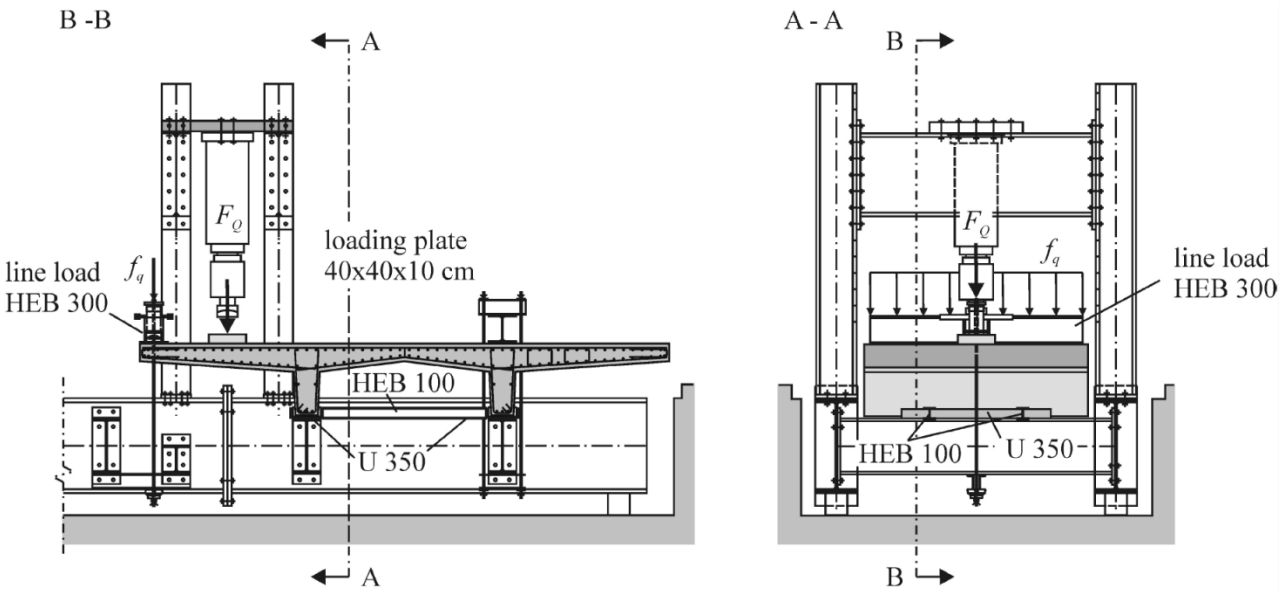

Figure 3.13 – Test setup and load arrangement of the cantilever tests [Rombach and Latte, 2009].

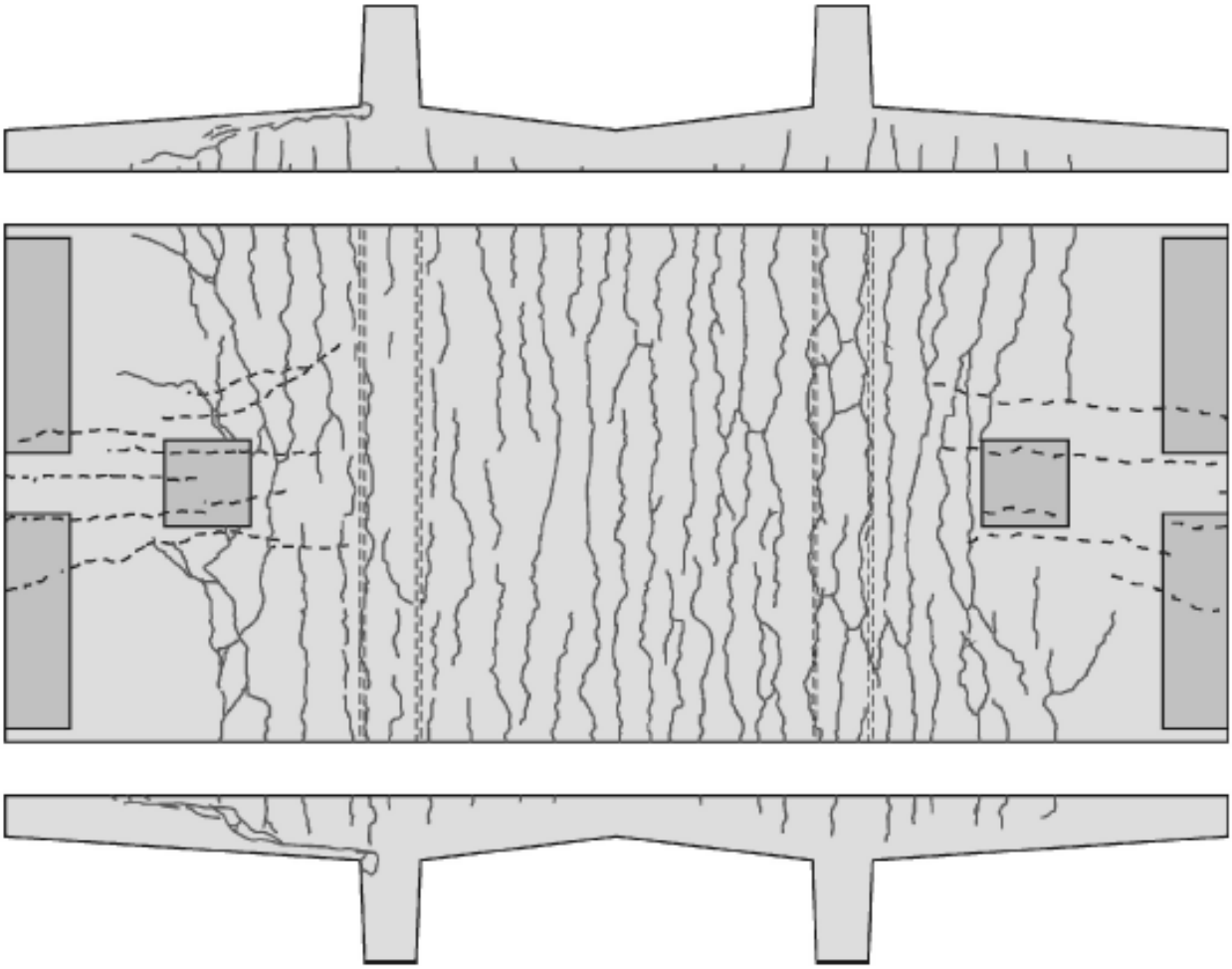

Figure 3.14 - Cracking pattern after test V1 without shear reinforcement (left cantilever) and test V2 (right cantilever) [Rombach and Latte, 2009].

3.3.2.3 Nonlinear finite element modelling and results

In this section the two experimental campaigns reported in §3.3.2.2.1 and §3.3.2.2.2 are analysed by means of NLFEA using the presented PARC_CL 1.0 crack model associated with the post-processing method according to CSCT.

3.3.2.3.1 [Natario et al., 2014] experimental campaign

All specimens were modelled with eight nodes shell elements with reduced integration (*S8R*). Shell element thickness was divided into three layers in order to consider top and bottom layers of steel reinforcement. Only a quarter of slab (Figure 3.15) was modelled due to the symmetrical conditions along *x* and *y* directions. The loading system was modelled as a region in which a constant pressure was applied. The aluminium profile was simulated by means of nonlinear spring elements that work only in compression with a very low stiffness in tension.

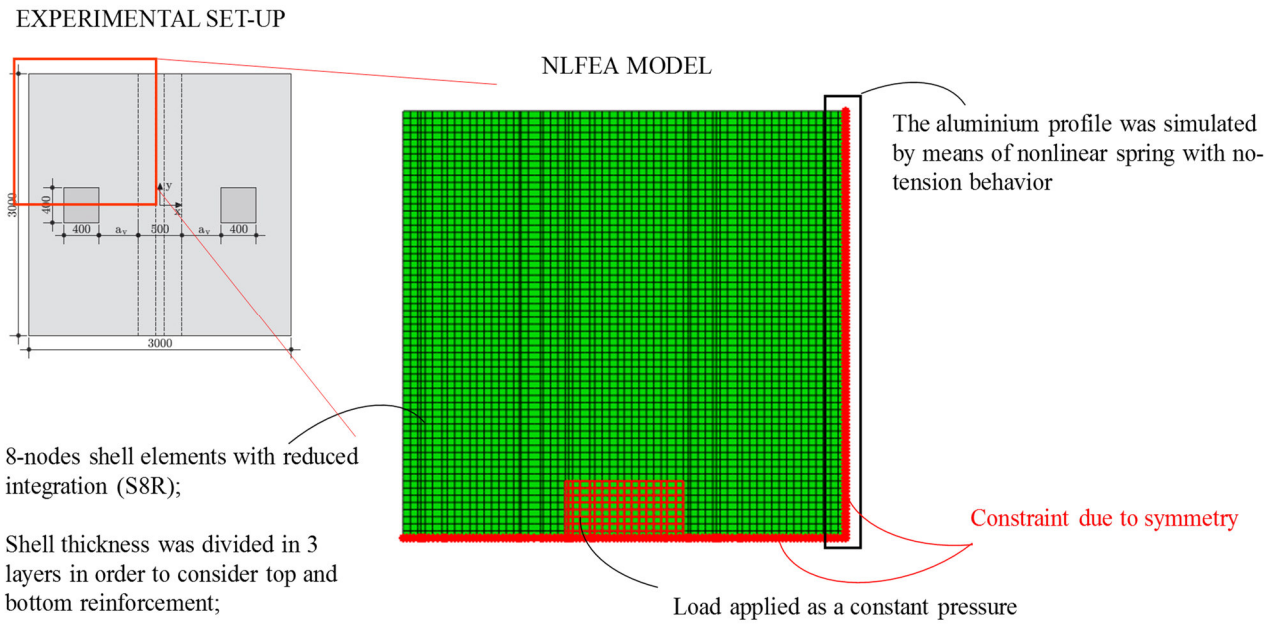

Figure 3.15 – NLFEA model for Natario's specimens.

The shear strength of the analysed slabs, derived as the intersection between the failure criterion reported in Eq.(3.25) and the curve obtained by means of NLFEA, is reported in Table 3.4 together with the shear strength evaluated following the analytical procedure proposed in §3.3.2.1 and the experimental outcomes. In Table 3.4 are also reported the average value and the coefficient of variation (COV) of the ratio experimental/NLFEA results and experimental/analytical results.

Table 3.4 – Comparison between experimental, analytical and NLFEA shear strength predictions for Natario's experimental campaign.

Specimen	$V_{exp.}$ [kN]	V_{NLFEA} [kN]	$V_{analytical}$ [kN]	$\frac{V_{exp.}}{V_{NLFEA}}$	$\frac{V_{exp.}}{V_{analytical}}$
SN1A	489	466.6	400.8	1.05	1.22
SN2A	330	336	314.3	0.98	1.05
SN3A	328	343.2	318.4	0.96	1.03
SN1B	437	452.7	390.2	0.97	1.12
SN2B	341	333.3	310	1.02	1.1
SN3B	330	340.4	314.3	0.97	1.05
SN4C	307	325.2	-	0.94	-
SN5C	266	250.2	-	1.06	-
SN6C	234	252.3	-	0.93	-
SN4D	494	457.9	392.1	1.08	1.26
SN5D	335	329.8	307.3	1.02	1.09
SN6D	327	337.3	311.4	0.97	1.05
Average				1.00	1.11
COV				0.05	0.07

The results reported in Table 3.4 point out how numerical results of PARC_CL 1.0 crack model post–processed in accordance to CSCT, are able to predict in the right way the trends and measured shear strength. The average value of the ratio between the experimental and calculated strength are closer to 1.0 with low values of the coefficient of variation (COV), with respect to the analytical calculation.

3.3.2.3.2 [Rombach and Latte, 2009] experimental campaign

As for the Natario's experimental campaign, all specimens were modelled with eight nodes shell elements with reduced integration point (*S8R*) and the shell element thickness was divided into three layers in order to consider top and bottom steel reinforcement. Both linear load f_q and concentrated load F_Q were modelled considering a region in which a constant pressure was applied. In order to have a good agreement with the test setup, the supporting beams were modelled in their middle plane. Such supporting systems were constrained so that the slab is not able to lift up. Due to the symmetry of the specimens only a half of the slabs were modelled as shown in Figure 3.16.

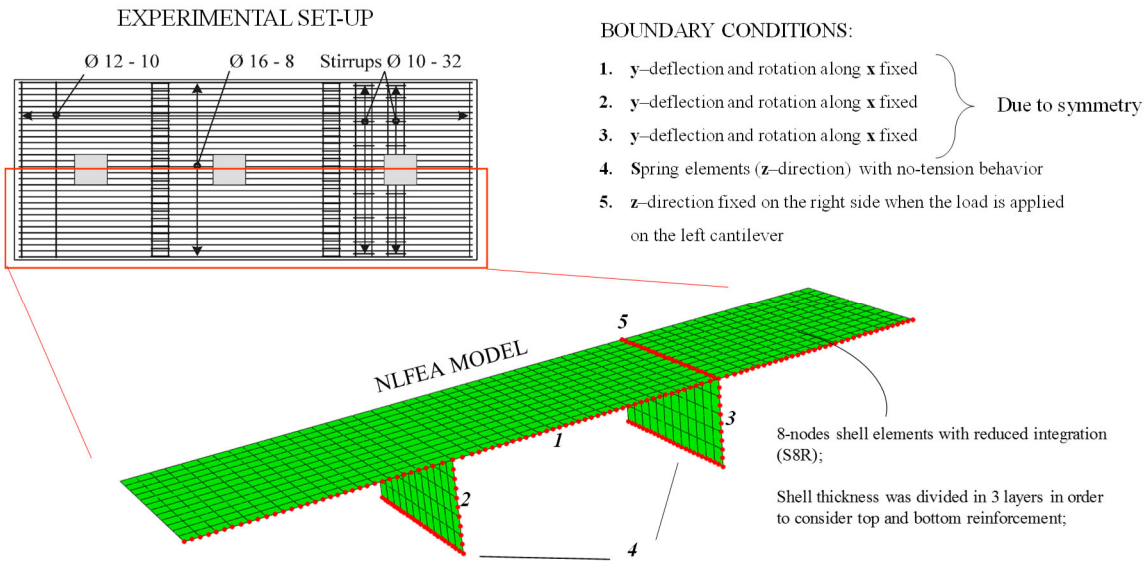

Figure 3.16 – NLFEA model for Rombach's specimens

The shear strength calculated by means of NLFEA post-processed according to the CSCT are reported in Table 3.5 together with the shear strength evaluated following the analytical procedure proposed in §3.3.2.1 and the experimental outcomes.

Table 3.5 – Comparison between experimental, analytical and NLFEA shear strength predictions for Rombach and Latte experimental campaign

Specimen	$V_{exp.}$ [kN]	V_{NLFEA} [kN]	$V_{analytical}$ [kN]	$\frac{V_{exp.}}{V_{NLFEA}}$	$\frac{V_{exp.}}{V_{analytical}}$
VK1 V1	690	599.1	507.4	1.15	1.36
VK2 V1	678	583	446.1	1.16	1.52
VK3 V1	672	667	505.3	1.01	1.33
VK4 V1	487	355.9	322.5	1.37	1.51
Average				1.17	1.43
COV				0.13	0.07

From Table 3.5 it can be highlight how numerical results of PARC_CL 1.0 Crack Model post–processed in accordance to CSCT, are able to predict in the right way the trends and measured shear strength. The average value of the ratio between the experimental and calculated strength are closer to 1.0 with low values of the Coefficient of Variation COV, with respect to the analytical calculation.

3.3.3 RC slabs subjected to punching shear

For slab subjected to concentrated load far from the support, Figure 3.5-b, the failure is characterized by punching shear and the failure criterion is defined as reported in §3.3.1.2. The punching shear failure occurs at the intersection of the load-rotation curve of the slab with the failure criterion, as shown in Figure 3.6-b. To

enable a calculation of the punching shear strength according to Eq.(3.28), the relationship between the rotation, ψ, and the applied load, V, needs to be known. The load-rotation relationship can be obtained using a nonlinear numerical simulation of the flexural behaviour of the slab by means, for example, of nonlinear finite element code. Moreover, in axisymmetric cases, a numerical integration of the moment-curvature relationship can be performed directly. The axisymmetric case of an isolated slab element can also be treated analytically after some simplifications.

In this section the experimental campaign carried out at the Ecole Polytechnique Fédérale de Lausanne (EPFL) by [Guadalini et al., 2009] was investigated as a first case study, in order to underline the capability of NLFEA post-processed using the CSCT to predict different failure modes (e.g. bending or punching shear) associated to different geometrical and mechanical properties of the specimens. The test series consisted in 11 simply supported square RC slabs loaded at the centre with different dimensions and reinforcement ratios. The experimental outcomes were compared with analytical formulation and NLFEA with PARC_CL 1.0 crack model results.

3.3.3.1 Analytical calculation [Muttoni, 2008]

The axisymmetric case of an isolated slab element can be treated analytically after some simplifications, according to the formulation proposed by [Muttoni, 2008], Figure 3.17.

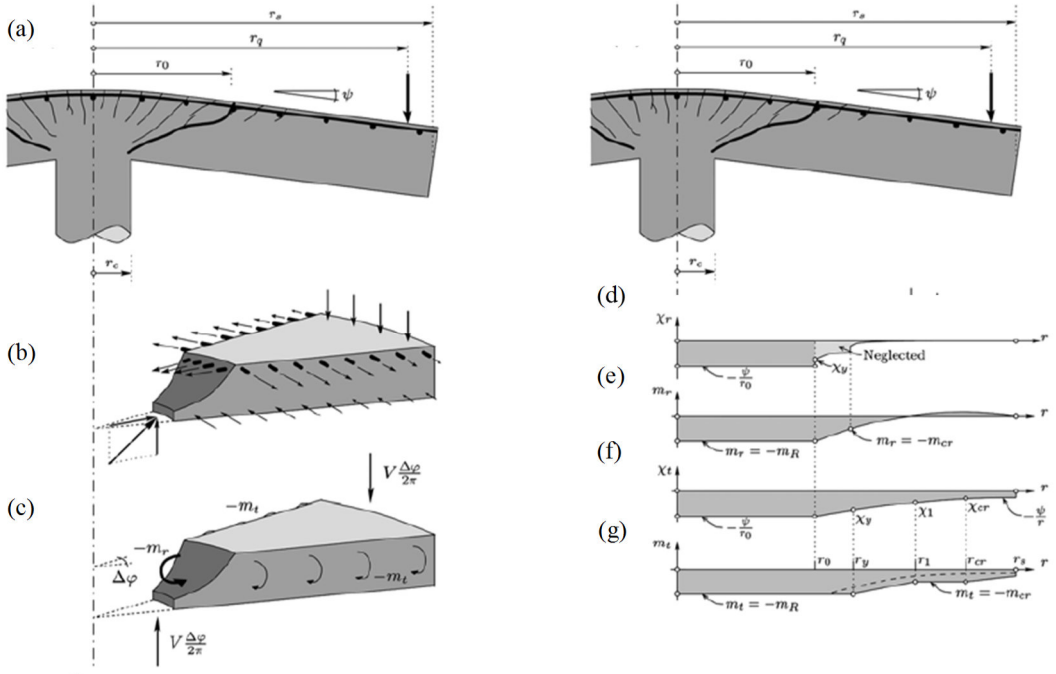

Figure 3.17 - Assumed behavior for axisymmetric slab: (a) geometrical parameters and rotation of slab; (b) forces in concrete and in reinforcement acting on slab sector; (c) internal forces acting on slab sector; (d) distribution of radial curvature; (e) distribution of radial moment; (f) distribution of tangential curvature; and (g) distribution of tangential moments for quadrilinear moment-curvature relationship (shaded area) and for bilinear moment-curvature relationship (dashed line) [Muttoni, 2008].

According to this model, the tangential cracks and the radial curvature are concentrated in the vicinity of the column. Outside the critical shear crack, located at a radius r_0 (assumed to be at a distance d from the

face of the column), the radial moment, and thus the radial curvature, decreases rapidly as shown in Figure 3.17-d and Figure 3.17-e. Consequently, it can be assumed that the corresponding slab portion deforms following a conical shape with a constant slab rotation ϕ, Figure 3.17-a. In the region inside the radius r_0, the radial moment is considered constant because the equilibrium of forces is performed along cross sections defined by the shape of the inclined cracks, Figure 3.17-b and Figure 3.17-c, where the force in the reinforcement remains constant (due to the fact that the shear force is introduced in the column by an inclined strut developing from outside the shear critical crack, Figure 3.17-b and Figure 3.17-c). Considering a quadrilinear moment-curvature relationship for the reinforced concrete section, as shown in Figure 3.18, the following expression results:

$$V = \frac{2\pi}{r_q - r_c}\left(-m_r r_0 + m_r\left\langle r_y - r_o\right\rangle + EI_1\psi\left\langle \ln(r_1) - \ln(r_y)\right\rangle + EI_1\chi_{TS}\left\langle r_1 - r_y\right\rangle + m_{cr}\left\langle r_{cr} - r_1\right\rangle + EI_0\psi\left\langle \ln(r_s) - \ln(r_{cr})\right\rangle\right) \quad (3.32)$$

where m_r is the radial moment per unit length acting in the slab portion at $r = r_0$ and the operator $\langle x \rangle$ is x for $x \geq 0$ and 0 for $x < 0$. A simpler moment-curvature relationship can be adopted by neglecting the tensile strength of concrete f_t and the effect of tension stiffening, leading to a bilinear relationship, reported in Figure 3.18.

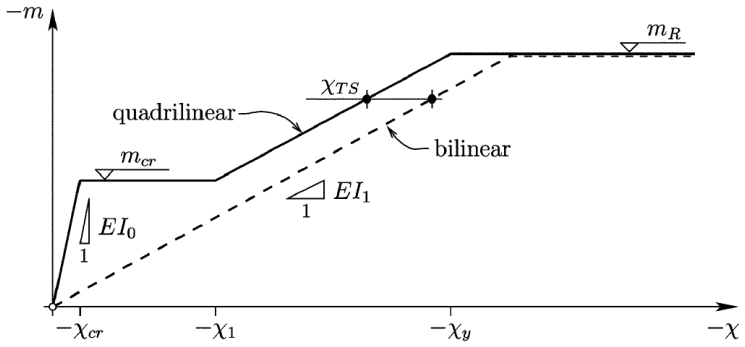

Figure 3.18 - Moment-curvature relationships: bilinear and quadrilinear laws [Muttoni, 2008].

The intersection between the load-rotation curve obtained with Eq.(3.32) and the failure criterion evaluated with Eq.(3.28) allows to calculate the punching shear resistance of an axisymmetric RC slab.

3.3.3.2 Experimental campaigns by [Guadalini et al., 2009]

In order to assess the capability of analytical formulation and NLFEA to predict the punching shear resistance the experimental campaign carried out by [Guadalini et al., 2009] has been used as a reference for the comparison. The test series consisted of 11 reinforced concrete square slabs without transverse reinforcement and subjected to a concentrated load. The slab geometry and the mechanical properties of concrete and reinforcing steel are listed in Table 3.6, where B is the side dimension of the test specimen, a_1, a_2, h and b are illustrated in Figure 3.19, f_t is the mean value of the concrete tensile strength, E_c is the modulus of elasticity, f_y is the mean value of the yield strength of the reinforcing steel, ϕ is the bar diameter, s is the bar spacing and ρ the flexural reinforcement ratio.

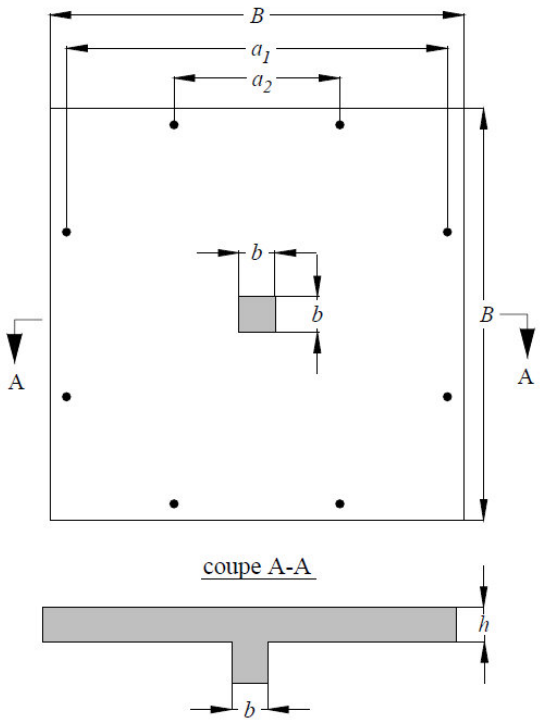

Figure 3.19 – Geometrical parameters of tested specimens [Guadalini, 2005]

The selected slabs are characterised by constant values of the ratio between the slab and column dimensions, *B/b*, and by approximately constant slenderness, a_λ/d (being $a_\lambda = B\text{-}b$), meaning that *h* is increasing as the dimension *B* is increasing. The slabs are reinforced with varying flexural reinforcement ratios ranging from 0.22 % to 1.5 %. The slab PG-4 was casted using a maximum aggregate size d_g = 4 mm, while for the other slabs this value always equals 16 mm.

Table 3.6 – Geometrical characterization and main mechanical properties for concrete and steel of Guadalini's experimental campaign.

Spec.	Geometry						Concrete				Steel			
	B [mm]	a_1 [mm]	a_2 [mm]	b [mm]	h [mm]	d [mm]	f_c [MPa]	f_t [MPa]	E_c [GPa]	d_g [mm]	f_y [MPa]	ϕ [mm]	s [mm]	ρ [%]
PG-1	3000	2760	1200	260	250	210	27.7	2	25.7	16	573	20	100	1.5
PG-2	3000	2760	1200	260	250	210	40.5	3	34.7	16	552	10	150	0.25
PG-3	6000	5160	2400	520	500	456	32.4	2.1	31.8	16	520	16	135	0.33
PG-4	3000	2760	1200	260	250	210	32.2	2	27.3	4	541	10	150	0.25
PG-5	3000	2760	1200	260	250	210	29.3	2.3	26.8	16	555	10	115	0.33
PG-6	1500	1380	600	130	125	96	34.7	2.4	33.7	16	526	14	110	1.5
PG-7	1500	1380	600	130	125	100	34.7	2.4	33.7	16	550	10	105	0.75
PG-8	1500	1380	600	130	140	117	34.7	2.4	33.7	16	525	8	155	0.28
PG-9	1500	1380	600	130	140	117	34.7	2.4	33.7	16	525	8	196	0.22
PG-10	3000	2760	1200	260	250	210	28.5	2.2	29.5	16	577	10	115	0.33
PG-11	3000	2760	1200	260	250	210	31.5	2.5	31	16	570	16/18	145	0.75

3.3.3.3 *Nonlinear finite element modelling and results*

The load-rotation curve can also be evaluated by means of nonlinear finite element analysis (NLFEA). In a similar way as just seen in case of shear failure, in this section NLFE analyses with PARC_CL 1.0 crack model are carried out using multi–layer shell elements modelling.

Due to the symmetry of geometric and loading conditions only a quarter of the slab was modelled. Eight node multi-layered shell elements with reduced integration were adopted for the reinforced concrete (S8R). The slabs were vertically supported in eight points along edges. Each element was divided across its thickness into three layers or two layers, depending on the orders of bars of the specimen; 5 Simpson integration points are used over the thickness of each layer.

In general, the load can be applied by choosing different modelling strategies: 1) a pressure applied to the elements in the area of the column, 2) a uniform displacement applied to all nodes in the area of the column and 3) interface elements with calibrated normal and tangential interface properties (e.g. based on Mohr Coulomb approach) [Belletti et al., 2014], [Sagaseta et al., 2014]. In general loading condition 1 is suitable for modelling the effect of tires loads in bridge decks, loading condition 2 for modelling the effects of columns in building floors and loading condition 3 for modelling experimental set-up (RC slab and loading and supporting devices) of laboratory tests. The specimens tested by [Guadalini et al., 2009] present a column in the center of the slab for full size and double size specimens (B=3 m and B=6 m) and a loading steel plate in the center of the slab for half size specimens (B=1.5 m). In this section loading condition 1 was chosen as reference loading condition for linear and nonlinear finite element analyses, as shown in Figure 3.20.

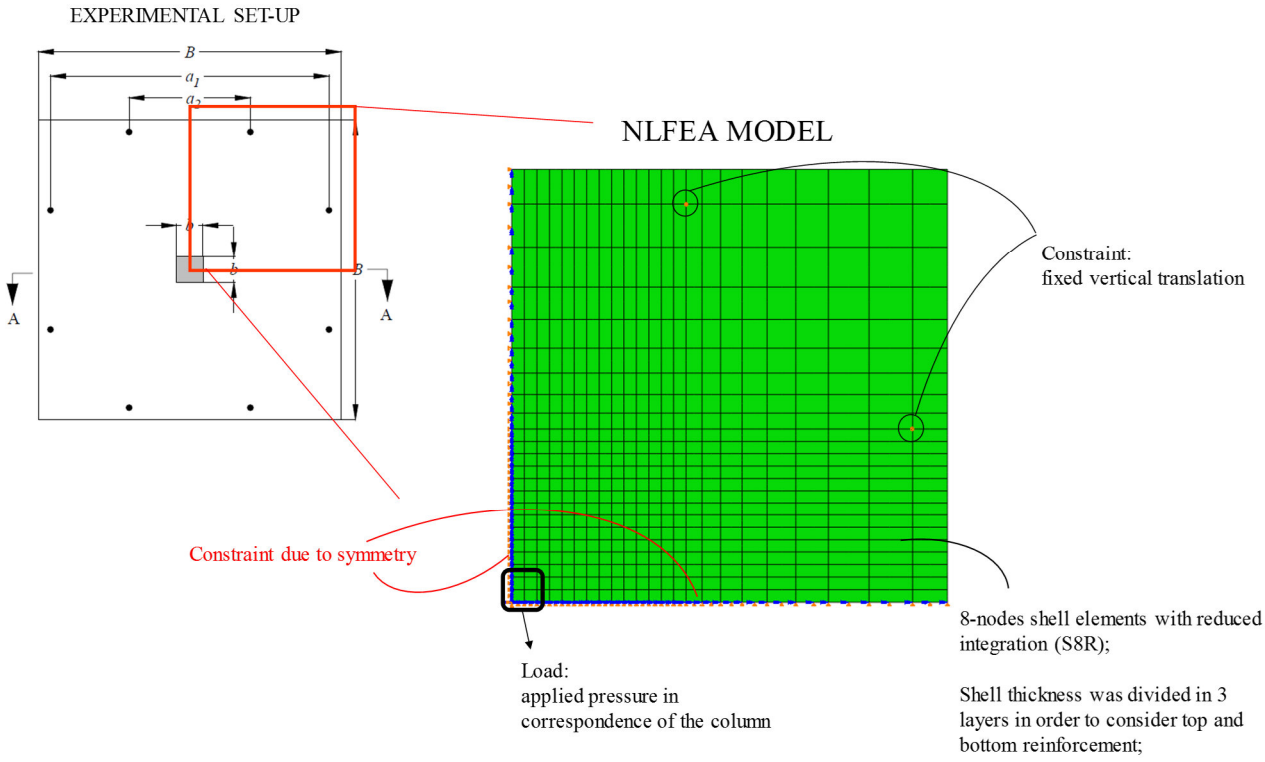

Figure 3.20 – NLFEA model for Guadalini's specimens.

The analyses were carried out using the mean values of the material properties as reported in Table 3.7. In Table 3.7 the a_m value is calculated on the basis of the bar spacing according to Eq.(3.33):

$$a_m = \frac{s_1 + s_2}{2\sqrt{2}} \tag{3.33}$$

where s_1 and s_2 represent the bar spacing in the two orthogonal directions of the upper reinforcement grid.

The fracture energy in tension (G_F) is evaluated according to the formulation proposed in [*fib*-Model Code 1990] while the fracture energy in compression (G_C) is set equal to 250 times the fracture energy in tension, according to Nakamura and Higai [Nakamura and Higai, 2001].

Table 3.7 – Mean mechanical properties used in NLFE model.

Spec.	Concrete (see §3.2.1)								Steel (see §3.2.3)				
	a_m [mm]	f_c [MPa]	G_C [N/mm^3]	$\varepsilon_{c,cr}$ [-]	$\varepsilon_{c,u}$ [-]	f_t [MPa]	G_F [N/mm^3]	$\varepsilon_{t,u}$ [-]	f_y [MPa]	E_s [MPa]	E_{sp} [MPa]	s_1 [mm]	s_2 [mm]
PG-1	71	27.7	15.3	0.020	0.032	2	0.061	0.0032	573	200000	1000	100	100
PG-2	106	40.5	20.0	0.020	0.027	3	0.080	0.0019	552	200000	1000	150	150
PG-3	95	32.4	17.1	0.020	0.028	2.1	0.068	0.0025	520	200000	1000	135	135
PG-4	106	32.2	17.0	0.020	0.027	2	0.068	0.0024	541	200000	1000	150	150
PG-5	81	29.3	15.9	0.020	0.030	2.3	0.064	0.0025	555	200000	1000	115	115
PG-6	78	34.7	17.9	0.020	0.030	2.4	0.072	0.0028	526	200000	1000	110	110
PG-7	74	34.7	17.9	0.020	0.030	2.4	0.072	0.0030	550	200000	1000	105	105
PG-8	110	34.7	17.9	0.020	0.027	2.4	0.072	0.0021	525	200000	1000	155	155
PG-9	139	34.7	17.9	0.020	0.026	2.4	0.072	0.0017	525	200000	1000	196	196
PG-10	81	28.5	15.6	0.020	0.030	2.2	0.062	0.0026	577	200000	1000	115	115
PG-11	103	31.5	16.7	0.020	0.028	2.5	0.067	0.0020	570	200000	1000	145	145

Since for RC slabs tested by [Guadalini et al., 2009] there is no the load eccentricity, according to the [*fib*-Model Code 2010] the shear resisting control perimeter b_0 is equal to the basic control perimeter and is simply calculated at a distance 0.5d from the supported area.

In Figure 3.21 are reported the load-rotation curves and the CSCT failure criterion for the analysed slabs. The load–rotation (V-ψ) curves obtained from NLFEA and from the analytical model proposed by [Muttoni, 2008] on the basis of a quadrilinear moment-curvature relationship for the reinforced concrete section are shown together with the experimental measurements reported in [Guadalini et al., 2009]. The rotation from NLFEA results is calculated by dividing the relative vertical displacement between the edge of the slab and the edge of the column by the distance between these two points. The experimental rotation was obtained dividing the relative displacement between the center of the column and the reaction points at the perimeter by the corresponding distance.

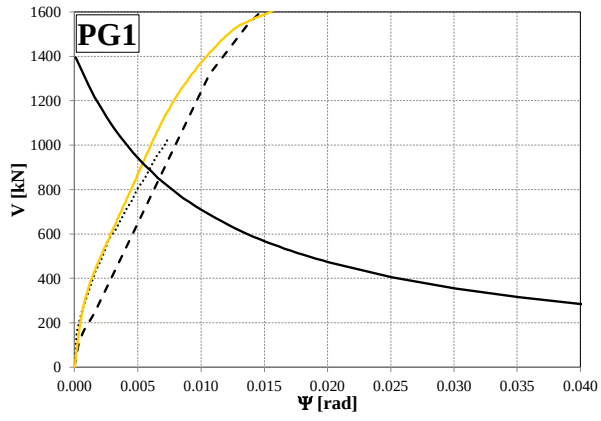
PG1
V [kN]
Ψ [rad]

(a)

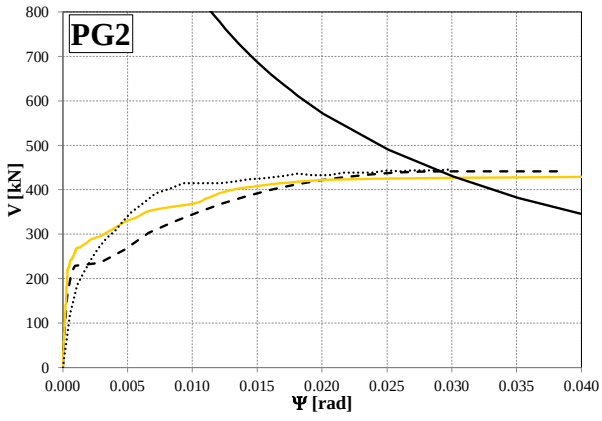
PG2
V [kN]
Ψ [rad]

(b)

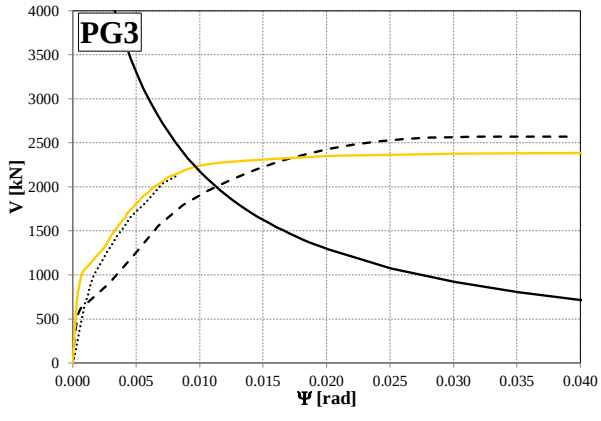
PG3
V [kN]
Ψ [rad]

(c)

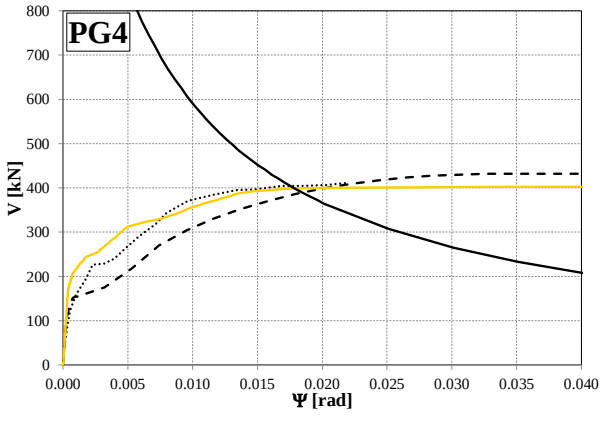
PG4
V [kN]
Ψ [rad]

(d)

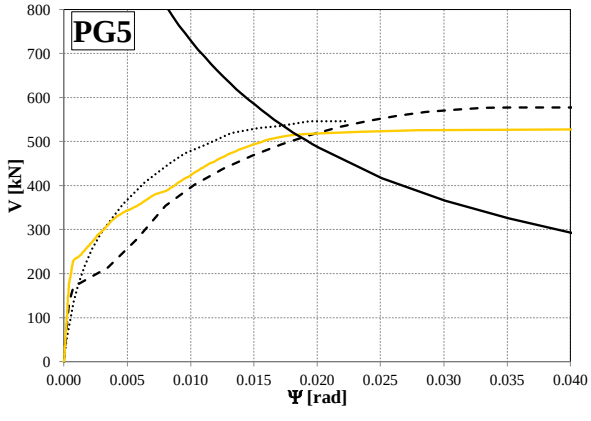
PG5
V [kN]
Ψ [rad]

(e)

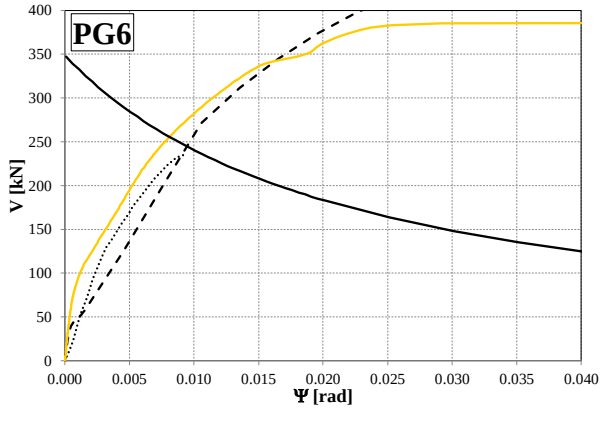
PG6
V [kN]
Ψ [rad]

(f)

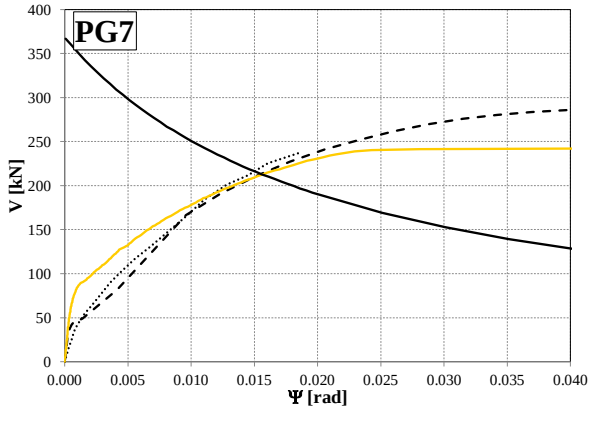
PG7
V [kN]
Ψ [rad]

(g)

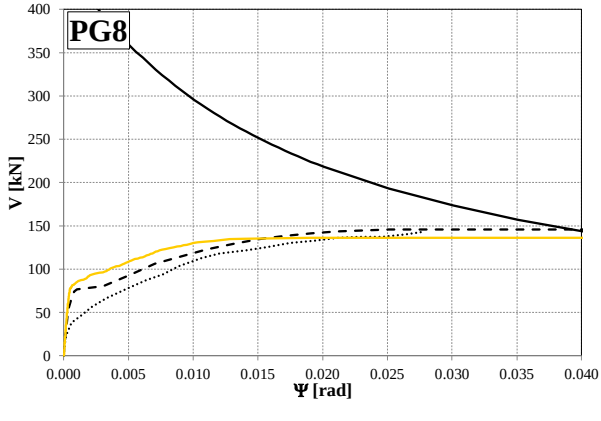
PG8
V [kN]
Ψ [rad]

(h)

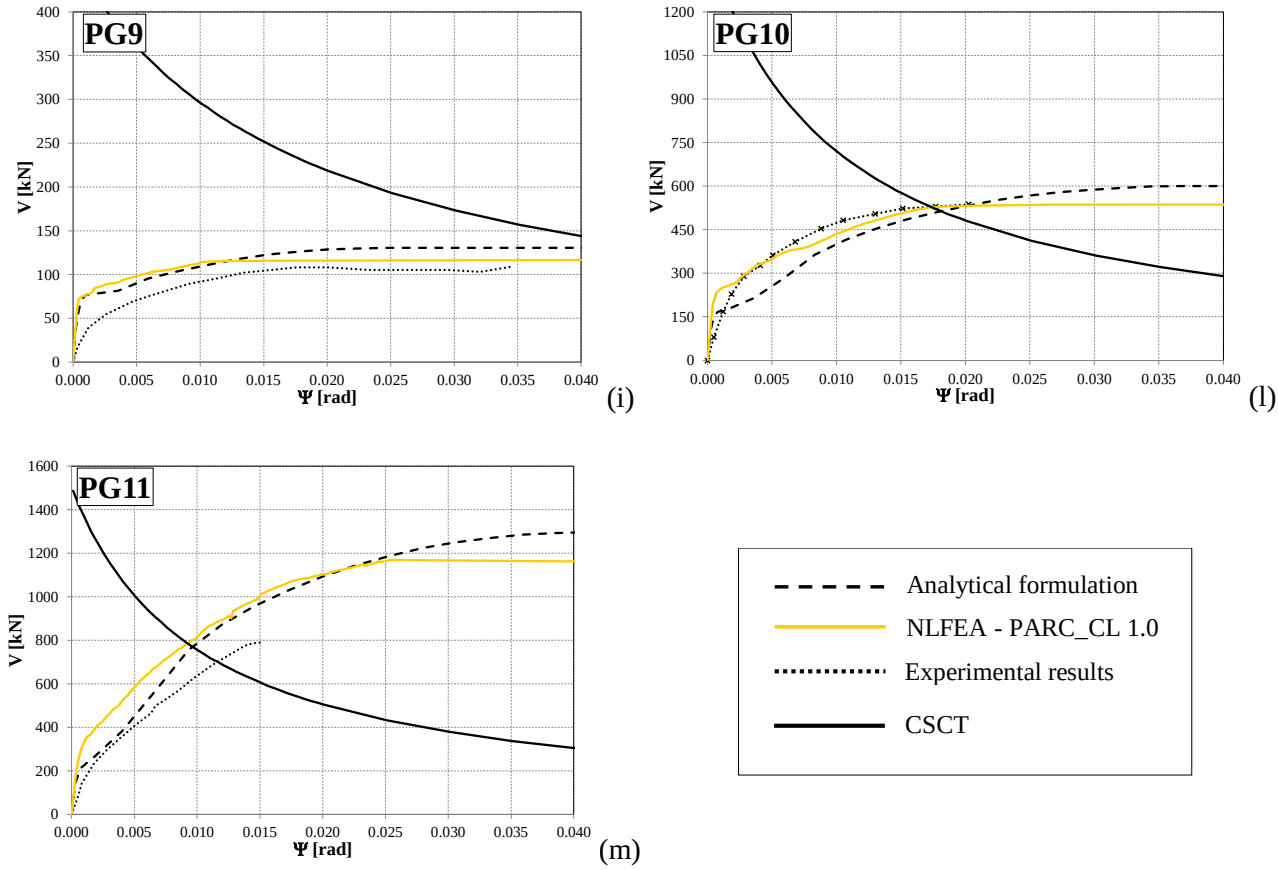

Figure 3.21 – Load-rotation curve and CSCT for:(a) PG1 specimen, (b) PG2 specimen, (c) PG3 specimen, (d) PG4 specimen, (e) PG5 specimen, (f) PG6 specimen, (g) PG7 specimen, (h) PG8 specimen, (i) PG9 specimen, (l) PG10 specimen, (m) PG11 specimen.

It is clear from Figure 3.21 that the NLFEA predicts the load-rotation curves of the slabs with good accuracy. Moreover, due to the absence of bending moment redistribution or compressive membrane action effects, related to the particular boundary and loading conditions, the differences between the load-rotation curves obtained using NLFEA and the analytical formulation are quite small.

The good agreement between NLFEA, analytical and experimental outcomes are confirmed by comparing the punching shear resistance as reported in Table 3.8. Table 3.8 shows a good agreement between the calculated and the experimental results, both in term of average values and coefficient of variation (COV).

Table 3.8 shows good agreement between the calculated and experimental results, thus validating the proposed analysis procedure.

As should be expected in the case of statically determinate slab panels subjected to centered load, the differences between the punching shear resistances obtained using NLFEA and the analytical method proposed in §3.3.3.1 for determining the load–rotation curve are small. Indeed, due to the simplicity of boundary and loading conditions, no bending moment redistribution or compressive membrane action effects occur and so

the analytical formulation, based on simplifying hypothesis, leads to accurate results, compared with NLFEA and experimental outcomes.

Table 3.8 – Punching shear strength obtained with mean mechanical properties of materials: comparison between NLFEA, analytical and experimental results.

Specimen	$V_{exp.}$ [kN]	V_{NLFEA} [kN]	$V_{analytical}$ [kN]	$\frac{V_{exp.}}{V_{NLFEA}}$	$\frac{V_{exp.}}{V_{analytical}}$
PG-1	1023	858	860	1.19	1.19
PG-2	440	426	440	1.03	1.00
PG-3	2153	2163	2036	1.00	1.06
PG-4	408	392	392	1.04	1.04
PG-5	550	500	511	1.10	1.08
PG-6	238	241	234	0.99	1.02
PG-7	241	205	199	1.18	1.21
PG-8	140	136	146	1.03	0.96
PG-9	115	116	115	0.99	1.00
PG-10	540	504	515	1.07	1.05
PG-11	763	740	767	1.03	0.99
Average				1.06	1.05
COV				0.06	0.08

3.3.4 Compressive membrane action effect

Previous sections highlighted that in case of simply supported slabs, tested in laboratory without any confinement effect, simplified analytical formulation can lead to results as accurate as NLFEA, due to the particular boundary and loading conditions. On the other hand, the real boundary and loading conditions of a RC slab placed within a whole structure could be completely different with respect to the simply supported conditions. In this case the simplifying assumptions made in the analytical formulations could lead to less accurate results compared with NLFEA.

In this context, it is widely recognized that compressive membrane action (CMA), also called arching action, increases both the bending and punching capacities of reinforced concrete (RC) structures.

Arching action can develop when the edges of the loaded member are restrained against lateral displacements; when the edges of the member are prevented from lateral displacement, in-plane compressive thrusts rise from the boundary enhancing the load carrying capacity, Figure 3.22.

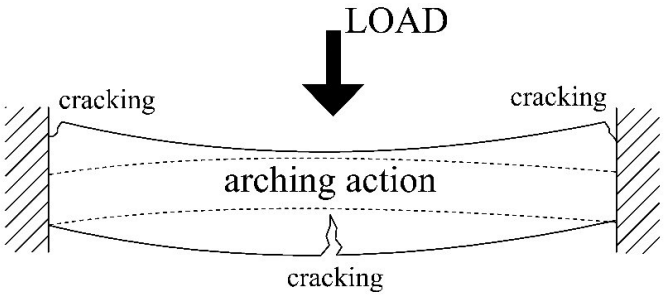

Figure 3.22 – Compressive membrane action in laterally restrained slab.

In order to assess the capability of NLFEA to account for CMA effects in this section the Corick bridge experimental campaign, tested by [Taylor et al., 2007], was investigated.

Both the simply supported slabs tested by [Guadalini et al., 2009], presented in §3.3.3.2, and the Corick bridge slabs [Taylor et al., 2007], presented in the following, was investigated using the level of approximation (LoA) approach proposed in [*fib*-Model Code 2010].

The LoA approach, as widely discuss in in the following, is a design strategy, based on the assumption that the structural member's response can be progressively refined through a better estimate of the physical parameters. By increasing the level of approximation, a better accuracy in the estimate of the structural response can be obtained; however, more time and resources have to be devoted to the analyses. In particular, the higher level of approximation is associated with the NLFEA.

The aim of this section was to demonstrate that for complex boundary and loading conditions, such as the Corick bridge experimental campaign [Taylor et al., 2007], the higher level of approximation, associated to NLFEA, can provide a higher prediction of the bearing capacity with respect to simplified analytical formulations.

3.3.4.1 Level of Approximation (LoA) approach

The level of approximation approach for the calculation of the design punching shear resistance is applied in this section. This approach is based on the idea that the bearing capacity of a structural member can be assess with different levels of accuracy. As the level of approximation increases (at the cost of the increasing time that is required to perform the analyses), more accurate and typically less conservative estimates of the structural capacity can be obtained. The lowest levels of approximation (LoA I and LoA II) are typically used when preliminary estimates of the strength of a member are required, and so the design expressions can be assessed in a simple (yet safe) manner. This allows the limits of strength to be determined even though very little time needs to be devoted to the analyses, which is normally sufficient for preliminary design purposes and even for many structural members without a given governing failure mode. However, in cases where such a degree of accuracy is not sufficient (e.g. critical elements, detailed design), the values of the mechanical

parameters can be refined in a number of steps. This means devoting more time to analyses, see Figure 3.23, but leads to better estimates ofthe behaviour and strength of members. The LoA approach thus allows the preliminary design phases as well as advanced designs and assessments to be covered with the same set of expressions.

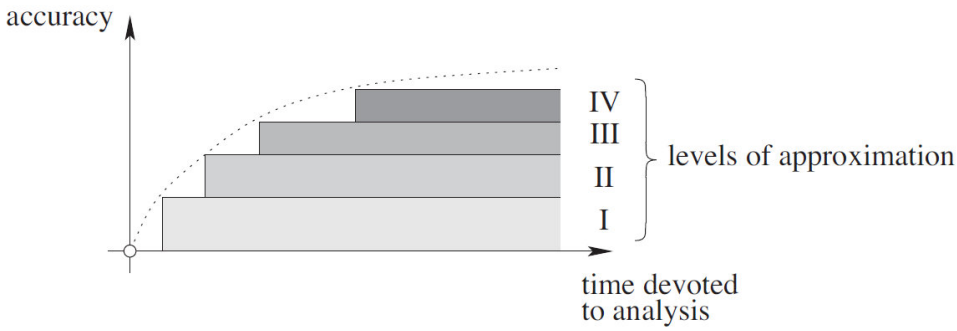

Figure 3.23 - Levels-of-approximation approach: accuracy of the estimate as a function of the time devoted to analyses [fib-Model Code 2010].

In particular, for the evaluation of punching shear resistance, LoA I and LoA II are based on simple analytical calculations, whereas LoA III and LoA IV call for the use of linear and nonlinear structural analysis methods respectively. The most refined level, LoA IV, is best suited to assessing the capacities of existing structures because it requires the determination of the slab rotation using nonlinear analysis methods. This section focuses on the application of LoA IV, using NLFEA, which could be a useful tool for the assessment of existing structures because it allows the beneficial effects of internal shear stress and bending moment redistributions and compressive membrane action effects to be taken into account.

According to the formulation proposed in *fib*-Model Code 2010, based on the CSCT, the design punching shear resistance, V_{Rd}, is obtained using Eq.(3.34):

$$\frac{V_{Rd}}{b_0 \cdot d_v \cdot \frac{\sqrt{f_{ck}}}{\gamma_c}} = \frac{1}{1.5 + 0.9 \cdot \psi \cdot d \cdot k_{dg}} \tag{3.34}$$

where d_v is the shear-resisting effective depth (assumed equal to d), $k_{dg}=32/(16+d_g)$ and d_g is the reference aggregate size. The adopted value of the partial safety factor for concrete material properties, γ_c, equals 1 and 1.5 for the evaluation of the characteristic and design punching shear resistance, respectively.

The rotation of the slab, proposed by [*fib*-Model Code 2010], for LoA I and LoA II is given by Eq.(3.35):

$$\psi = 1.5 \cdot \frac{r_s}{d} \frac{f_{yd}}{E_s} \left(\frac{m_{Ed}}{m_{Rd}} \right)^{1.5} \tag{3.35}$$

where r_s represents the position where radial bending moment is zero. m_{Ed} is set equal to the average moment per unit length for calculating flexural reinforcement in support strip and m_{Rd} represents the design flexural strength of the slab.

For LoA I the ratio m_{Ed}/m_{Rd} is set equal to 1, which is equivalent to assuming full utilization of the flexural reinforcement. For LoA II the rotation is calculated with Eq.(3.35) by adopting an iterative procedure. The moment acting along the support m_{Ed} is obtained with an analytical expression relating the moment at the support to the applied load, as shown in Eq.(3.36)

$$m_{Ed} = \frac{V_{Ed}}{8} \tag{3.36}$$

The convergence of the iterative procedure is completed when the V_{Ed} value matches the V_{Rd} value. For both LoA I and II, the shear resisting control perimeter b_0 is usually determined based on simple equations depending on the eccentricity of the applied force and r_s can be approximated as $0.22 \cdot L_x$ or $0.22 \cdot L_y$ for the x- and y directions, respectively, with L_x and L_y being the corresponding spans.

For LoA III the moment m_{Ed} is calculated as the average value of LFEA results measured over a support strip having a width, b_s, equal to *0.75B*. Therefore, the relationship between the moment acting at the support, m_{Ed}, and the applied load, V_{Ed}, was evaluated by performing a linear-elastic analysis. The rotation for LoA III is calculated following Eq.(3.35) by adopting an iterative procedure that stops when the value of V_{Ed} matches with the value of V_{Rd}. The coefficient 1.5 in Eq.(3.35) was replaced by 1.2.

Finally, for LoA IV, NLFEA was performed for the evaluation of the load-rotation curve and consequently for the definition of the design punching shear strength. ECOV method, proposed in [*fib*-Model Code 2010], was adopted to obtain the design punching shear resistance using LoA IV.

In order to clarify these concept, in Figure 3.24 is reported the CSCT calculated according to Eq.(3.34) for one of the analyzed slabs. From Figure 3.24 it can be noticed that, using the same failure criterion, changing the definition of the rotation, ψ, the punching shear resistance changes. In particular, the higher the level of approximation is associated to the lower rotation of the slab and hence to a less conservative prediction of the bearing capacity.

In the following the LoA approach is applied to two different experimental campaigns: the simply supported slabs tested by [Guadalini et al., 2009], presented in §3.3.3.2, and the Corick bridge slabs tested by [Taylor et al. 2007].

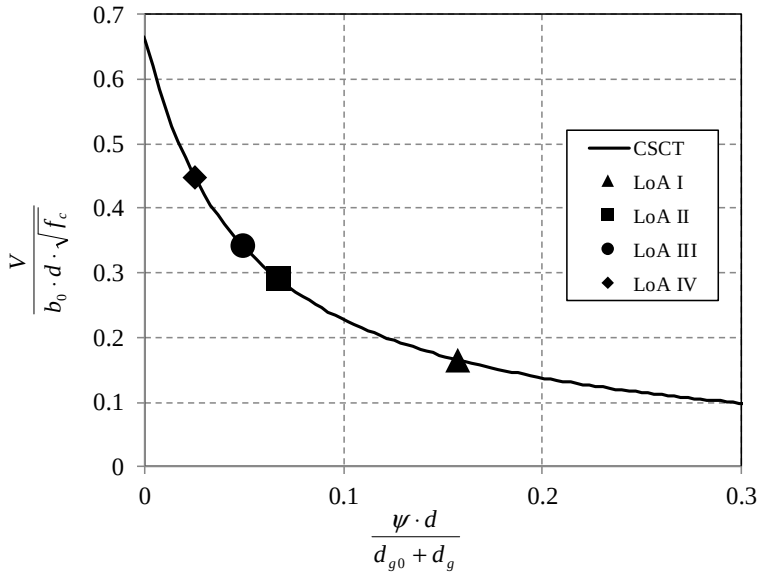

Figure 3.24 – Example of assessment of punching shear resistance using different levels of approximation

3.3.4.1.1 Experimental campaign by [Guadalini et al., 2009]

The slabs tested by [Guadalini et al., 2009] and presented in §3.3.3.2 are taken as an example. In this case no redistribution of forces is possible because the structure is statically determinate. The design punching shear resistance obtained with different levels of approximation for the slabs analysed is listed in Table 3.9. The results reported in Table 3.9 confirm that the estimation of the design punching shear resistance can be refined progressively by using the LoA approach.

As jus mentioned the design punching shear resistance obtained with nonlinear finite element analysis is calculated following the ECOV method proposed in [*fib*-Model code 2010]. According to the ECOV method the design resistance is calculated with Eq.(3.37):

$$V_{Rd} = \frac{V_{Rm}}{\gamma_R \gamma_{Rd}} \tag{3.37}$$

where V_{Rm} is determined by the intersection of the load-rotation curve obtained from NLFEA with the mean failure criterion reported in Eq.(3.28). The model uncertainty factor γ_{Rd}, according to [*fib*-Model code 2010] is set equal to 1.06 and the global resistance safety factor is obtained with Eq.(3.38):

$$\gamma_R = e^{(\alpha_R \cdot \beta \cdot V_R)} \tag{3.38}$$

where α_R=0.8, β=3.8 and V_R is calculated using Eq.(3.39):

$$V_R = \frac{1}{1.65} \ln\left(\frac{V_{Rm}}{V_{Rk}}\right) \tag{3.39}$$

In Eq.(3.39) V_{Rk} represents the characteristic value of the punching shear strength and is determined using the characteristic failure criterion of (3.29).

Moving from LoA I to LoA IV an increase of the design punching shear resistance is noted due to a better estimation of the physical parameters. The highest values of the punching shear resistance are obtained using NLFEA. The increase in design punching shear resistance obtained using higher levels of approximation is not constant for the analyzed slabs. Indeed, Figure 3.25, shows that the differences among the LoA predictions depends on several parameters, such as the reinforcing ratio, and the effective depth. To make easier the presented comparisons, constant values for the compressive strength of concrete and the yielding strength of reinforcing steel were used in Figure 3.25 for LoA I to III by averaging the values of RC slabs reported in Table 3.7.

Table 3.9 – Design punching shear resistance obtained with different levels of approximation for slabs tested by [Guadalini et al. 2009].

Specimen	LoA I	LoA II	LoA III	LoA IV
	V_{Rd} [kN]	V_{Rd} [kN]	V_{Rd} [kN]	V_{Rd} [kN]
PG-1	174	489	504	531
PG-2	230	295	311	338
PG-3	538	1132	1224	1573
PG-4	139	233	245	306
PG-5	185	300	314	347
PG-6	76	138	146	158
PG-7	77	123	132	140
PG-8	92	110	120	118
PG-9	92	99	113	98
PG-10	176	298	312	363
PG-11	191	431	448	492

For RC slabs with low reinforcing ratio (PG-2, PG-8 and PG-9), characterized by bending failure or punching shear failure occurred after the full yielding of the reinforcement, Figure 3.25-a-c-e demonstrate that the design resistance obtained using LoA I, LoA II and LoA III is approximately the same. Furthermore, Figure 3.25-a-c-e confirms that for RC slabs failing before reaching the first yielding of reinforcement (PG-1, PG-6, PG-11), the design resistance is strongly dependent on the reinforcement ratio. Also Table 3.9 shows that, for slabs having the same dimensions (*B, b, d*), the differences between LoA I and LoA II (or LoA III) increases for higher reinforcement ratio. Figure 3.25-b-d-f show the influence of the effective depth, *d*, on the design punching shear resistance assessment, keeping constant the reinforcement ratio, ρ, and the slab slenderness, a_λ.

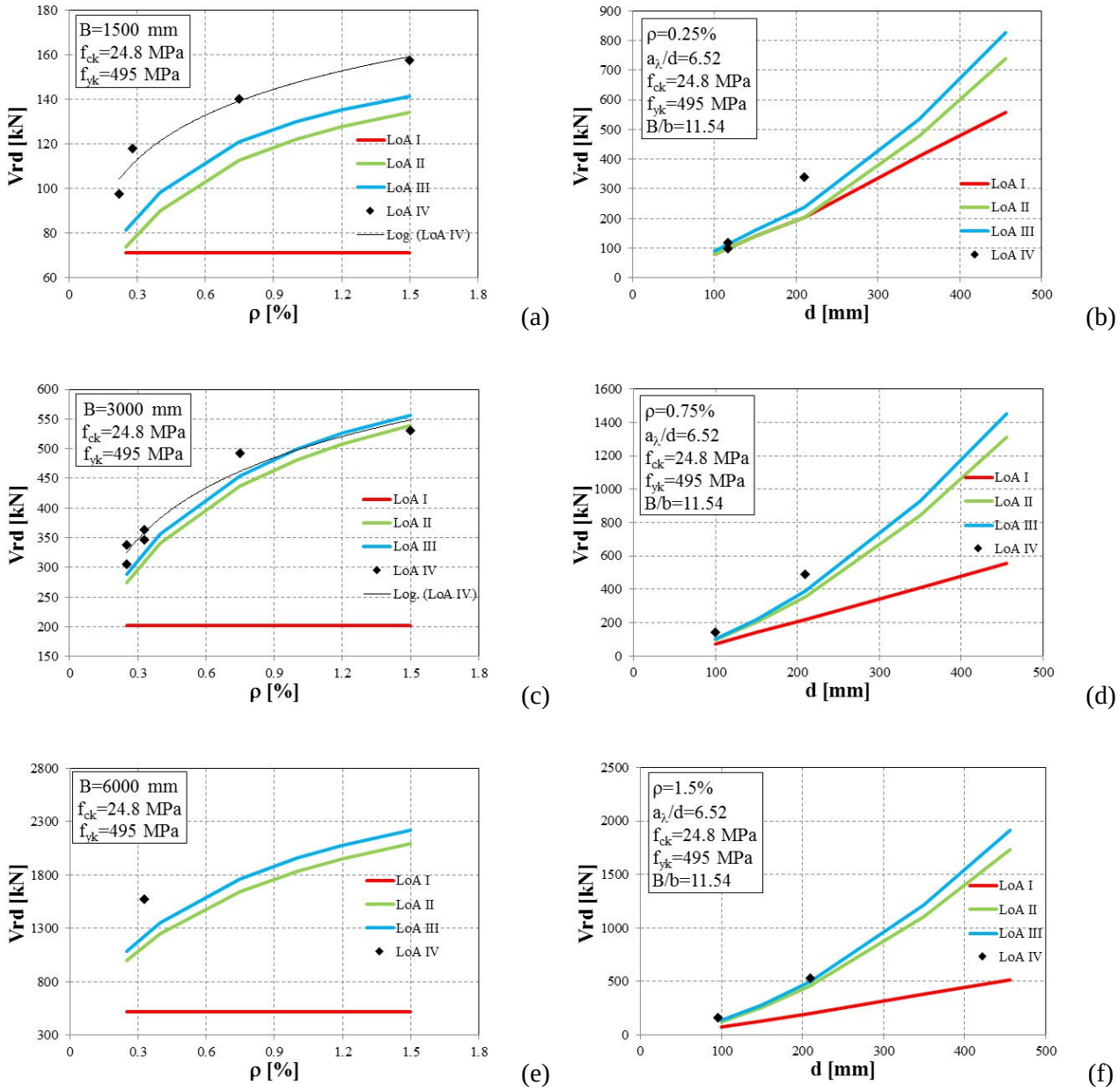

Figure 3.25 – (a), (c) and (e), influence of flexural reinforcement ratio, ρ, in the design punching shear resistance using the LoA approach; (b), (d) and (f) influence of effective depth, d, in the design punching shear resistance using the LoA approach.

The results reported in Table 3.9 and in Figure 3.25 highlighted that in case of structure statically determinate without redistribution of forces, the increasing of the design punching shear resistance obtained with LoA IV with respect to LoA III (or LoA II) is quite small.

3.3.4.1.2 Corick bridge test [Taylor et al., 2007]

In this section the design punching shear resistance, calculated according to LoA approach, is evaluated for the Corick Bridge [Taylor et al., 2007] whose behaviour is highly dependent on compressive membrane action phenomena. The experimental campaign consists of of five I-shaped prestressed concrete beams supporting a 160 mm in-situ reinforced concrete deck slab. The bridge deck was subdivided into 12

slabs having different reinforcement ratios, reinforcement layouts, concrete compressive strengths and polypropylene fiber volume, Figure 3.26. In particular, 4 out of the 12 slabs were analyzed in this section.

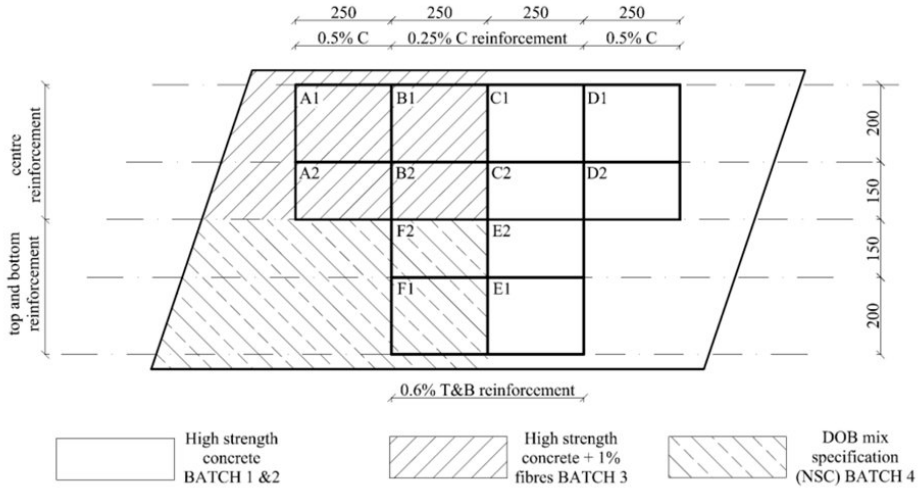

Figure 3.26 – Corick bridge experimental campaign: slabs arrangement (dimension in cm) [Taylor et al., 2007].

The geometrical and mechanical properties of the analyzed slabs are summarized in Table 3.10. All the analyzed specimens are characterized by a double layer of reinforcement in the top and the bottom of the slab.

Table 3.10 – Geometrical characterization and main mechanical properties for concrete and steel of Corick bridge experimental campaign.

Specimen	Geometry					Steel*						
	B [mm]	H [mm]	d [mm]	*clear span* [mm]	f_c [MPa]	f_y [MPa]	ϕ_x [mm]	s_x [mm]	ρ_x [%]	ϕ_y [mm]	s_y [mm]	ρ_y [%]
E1	2500	2000	105	1740	49	500	12	240	0.3	12	240	0.3
E2	2500	1500	105	1240	49	500	12	240	0.3	12	240	0.3
F1	2500	2000	103	1740	41.9	500	12	240	0.3	12	240	0.3
F2	2500	1500	103	1240	44.1	500	12	240	0.3	12	240	0.3

* Top and bottom reinforcement grid have the same mechanical and geometrical properties

A detail of the experimental set-up is shown in Figure 3.27. The load was experimentally applied in two steps: initially the slabs were loaded to a level just over the cracking load, subsequently the load was removed and the slabs were reloaded to a higher level. The aim of this experimental campaign was to demonstrate that the existing bridges have a safety margin with respect to the design capacity.

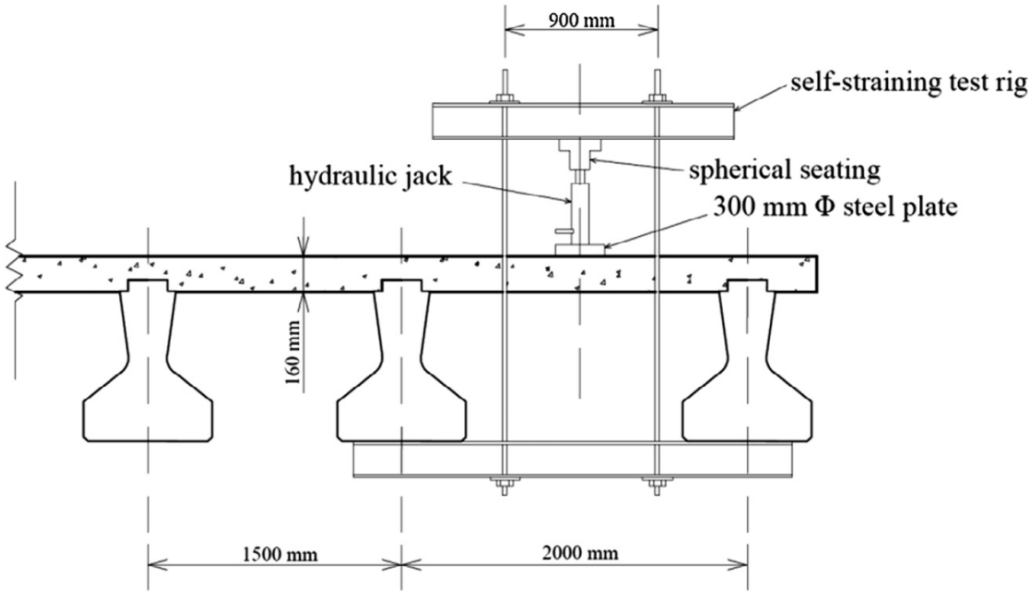

Figure 3.27 – Corick bridge experimental set-up [Taylor et al., 2007].

The entire bridge was modelled with 4-nodes and 3-nodes linear shell elements with classical integration scheme (S4 and S3 elements respectively). The girders were modelled with rectangular 4 nodes elements with different thicknesses according to the girders geometry. The girders were considered simply supported at their ends. In correspondence of the part of the mesh related to the tested slab, a finer mesh of nonlinear multi-layer shell elements was adopted. Figure 3.28 shows a detail of the adopted mesh when load is applied to E1 panel. Over its thickness each element was divided into three layers, with 5 Simpson integration point for layer, in order to consider both the top and the bottom reinforcement grids in their exact position.

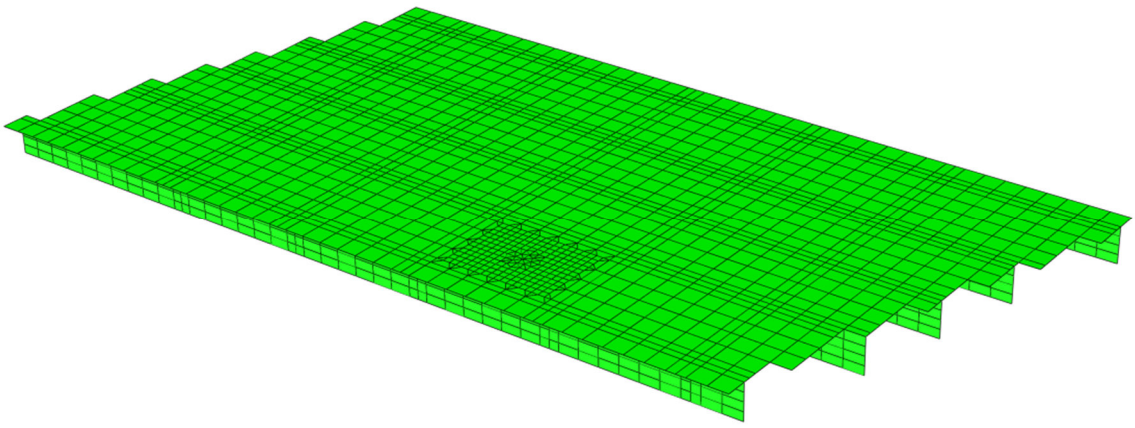

Figure 3.28 – Mesh adopted for the Corick bridge with loaded panel E1.

The mean mechanical properties and the main parameters used in NLFEA to define the behavior of concrete and steel are listed in Table 3.11.

Table 3.11 – Mean mechanical properties used in NLFE model.

Spec.	Concrete (see §3.2.1)									Steel (see §3.2.3)			
	a_m [mm]	Ec [Mpa]	f_c [MPa]	G_C [N/mm^3]	$\varepsilon_{c,cr}$ [-]	$\varepsilon_{c,u}$ [-]	f_t [MPa]	G_F [N/mm^3]	$\varepsilon_{t,u}$ [-]	f_y [MPa]	E_s [MPa]	s_1 [mm]	s_2 [mm]
E1	170	36325	49	22.8	0.020	0.024	3.6	0.091	0.0012	500	200000	240	240
E2	170	36325	49	22.8	0.020	0.024	3.6	0.091	0.0012	500	200000	240	240
F1	170	34496	41.9	20.4	0.020	0.024	3.1	0.082	0.0012	500	200000	240	240
F2	170	35084	44.1	21.2	0.020	0.024	3.3	0.085	0.0012	500	200000	240	240

As for the Guadalini's slabs also in this case the design punching shear resistance obtained with nonlinear finite element analysis is calculated following the ECOV method proposed in [*fib*-Model code 2010]. According to the ECOV method the design resistance is calculated with Eq.(3.40):

$$V_{Rd} = \frac{V_{Rm}}{\gamma_R \gamma_{Rd}} \tag{3.40}$$

where V_{Rm} is determined by the intersection of the load-rotation curve obtained from NLFEA with the mean failure criterion reported in Eq.(3.28). The model uncertainty factor γ_{Rd}, according to fib-Model code 2010 is set equal to 1.06 and the global resistance safety factor is obtained with Eq.(3.41):

$$\gamma_R = e^{(\alpha_R \cdot \beta \cdot V_R)} \tag{3.41}$$

where α_R=0.8, β=3.8 and V_R is calculated using Eq.(3.42):

$$V_R = \frac{1}{1.65} \ln\left(\frac{V_{Rm}}{V_{Rk}}\right) \tag{3.42}$$

In Eq.(3.42) V_{Rk} represents the characteristic value of the punching shear strength and is determined using the characteristic failure criterion of (3.29).

The punching shear resistance obtained analyzing the Corick bridge experimental campaign, using different level of approximation, are listed in Table 3.12.

Table 3.12 – Design punching shear resistance obtained with different levels of approximation for slabs tested by Taylor et al. [Taylor et al. 2007].

Specimen	LoA I V_{Rd} [kN]	LoA II V_{Rd} [kN]	LoA III V_{Rd} [kN]	LoA IV V_{Rd} [kN]
E1	199	199	212	455
E2	225	225	235	472
F1	180	180	192	378
F2	211	211	220	423

The results reported in Table 3.12 shows the increasing of the design punching shear resistance using the higher levels of approximation. Moreover, due to the fact that the formulation proposed by [*fib*-Model code 2010] for LoA I, LoA II and LoA III cannot consider the effects of Compressive Membrane Action (CMA) the resulting punching shear resistance values are lower than the values obtained with LoA IV. This example clarifies the advantages related to the use of refined NLFEA when redistribution of internal stresses and CMA phenomena govern slab behaviour.

3.3.5 Synopsis

In this section the monotonic out-of-plane behaviour of RC slabs was investigated by means of NLFEA carried out using the PARC_CL 1.0 crack model. The aim of this section was to validate the capability of such kind of modelling approach to predict out-of-plane failure through the thickness of the element. A summary of the main observations and findings is presented hereafter:

- The critical shear crack theory (CSCT), proposed by [Muttoni, 2008] and [Muttoni and Fernandez 2008[b]], is adopted to post-process the NLFEA results in order to achieve the shear and punching shear failure. The post-processing method, proposed herein, was validated by means of comparison with several simply supported RC slabs tested in literature.
- The comparison between experimental and NLFEA results, post-processed according to CSCT, highlighted that the multi-layer shell elements approach allows to capture different failure modes through the thickness of the element (bending and shear).
- It was underlined that, in case of statically determined slab panels, due to the simplicity of boundary and loading conditions, no bending moment redistribution or compressive membrane action (CMA) effects occur and so the analytical formulation, based on simplifying assumptions, leads to accurate results, compared with NLFEA and experimental outcomes.
- In order to clarify the effects of CMA on the punching shear resistance a further experimental campaign, which consists in an in situ proof loading, was analysed. The Levels of Approximation (LoA) approach, proposed in [*fib*-Model Code 2010], has been applied on the assessment of the design punching shear resistance.
- The results highlighted in the case of the highly restrained bridge decks, the differences between the slab resistances evaluated using analytical formulation (LoA II and LoA III) and NLFEA (LoA IV) are quite significant, and the benefits related to the use of NLFEA are not negligible.
- It can be established that in the case of existing structures, e.g. flat slabs in buildings or bridge decks, characterized by bending moment redistribution or compressive membrane action effects, the scatter between the slab resistances evaluated using LoA III and LoA IV could be quite high and could justify the use of advanced tools when determining the bearing resistances of RC slabs. In light of this, the proposed numerical procedure represents a good compromise between numerical accuracy and time and memory requirements.

3.4 Simulation of monotonic and cyclic in-plane behaviour

In this section the monotonic and cyclic in-plane behaviour of RC members is investigated by means of NLFEA. In particular, the structural response of RC walls was deeply investigated by using multi-layer shell elements associated with the PARC_CL 1.0 crack model.

Structural RC walls are frequently used both in common civil and industrial buildings and in power plant buildings. Slender structural RC walls, that can come in a variety of geometrical shapes, are commonly used in medium and high rise buildings as lateral force resisting systems, thanks to their capacity to provide strength and stiffness towards seismic actions and allowing a good displacement control [Riva et al. 2003]. Squat walls are instead mostly widespread as main lateral force resisting structures in precast concrete blocks buildings and in power plant facilities. In fact, in nuclear facilities walls are supposed to be designed with few openings in order to prevent radiation leaks [Whyte and Stojadinovic, 2013]. Thus, these squat walls result often to be long and generally short height. It is common then that aspect ratio is equal to 0.5 or even lower.

Many experimental programs have been driven through the last 40 years to investigate the nonlinear behaviour of RC walls subjected to horizontal forces. From 1976 to 1984 Oesterle et al. [Oesterle et al. 1976] tested many slender walls subjected both to monotonic and cycling loading in order to evaluate their inelastic behaviour. In these tests flanged, barbell and rectangular sections were analysed. Many other experimental tests have been carried out to investigate the seismic behaviour of slender walls, also underlying some issues that still need to be addressed for a good performance assessment (e.g. overestimation of the initial stiffness, schematisation of boundary conditions, difficulty in the prediction of the crack pattern [Thomsen and Wallace 2004, Dazio et al. 2009, Zhang et al. 2014, Kono et al. 2014, Beyer et al. 2008[b]]). Also the behaviour of RC squat walls has been widely investigated [Lefas and Kotsovos 1990, Wood 1990, Hidalgo et al. 2002, Greifenhagen and Lestuzzi 2005, Grifenhagen 2006, Martinelli 2007, Gulec and Whittaker 2009]

The scientific research has therefore made significant advancements in understanding the nonlinear behaviour of RC walls subjected to horizontal forces and several numerical methods have been developed and tailored to analyse such kind of structural member. In particular, in this section, the focus is pointed on the assessment of RC squat walls by means of NLFEA and multi-layer shell elements. In order to investigate the prediction capacity and to reduce the uncertainties related to of NLFE tools, round robin competitions and blind prediction were recently organized and are in progress nowadays (e.g. Concrack2 benchmark [Concrack2, 2011], SMART-2013 [Richard et al., 2014], CASH benchmark [Le Corvec et al., 2015], etc.)

In the following the results obtained analysing the squat walls object of the CASH benchmark is presented. The main objective of this benchmark is to evaluate the seismic nonlinear response of squat walls, representative of a real nuclear power plant (NPP) building structure. According to the purpose of the benchmark, three different kind of analyses have been carried out: pushover, cyclic and dynamic analysis. For this reason, the present benchmark has been chosen for the assessment of NLFEA using PARC_CL 1.0 crack model not only for monotonic loading but also for cyclic and dynamic loading condition.

3.4.1 RC squat walls (CASH benchmark)

In this section the RC squat walls, object of the CASH benchmark project, have been analysed by means of NLFEA using multi-layer shell elements and PARC_CL 1.0 crack model.

CASH benchmark is an international benchmarking program organized under an initiative of the OEDC-NEA (Nuclear Energy Agency). The main objective of CASH is to evaluate the reliability of predictive analysis tools and methods as well as engineering practice know how to assess the seismic capacity of reinforced concrete squat walls. The CASH benchmark consists of two phases. The first phase, based on the "SAFE" experimental campaign [Pegon, 1998], invited to calibrate the adopted numerical model by means of different analyses (static pushover, static cyclic and dynamic). During the second phase, the participants would have to assess the capacity of a scale 1 squat wall extracted from a NPP building. In the following the comparison between experimental and NLFEA results, obtained on the phase 1 of CASH benchmark, is presented.

In particular, for the purpose of this chapter, the analyses are limited to the static pushover and static cyclic analysis. Indeed the aim of this section is to assess the capability of the PARC_CL 1.0 crack model to predict not only the monotonic behavior of a RC members but also the cyclic response. The same experimental campaign is used also for the assessment of PARC_CL 2.0 presented in the following chapter.

3.4.1.1 Analytical formulation

In this section the results obtained with NLFEA analyzing reinforced concrete squat walls are compared not only with the experimental outcomes but also with an analytical formulation. Generally, structures can be subdivided into B-regions, where the assumption of a plane section may be used (B is for Bernoulli) and D-regions which is typically located at supports or at places of concentrated loads (D is for Discontinuity). In particular squat walls, as the analyzed case study, behave strongly like a D-region and so the shear capacity can be evaluated analytically with a strut and tie method. In the following is proposed a formulation for the assessment of the shear capacity according to the prescription of [*fib*-Model Code 2010] and [Paulay and Priestley, 1992]. For the squat wall object of the analysis the concrete strut runs form the loading plate, placed at the top left corner of the specimen, to the bottom right corner, Figure 3.29.

According to the schematization reported in Figure 3.29, the evaluation of the analytical shear resistance, carried out using material mean values, can be derived from Eq.(3.43):

$$V_R = \sigma_{Rd,\max} \cdot A_{str} \cdot \cos\theta \tag{3.43}$$

where θ is the strut inclination angle, $\sigma_{Rd,max}$ is the maximum stress at the edge of the node calculated according to Eq.(3.44) and A_{str} represents the area of the concrete strut, calculated following Eq.(3.49).

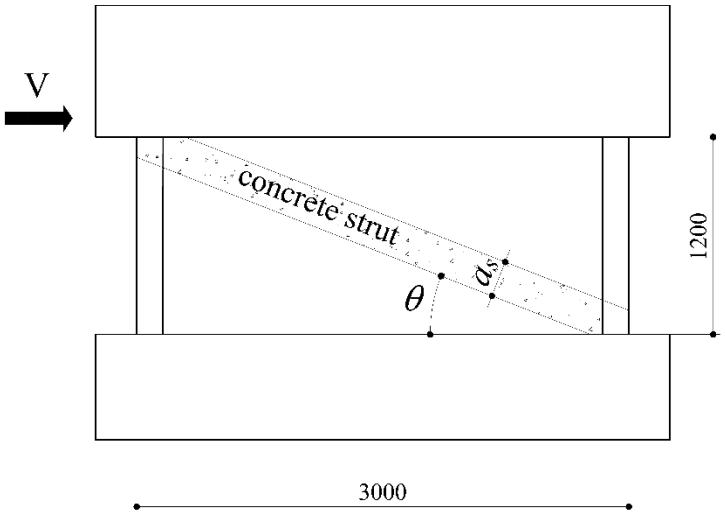

Figure 3.29 – Schematization of the analyzed squat wall according to the strut and tie model.

The maximum stress at the edge of node, $\sigma_{Rd,max}$, can be calculated as follow, according to the [*fib*-Model Code 2010] prescriptions:

$$\sigma_{Rd,\max} = k_c \cdot f_{cm} \tag{3.44}$$

where k_c is a reduction coefficient related to the state of stress which can assume different values for the various states of stress, Figure 3.30.

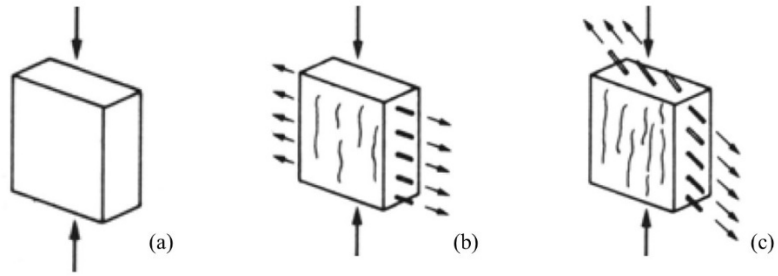

Figure 3.30 – Different states of stress: (a) uniaxial compression, (b) tension perpendicular to the direction of compression and (c) tension oblique with respect to the direction of compression [fib-Model Code 2010].

For undistributed uniaxial compression states, Figure 3.30-a, the reduction factor is given in Eq.(3.45):

$$k_c = 1.0 \cdot \eta_{fc} \tag{3.45}$$

For stress fields where cracks are parallel to the direction of compression and tension reinforcement perpendicular to this, Figure 3.30-b, the reduction factor can be calculated following Eq.(3.46):

$$k_c = 0.75 \cdot \eta_{fc} \tag{3.46}$$

Finally, for stress fields where the reinforcements are inclined, with angle smaller than 65°, with respect to the compressive direction, Figure 3.30-c, the reduction factor can be calculated according to Eq.(3.47):

$$k_c = 0.5 \cdot \eta_{fc} \tag{3.47}$$

The parameter η_{fc}, according to [*fib*-Model Code 2010] prescription is set equal to:

$$\eta_{fc} = \left(\frac{30}{f_{cm}} \right)^{1/3} \tag{3.48}$$

The area of the concrete strut, A_{str}, is calculated in Eq.(3.54):

$$A_{str} = t_w \cdot a_s \tag{3.49}$$

where t_w is the web thickness and a_s is the depth of the concrete compressive strut. According to [Hwang et al. 2001] the depth of the concrete compressive strut, a_s, can be approximated with the equation proposed by [Paulay and Priestley, 1992] for the depth of the flexural compression zone of an elastic column, Eq.(3.50):

$$a_s = \left(0.25 + 0.85 \cdot \frac{N}{A_c \cdot f_{cm}} \right) \cdot l_w \tag{3.50}$$

where A_c represents the net concrete area bounded by the web thickness t_w and N the axial vertical load acting on the wall.

In Table 3.13 are reported all the parameters herein presented for the analyzed case studies and the analytically calculated shear resistance. Further detail on the analyzed case studies are presented in the following section.

Table 3.13 – Mechanical parameters used in the strut and tie calculation for the analyzed case studies and analytical shear resistance.

Spec.	H [mm]	l_w [mm]	t_w [mm]	A_c [mm^2]	θ [deg]	f_c [MPa]	k_c [-]	$\sigma_{Rd,max}$ [MPa]	N [kN]	a_s [mm]	A_{str} [mm^2]	V_R [kN]
T6	1200	3000	200	600000	21.8	33.1	0.53	17.6	550	821	164124	2685
T7	1200	3000	200	600000	21.8	36.4	0.52	18.8	550	814	162843	2838
T8	1200	3000	200	600000	21.8	28.6	0.56	16.0	0	750	150000	2226

3.4.1.2 Experimental campaign

The phase 1 of the CASH benchmark [Le Corvec et al., 2015], presented in this section, is based on the SAFE experimental campaign carried out at the JRC Ispra Laboratory in Italy [Pegon, 1998]. The SAFE experimental campaign consists of a series of pseudo-dynamic (PSD) tests on 13 different squat walls, with different reinforcement ratio representative of the nuclear industry practice.

The conceptual design of the SAFE experimental programme is schemed in Figure 3.31. The wall is clamped at the base on a rigid body and equipped at the top with another rigid body, with mass M1, in such a

way that the rotation of the wall is fixed and so it constitutes a single degree of freedom (SDOF) dynamic system in shear. An additional mass M2, acting only n the horizontal direction, is calibrated in order to obtain a theoretical natural frequency equal to 4 Hz, 8 Hz or 12 Hz. This SDOF system is subjected to a seismic input motion. A unique input signal is used for the whole campaign, for every specimen the signal is first calibrated and then, in order to identify the seismic design margin, a series of run is carried out with increasing levels of input motion until the ultimate wall capacity is reached.

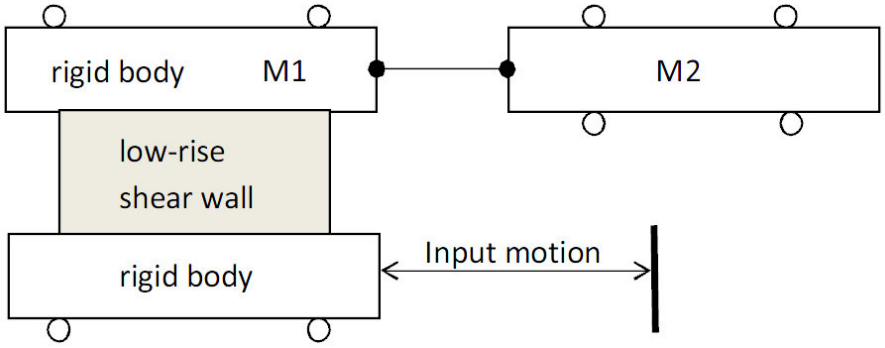

Figure 3.31 – SAFE conceptual design [Pegon, 1998].

The SAFE conceptual design just presented cannot be tested on a shaking table because either M_2 is too large (hundreds of tons) or it would result in a too small scale mock-up. For this reason at the JRC laboratory a pseudo-dynamic (PSD) test is carried out in such a way that the mass M_2 is considered as a virtual mass. Following this assumption the specimen is clamped on the strong floor and the input motion is replaced by a horizontal force applied at the top, according to the scheme reported in Figure 3.32.

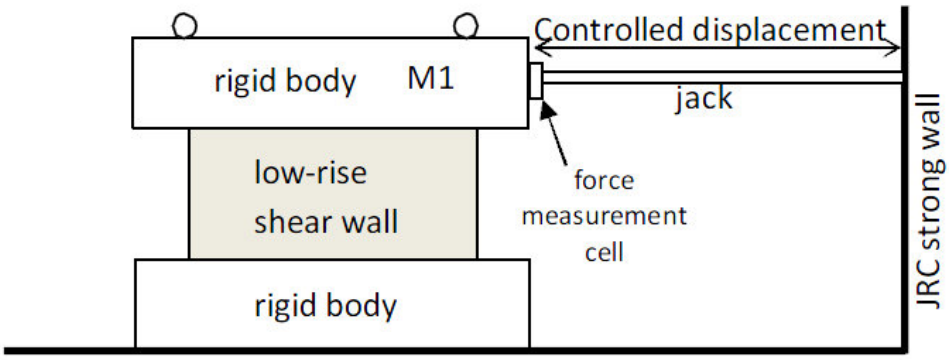

Figure 3.32 – SAFE experimental design [Pegon, 1998].

The SAFE campaign consisted of 13 specimens numbered T1 to T13. In particular, for the purpose of phase 1 of CASH benchmark, 3 out of the 13 specimens were selected: T6 wall [Pegon et al. 1998a], T7 wall [Pegon et al. 1998[b]] and T8 wall [Pegon et al. 1998[c]]. A detail of the experimental set-up is shown in Figure 3.33.

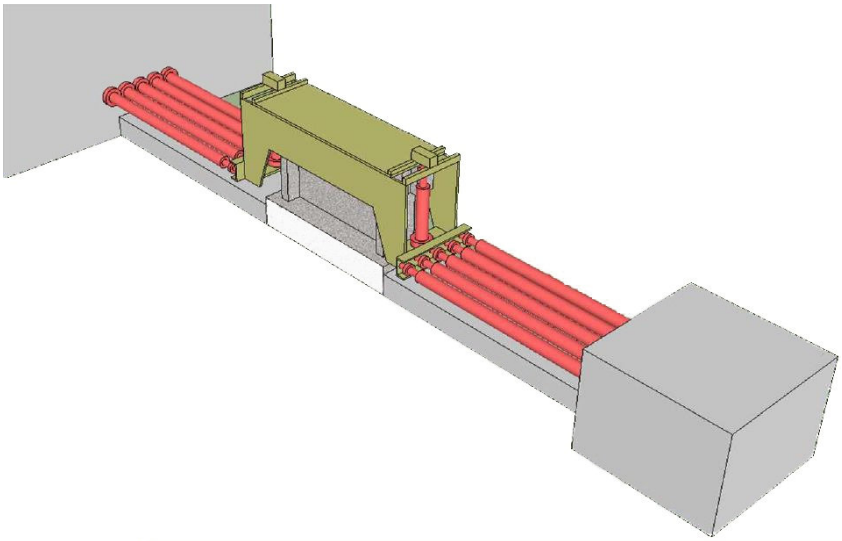

Figure 3.33 – SAFE experimental set-up [Le Corvec et al., 2015].

All the specimens have the same geometrical properties: a length l = 3000 mm an height h = 1200 mm and a thickness t = 200 mm. In order to reproduce the effect of perpendicular walls, at both the ends of each specimen two flanges were added. The top and the bottom part of the specimen are made of rigid concrete beams, as shown in Figure 3.34.

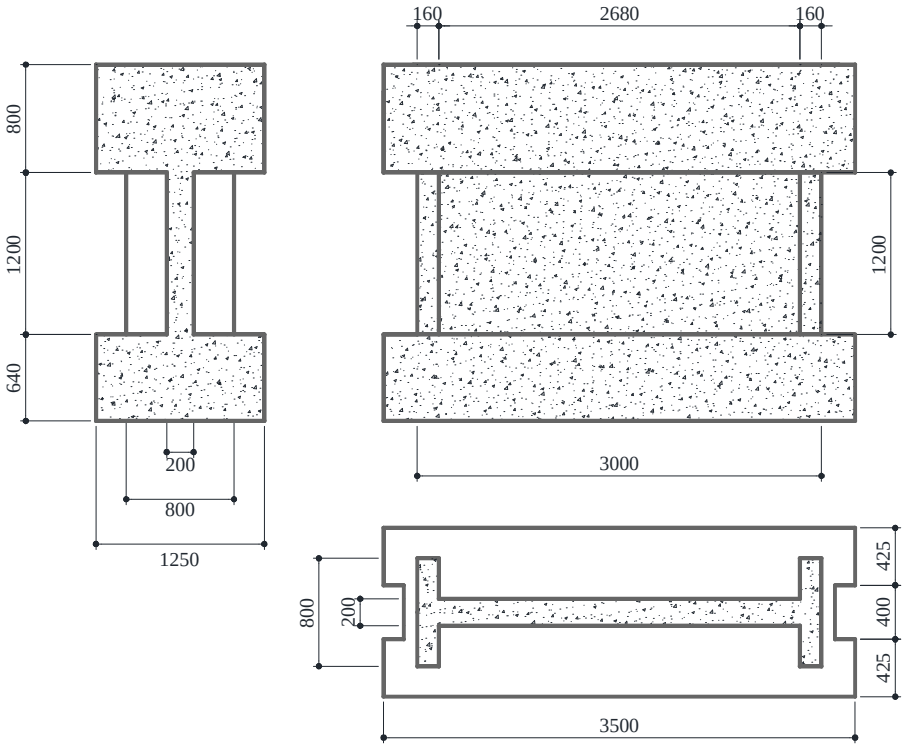

Figure 3.34 – Geometrical properties for T6,T7 and T8(measure in mm).

The differences in the specimens are in percentage of steel, ρ, in vertical compressive stress, σ_n, in the numerical mass applied in the PSD test, M_2, and in the first vibration frequency, f. The mechanical and geometrical properties of the specimens are listed in Table 3.14. In Table 3.14 the mass M_1 represents the physical mass of the top beam including the steel cover, the mass M_2 represents the numerical mass applied in

the PSD test, N the vertical load imposed at the top beam of each specimen and σ_n the vertical stress due to the combination of self-weight and imposed vertical load.

Table 3.14 – Mechanical and geometrical properties of the specimens.

	T6	T7	T8
Geometry			
b [mm]	3000	3000	3000
h [mm]	1200	1200	1200
t [mm]	200	200	200
Mass			
M_1 [ton]	25	25	25
M_2 [ton]	1252	11272	1252
Load			
N [kN]	550	550	0
σ_v [MPa]	1.01	1.01	0.32
Concrete			
f_c [MPa]	33.1	36.4	28.6
f_t [MPa]	3.1	3.3	2.8
$E_{c,MC2010}$ [MPa]	31900	32900	30400
$E_{c,effective}$ [MPa]	22330	23030	21280
Steel			
Horizontal rebar	ϕ 10@125	ϕ 10@125	ϕ 8@125
ρ_H [%]	0.628	0.628	0.402
f_y [MPa]	572.8	572.8	594.4
f_t [MPa]	651	651	672
E_s [MPa]	200000	200000	200000
Vertical rebar	ϕ 8@125	ϕ 8@125	ϕ 8@125
ρ_V [%]	0.402	0.402	0.402
f_y [MPa]	594.4	594.4	594.4
f_t [MPa]	672	672	672
E_s [MPa]	200000	200000	200000

The modulus of elasticity of concrete was not directly obtained by tests. It can be derived adopting the formulation proposed in [*fib*–Model Code 2010], according to Eq.(3.51):

$$E_{C,MC2010} = 21500 \cdot \left(\frac{f_{cm}}{10} \right)^{1/3} \tag{3.51}$$

Consequently, assuming a Poisson's ratio equal to 0.2 the conventional isotropic shear modulus for concrete, *G*, could be derived. The analytical shear stiffness of the wall, K_A, is evaluated with Eq.(3.52):

$$K_A = \frac{G \cdot (b \cdot t)}{h} \tag{3.52}$$

where *b*, *t* and *h* represent the base, the thickness and the height of the wall, respectively.

Finally, knowing the mass of each wall, *M*, (considered as the sum of physical mass, M_1, and numerical mass, M_2), the frequency of the wall could be analytically derived, using Eq.(3.53).

$$f_A = \frac{\omega}{2\pi} = \frac{\sqrt{K_A / M}}{2\pi} \tag{3.53}$$

where ω represents the natural frequency. The analytical calculation of the main features of the specimens are listed in Table 3.15.

Table 3.15 – Main features of the specimens: analytical calculation.

Spec.	*b* [m]	*t* [m]	*h* [m]	*E* [MPa]	*G* [MPa]	K_A [MN/m]	*M* [ton]	f_A [Hz]
T6	3	0.2	1.2	31900	13292	6646	1252	11.6
T7	3	0.2	1.2	32900	13708	6854	11272	3.9
T8	3	0.2	1.2	30400	12667	6333	1252	11.3

Prior to run the experimental PSD tests, the eigenfrequency of each specimen, f_{exp}, was experimentally measured by low level vibration and the corresponding elastic stiffness, K_{exp}, was derived. The obtained experimental results and the comparison with the analytical values are reported in Table 3.16.

Table 3.16 – Main features of the specimens: comparison between analytical calculation and experimental results.

Spec.	*M*	Analytical		Experimental		K_{EXP}/K_A
		K_A	f_A	K_{EXP}	f_{EXP}	
	[ton]	[MN/m]	[Hz]	[MN/m]	[Hz]	[-]
T6	1252	6649	11.6	5348	10.4	0.80
T7	11272	6861	3.9	5767	3.6	0.84
T8	1252	6336	11.3	4557	9.6	0.72
				Average		0.79

Interestingly, from Table 3.16 it appears that the conventional design stiffness significantly overestimates the measured one. The average value of the ratio between the experimental and the analytical stiffness is equal to 0.79, very close to the 0.7 median value obtained by [Sozen and Moehle, 1993]. According to the results of these preliminary studies in the NLFEA, the modulus of elasticity of concrete was reduced by

a factor 0.7 with respect to the one calculated according to Eq.(3.51). In Table 3.14 the adopted elastic modulus is also reported, $E_{c,effective}$.

The vertical stress at the base of the wall due to the masses of the specimen, of the upper beam and of the loading devices, resulted in σ_n=0.32 MPa for T8 specimen. For T6 and T7 specimens an additional vertical load was added, by means of two vertical actuator, in order to led the vertical stress to σ_n=1 MPa. In order to apply pure shear to the walls, the rotation of the upper beam was prevented adopting two vertical jack positioned at the end of the specimen.

The reference seismic input motion used in the SAFE programme is described by the response spectrum, $s_0(f,\xi)$ reported in Figure 3.35.

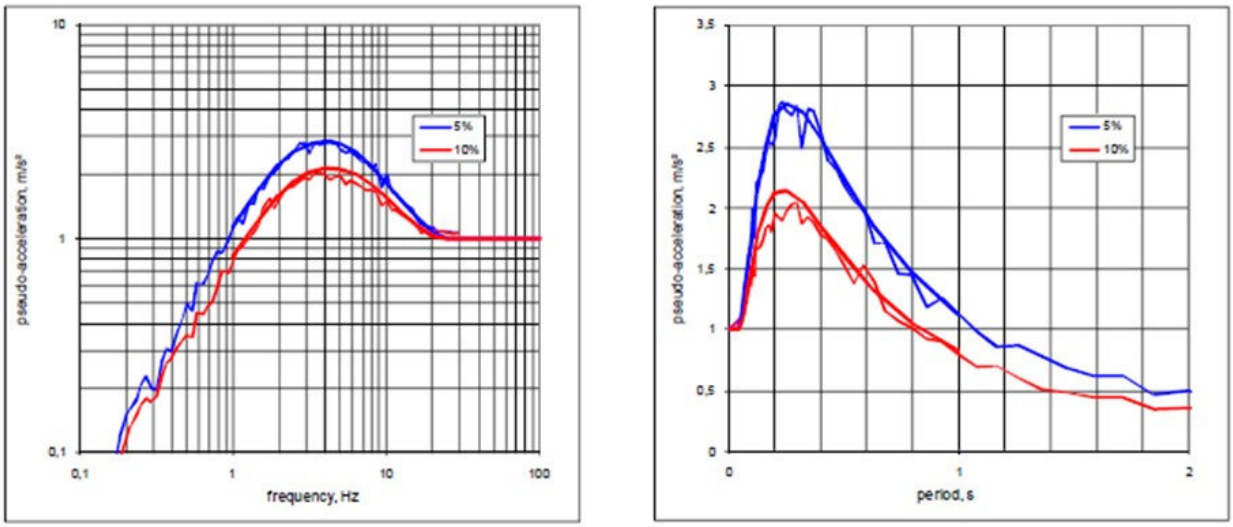

Figure 3.35 – Response spectra, $s_0(f,\xi)$, of the reference input motion.

The reference accelerogram $g_0(t)$, derived from the presented spectrum, is shown in Figure 3.36.

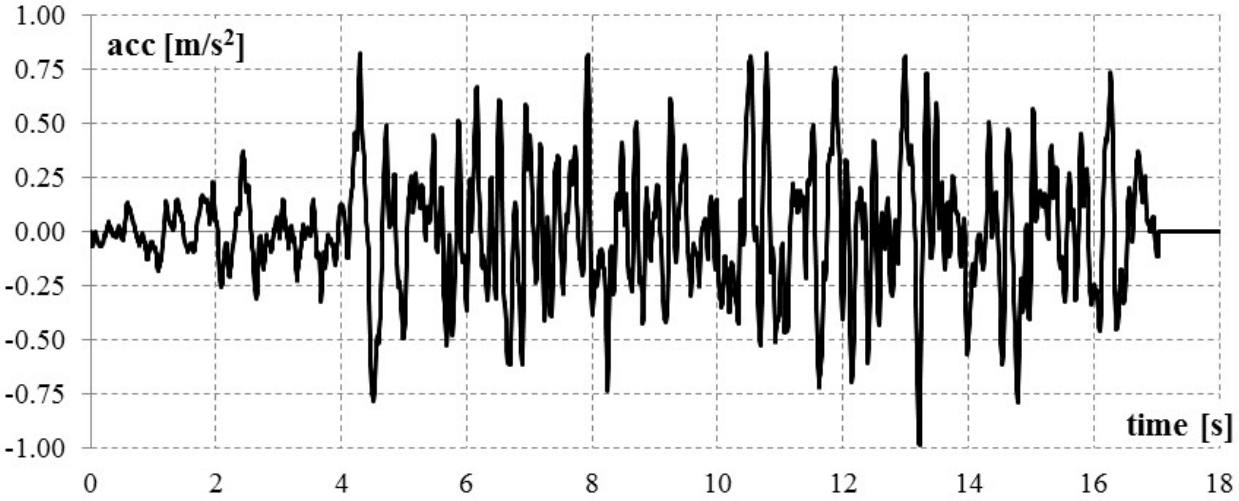

Figure 3.36 – Reference input motion, $g_0(t)$.

Under $s_0(f,\xi)$ the conventional top relative displacement of the *i*-th specimen is calculated with Eq.(3.54)

$$u_{0i} = \frac{s_0(f_i, \xi_i)}{(2\pi \cdot f_i)^2} \tag{3.54}$$

where f_i represents the frequency of the specimen and ξ_i represents the damping ratio, assumed equal to 7% according to the nuclear industry practice.

The corresponding shear stress can be calculated according to Eq.(3.55)

$$\tau_{0i} = \frac{G^{SAFE} \cdot u_{0i}}{H} \tag{3.55}$$

where G^{SAFE} represents the shear modulus, fixed equal to 14240 MPa for all the specimens in the design of the SAFE programme, and *H* the height of the specimen.

At the moment when SAFE programme was conceived, according to a conventional building code criterion [AFNOR, 1992], in a squat wall subjected to a vertical compressive stress σ_n the conventional acceptable design shear stress τ_i was strictly related to the reinforcement ratio by Eq.(3.56)

$$\tau_i = \rho_v \cdot f_y + \sigma_n \tag{3.56}$$

where ρ_v represents the vertical reinforcement ratio, f_y the yielding stress of steel and σ_n the applied vertical compressive stress.

Therefore, in order to get a shear stress that fits the above calculated conventional design, τ_i, the reference input motion should be multiplied by the scaling factor β_i calculated following Eq.(3.57):

$$\beta_i = \frac{\tau_i}{\tau_{0i}} \tag{3.57}$$

According to the presented procedure the design input motion for each specimen is defined as:

$$g_i(t) = \beta_i \cdot g_0(t) \tag{3.58}$$

where $g_0(t)$ represent the reference input motion presented in Figure 3.36.

Once $g_i(t)$ is determined, the test consists of a series of runs of increasing levels, with an input motion defined by:

$$G_{i,j}(t) = \alpha_{i,j} \cdot g_i(t) \tag{3.59}$$

where the index *i* represents the different specimen and the index *j* represents the run of the analysis. α_{ij} is the amplification factor of the run *j* for the specimen T_i. for every specimen the first run corresponds to α_{ij}=1. In Table 3.17 the main characteristic of the input motion applied to each specimen are resumed.

Table 3.17 – Main characteristics of the input motion applied to each specimen.

Spec.	G^{SAFE}	M	f^{SAFE}	ξ	$s_0(f,\xi)$	u_0	τ_0	ρv	fy	σ_v^{SAFE}	τ_i	β	ampificatio factors			
													α_1	α_2	α_3	α_4
	[MPa]	[ton]	[Hz]	[%]	[m/s^2]	[mm]	[MPa]	[%]	[MPa]	[MPa]	[m/s^2]	[-]	[-]	[-]	[-]	[-]
T6	14240	1252	12	7	1.49	0.26	3.1	0.40	500	1	3	0.964	1	1.3	1.5	1.8
T7	14240	11272	4	7	2.55	4.04	48.0	0.40	500	1	3	0.063	1	2	5	10
T8	14240	1252	12	7	1.49	0.26	3.1	0.40	500	0	2	0.642	1	1.4	1.8	-

3.4.1.3 Nonlinear finite element modelling and results

NLFEA have been carried out with ABAQUS code adopting the PARC_CL1.0 crack model. Due to the fact that, as just mentioned, in this section the analyses are limited to the pushover and static cyclic analysis only 2 out of the 4 specimens was analysed (T6 and T8). Indeed, the only difference between T6 and T7 specimens is the numerical mass applied to the dynamic analysis, as shown in Table 3.14.

All the specimens are modelled using 4 nodes multi-layer shell elements. The Gauss integration scheme is adopted with 4 Gauss integration points (S4); along the thickness each element is divided in 2 layers with 3 Simpson section integration points. Reinforcement is modelled using a smeared approach according to the PARC_CL 1.0 crack model prescriptions. The average element length is equal to 50 mm. In Figure 3.37 is reported a solid view of the mesh adopted for NLFEA.

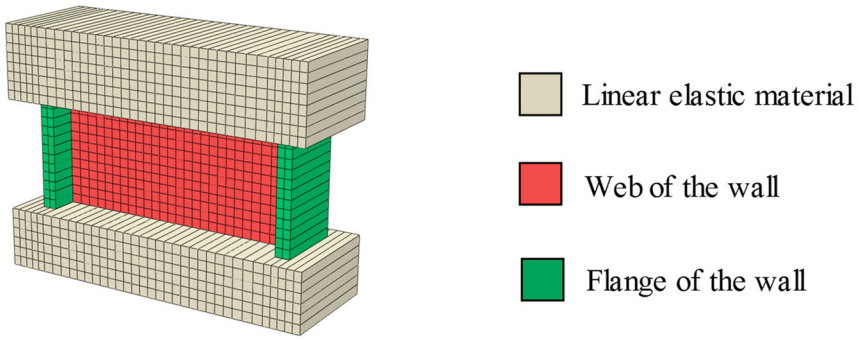

Figure 3.37 – Solid view of the adopted mesh.

The top and the bottom beams have been modelled using linear elastic material, while the web and the two flanges of the wall have been modelled using PARC_CL 1.0 crack model. Furthermore, due to the confining effect of stirrups, the flanges are modelled considering a confined concrete, calculated according to the formulation proposed by [Mander et al., 1988], which leads to an increasing of both the compressive strength and the ultimate compressive strain.

The analyses have been carried out using the mean values of the material properties as reported in Table 3.18. In Table 3.18 the a_m value is calculated on the basis of the bar spacing according to Eq.(3.60):

$$a_m = \frac{s_1 + s_2}{2\sqrt{2}} \tag{3.60}$$

where s_1 and s_2 represent the bar spacing in the two orthogonal directions of the upper reinforcement grid.

The fracture energy in tension (G_F) is evaluated according to the formulation proposed in [*fib*-Model Code 1990]. The fracture energy in compression (G_C) is set equal to 250 times the fracture energy in tension, according to Nakamura and Higai [Nakamura and Higai, 2001], for the unconfined concrete, while for the confined concrete the fracture energy in compression is derived in order to obtain the ultimate compressive strain in accordance to [Mander et al., 1988].

Table 3.18 – Mean mechanical properties used in NLFE model.

Spec.	Concrete (see §3.2.1)													Steel (see §3.2.3)		
						un-confined				confined						
	a_m	Ec	f_t	G_F	$\varepsilon_{t,u}$	f_c	G_C	$\varepsilon_{c,cr}$	$\varepsilon_{c,u}$	f_c	G_C	$\varepsilon_{c,cr}$	$\varepsilon_{c,u}$	E_s	$f_{y,vert}$	$f_{y,hor}$
	[mm]	[Gpa]	[MPa]	[N/mm^3]	[-]	[MPa]	[N/mm^3]	[-]	[-]	[MPa]	[N/mm^3]	[-]	[-]	[GPa]	[MPa]	[MPa]
T6	88	22.3	3.1	0.069	0.002	33.1	17.3	0.002	0.011	38.9	39.0	0.003	0.019	200	594	572
T8	88	21.3	2.8	0.063	0.002	28.6	15.7	0.002	0.011	33.2	21.0	0.002	0.013	200	594	594

The boundary and loading conditions applied for static pushover and cyclic analyses are presented in Figure 3.38.

The translation in the *x*-direction is fixed in correspondence of the anchor elements of the experimental specimens; the translation along the *z*-direction is fixed at the base of the bottom beam and the out-of-plane behaviour is prevented by fixing the translation along the *y*-direction of the whole model.

Load is applied in two different steps: in a first step the self-weight and the vertical pressure is applied; in a second step the horizontal displacement is imposed in correspondence of the section defined “Sec T”, Figure 3.38.

During the experimental tests, in order to apply pure shear condition to the wall, the rotation of the top beam was prevented by means of two vertical jacks. In NLFEA the same condition is obtained by applying a multi-point constraint in “Sec T”, Figure 3.38.

The pushover analyses have been carried out increasing the horizontal displacement till the failure.

The cyclic analyses have been carried out applying to “Sec T” the horizontal displacement measured during the experimental PSD tests.

The implicit method was adopted by the solver while the Newton-Rhapson method was used as convergence criterion. The force and displacement tolerance was fixed to $5 \cdot 10^{-3}$ for forces and 10^{-2} for displacements.

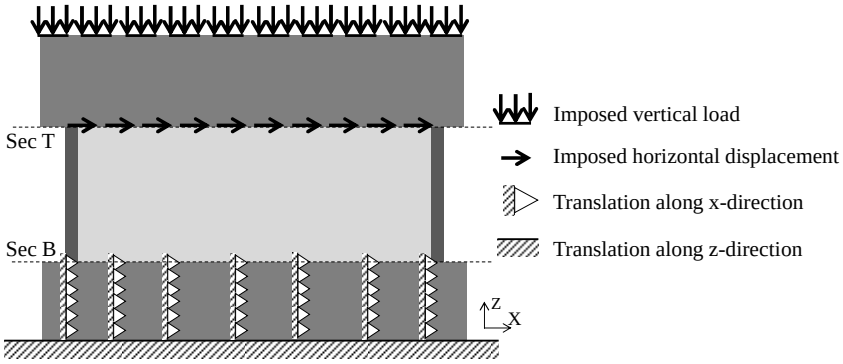

Figure 3.38 – Boundary and loading conditions for static pushover and cyclic analyses.

In Figure 3.39 is presented the comparison between the experimental results and the static pushover analysis, in terms of shear force vs top displacement, for T6 specimen. In Figure 3.39 the main events registered by NLFEA are marked using different colors, NLFEA results are stopped when the crushing of concrete is reached. Crushing of concrete is achieved when the compressive strain of concrete reaches the ultimate value, $\varepsilon_{c,u}$, highlighted in Table 3.18.

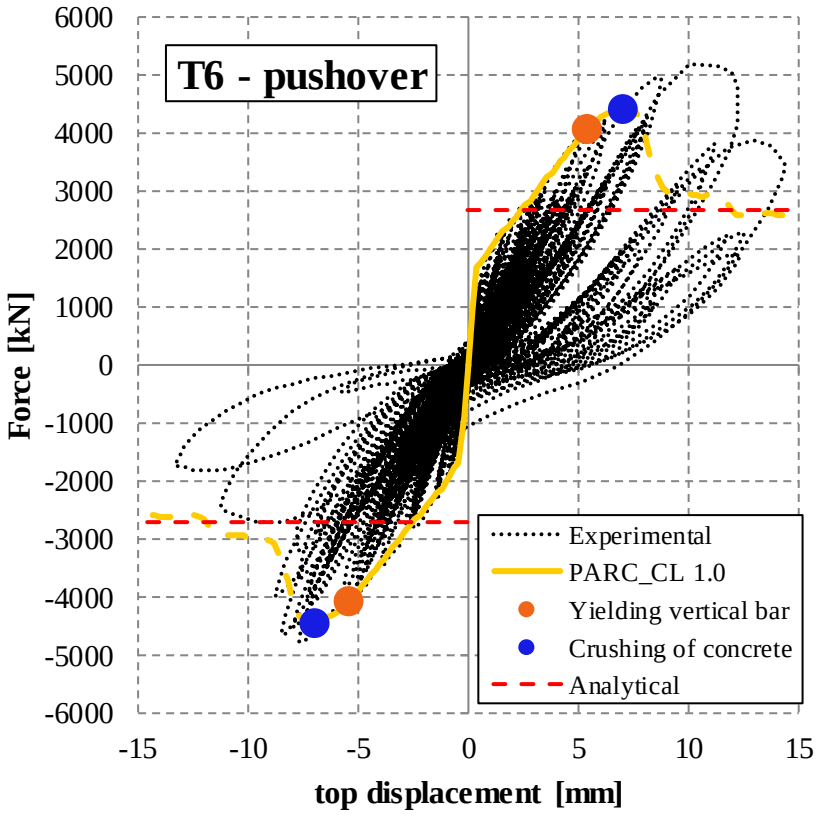

Figure 3.39 - Static pushover analysis: T6 wall, comparison between NLFEA using PARC_CL 1.0 and experimental results.

The main events, highlighted in Figure 3.39 are reported with their contours in Figure 3.40. As shown in Figure 3.39 and Figure 3.40 before the failure, characterized by crushing of compressive concrete, only the vertical reinforcement reached the yielding while the horizontal reinforcements remains in the elastic field.

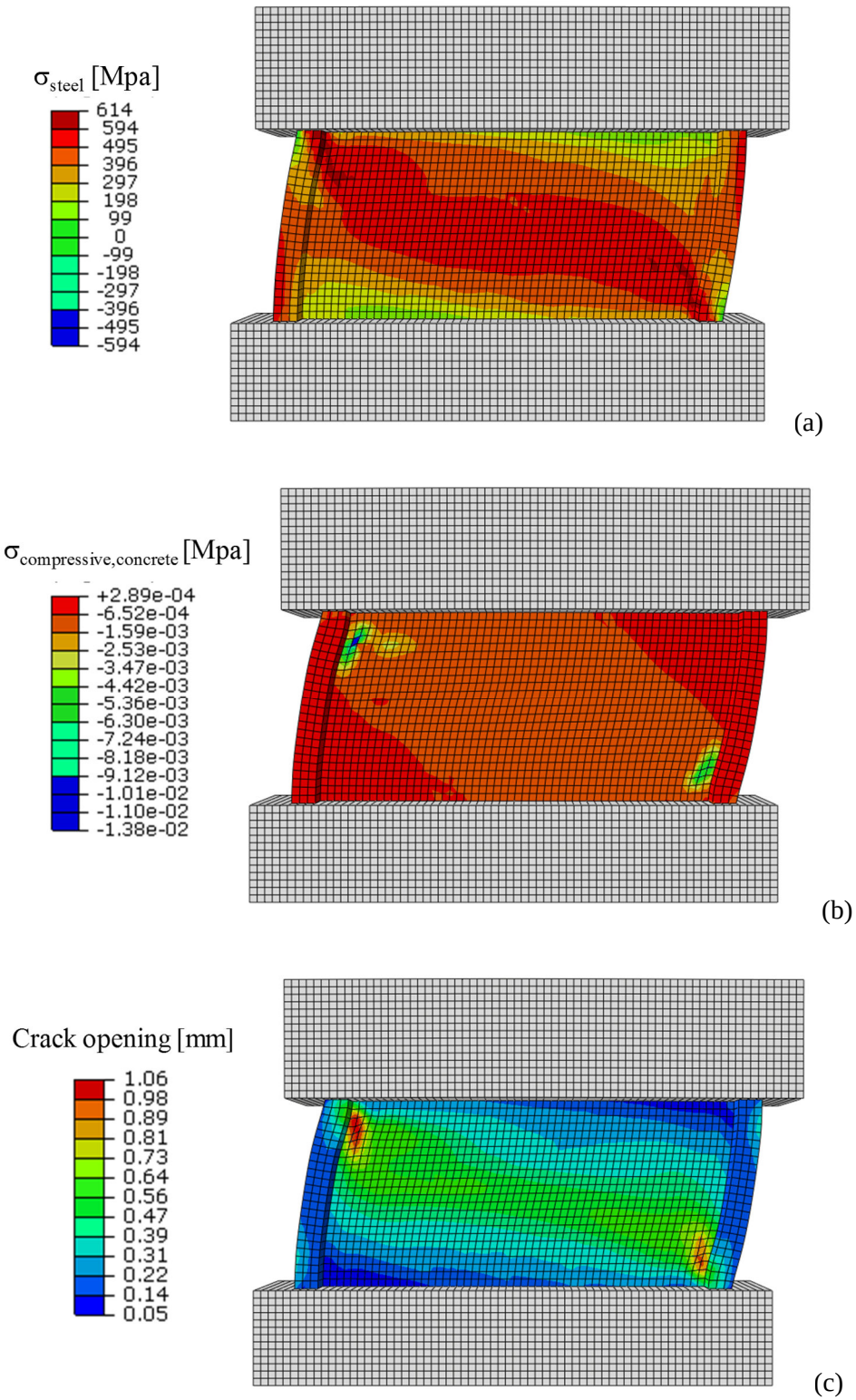

Figure 3.40 - Static pushover analysis: contours of main events registered for T6 specimen: (a) yielding of vertical bars, (b) crushing of compressive concrete and (c) crack pattern when the crushing of concrete is reached.

The results reported in Figure 3.39 shows that NLFEA using the PARC_CL 1.0 crack model are quite able to envelope the results of the Pseudo-Dynamic experimental test.

Similar results can be obtained analysing the T8 specimen, as reported in Figure 3.41 where the comparison between experimental and NLFEA results are presented in term of force-displacement curve. As for the previous specimen the main events occurred during the NLFEA are also highlighted in Figure 3.41.

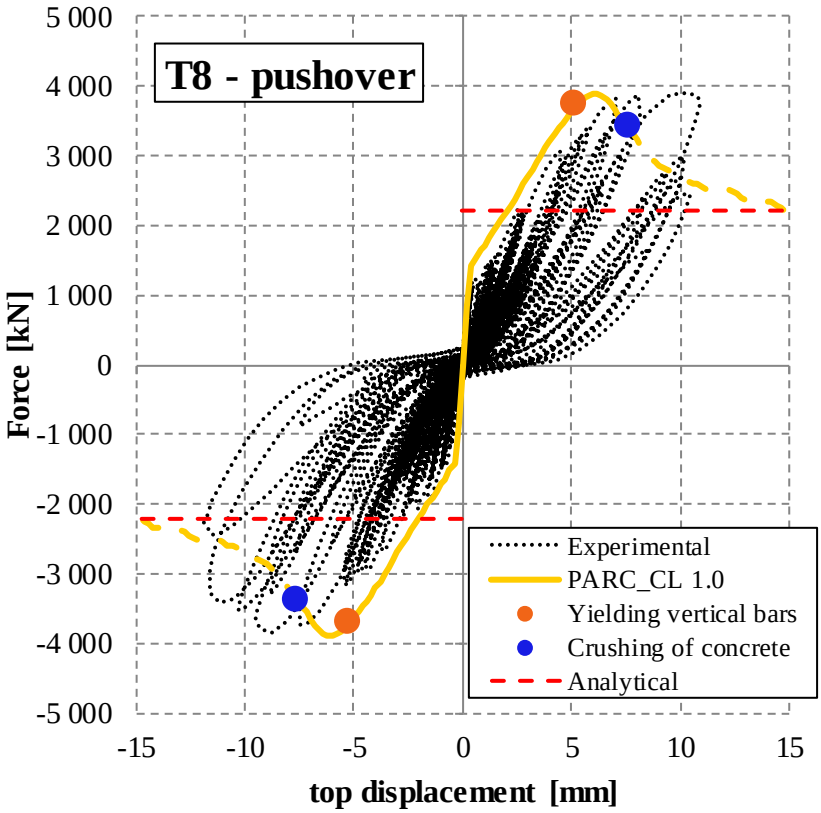

Figure 3.41 - Static pushover analysis: T8 wall, comparison between NLFEA using PARC_CL 1.0 and experimental results.

The main events, highlighted in Figure 3.41 are reported with their contours in Figure 3.42. according to the T6 specimen, also in this case before the failure only the vertical reinforcement yielded while the horizontal ones remained in the elastic field, as shown in Figure 3.42.

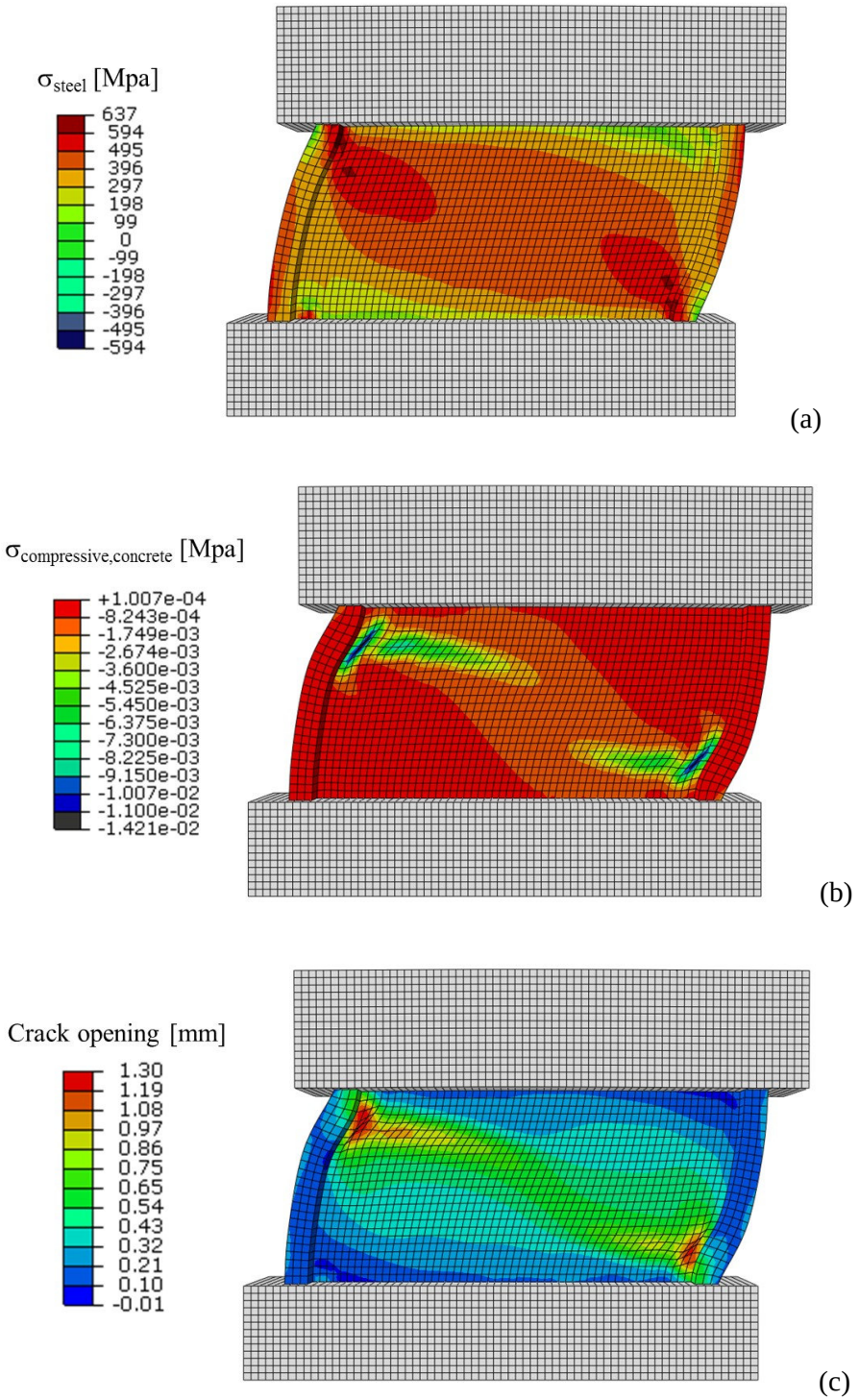

Figure 3.42 - Static pushover analysis: contours of main events registered for T8 specimen: (a) yielding of vertical bars, (b) crushing of compressive concrete and (c) crack pattern when the crushing of concrete is reached.

The assessment of the NLFEA carried out using PARC_CL 1.0 is then extended to static cyclic analysis obtained by imposing at the top of the specimen the horizontal displacement measured during the experimental PSD tests.

In Figure 3.43 is presented the comparison between cyclic NLFEA results and experimental PSD outcomes.

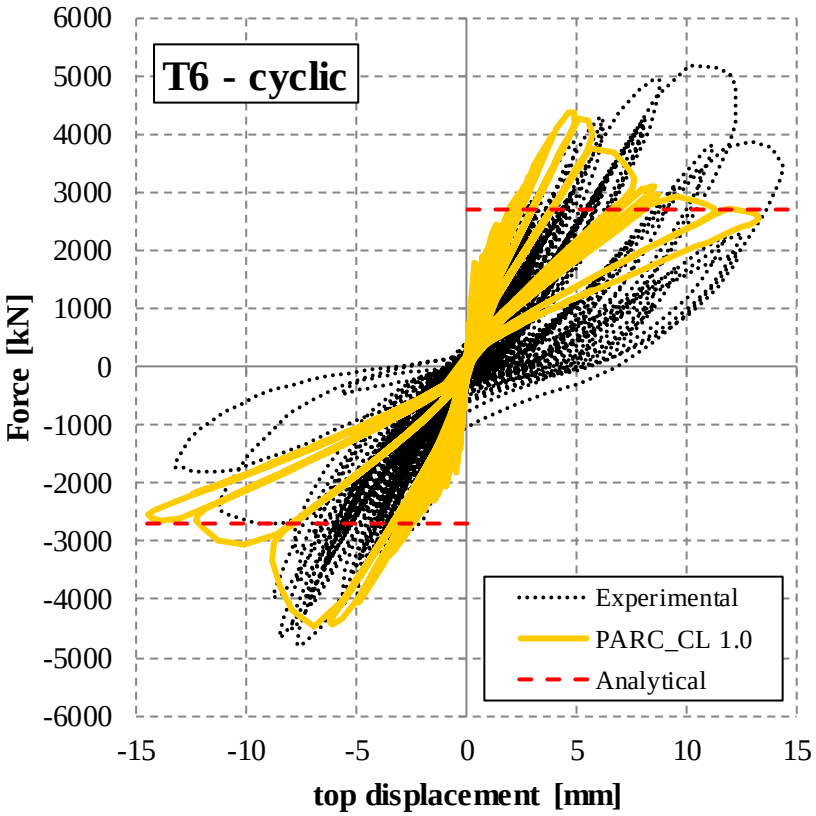

Figure 3.43 - Static cyclic analysis: T6 wall, comparison between NLFEA using PARC_CL 1.0 and experimental results.

The results plotted in Figure 3.43 show that while the NLFEA curve is quite able to reproduce the experimental behaviour in the loading phase, especially in the negative side of the imposed displacement. On the other hand, the unloading-reloading behaviour obtained with NLFEA is absolutely different compared with the experimental outcomes. This fact can be explained analysing the cyclic behaviour of both concrete and steel presented in §3.2; the secant path in the unloading-reloading phase cannot consider the plastic deformation and the hysteretic cycles and so the NLFEA are not able to reproduce the overall cyclic experimental behaviour of the specimen.

In order to highlight the stability of the analysis in Figure 3.44 is plotted the curve related to the number of iteration needed to obtain the convergence at each time increment. The red dotted line in Figure 3.44 represents the maximum number of iteration allowed for each time increment. The solution of a time increment is accepted after the maximum number of iteration allowed has been completed, even if the equilibrium tolerances are not satisfied. However, this condition should be avoided because it could lead to a loss of stability and reliability of the results.

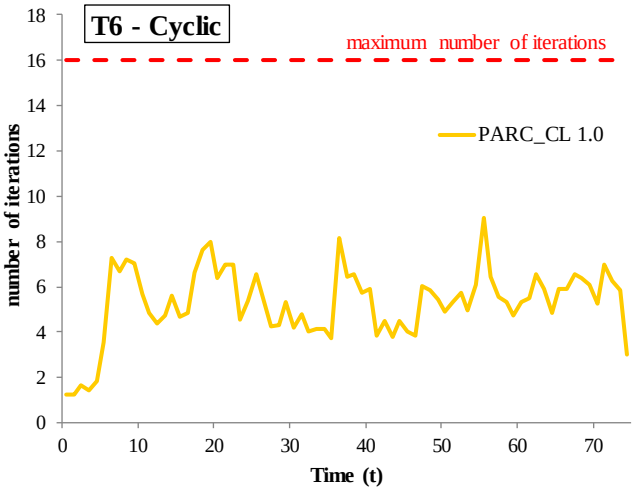

Figure 3.44 - Static cyclic analysis: T6 wall, number of iteration used to obtain the convergence of the Newton-Raphson implicit method.

The results plotted in Figure 3.44 show that the PARC_CL 1.0 crack model is quite able to reach the convergence at each time increment. This is due to the simplicity of the model in unloading-reloading phase; indeed, the unloading-reloading path, characterized by a straight line secant to the origin, can surely help the analysis to reach the convergence.

Similar conclusion can be deduced analysing the cyclic behaviour of T8 specimen, reported in Figure 3.45.

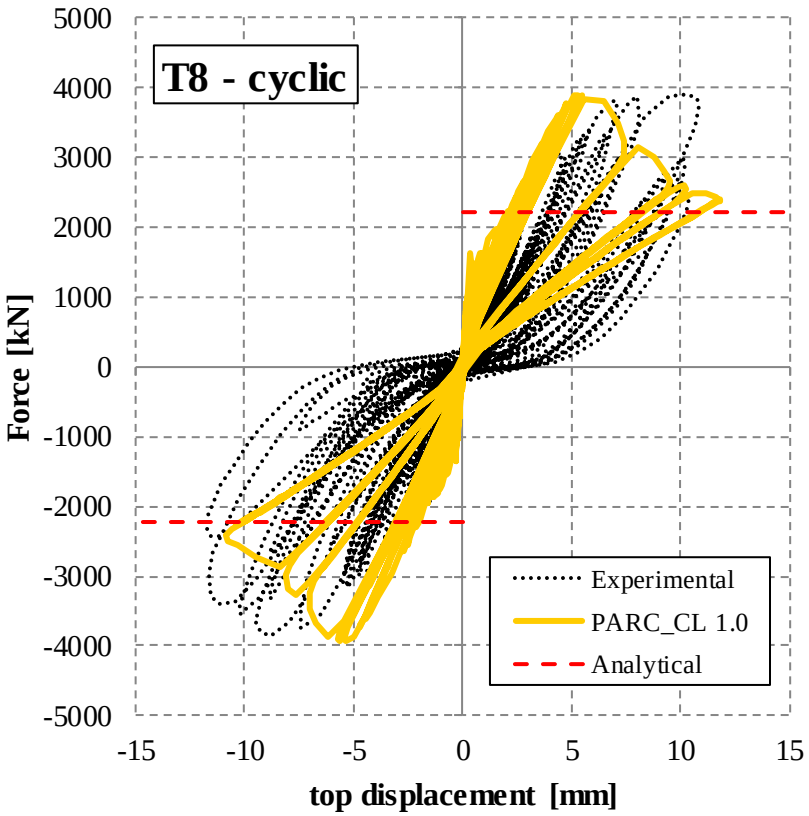

Figure 3.45 - Static cyclic analysis: T8 wall, comparison between NLFEA using PARC_CL 1.0 and experimental results.

Also for the T8 specimen in Figure 3.46 is reported the number of iteration needed to obtain the convergence at each time increment. The red dotted line in Figure 3.46 represents the maximum number of iteration allowed for each time increment.

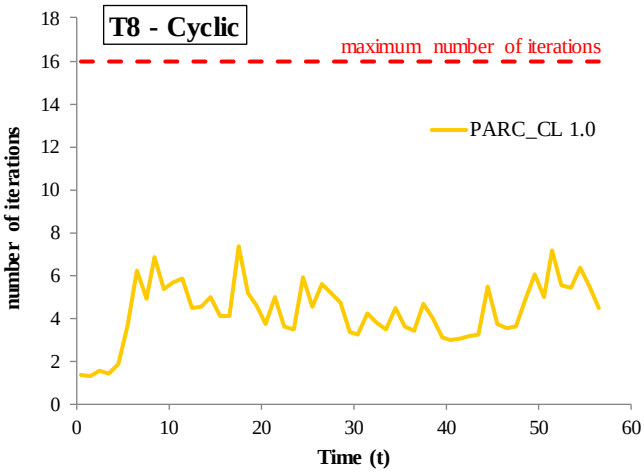

Figure 3.46 - Static cyclic analysis: T8 wall, number of iteration used to obtain the convergence of the Newton-Raphson implicit method.

The results plotted in Figure 3.46, similarly to the ones reported in Figure 3.44, show that the PARC_CL 1.0 crack model is quite able to reach the convergence at each time increment.

3.4.2 Synopsis

The results presented in this section highlighted the capability of PARC_CL 1.0 crack model to predict the experimental behaviour of RC squat wall in term of pushover analysis. Indeed, the results obtained with NLFEA are quite able to reproduce the envelope curve of the experimental PSD test, not only in term of load-displacement curve but also with respect to the failure mode. Moreover, the shear strength evaluated by means of NLFEA is closer to the experimental shear strength compared with the analytical formulation. On the other hand, in order to obtain a more realistic response of the structure subjected to cyclic loading the PARC_CL 1.0 need to be refined to consider the plastic and irreversible deformation in the unloading phase.

3.5 Discussion and conclusions

In this chapter the potentiality of NLFEA with multi-layer shell elements and PARCL_CL 1.0 was investigated. Different kind of reinforced concrete members were analysed, eg. RC slabs and RC squat walls. The obtained results are in accordance with the philosophy of [*fib*-Model Code 2010] and so the increasing of complexity associated to NLFEA with respect to simplified analytical formulation is strictly related to an increasing in the precision of the structural response evaluation. These results demonstrated that it makes sense to invest in a more advanced and time-consuming calculation if this can show that an existing structure is reliable enough and does not need strengthening.

Moreover, while the monotonic behaviour of RC members can be well reproduced using the presented PARC_CL 1.0 crack model, the last proposed application on RC squat walls highlighted that the presented crack model was not able to reproduce the cyclic response of a structure, due to the fact that the PARC_CL 1.0 crack model does not take into account the component of irreversible plastic deformation neither in concrete and steel. The search for a more accurate and realistic modelling for structures subjected to seismic actions, leading to the need of more complex models.

For this reasons the research is continued in this direction, as shown in the following chapter. In chapter 4 the implemented PARC_CL 2.0 crack model is presented. The PARC_CL 2.0 crack model is the main topic of this Ph.D. thesis and allows to consider plastic deformation both in concrete and steel. This model is applied to simulate the cyclic behaviour of the same squat walls analysed herein with the aim to assess the improvements with respect to the PARC_CL 1.0. Moreover some different case studies were analysed in chapter 4 using PARC_CL 2.0 crack model.

PART III

THE PARC_CL 2.0

4 Implementation of PARC_CL 2.0 crack model and its applications

"The use of this subroutine generally requires considerable expertise. You are cautioned that the implementation of any realistic constitutive model requires extensive development and testing. Initial testing on a single-element model with prescribed traction loading is strongly recommended."

ABAQUS user's manual

4.1 Introduction

The results presented in the previous chapter highlighted the importance of refining the PARC_CL 1.0 crack model in order to obtain a more realistic response from a RC member subjected to cyclic loading. Indeed, the monotonic behaviour can be well predict using the PARC_CL 1.0 crack model, but, on the other hand, the cyclic behaviour, defined by an unloading-reloading path secant to the origin, needs to be improved. For this reason, a new version of the model, the PARC_CL 2.0 crack model, was developed.

The PARC_CL 2.0 crack model is implemented as a user subroutine UMAT.for in Fortran language within ABAQUS code [Abaqus 6.12, 2012] and it is widely described in §4.2. The PARC_CL 2.0 crack model allows considering plastic and irreversible deformation in the unloading phase and therefore to take into account the hysteretic cycles of both concrete and steel reinforcement. Moreover, in order to proper analyse the dynamic behaviour, the Rayleigh damping stiffness-proportional coefficient was developed and introduced in §4.2.2.

In order to highlight the improvement produced by the PARC_CL 2.0 crack model in the prediction of the cyclic in-plane behaviour of a RC member, the same squat walls analysed with the PARC_CL 1.0 crack model in §3.4.1 are analysed in this section using the PARC_CL 2.0 crack model, as presented in §4.3.

Finally in §4.4, the PARC_CL 2.0 crack model was adopted to analyse the out-of-plane instability of RC slender walls subjected to cyclic horizontal loading. Three different specimens were analyzed: in §4.4.1

two “T shaped” walls were studied, subjected to: in-plane horizontal cyclic loading (TW1 specimen) and a combination of in-plane and out-of-plane horizontal cyclic load (TW4 specimen); in §4.4.2 a “U shaped” wall subjected to cyclic load was analysed.

4.2 Description of PARC_CL 2.0 crack model

Likewise the PARC_CL 1.0 crack model, the PARC_CL 2.0 crack model is based on a fixed total strain crack approach. The basic hypotheses still stand, therefore at each integration point two reference systems are defined: the local *x,y* coordinate system and the *1,2* coordinate system along the orthotropic axes. The angle between the *1*-direction and the *x*-direction is denoted as ψ, whereas $\alpha_i = \theta_i - \psi$ is the angle between the direction of the *i*th order of the bar and the *1*-direction, Figure 4.1-a. When the value of the principal tensile strain in concrete exceeds the concrete tensile limit strain $\varepsilon_{t,cr}$, for the first time, the first crack is formed, and for following loading stages, the *1,2*-coordinate system is fixed, Figure 4.1.

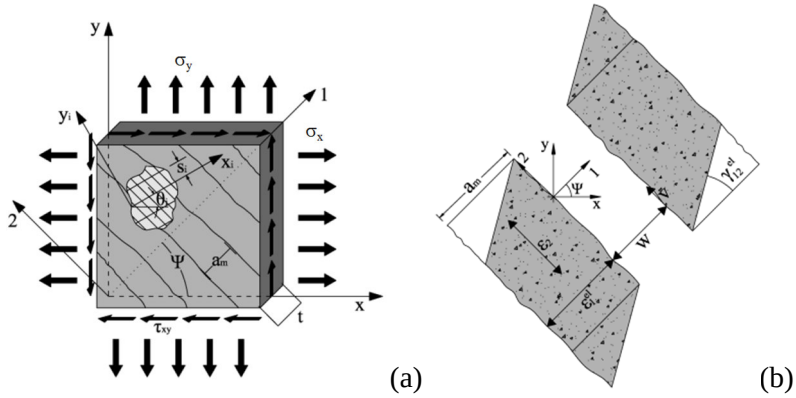

Figure 4.1 – (a) RC element subjected to plane stress state and (b) crack parameters.

One of the main difference between the PARC_CL 2.0 and the previous PARC_CL 1.0 are related to cyclic behaviour of both concrete and steel. The concrete cyclic behaviour, presented in §4.2.1.1, allows to consider plastic deformation in the compressive unloading branch; moreover, also the aggregate interlock phenomenon is modelled with a cyclic behaviour, as shown in §4.2.1.3. the hysteretic behaviour of steel subjected to cyclic loading are implemented in the PARC_CL 2.0 crack model, as reported in §4.2.1.2, according to the formulation proposed by [Menegotto and Pinto, 1973].

Another important difference between PARC_CL 2.0 and PARC_CL 1.0 is related to the dynamic behaviour. Indeed, in the PARC_CL 2.0 the stiffness proportional damping is introduced in the model following the procedure illustrated in §4.2.2.2.

In the following section the static cyclic and dynamic behaviour of PARC_CL 2.0 crack model is presented; moreover, the model is validated by means of comparison with simple case studies found in literature and analytical formulation.

In Figure 4.2 the flow-chart of the implements PARC_CL 2.0 crack model is presented.

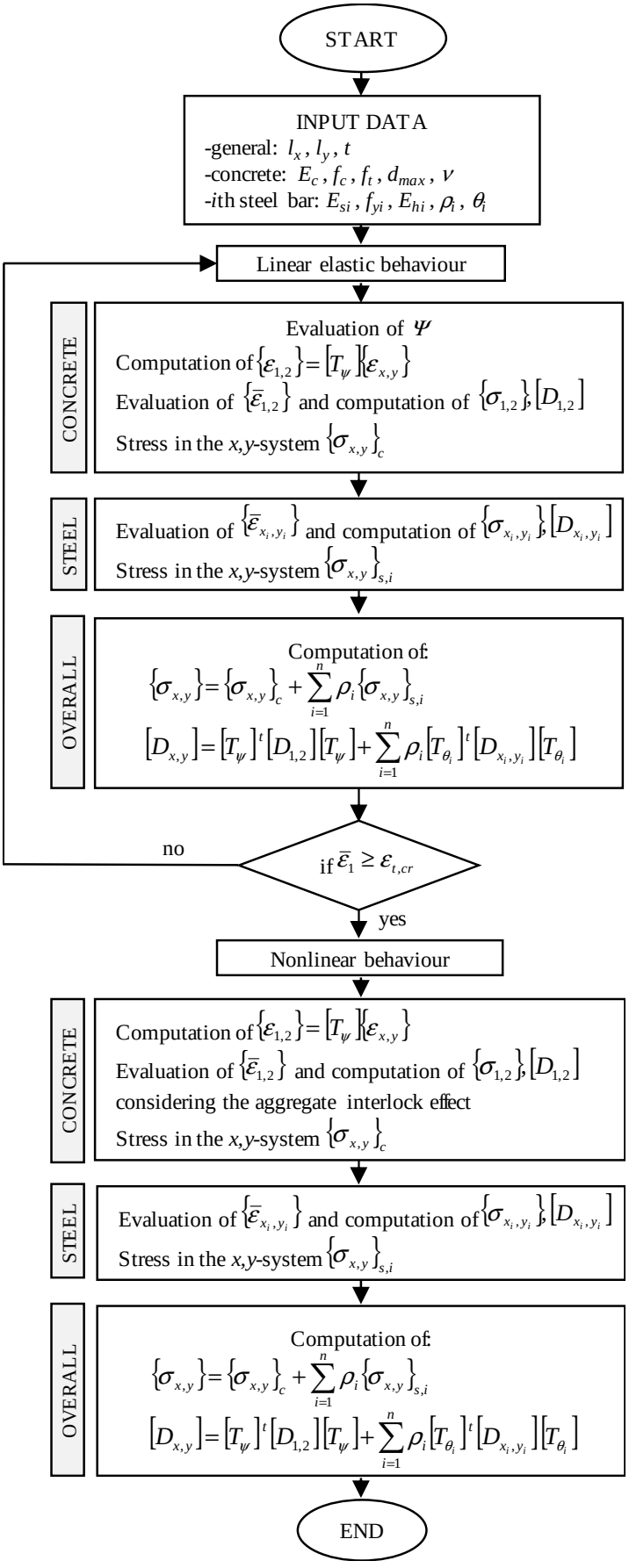

Figure 4.2 – Flow-chart of PARC_CL 2.0 crack model.

4.2.1 Cyclic behaviour

4.2.1.1 Concrete model

4.2.1.1.1 Biaxial versus uniaxial strains

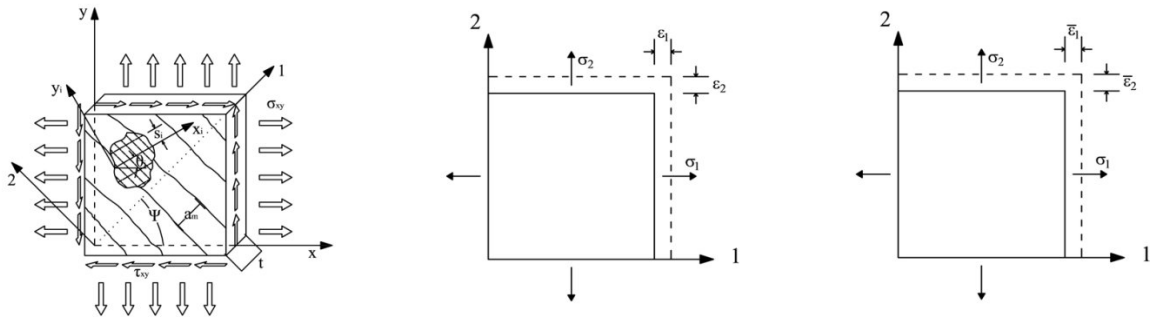

(a) RC membrane element subjected to plane stress state

(b) Biaxial strain condition

(c) Uniaxial strain condition

Figure 4.3 – (a) Reinforced concrete member subjected to plane stress state; (b) biaxial strain condition and (c) uniaxial strain condition.

The concrete behaviour is assumed orthotropic both before and after cracking and the total strains at each integration point are calculated in the orthotropic *1,2*-system, Figure 4.3-a:

$$\{\varepsilon_{1,2}\} = [T_\psi] \cdot \{\varepsilon_{x,y}\} \tag{4.1}$$

where $[T_\psi]$ is the transformation matrix, shown in Eq.(4.2):

$$[T_\psi] = \begin{bmatrix} \cos^2\psi & \sin^2\psi & \cos\psi \cdot \sin\psi \\ \sin^2\psi & \cos^2\psi & -\cos\psi \cdot \sin\psi \\ -2\cdot\cos\psi\cdot\sin\psi & 2\cdot\cos\psi\cdot\sin\psi & \cos^2\psi - \sin^2\psi \end{bmatrix} \tag{4.2}$$

$\{\varepsilon_{1,2}\}$ and $\{\varepsilon_{x,y}\}$ represents respectively the biaxial strain vector in *1,2*-system and *x,y*-system, as shown in Eq.(4.3) and Eq.(4.4), Figure 4.3-b.

$$\{\varepsilon_{1,2}\} = \{\varepsilon_1 \quad \varepsilon_2 \quad \gamma_{12}\}^t \tag{4.3}$$

$$\{\varepsilon_{x,y}\} = \{\varepsilon_x \quad \varepsilon_y \quad \gamma_{xy}\}^t \tag{4.4}$$

The stress-strain behavior presented herein is calculated on the base of the uniaxial strains in the *1,2*-coordinate system, calculated according to Eq.(4.5), Eq.(4.6) and Eq.(4.7), and shown in Figure 4.3-c.

$$\bar{\varepsilon}_1 = \frac{1}{1-\nu^2}\varepsilon_1 + \frac{\nu}{1-\nu^2}\varepsilon_2 \tag{4.5}$$

$$\bar{\varepsilon}_2 = \frac{\nu}{1-\nu^2}\varepsilon_1 + \frac{1}{1-\nu^2}\varepsilon_2 \tag{4.6}$$

$$\bar{\gamma}_{12} = \gamma_{12} \tag{4.7}$$

After the first crack, the Poisson's ratio is assumed to be zero, therefore in Eq.(4.5), Eq.(4.6) and Eq.(4.7), the biaxial strains are the same as the uniaxial strains. This condition is illustrated in Figure 4.3-b and Figure 4.3-c, where the stresses σ_1 and σ_2 are related to the uniaxial strains and represent both the biaxial stresses and the uniaxial stresses.

4.2.1.1.2 Envelope curve

The envelope curve for concrete, shown in Figure 4.4, is defined by Eq.(4.8) for tensile behaviour and Eq.(4.9) for compressive behaviour:

Tensile behavior:

$$\sigma = \begin{cases} E_c \cdot \varepsilon & 0 \le \varepsilon < \varepsilon_{t,el} \\ 0.9 \cdot f_t + 0.1 \cdot f_t \left(\dfrac{\varepsilon - \varepsilon_{t,el}}{\varepsilon_{t,cr} - \varepsilon_{t,el}} \right) & \varepsilon_{t,el} \le \varepsilon < \varepsilon_{t,cr} \\ f_t \left\{ \left[1 + \left(c_1 \cdot \dfrac{\varepsilon - \varepsilon_{t,cr}}{\varepsilon_{t,u}} \right)^3 \right] \cdot \exp\left(-c_2 \cdot \dfrac{\varepsilon - \varepsilon_{t,cr}}{\varepsilon_{t,u}} \right) - \dfrac{\varepsilon - \varepsilon_{t,cr}}{\varepsilon_{t,u}} \cdot \left(1 + c_1^{\,3} \right) \cdot \exp\left(-c_2 \right) \right\} & \varepsilon_{t,cr} \le \varepsilon < \varepsilon_{t,u} \\ 0 & \varepsilon \ge \varepsilon_{t,u} \end{cases} \tag{4.8}$$

Compressive behavior:

$$\sigma = \begin{cases} E_c \cdot \varepsilon & \varepsilon_{c,el} < \varepsilon \le 0 \\ \dfrac{f_c}{3} \cdot \left[1 + 4 \cdot \left(\dfrac{\varepsilon - \varepsilon_{c,el}}{\varepsilon_{c,cr} - \varepsilon_{c,el}} \right) - 2 \cdot \left(\dfrac{\varepsilon - \varepsilon_{c,el}}{\varepsilon_{c,cr} - \varepsilon_{c,el}} \right)^2 \right] & \varepsilon_{c,crl} < \varepsilon < \varepsilon_{c,el} \\ f_c \cdot \left[1 - \left(\dfrac{\varepsilon - \varepsilon_{c,cr}}{\varepsilon_{c,u} - \varepsilon_{c,cr}} \right)^2 \right] & \varepsilon_{c,u} < \varepsilon < \varepsilon_{c,cr} \\ 0 & \varepsilon \le \varepsilon_{c,u} \end{cases} \tag{4.9}$$

where:

$$\varepsilon_{t,el} = 0.9 \cdot f_t / Ec \qquad \varepsilon_{c,el} = f_c / (3 \cdot Ec) \qquad \varepsilon_{t,u} = 5.136 \, G_F / (h \cdot f_t) \qquad \varepsilon_{c,u} = \varepsilon_{c,cr} + 1.5 \cdot G_C / (h \cdot f_c)$$

$$\varepsilon_{t,cr} = 0.00015 \qquad \varepsilon_{c,cr} = 5 \cdot \varepsilon_{c,el} \qquad c_1 = 3 \qquad c_2 = 6.93$$

The value of h in the PARC_CL 2.0 crack model is fixed equal to the square root of the average element area, according to [Hendriks et al., 2012].

The value of G_F represents the fracture energy of concrete in tension and can be evaluated according to [*fib*-Model Code 1990]. The value of G_F is defined as the energy required to propagate a tensile crack in a unit area of concrete. The transition between the dissipated energy by a single macro-crack in concrete, G_F, and the energy dissipated by several macro-crack in reinforced concrete, G^{RC}_F, is defined in accord with Eq.(4.10):

$$G_F^{RC} = G_F\left(1+\frac{h}{a_m}\right) \tag{4.10}$$

where a_m is set as the average crack spacing and can be calculated on the base of the length over which the sleep between concrete and steel occurs, $l_{s,max}$, as define in [*fib*-Model Code 2010].

G_C represents the fracture energy of concrete in compression. The ratio between the fracture energy of concrete in compression and in tension is assumed equal to 250 according to [Nakamura and Higai, 2001].

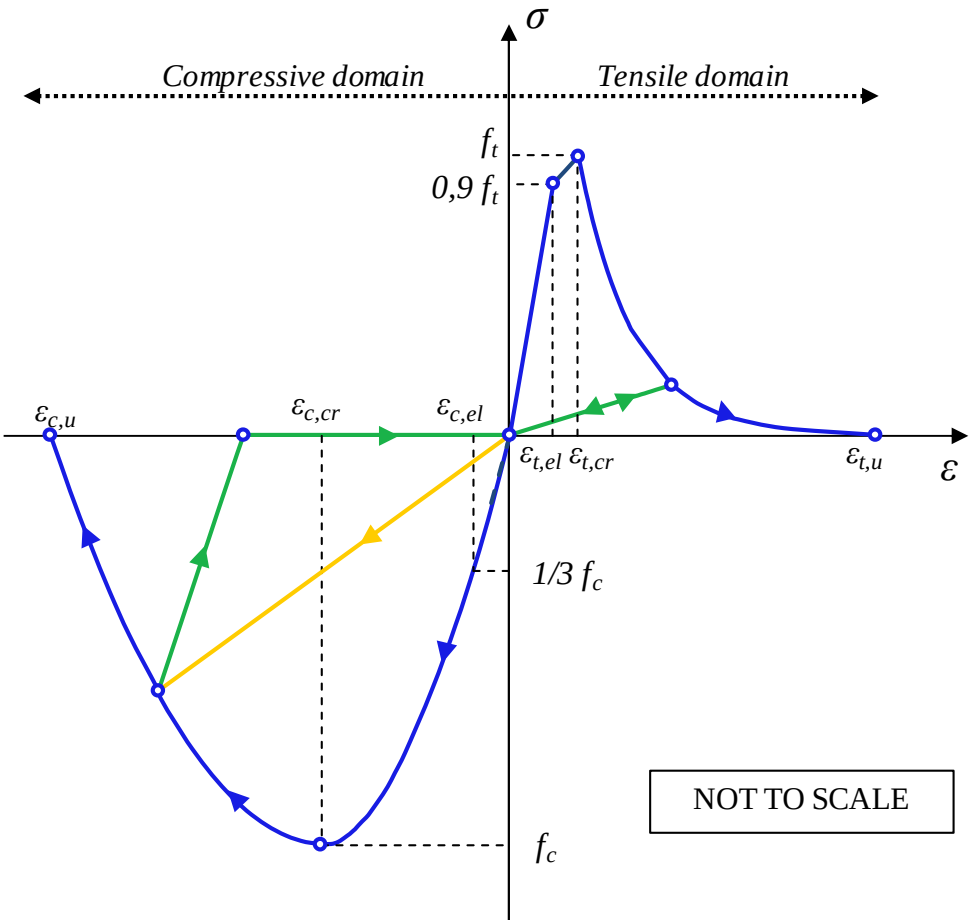

Figure 4.4 – PARC_CL 2.0, cyclic behaviour of concrete.

Multi-axial state of stress is considered by reducing the compressive strength and the corresponding peak strain due to lateral cracking, as given in Eq. (4.11) and shown in Figure 4.5, according to [Vecchio and Collins, 1993].

$$\zeta = 1\Big/\left(0.85 - 0.27\,\varepsilon_1/\varepsilon_2\right) \tag{4.11}$$

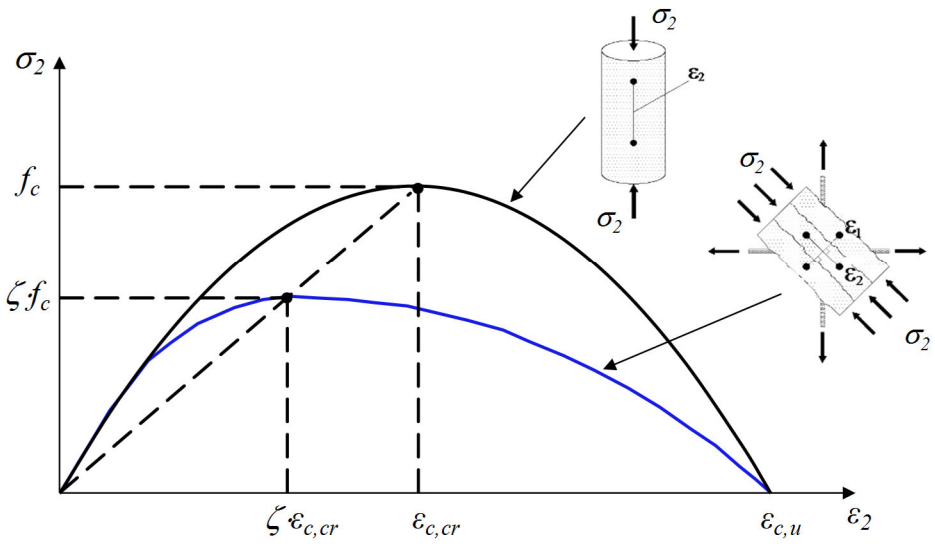

Figure 4.5 – Compression softening model according to [Vecchio and Collins, 1993].

4.2.1.1.3 Cyclic behaviour

As stated in the introduction of the present chapter the PARC_CL 2.0 crack model allows to consider plastic and irreversible deformation in the unloading phase.

The tensile unloading-reloading scheme is defined with a secant behaviour, similarly to PARC_CL 1.0 crack model, since the plastic deformations in the tensile domain are considered negligible.

The compressive unloading-reloading scheme allows the accounting of plastic deformations following the procedure presented in Figure 4.6 and based on the definition of two further variables: $\varepsilon_{c,re}$ and $\sigma_{c,re}$; $\varepsilon_{c,pl}$ is the plastic compressive strain and is updated on the envelope curve with Eq.(4.12)

$$\varepsilon_{c,pl} = \varepsilon_{c,re} - \sigma_{c,re} \cdot E_c \tag{4.12}$$

The unloading phase is determined considering two different paths: the CC→CD path and the CD→CE path, defined according to the notation presented in Figure 4.6.

The CC→CD path is achieved following Eq.(4.13) while in the CD→CE path the stress is fixed at zero as in Eq.(4.14):

$$\sigma = \begin{cases} \dfrac{\sigma_{c,re}}{\left(\varepsilon_{c,re} - \varepsilon_{c,pl}\right)} \cdot \left(\varepsilon - \varepsilon_{c,pl}\right) & \text{if } \varepsilon_{c,re} \le \varepsilon < \varepsilon_{c,pl} \quad (4.13) \\ 0 & \text{if } \varepsilon_{c,pl} < \varepsilon \le 0 \quad (4.14) \end{cases}$$

During all the unloading-reloading cycles the values of $\varepsilon_{c,re}$ and $\sigma_{c,re}$ remain fixed: they change only after the stress-strain relationship experiences again the envelope curve. On the other hand, $\varepsilon_{c,pl}$ is updated once the unloading phase moves through the interval $\varepsilon_{c,re} < \varepsilon < \varepsilon_{c,pl}$ and it assumes the value of the last experienced

strain. This consideration allows to calculate the reloading behaviour using the same equation reported in Eq.(4.13) and Eq.(4.14). Indeed, using Eq.(4.13) it is possible to define the reloading CE→CF path based on the updated $\varepsilon_{c,pl}$.

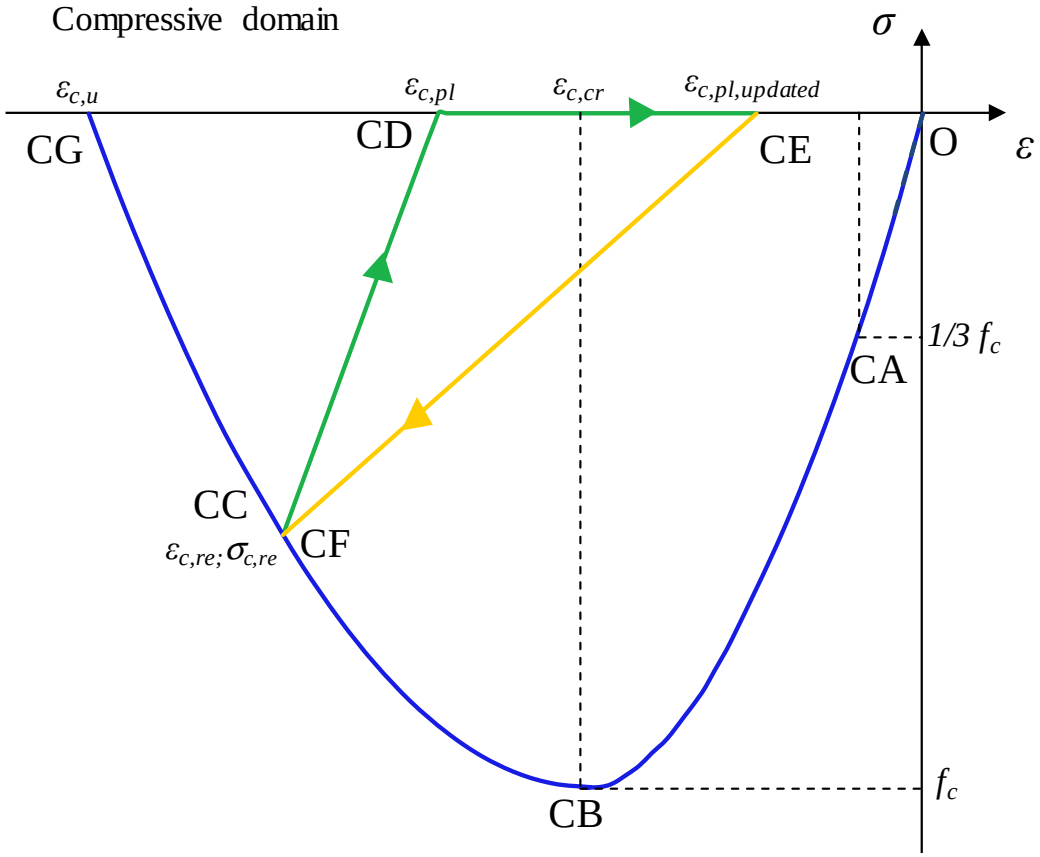

Figure 4.6 – PARC_CL 2.0, cyclic behaviour of compressive concrete

4.2.1.2 Steel model

The reinforcement is assumed smeared in concrete. Rotating the uniaxial strains of the concrete, defined in the *1,2*-system, it is possible to obtain the uniaxial strains along each steel bars axes, as follow:

$$\bar{\varepsilon}_{xi} = \bar{\varepsilon}_1 \cos^2 \alpha_i + \bar{\varepsilon}_2 \sin^2 \alpha_i - \gamma_{12} \cos\alpha_i \sin\alpha_i \tag{4.15}$$

The constitutive relation for steel, employed in PARC_CL 2.0 crack model, is based on [Menegotto and Pinto, 1973] and allows to represent the hysteretic stress-strain behaviour of reinforcing steel bar also including yielding, strain hardening and Baushinger effect, Figure 4.7.

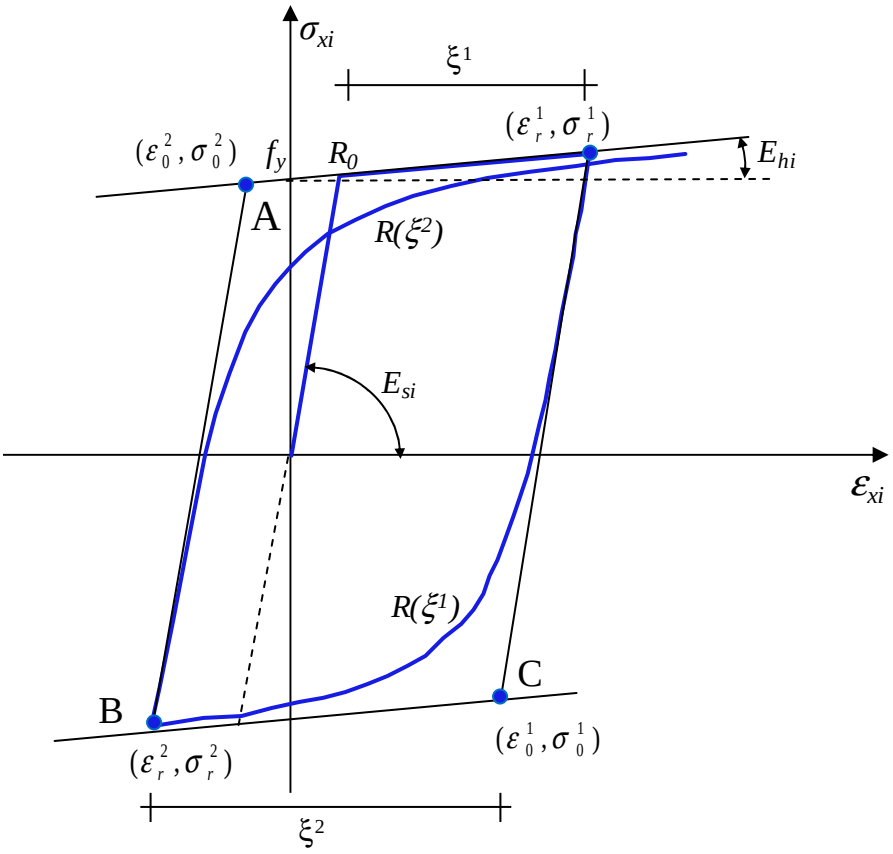

Figure 4.7 – PARC_CL 2.0, cyclic behaviour of reinforcing steel.

The [Menegotto and Pinto, 1973] formulation can be expressed following Eq.(4.16):

$$\sigma_{xi} = \sigma^* \cdot (\sigma_0 - \sigma_r) + \sigma_r \tag{4.16}$$

where:

$$\sigma^* = b \cdot \varepsilon^* + \frac{(1-b)\varepsilon^*}{\left(1+\varepsilon^{*R}\right)^{1/R}} \tag{4.17}$$

$$\varepsilon^* = \frac{\varepsilon_{xi} - \varepsilon_r}{\varepsilon_0 - \varepsilon_r} \tag{4.18}$$

Eq.(4.17) represents a curved transition from a straight line asymptote with E_{si} inclination to another asymptote with E_{hi} inclination, Figure 4.7. In Eq.(4.16) and Eq.(4.18), σ_0 and ε_0 represent the stress and the strain in the point where the two asymptotes of the considered branch meet (eg. point A in Figure 4.7); similarly σ_r and ε_r are the stress and the strain in the point where the last strain reversal occurs (eg. point B in Figure 4.7). As indicated in Figure 4.7, (σ_0,ε_0) and (σ_r,ε_r) are updated at each strain reversal; b is the strain-hardening ratio and can be calculated as the ratio between E_{hi} and E_{si}:

$$b = \frac{E_{hi}}{E_{si}} \tag{4.19}$$

Finally, *R* is the parameter that influences the shape of the transition curve between the two asymptotes and allows a good representation of Baushinger effect. *R* is considered dependent on the strain difference between the point in which the last strain reversal occurs (e.g. point B in Figure 4.7 for the considered branch) and the previous asymptotes meeting point (eg. point C in Figure 4.7 for the considered branch). The expression of *R* is reported in Eq.(4.20):

$$R = R_0 - \frac{a_1 \cdot \xi}{a_2 + \xi} \tag{4.20}$$

where R_0 is the value of the parameter *R* during the first loading cycle, a_1 and a_2 are experimentally determined parameters. The influence of *R* in the shape of the curve is depicted in Figure 4.7.

In order to investigate the influence of R_0, a_1 and a_2 parameters on the stress-strain relationship a preliminary parametric study was carried out. The parametric study was based on the experimental campaign carried out on ϕ12 bars tested at the ETH Zurich by [Thiele et al. ,2001], Figure 4.8.

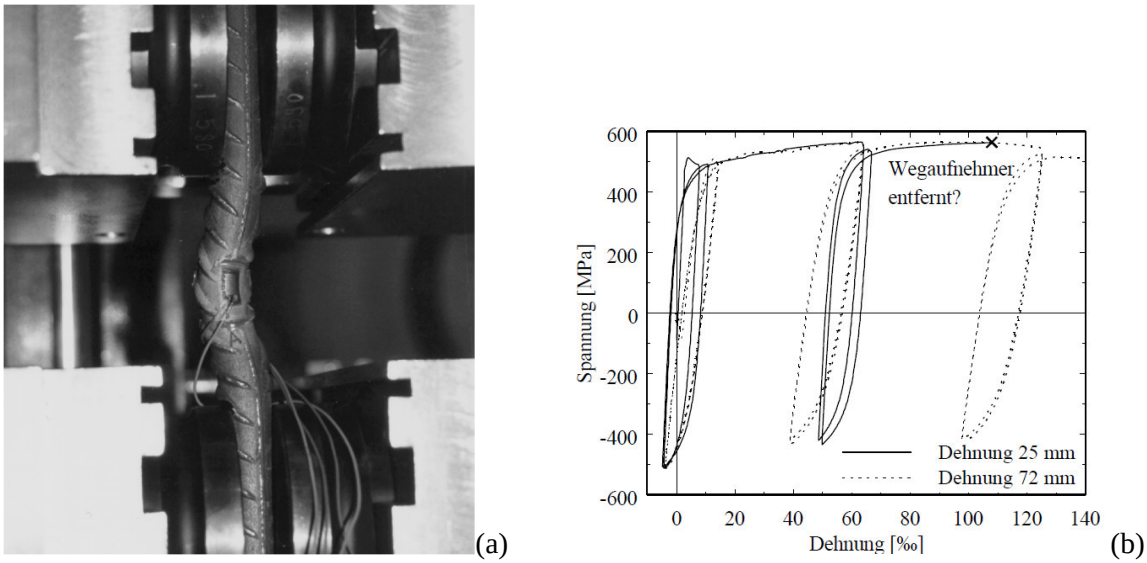

Figure 4.8 – Reference experimental campaign for parametric study on R_0, a_1 *and* a_2 *parameters: (a) experimental set-up, (b) experimental results [Thiele et al., 2001].*

The reference parameters, according to [Fragiadakis et al., 2007], were set equal to R_0=20, a_1=18.45 and a_2=0.15. The results obtained by changing the parameter R_0 (Figure 4.9), the parameter a_1 (Figure 4.10), and the parameter a_2 (Figure 4.11) are reported below.

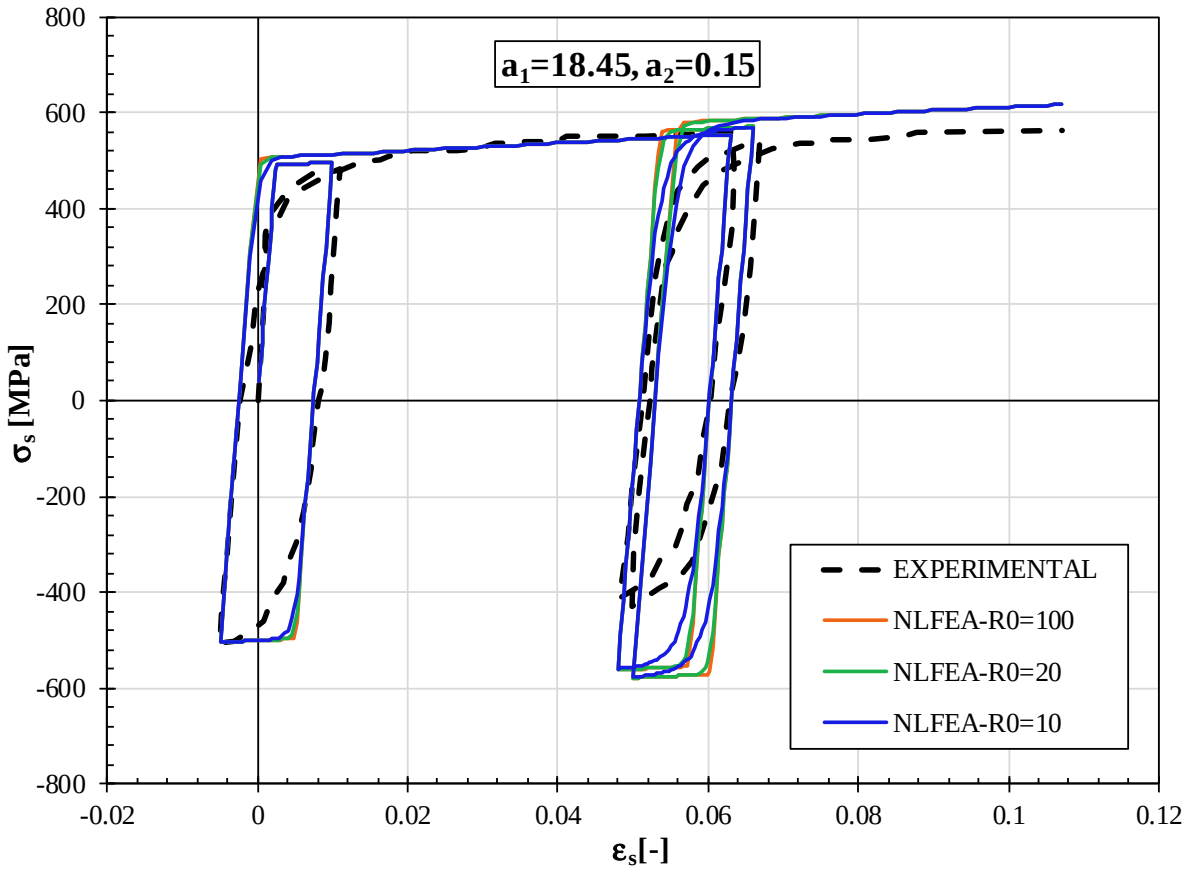

Figure 4.9 – influence of R_0 parameter in the slope of the steel behaviour.

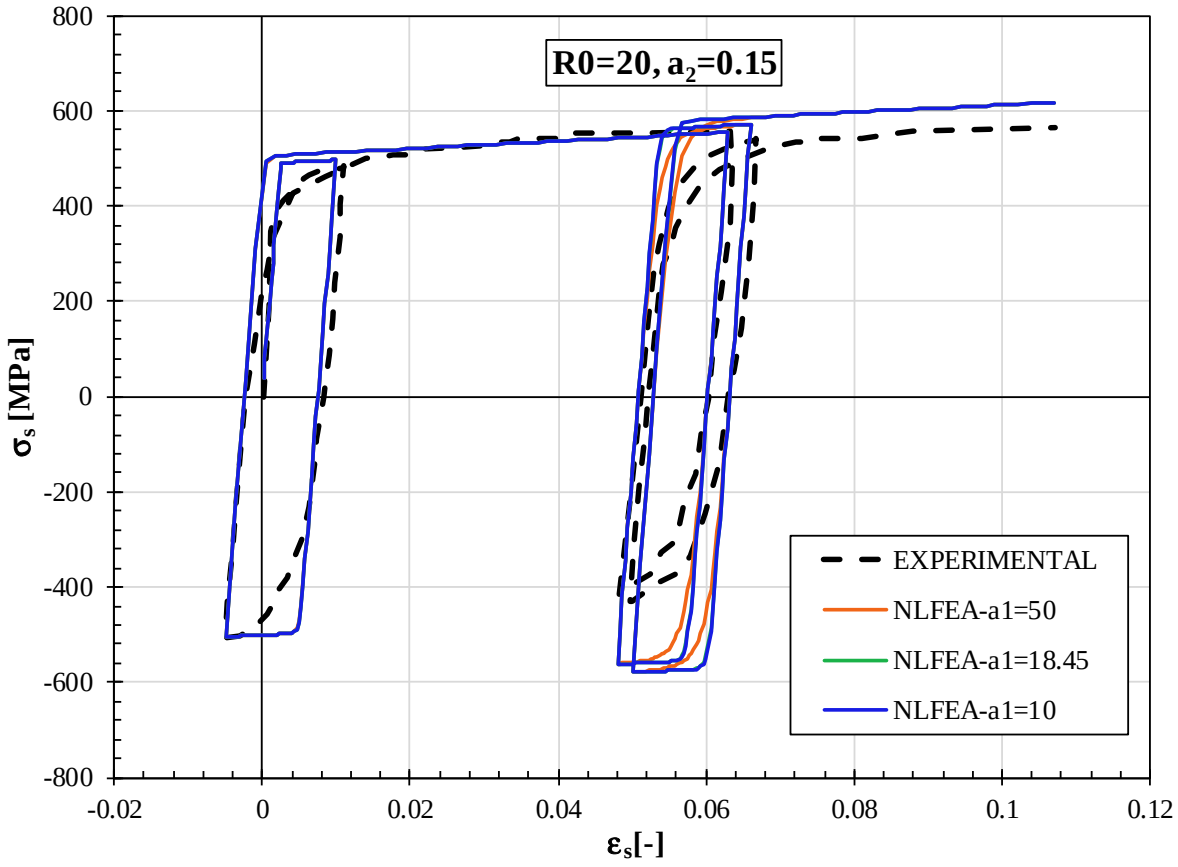

Figure 4.10 – influence of a_1 parameter in the slope of the steel behaviour.

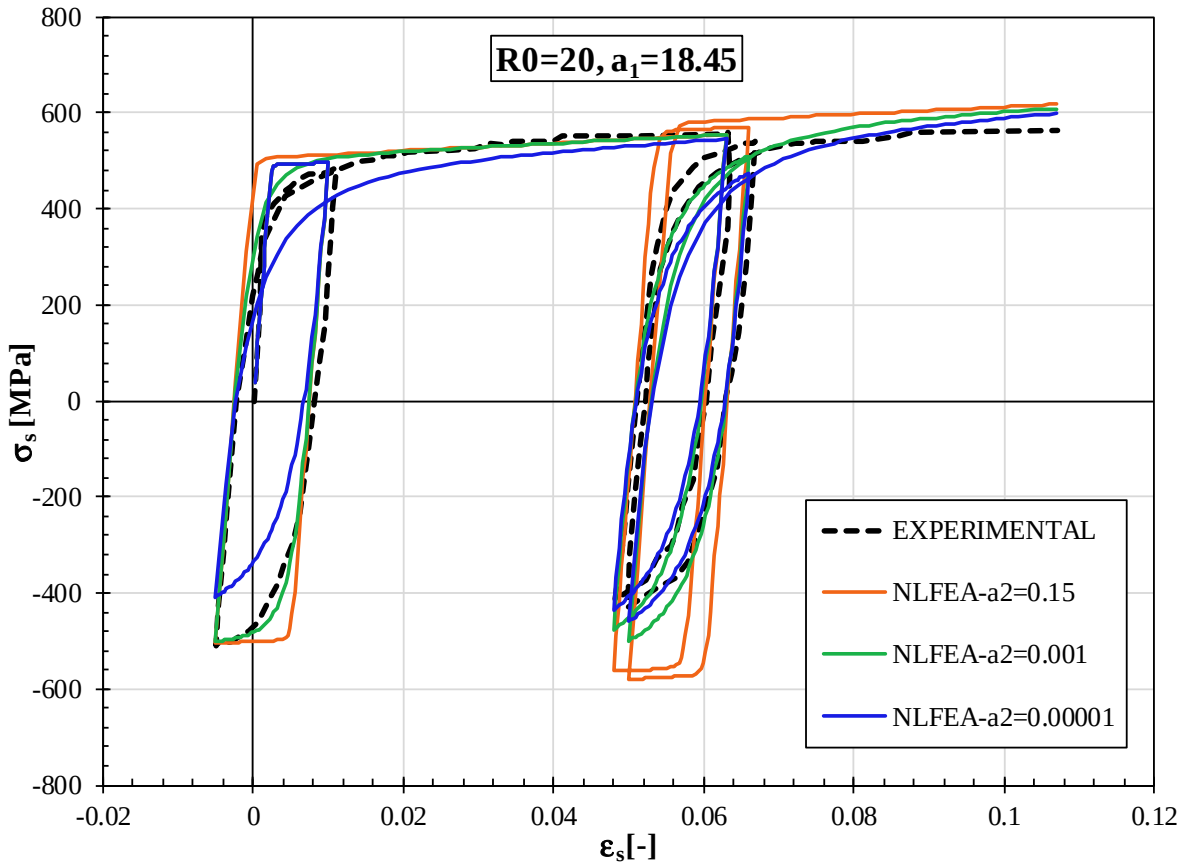

Figure 4.11 – influence of a_2 parameter in the slope of the steel behaviour.

From Figure 4.9 it can be noted that the increasing of the parameter R_0 leads to a decreasing of the curvature of the stress-strain relationship, even if the scatter in NLFEA results is rather small and all the curves obtained by means of NLFEA do not quite match the experimental results.

The results reported in Figure 4.10 highlight how, by increasing the a_1 parameter, the curvature increases; also in this case the scatter between the experimental and the NLFEA results is relatively large for all the different values of the a_1 parameter.

Finally, the curves reported in Figure 4.11 shown that the slope of the stress-strain relationship strongly depends on the a_2 parameter. In particular assuming a_2=0.001 the NLFEA curve fits well the experimental results. For this reason, in the PARC_CL 2.0 crack model the following final set of parameters is used (R_0=20, a_1=18.45 and a_2=0.001).

4.2.1.3 Aggregate interlock model

The PARC_CL 2.0 is a fixed crack model and, as a consequence of this, a proper definition of the shear stress vs shear strain behaviour is fundamental. Indeed, due to the fact that after cracking the orthotropic coordinate system is fixed and determined by the crack direction, shear stresses and strains may develop along the crack.

According to the total strain concept, the PARC_CL 2.0 crack model assumes that the un-cracked concrete, characterized by the elastic shear deformation $\gamma_{12,el}$, and the cracked concrete, characterized by the cracking shear deformation $\gamma_{12,cr}$, behave like two springs in series, Figure 4.12-a. Therefore, the equivalent overall shear modulus, G_{eq}, in the cracked phase can be calculated according to Eq.(4.21), as schematically reported in Figure 4.12-b:

$$G_{eq} = \frac{G \cdot G_{cr}}{G + G_{cr}} \tag{4.21}$$

where G is the elastic shear modulus, Eq.(4.22), while G_{cr} is the cracked shear modulus.

$$G = \frac{E_c}{2 \cdot (1 + \upsilon)} \tag{4.22}$$

The cracked shear modulus, G_{cr}, is related to the effect of aggregate interlock and is calculated according to the formulation proposed by [Gambarova, 1983], presented herein.

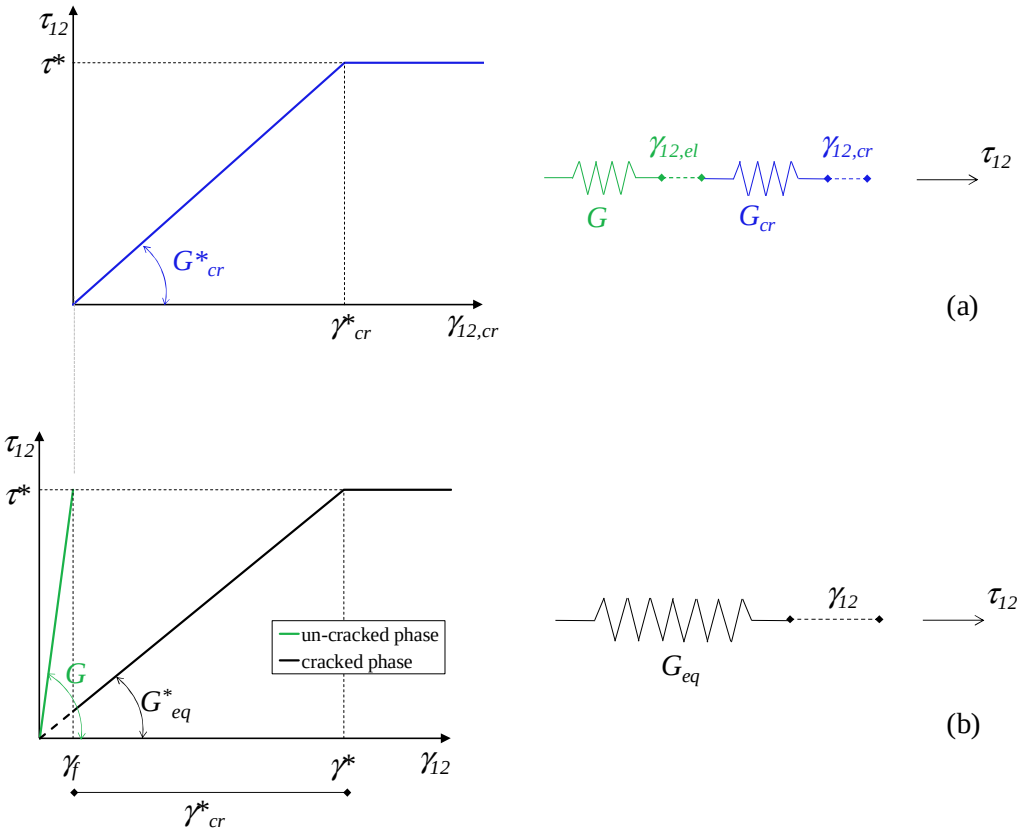

Figure 4.12 – Aggregate interlock, overall τ_{12}-γ_{12} behavior based on the total strain assumption as stated in Eq.(4.28).

According to the formulation proposed by [Gambarova, 1983], the shear stress, caused by the effect of aggregate interlock, depends on the crack opening, w, and on the crack sliding, v. From the shear sliding, v, the shear strain in the cracked phase, $\gamma_{12,cr}$, can be evaluated by using the crack bandwidth h, introduced in §4.2.1.1.2, according to Eq.(4.23).

$$\gamma_{12,cr} = \frac{v}{h} \tag{4.23}$$

Finally, the bilinear formulation proposed by [Gambarova, 1983] for monotonic loading, shown in Figure 4.13-a, can be written as follow:

$$\begin{cases} \tau_{12} = \dfrac{\tau^*}{\gamma^*_{cr}} \cdot \gamma_{12,cr} = G^*_{cr} \cdot \gamma_{12,cr} & if\ \gamma_{12,cr} \le \gamma^*_{cr} \\ \tau_{12} = \tau^* & if\ \gamma_{12,cr} > \gamma^*_{cr} \end{cases} \tag{4.24}$$

where τ^* and γ^*_{cr} represent the point corresponding to the end of the first linear branch when cracking is occurred, as shown in τ_{12}-$\gamma_{12,cr}$ curve of Figure 4.13-a, and they can be calculated respectively with Eq.(4.25) and Eq.(4.26), for different values of crack opening, *w*.

$$\tau^* = \bar{\tau} \cdot \left(1 - \sqrt{\frac{2\,w}{d_{\max}}}\right) \frac{a_3 + a_4 \left|\dfrac{v^*}{w}\right|^3}{1 + a_4 \left(\dfrac{v^*}{w}\right)^4} \frac{1}{w} v^* \tag{4.25}$$

$$\gamma^*_{cr} = \frac{v^*}{h} \tag{4.26}$$

where $\bar{\tau} = 0.27 \cdot f_c$; $v^* = \dfrac{f_c}{a_5} w + a_6$; $a_3 = \dfrac{2.45}{\bar{\tau}}$; $a_4 = 2.44\left(1 - \dfrac{4}{\bar{\tau}}\right)$, $a_5 = 0.366 \cdot f_c + 3.333$ and $a_6 = f_c/110$

The obtained τ_{12}-$\gamma_{12,cr}$ bilinear curve is schematized in Figure 4.13-a, while in Figure 4.13-b the influence of crack opening, *w*, is reported.

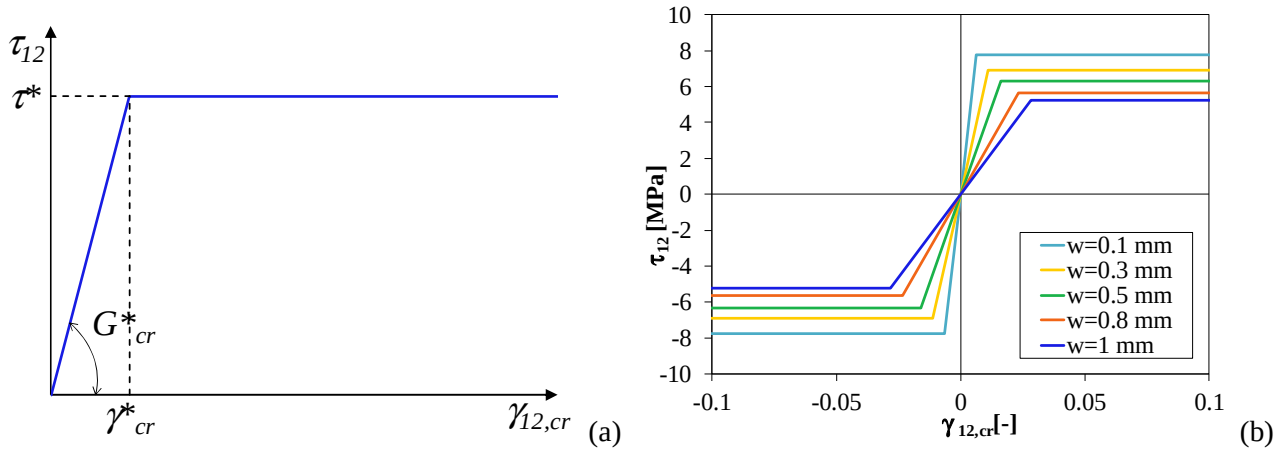

Figure 4.13 – Aggregate interlock, monotonic behaviour: (a) τ_{12}-$\gamma_{12,cr}$ curve and (b) influence of crack opening on τ_{12}-$\gamma_{12,cr}$ curve.

From Eq.(4.24), the cracked shear modulus, G_{cr}, can be derived as expressed in Eq.(4.27):

$$\begin{cases} G_{cr} = \dfrac{\tau_{12}}{\gamma_{12,cr}} = \dfrac{\tau^*}{\gamma^*_{cr}} = G^*_{cr} & if\ \gamma_{12,cr} \le \gamma^*_{cr} \\ G_{cr} = \dfrac{\tau_{12}}{\gamma_{12,cr}} = \dfrac{\tau^*}{\gamma_{12,cr}} & if\ \gamma_{12,cr} > \gamma^*_{cr} \end{cases} \tag{4.27}$$

where G^*_{cr} represents the secant shear modulus associated to the first linear branch in the cracked phase, as shown in Figure 4.13-a.

The formulation herein proposed allows to calculate the shear behaviour only for monotonic loading; in the PARC_CL 2.0 crack model the cyclic behaviour is also taken into account considering, in the unloading phase, a branch with slope G^*_{cr}, as shown in Figure 4.14-a. Changing the crack opening, w, the value of G^*_{cr} change and hence different cyclic curves can be obtained as shown in Figure 4.14-b.

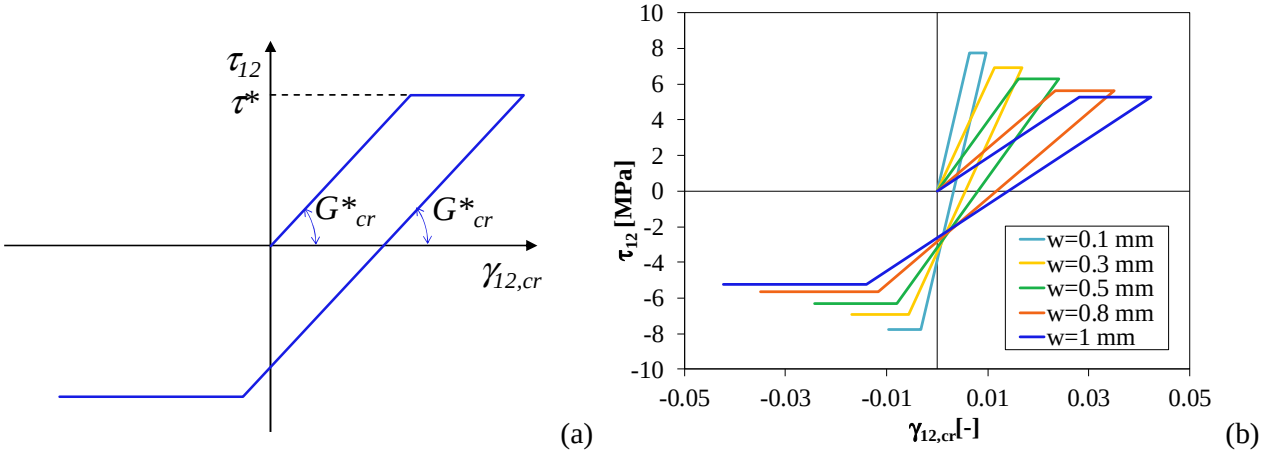

Figure 4.14 – Aggregate interlock, cyclic behaviour: (a) τ_{12}-$\gamma_{12,cr}$ curve with loading and unloading phase (b) influence of crack opening on τ_{12}-$\gamma_{12,cr}$ cyclic curves.

Combining the just obtained cracked shear modulus, G_{cr}, with the elastic shear modulus, G, using Eq.(4.21), the overall τ_{12}-γ_{12} behavior, reported in Figure 4.12-b, can be derived as reported in Eq.(4.28):

$$\begin{cases} \tau_{12} = G \cdot \gamma_{12} & if\ \gamma_{12} \le \gamma_f \\ \tau_{12} = G^*_{eq} \cdot \gamma_{12} & if\ \gamma_f < \gamma_{12} \le \gamma^* \\ \tau_{12} = \tau^* & if\ \gamma_{12} > \gamma^* \end{cases} \tag{4.28}$$

where γ_f corresponds to the shear strain at the onset of concrete cracking and γ^* defines the point after which the shear strain remains constant and is equal to:

$$\gamma^* = \gamma^*_{cr} + \gamma_f \tag{4.29}$$

In Eq.(4.28), G^*_{eq} is calculated using Eq.(4.21) by substituting G_{cr} with G^*_{cr}.

4.2.1.4 Overall behaviour

The concrete and steel behaviours as well as their interaction effects are modelled with constitutive relationships for loading-unloading-reloading conditions as presented in the previous paragraphs. Moreover,

the concrete behaviour is defined along the orthotropic axes (*1,2*-system in Figure 4.15), while the steel behaviour is defined along the coordinate system defined by the inclination of the *i*th order of bar (x_i,y_i-system in Figure 4.15).

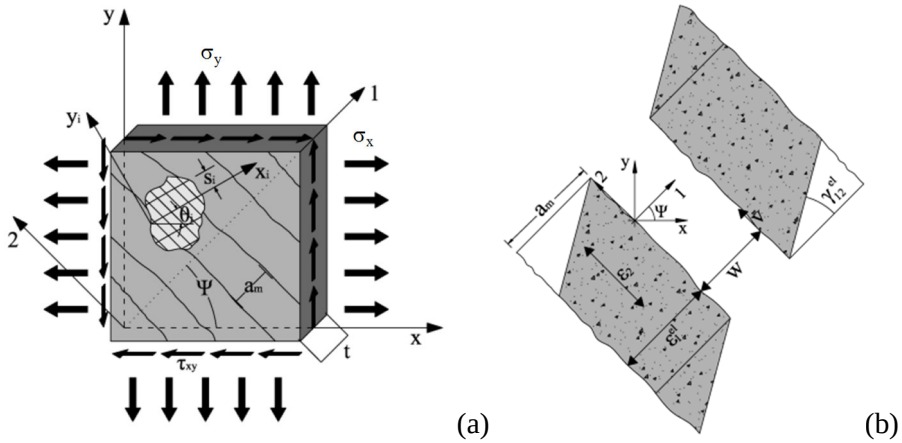

Figure 4.15 – (a) RC element subjected to plane stress state and (b) crack parameters.

The concrete stress vector, in the *1,2*-coordinate system can be generated as follow:

$$\{\sigma_{1,2}\}=\begin{Bmatrix}\sigma_1\\ \sigma_2\\ \tau_{12}\end{Bmatrix} \tag{4.30}$$

where σ_1 and σ_2 represent the stresses in concrete in the normal directions calculated following the relation presented in §4.2.1.1, while τ_{12} is the shear stress in concrete calculated according to the aggregate interlock model presented in §4.2.1.3.

The steel stress vector, defined for each *i*th order of bar in the x_i,y_i-coordinate system, can be generated as follow:

$$\{\sigma_{x_i,y_i}\}=\begin{Bmatrix}\sigma_{x_i}\\ 0\\ 0\end{Bmatrix} \tag{4.31}$$

where σ_{xi} represents the stress along the axis of the *i*th order of bar and it can be calculated following the procedure explained in §4.2.1.2. From Eq.(4.31) it can be noted that no stresses in the direction perpendicular to the axis of the bar develop, due to the fact that the dowel action phenomenon has not been considered yet.

Both the concrete and the steel stress vectors can be transformed from their local coordinate system to the overall global *x,y* coordinate system using respectively Eq.(4.32) and Eq.(4.33):

$$\{\sigma_{x,y}\}_c=[T_\psi]^t\cdot\{\sigma_{1,2}\} \tag{4.32}$$

$$\{\sigma_{x,y}\}_{s,i}=[T_\theta]^t\cdot\{\sigma_{x_i,y_i}\} \tag{4.33}$$

where $[T_\psi]^t$ is the transpose of the transformation matrix, reported in Eq.(4.2), and can be expressed as shown in Eq.(4.34):

$$[T_\psi]^t = \begin{bmatrix} \cos^2\psi & \sin^2\psi & -2\cdot\cos\psi\cdot\sin\psi \\ \sin^2\psi & \cos^2\psi & 2\cdot\cos\psi\cdot\sin\psi \\ \cos\psi\cdot\sin\psi & -\cos\psi\cdot\sin\psi & \cos^2\psi-\sin^2\psi \end{bmatrix} \tag{4.34}$$

The total stress in the *x*,*y*-system is obtained by assuming that concrete and reinforcing bars behave like two springs placed in parallel:

$$\{\sigma_{x,y}\} = \{\sigma_{x,y}\}_c + \sum_{i=1}^{n} \rho_i \{\sigma_{x,y}\}_{s,i} \tag{4.35}$$

where n is the total number of the orders of bars and ρ_i represents the reinforcement ratio for every ith order of bars.

The proposed PARC_CL 2.0 model is based on a tangent approach, in which the Jacobian matrix in the local coordinate system for each material is composed by derivatives as shown in Eq.(4.36) for concrete and in Eq.(4.37) for each ith order of bars.

$$[D_{1,2}] = \begin{bmatrix} \frac{\partial\sigma_1}{\partial\varepsilon_1}\frac{1}{(1-\nu^2)} & \frac{\partial\sigma_1}{\partial\varepsilon_2}\frac{\nu}{(1-\nu^2)} & 0 \\ \frac{\partial\sigma_2}{\partial\varepsilon_1}\frac{\nu}{(1-\nu^2)} & \frac{\partial\sigma_2}{\partial\varepsilon_2}\frac{1}{(1-\nu^2)} & 0 \\ 0 & 0 & \frac{\partial\tau_{12}}{\partial\gamma_{12}} \end{bmatrix} \tag{4.36}$$

$$[D_{x_i,y_i}] = \begin{bmatrix} \frac{\partial\sigma_{xi}}{\partial\varepsilon_{xi}} & 0 & 0 \\ 0 & 0 & 0 \\ 0 & 0 & 0 \end{bmatrix} \tag{4.37}$$

After the first crack the Poisson's ratio is assumed to be zero and the terms out of the diagonal become zero.

Finally, the global stiffness matrix is obtained from Eq.(4.38):

$$[D_{x,y}] = [T_\psi]^t \cdot [D_{1,2}] \cdot [T_\psi] + \sum_{i=1}^{n} \rho_i [T_{\theta i}]^t \cdot [D_{x_i,y_i}] \cdot [T_{\theta i}] \tag{4.38}$$

4.2.1.5 Validation of the model under cyclic loading

In order to assess the efficiency of the presented PARC_CL 2.0 crack model under cyclic static loading, some experimental tests on RC panels found in literature were investigated.

The reference experimental program, referred to [Mansour and Hsu, 2005], was performed using the "Universal Element Tester" facility at the University of Houston and consists in 12 panel specimens tested under reversed cyclic shear stresses. 8 out of the 12 specimens are investigated in this section by means of NLFEA and PARC_CL 2.0 crack model.

The test program was aimed to investigate the effects of steel bars orientation and reinforcement ratio on panel behaviour. All panels were 1398x1398x178 mm in size, except panels CE4, CA4 and CB4, which were 1398x1398x203 mm in size. The properties of the panels are given in Table 4.1, including the maximum compressive stress of concrete f_c, the fracture energy in tension, G_F, and in compression , G_C, used in NLFEA, the yield stresses of steel, f_y, and the orientation of the *x*-*i* steel bar, θ_i.

Table 4.1 – Steel Bar arrangement, material properties and primary variables of panels tested by [Mansour and Hsu, 2005].

		Concrete			steel in *x*-*i* direction		steel in *y*-*i* direction		
Series	Panel	f_c [MPa]	G_F [N/mm]	G_C [N/mm]	$\rho_{x\text{-}i}$ [%]	f_y [MPa]	$\rho_{y\text{-}i}$ [%]	f_y [MPa]	θ_i [degrees]
CE	CE2	49	0.147	36.78	0.54	424.1	0.54	424.1	0
	CE3	50	0.148	36.90	1.20	425.4	1.20	425.4	0
	CE4	47	0.146	36.50	1.90	453.4	1.90	453.4	0
CA	CA2	45	0.145	36.20	0.77	424.1	0.77	424.1	45
	CA3	44.5	0.145	36.20	1.70	425.4	1.70	425.4	45
	CA4	45	0.145	36.20	2.70	453.4	2.70	453.4	45
CB	CB3	48	0.147	36.63	1.70	425.4	0.77	424.1	45
	CB4	47	0.146	36.50	2.70	453.4	0.67	424.1	45

Regarding the loading method, the test panels were subjected to reversed stresses in the horizontal and vertical directions using the Universal Panel Tester [Hsu et al., 1995[a]]. The Universal Panel tester allows to switch from stress control to strain control. In particular, the stress control mode was used up to yielding, followed by the strain control mode after yielding. Before yielding, in the stress control mode, the horizontal stress was used to control the vertical stress such as they were equal in magnitude and opposite in direction, in order to obtain a state of pure shear stress in the *i*,*j*-system inclined at 45° with respect to the *x*,*y*-system, Figure 4.16. The testing facility was able to switch from stress control mode to strain control mode just before yielding [Hsu et al., 1995[b]]. After yielding, in the strain control mode, the shear strain (the algebraic sum of the horizontal and vertical strain) was used to control the horizontal principal stress which was used to control the

vertical principal stress such that they were always equal in magnitude and opposite in direction, in order to obtain, also in this condition, a state of pure shear stress in the *i*,*j*-system inclined at 45° with respect to the *x*,*y*-system, Figure 4.16.

The loads were applied through 20 horizontal and 20 vertical jacks. The horizontal and vertical applied stresses were measured using 40 load cells. The shear stress in the *i*,*j*-system inclined at 45° with respect to the *x*,*y*-system was then calculated by means of stress transformation.

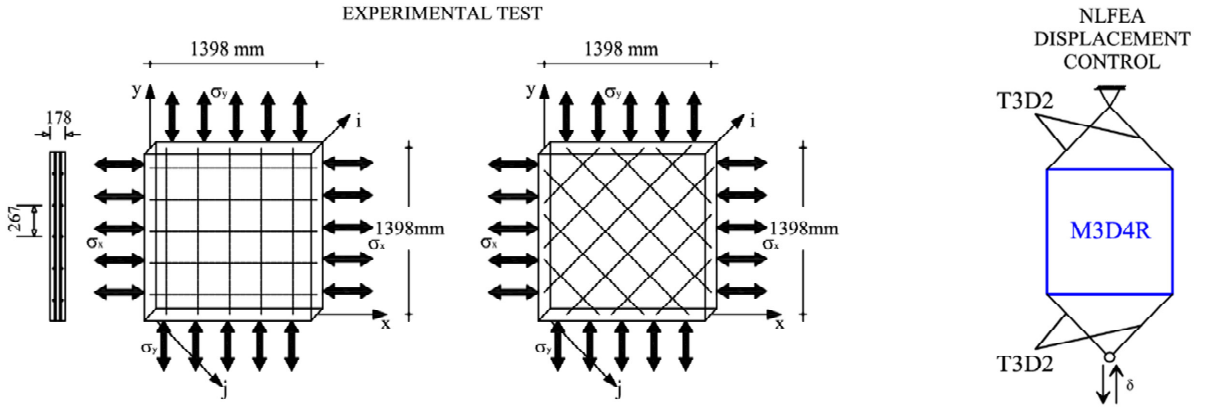

(a) Panels of CE-series (θ_i=0°) (b) Panels of CA-and CB-series (θ_i=45°) (c) Modeling of test panels

Figure 4.16 – Experimental program, steel bar orientation in test panels: (a) panels with θ_i=0° and (b) panels with θ_i=45°. (c) NLFE model of the tested panels

NLFEA analysis was carried out using a single three-dimensional, 4-node membrane element with reduced integration (defined M3D4R in [Abaqus 6.12, 2012]), Figure 4.16-c. An external frame, modelled with 2 nodes with regular integration scheme (defined T3D2 in [Abaqus 6.12, 2012]), with a very high stiffness compared to the panel, was used to simulate the same loading condition experimentally imposed. At the frame end the cyclic displacement time history was imposed. Each truss of the frame was inclined of 45 degrees so that in correspondence of each node of the panel, the nodal force acting on the panel was inclined of 45 degrees too. In this way, the horizontal and the vertical forces acting on the panel presented equal magnitude and opposite direction, as in the experimental set-up.

In Figure 4.17 the experimentally-measured shear stress vs. shear strain responses for panels of CA, CB and CE series are compared with the analytical model predictions. The results plotted in Figure 4.17 are referred to a plane inclined of 45° with respect to the *x*,*y*-system, the *i*,*j*-system.

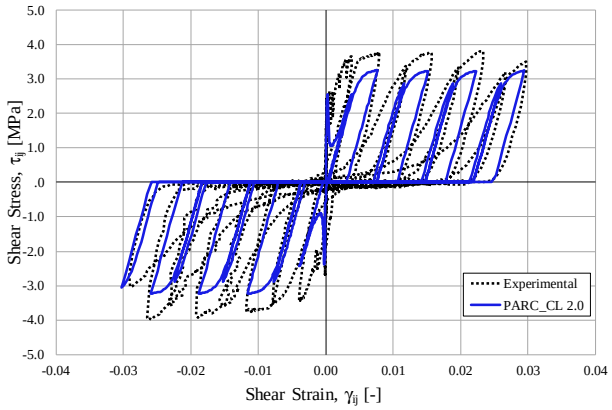

(a) CA2 (θ_i=45°,$\rho_{x\text{-}i}$=$\rho_{y\text{-}i}$=0.77%)

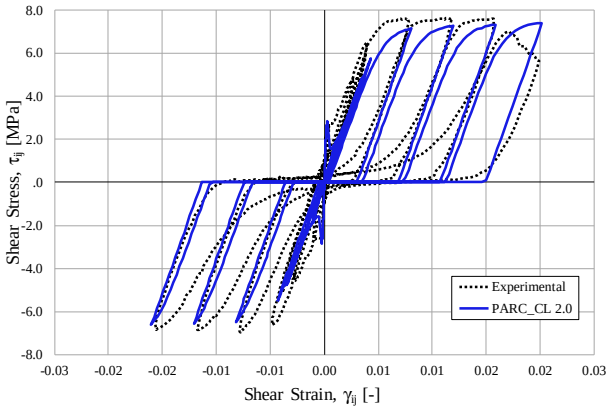

(b) CA3 (θ_i=45°,$\rho_{x\text{-}i}$=$\rho_{y\text{-}i}$=1.7%)

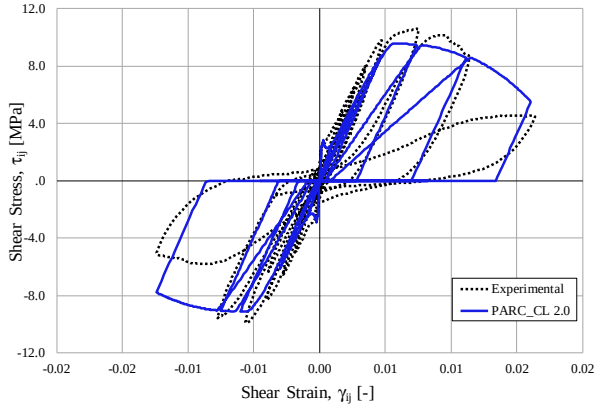

(c) CA4 (θ_i=45°,$\rho_{x\text{-}i}$=$\rho_{y\text{-}i}$=2.7%)

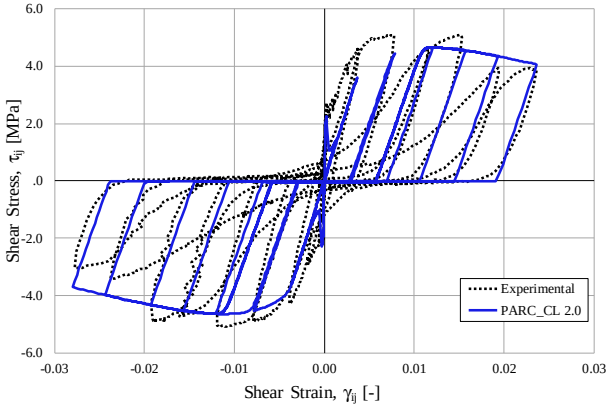

(d) CB3 (θ_i=45°,$\rho_{x\text{-}i}$=1.7%;$\rho_{y\text{-}i}$=0.77%)

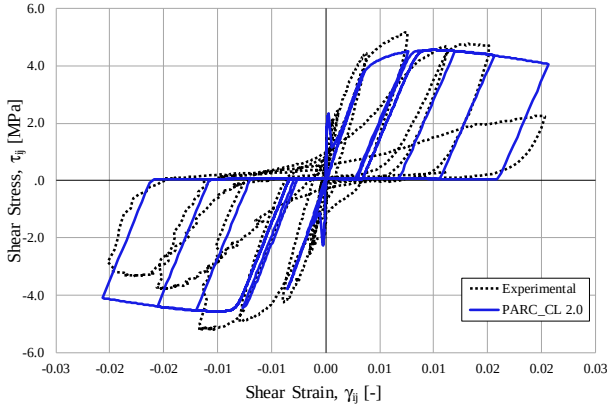

(e) CB4 (θ_i=45°,$\rho_{x\text{-}i}$=2.7%;$\rho_{y\text{-}i}$=0.67%)

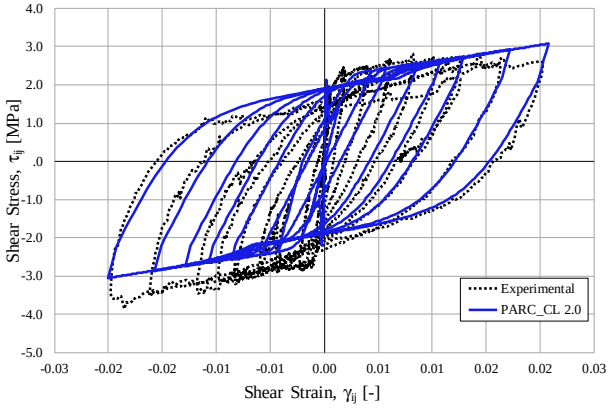

(f) CE2 (θ_i=0°,$\rho_{x\text{-}i}$=$\rho_{y\text{-}i}$=0.54%)

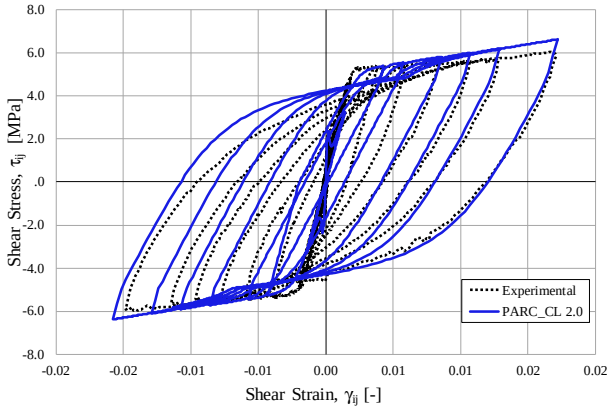

(g) CE3 (θ_i=0°,$\rho_{x\text{-}i}$=$\rho_{y\text{-}i}$=1.2%)

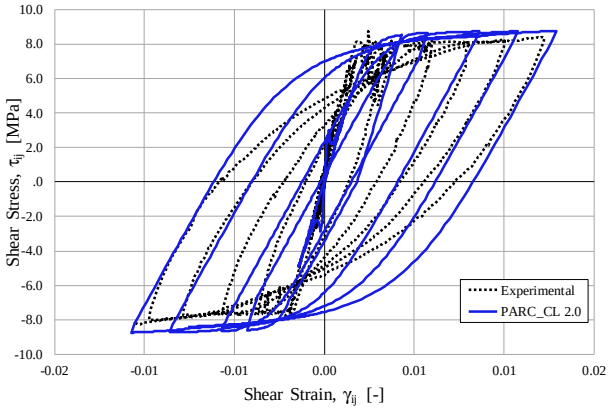

(h) CE4 (θ_i=0°,$\rho_{x\text{-}i}$=$\rho_{y\text{-}i}$=1.9%)

Figure 4.17 – Comparison between experimental and NLFEA results.

The results reported in Figure 4.17 highlighted that the PARC_CL 2.0 crack model provides reasonably accurate response predictions, for varying reinforcement ratios and orientations. An acceptable level of agreement is observed between model and test results in terms of shear stress capacity, stiffness, ductility, shape of the unloading/reloading loops, and pinching characteristics of the response. Furthermore, the behaviour characteristics and failure modes observed during the tests, including yielding of reinforcement and crushing of concrete, were observed to be consistent with the analytically-predicted responses.

As stated before, one of the aim of the experimental tests carried out by [Mansour and Hsu, 2005] was to investigate the effect of the steel bar orientation on the cyclic behaviour. Indeed, the steel bar orientation produces different cyclic response of the shear members: this becomes evident comparing the hysteretic loops of two RC 2-D elements, CA3 (Figure 4.17-b) and CE3 (Figure 4.17-g). According to [Hsu and Mo, 2010], a detailed study of the different behaviors of the panels with different steel bars orientation is conducted to check the PARC_CL 2.0 validity. Each tested panel can represent a 2-D element taken from the web of squat wall subjected to horizontal load *V* neglecting the effects of vertical loads. In Figure 4.18-a it is presented the panel CA3, in which the angle α_i between the bar (*x-i*,*y-i* system) and the *1*,*2*-coordinate system is 45°; in Figure 4.18-b it is presented the panel CE3 in which the angle α_i is equal to 0°.

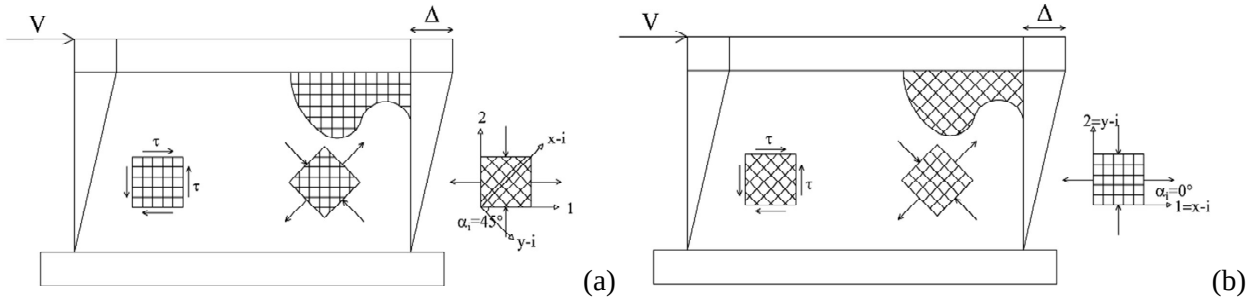

Figure 4.18 – Squat walls and relative 2-D panel element: (a) conventional horizontal and vertical steel bar configuration and (b) diagonal steel bar configuration.

The most important difference between the shapes of the two sets of hysteretic loops is due the pinching effect. The comparison between the results obtained analysing CA3 and CE3 panel (Figure 4.17-b and Figure 4.17-g, respectively) shows the effect of the steel bar orientation in terms of shear ductility and energy dissipation capacity. When the steel bars are oriented in the *1*,*2*-system (CE3 panel and Figure 4.18-b), the hysteretic loops are fully rounded and the behaviour is ductile, while when they are oriented at 45° (CA3 panel and Figure 4.18-a), the behaviour is much less ductile. PARC_CL 2.0 model is capable of predicting the pinched shape as well as the fully rounded of the hysteretic loops, in fact the PARC_CL 2.0 curve of the CA3 panel (and of the CA series in general) is severely 'pinched' near the origin, while the CE3 panel (and all the panels of the CE series in general) is fully rounded and robust.

In Figure 4.19 is presented a detail of the first cycles obtained by means of NLFEA for CA3 and CE3 panel in order to show the pinching effect due to the different orientation of the steel bar.

The pinching effect in the two panels presented in Figure 4.19 can be explained by examining cracked elements, in which the cracks are both vertical and horizontal because of previous cycles of positive and negative shear stresses.

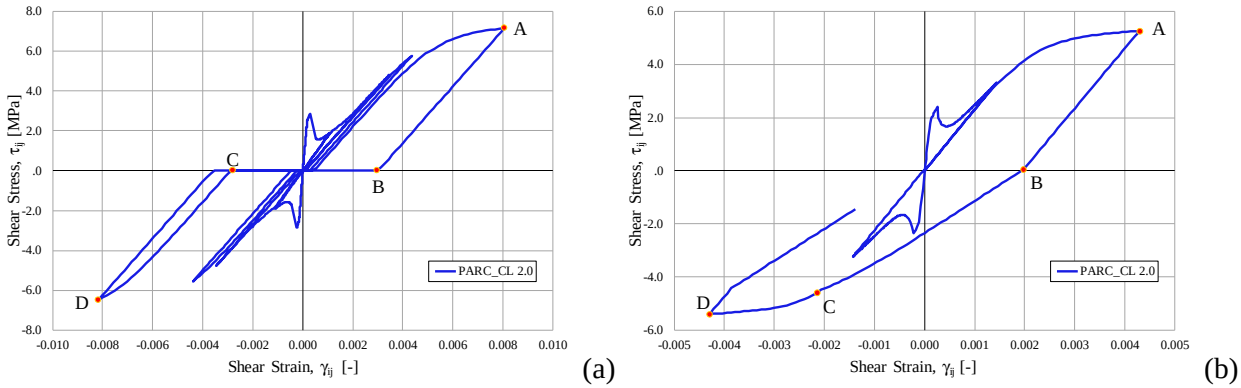

Figure 4.19 – Pinching mechanism: (a) CA3 panel with presence of pinching effect and (b) CE3 with absence of pinching effect.

For panel CA3, since both the vertical and horizontal cracks are opened, the applied stress (σ_H and σ_V) must be resisted by the two 45° steel bars, Figure 4.20-a. The effect of stresses can be separated, as shown in Figure 4.20-a: while the horizontal stress induces a compressive stress in the bars, the vertical stress induces an equal tensile stress, so the stresses in the two 45° steel bars cancel each other out and the shear stiffness in the B-C branch of Figure 4.19-a becomes zero. Instead, the B-C branch in the panel CE3 (Figure 4.19-b) shows a large shear stiffness, that is sustained until the yielding of steel bars at point C. This is due to the fact that in the panel CE3 the horizontal compressive stress σ_H is absorbed by horizontal steel bars while the vertical tensile stress is absorbed by vertical bars, as shown in Figure 4.20-b. Both the compressive stresses in the horizontal steel bars and the tensile stresses in the vertical steel bars contribute to the shear stress in the 45° direction.

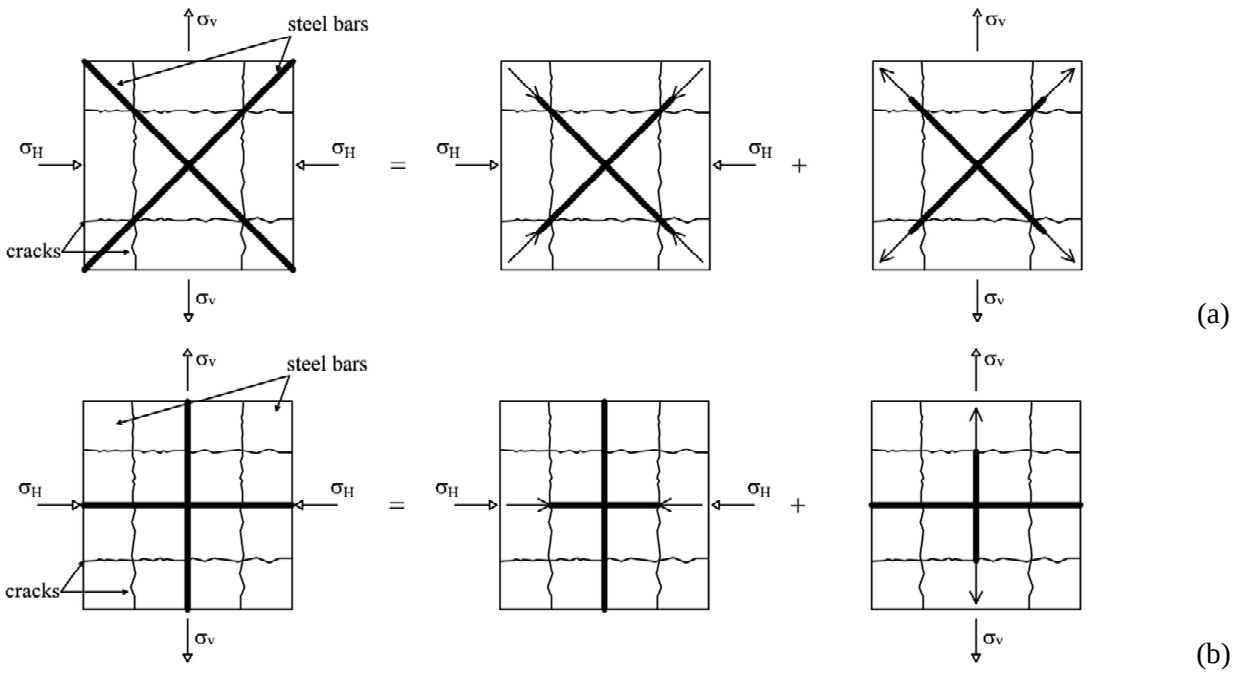

Figure 4.20 – Cracked RC element, effect of steel bar orientation on the pinching mechanism: (a) CA3 panel with 45° steel bar orientation and (b) CE3 panel with 0° steel bar orientation.

To conclude, in this section it has been demonstrated through comparison with experimental tests that the PARC_CL 2.0 crack model is capable of providing reasonably accurate predictions of the nonlinear

response of RC panels, thanks to the tangent approach which allows to take into account plastic strains in case of cyclic loads.

4.2.2 Dynamic behaviour

4.2.2.1 Damping

Damping is a peculiar energy dissipation mechanism, which happens during structure vibration. The matrix equation of motion takes the well-known form of Eq.(4.39):

$$[M]\cdot\{\ddot{u}(t)\}+[C]\cdot\{\dot{u}(t)\}+[K]\cdot\{u(t)\}=\{F\} \tag{4.39}$$

In this section the focus is pointed on the definition of the damping matrix [*C*] and in particular the most widely used Rayleigh damping is investigated. For Rayleigh damping the damping matrix [*C*] is expressed as in Eq.(4.40):

$$[C]=\alpha\cdot[M]+\beta\cdot[K] \tag{4.40}$$

Thus, the matrix [*C*] consists in a mass-proportional term and a stiffness proportional term.

Considering only the mass-proportional term of Eq.(4.40), the mass-proportional damping coefficient, α, can be derived considering the generalized damping for the *n*th mode:

$$C_n=\alpha\cdot M_n \tag{4.41}$$

C_n can also be expressed as in Eq.(4.42):

$$C_n=2\cdot\xi_n\cdot\omega_n\cdot M_n \tag{4.42}$$

Finally, combining Eq.(4.41) and Eq.(4.42) the mass-proportional damping coefficient, α, can be derived according to:

$$\alpha=2\cdot\xi_n\cdot\omega_n \tag{4.43}$$

Similarly, the stiffness-proportional damping coefficient, β, can be derived considering the generalized damping for the *n*th mode and considering only the stiffness-proportional term of Eq.(4.40):

$$C_n=\beta\cdot K_n \tag{4.44}$$

As in the previous case C_n can also be expressed according to Eq.(4.45):

$$C_n=2\cdot\xi_n\cdot\omega_n\cdot M_n=2\cdot\xi_n\cdot\omega_n\cdot\frac{K_n}{\omega_n^2}=2\cdot\xi_n\cdot\frac{K_n}{\omega_n} \tag{4.45}$$

Combining Eq.(4.44) and Eq.(4.45) the stiffness-proportional damping coefficient, β, can be expressed according to:

$$\beta = \frac{2 \cdot \xi_n}{\omega_n} \tag{4.46}$$

The mass-proportional damping, expressed in Eq.(4.43), and the stiffness-proportional damping, expressed in Eq.(4.46) are plotted in Figure 4.21-a. As shown in Figure 4.21-a the mass-proportional damping allows to damp the low-frequency modes while the stiffness-proportional damping allows to damp the high-frequency modes and it is quite important in NLFEA because it can provide sufficient dissipation to suppress the high-frequency numerical noise. Nevertheless, by themselves neither of the two damping models are appropriate for practical application of Multi Degrees of Freedom (MDF) systems.

The Rayleigh damping is introduced as the algebraic sum of the mass-proportional and the stiffness-proportional damping on the base of Eq.(4.47):

$$C_n = \alpha \cdot M_n + \beta \cdot K_n \tag{4.47}$$

By substituting Eq.(4.42) into Eq.(4.47) the Rayleigh damping coefficient can be derived as a function of α and β as expressed in Eq.(4.48) and shown in Figure 4.21-b.

$$\xi_n = \frac{\alpha}{2} \cdot \frac{1}{\omega_n} + \frac{\beta}{2} \cdot \omega_n \tag{4.48}$$

In that case the coefficients α and β can be determined by specifying damping ratio ξ for the *i*th and *j*th modes, as illustrated in Figure 4.21-b. The solution of the obtained system leads to the following equation:

$$\alpha = 2 \cdot \xi \cdot \frac{\omega_i \cdot \omega_j}{\omega_i + \omega_j} \tag{4.49}$$

$$\beta = \xi \cdot \frac{2}{\omega_i + \omega_j} \tag{4.50}$$

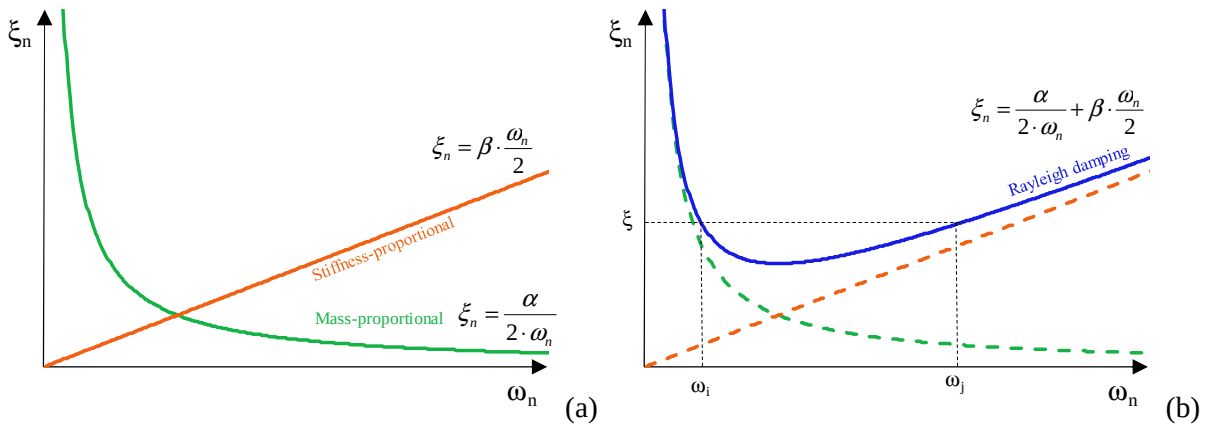

Figure 4.21 – Variation of damping ratios with natural frequency: (a) mass-proportional and stiffness-proportional damping and (b) Rayleigh damping.

4.2.2.2 Implementation of Rayleigh damping in PARC_CL 2.0

ABAQUS code [Abaqus 6.12, 2012] allows the definition of the mass-proportional damping, α, as an input value for the nonlinear finite element analysis. On the other hand, due to the fact that the stiffness matrix is modified by means of a user defined subroutine (the PARC_CL 2.0 crack model) it is not possible to define the stiffness-proportional damping, β, as an input value. For this reason, in order to consider the energy dissipation due to the material behaviour, it was necessary to introduce the stiffness proportional damping in the PARC_CL 2.0 crack model.

The stiffness-proportional Rayleigh damping is introduced in the PARC_CL 2.0 according to the following Eq.(4.52):

$$\sigma_{damp} = \beta \cdot E' \cdot \dot{\varepsilon} \tag{4.51}$$

The damping contribute on the concrete stress vector can be calculated as follow:

$$\left\{\sigma_{1,2}\right\}_{damp} = \begin{Bmatrix} \beta \cdot E'_{c1} \cdot \dot{\varepsilon}_1 \\ \beta \cdot E'_{c2} \cdot \dot{\varepsilon}_2 \\ \beta \cdot G'_{12} \cdot \dot{\gamma}_{12} \end{Bmatrix} \tag{4.52}$$

In the same way the damping contribute on the steel stress vector can be calculated as follow:

$$\left\{\sigma_{x_i,y_i}\right\}_{damp} = \begin{Bmatrix} \beta \cdot E'_{si} \cdot \dot{\varepsilon}_{xi} \\ 0 \\ 0 \end{Bmatrix} \tag{4.53}$$

The overall dynamic concrete stress vector, $\{\sigma_{1,2}\}_{dyn}$, is calculated as the sum of the static contribution of the material, $\{\sigma_{1,2}\}$, already calculated in Eq.(4.30) and the damping contribution, $\{\sigma_{1,2}\}_{damp}$, just calculated according to Eq.(4.52):

$$\left\{\sigma_{1,2}\right\}_{dyn} = \left\{\sigma_{1,2}\right\} + \left\{\sigma_{1,2}\right\}_{damp} \tag{4.54}$$

Similarly, the overall dynamic steel stress vector, $\{\sigma_{xi,yi}\}_{dyn}$, is calculated as the sum of the static contribution of the material, $\{\sigma_{xi,yi}\}$, as calculated in Eq(4.31) and the damping contribution, $\{\sigma_{xi,yi}\}_{damp}$, reported in Eq.(4.53):

$$\left\{\sigma_{x_i,y_i}\right\}_{dyn} = \left\{\sigma_{x_i,y_i}\right\} + \left\{\sigma_{x_i,y_i}\right\}_{damp} \tag{4.55}$$

Both the concrete and each steel dynamic stress vector can be transformed from their local coordinate system to the overall global *x*,*y* coordinate system using respectively Eq.(4.56) and Eq.(4.57):

$$\left\{\sigma_{x,y}\right\}_{c,dyn} = \left[T_{\psi}\right]^t \cdot \left\{\sigma_{1,2}\right\}_{dyn} \tag{4.56}$$

$$\left\{\sigma_{x,y}\right\}_{s,i,dyn} = \left[T_{\theta i}\right]^{t} \cdot \left\{\sigma_{x_i,y_i}\right\}_{dyn} \tag{4.57}$$

The total dynamic stress in the *x*,*y*-system is obtained by assuming that concrete and reinforcing bars behave like two springs placed in parallel:

$$\left\{\sigma_{x,y}\right\}_{dyn} = \left\{\sigma_{x,y}\right\}_{c,dyn} + \sum_{i=1}^{n} \rho_i \left\{\sigma_{x,y}\right\}_{s,i,dyn} \tag{4.58}$$

where *n* is the total number of the orders of bars.

In the finite element implicit calculation, using Newton-Raphson's algorithm to solve the balance equations, the tangent stiffness modulus is needed. The tangent stiffness modulus, for the damping contribution can be expressed, on the base of Eq.(4.51), as follow:

$$\frac{d\sigma_{damp}}{d\varepsilon} = \beta \cdot E' \cdot \frac{1}{dt} \tag{4.59}$$

where *dt* denotes the increment of time.

The Jacobian tangent stiffness matrix for static contribution, already reported in Eq.(4.36) for concrete and Eq.(4.37) for steel, contains itself the tangent stiffness modulus. As a consequence of this the Jacobian tangent stiffness matrix related to the damping contribution can be express as in Eq.(4.60) for concrete and in Eq.(4.61) for steel:

$$\left[D_{1,2}\right]_{damp} = \left[D_{1,2}\right] \cdot \left(\beta \cdot \frac{1}{dt}\right) \tag{4.60}$$

$$\left[D_{x_i,y_i}\right]_{damp} = \left[D_{x_i,y_i}\right] \cdot \left(\beta \cdot \frac{1}{dt}\right) \tag{4.61}$$

where $[D_{1,2}]$ and $[D_{xi,yi}]$ represent the static Jacobian matrix for concrete and steel as reported in Eq.(4.36) and Eq.(4.37).

Finally, the overall dynamic Jacobian matrix can be calculated as the sum of static and damping contribution:

$$\left[D_{1,2}\right]_{dyn} = \left[D_{1,2}\right] + \left[D_{1,2}\right]_{damp} = \left[D_{1,2}\right] \cdot \left(1 + \beta \cdot \frac{1}{dt}\right) \tag{4.62}$$

$$\left[D_{x_i,y_i}\right]_{dyn} = \left[D_{x_i,y_i}\right] + \left[D_{x_i,y_i}\right]_{damp} = \left[D_{x_i,y_i}\right] \cdot \left(1 + \beta \cdot \frac{1}{dt}\right) \tag{4.63}$$

4.2.2.3 Validation of the model, simple 1 DOF model

In order to validate the proposed model and to assess its capability to predict the damping effect on a RC member, a comparison between NLFEA and analytical formulation is presented.

A Single Degree of Freedom (SDF) system, represented by the cantilever tower of Figure 4.22-a, was used as a reference system. The cantilever tower is characterized by a section of 100x100 mm and a height of 1000 mm. The system is fixed at the base and it presented a lumped mass at the top equal to 50 Kg. The elastic modulus of the material was set equal to 28000 MPa.

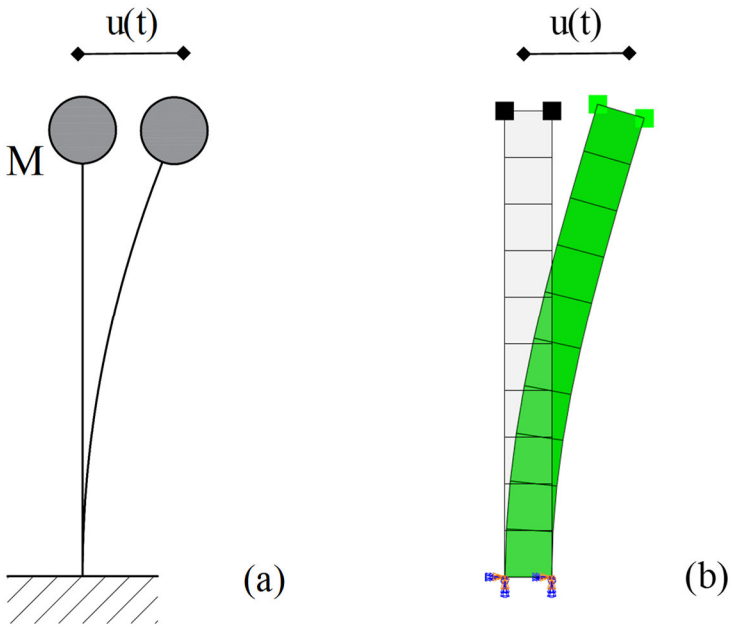

Figure 4.22 – Free vibration oscillator: (a) SDF analytical system and (b) NLFE model.

4.2.2.3.1 Analytical formulation

The cantilever tower of Figure 4.22-a was subjected to an horizontal displacement at the top equal to 0.01 mm, such as to avoid cracking and to keep the material in the elastic field. After the top mass was released, the system was subjected to free vibration based on the dynamic equation of motion reported in Eq.(4.64):

$$K \cdot u + C \cdot \dot{u} + m \cdot \ddot{u} = 0 \tag{4.64}$$

where *K* represents the stiffness of the SDF system, *C* the damping coefficient and *M* the mass applied to the system. *u* is the horizontal displacement as a function of time and an over dot represents a time derivative.

Being *M* the mass applied on the system, equal to 50Kg, the stiffness, *K*, and the damping coefficient, *C*, can be derived as follow:

$$K = \omega^2 \cdot M \tag{4.65}$$

$$C = 2 \cdot \xi \cdot \omega \cdot M$$

where ω represents the natural frequency of the system, expressed by Eq.(4.66), and ξ represents the damping ratio.

$$\omega = 2 \cdot \pi \cdot f \tag{4.66}$$

where *f* is the frequency of the system.

To solve the analytical dynamic equation of motion, the frequency derived from NLFEA, equal to *19.7 Hz*, is used. This assumption permits to compare analytical and NLFEA results, with the same basic hypotheses. It is still important to underline that the frequency deduced from NLFEA is quite similar to the analytically calculated one ($f_{analitycal}$*=18.8 Hz*).

Free vibration for un-damped oscillator

The analytical solution of Eq.(4.64) for un-damped system can be derived by imposing *C* equal to 0 and leads to the following equation:

$$u(t) = C_1 \cdot \cos \omega t + C_2 \cdot \sin \omega t \tag{4.67}$$

where C_1 and C_2 are the constants of integration and can be obtained by imposing the boundary conditions to the system:

$$u_{(t=0)} = u_0 = 0.01\,mm \quad \rightarrow \quad C_1 = u_0 = 0.01\ mm \tag{4.68}$$

$$\dot{u}_{(t=0)} = \dot{u}_0 = 0 \quad \rightarrow \quad C_2 = \frac{\dot{u}_0}{\omega} = 0 \tag{4.69}$$

Finally the equation of motion, for the analysed un-damped case study, can be expressed as in Eq.(4.70). Eq.(4.70) is graphically plotted in Figure 4.23-a.

$$u(t) = u_0 \cdot \cos \omega t \tag{4.70}$$

Free vibration for damped oscillator

By solving the dynamic equation of motion reported in Eq.(4.64), the analytical solution of a damped system subjected to free vibration can be derived as follow:

$$u(t) = e^{-\nu\omega t} \cdot \left(C_1 \cdot \cos \omega_d t + C_2 \cdot \sin \omega_d t\right) \tag{4.71}$$

where ω_d represents the damped frequency and it can be calculated according to Eq.(4.72). C_1 and C_2 are the constants of integration and it can be derived by imposing the boundary conditions to the system as reported in Eq.(4.73) and Eq.(4.74).

$$\omega_d = \omega \cdot \sqrt{1-\xi^2} \tag{4.72}$$

$$u_{(t=0)} = u_0 = 0.01\,mm \quad \rightarrow \quad C_1 = u_0 = 0.01\ mm \tag{4.73}$$

$$\dot{u}_{(t=0)} = \dot{u}_0 = 0 \quad \rightarrow \quad C_2 = \frac{\dot{u}_0 + \upsilon \cdot \omega \cdot u_0}{\omega_d} \tag{4.74}$$

Finally the equation of motion, for the analysed damped case study, can be expressed as in Eq.(4.75). Eq.(4.75) is graphically plotted in Figure 4.23-b.

$$u(t) = e^{-\nu\omega t} \cdot \left(u_0 \cdot \cos \omega_d t + \frac{\upsilon \cdot \omega \cdot u_0}{\omega_d} \cdot \sin \omega_d t \right) \tag{4.75}$$

In can be observed that for an un-damped system (ξ=0), the Eq.(4.75) is reduced to Eq.(4.70).

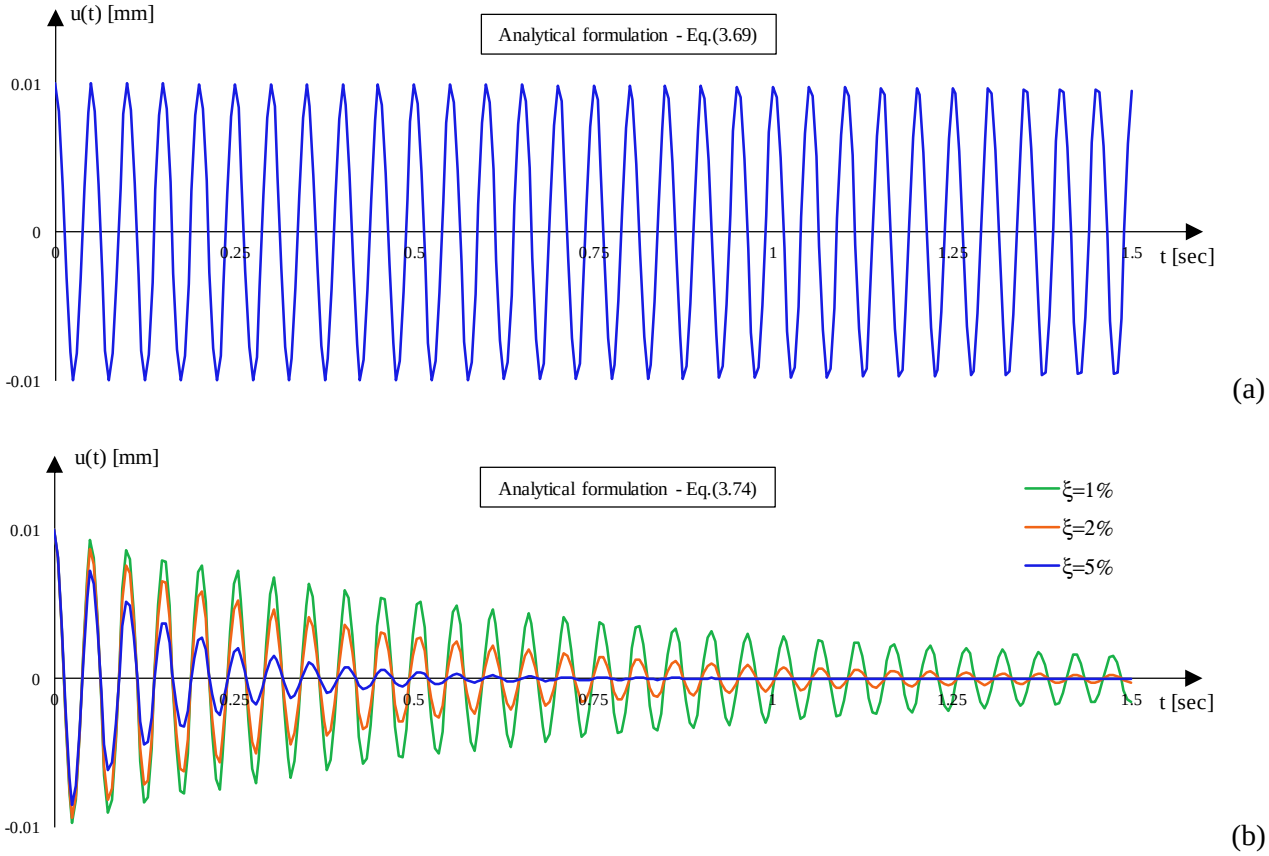

Figure 4.23 – Free vibration oscillator analytical response: (a) un-damped system (b) damped system.

4.2.2.3.1 Nonlinear finite element analysis

NLFEA was carried out in order to assess the proposed damping model in the PARC_CL2.0 crack model. The same cantilever tower, representing a SDF system, reported in Figure 4.22-a was modelled by means of NLFEA as shown in Figure 4.22-b.

The height of the tower was subdivided into 10 shell elements with 4 nodes and 4 Gauss integration points (defined S4 in ABAQUS code [Abaqus 6.12, 2012]), so each element presents a 100x100 mm size in plane. The thickness of each element was set equal to 100 mm in order to achieve the same cross section as the reference analytical specimen. The two nodes at the base of the tower were fixed and at the top of the tower two mass elements of 25 Kg were added.

In order to highlight the frequency of the numerical system, a frequency analysis was carried out before running the dynamic analysis. The frequency analysis highlight that the first vibration mode, able to excite the

99.4% of the mass, presents a frequency, *f=19.7 Hz*, so that the corresponding natural frequency was equal to *ω=123.8 Hz*.

This frequency was used to calculate the stiffness-proportional damping coefficient, introduced in the PARC_CL 2.0 crack model, according to the formulation proposed in Eq.(4.46).

Due to the fact that the analysed system presents a single degree of freedom, it was necessary only a single frequency to calibrate the damping coefficient. In order to validate the stiffness-proportional damping introduced in the PARC_CL 2.0 crack model, only the stiffness-proportional damping coefficient was calculated.

The NLFE model was firstly subjected to an horizontal displacement at the top of the specimen equal to 0.01 mm. In a second phase the system was released to experience free vibration in dynamic field.

The time step was set equal to 0.0005 sec and the numerical solution is obtained by means of the Newmark's implicit method considering average acceleration.

In Figure 4.24 are presented the comparison between NLFEA and analytical formulation for different values of damping ratio.

The results reported in Figure 4.24 show that the stiffness-proportional damping introduced in the PARC_CL 2.0 crack model allows to reproduce well the dissipation of energy due to damping in a linear elastic system.

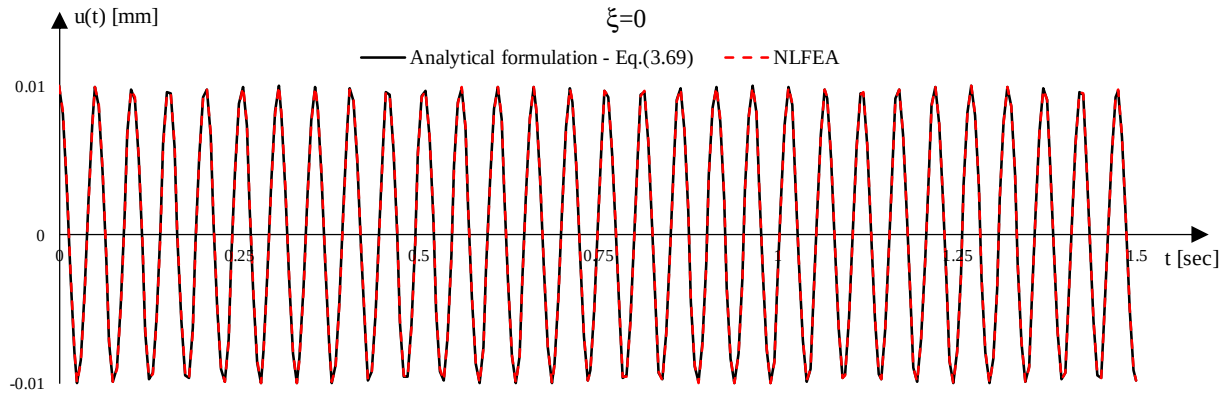

(a)

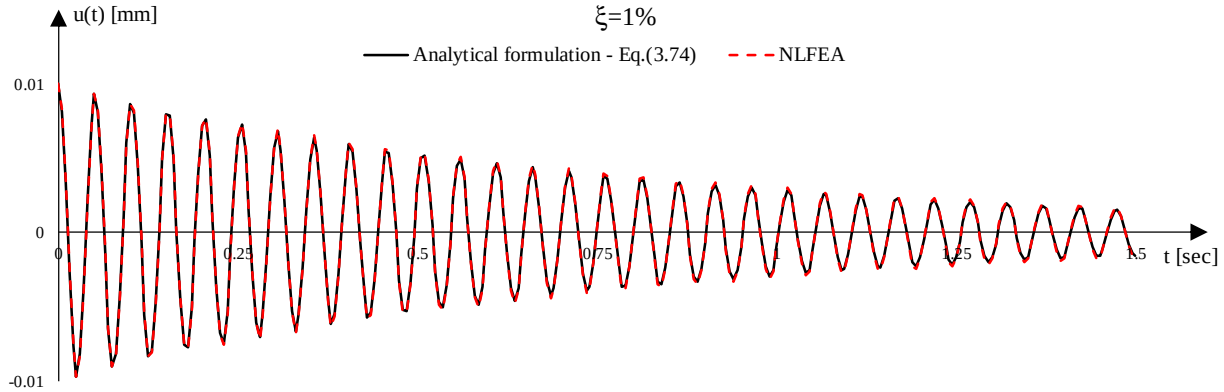

(b)

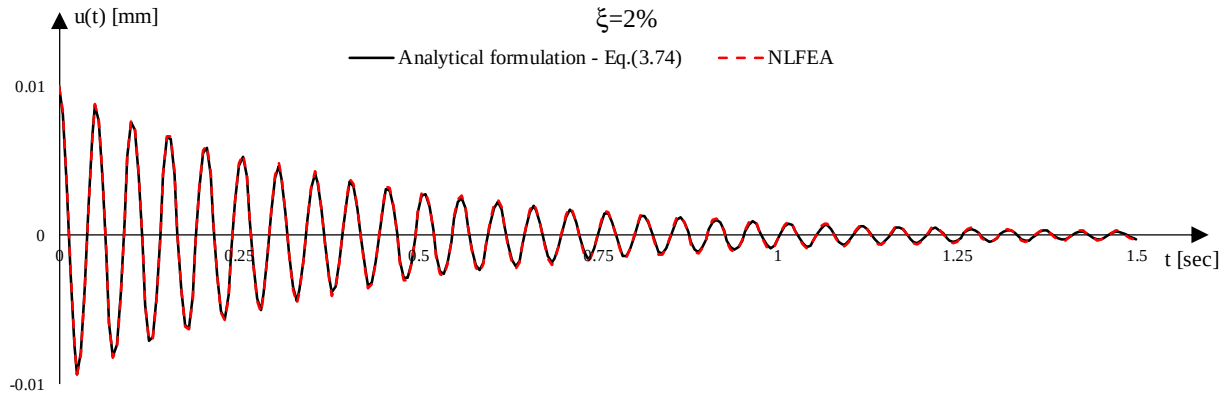

(c)

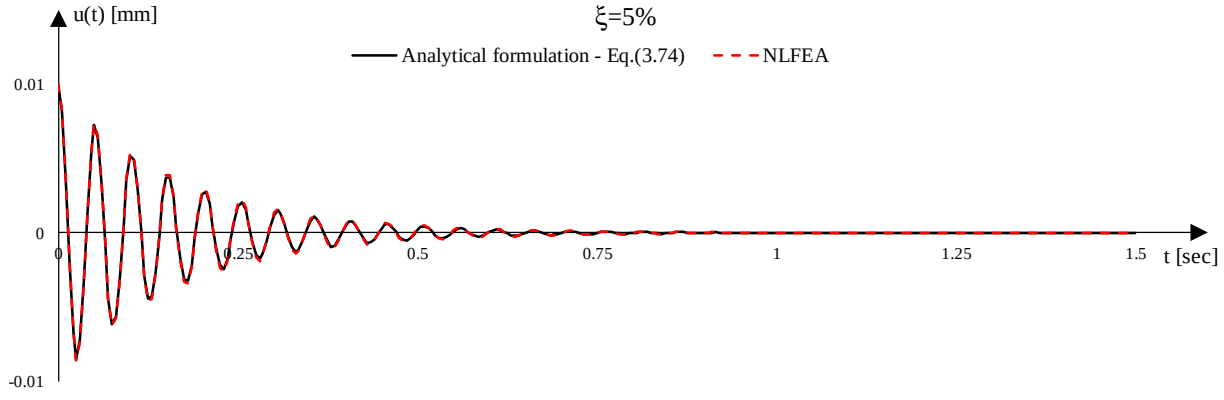

(d)

Figure 4.24 – Free vibration, comparison between NLFEA and analytical formulation for different values of damping ratio: (a) un-damped system, (b) ξ=1%, (c) ξ=2% and (d) ξ=5%.

4.3 Simulation of monotonic, cyclic and dynamic in-plane behaviour

As just discussed at the beginning of this chapter, in the following the same squat walls, analysed by means of PARC_CL 1.0 crack model in §3.4.1 and object of the CASH benchmark project [Le Corvec et al., 2015], are investigated using the implemented PARC_CL 2.0 crack model, in order to highlight the differences between the two models especially related to the cyclic behaviour.

4.3.1 RC squat walls (CASH benchmark)

For the purpose of this chapter, nonlinear finite element pushover and static cyclic analyses have been carried out and the obtained results are compared not only with experimental outcomes and analytical formulation but also with the results obtained using PARC_CL 1.0, presented in §3.4.1. Moreover, in this chapter the analysis is extended to the dynamic time history analysis in order to assess the capability of PARC_CL 2.0 crack model to predict the dynamic behaviour of a RC member as well as the static cyclic behaviour.

The experimental campaign, object of the analyses of this section, is widely investigated and discussed in §3.4.1.2 and hence is not reported herein.

4.3.1.1 Nonlinear finite element modelling and results (using mesh regularization technique)

NLFEA have been carried out with ABAQUS code adopting the PARC_CL 2.0 crack model. As shown in Table 3.14, T6 and T7 specimens differ only on the numerical mass applied in the Pseudo-Dynamic test (the differences in the concrete properties are considered negligible). For the purpose of this chapter three different kinds of analyses are carried out: pushover, static cyclic and dynamic analysis.

The pushover analyses are limited to T6 and T8 specimens; in particular, for each specimen three different mesh configurations are analysed, characterized by an average element size of 200 mm (coarse mesh), 100 mm (medium mesh) and 50 mm (fine mesh). The aim of this analyses was to investigate the capability of the proposed method (in §4.2.1.1 the fracture energy for reinforced concrete is presented as a function of both element length and average crack spacing) to minimize the mesh dependency effect.

The same specimens are analysed also for static cyclic loading in order to compare the obtained results with the ones obtained using PARC_CL 1.0 crack model presented in §3.4.1.3.

Finally, the dynamic analyses are limited to T6 and T7 specimens, in order to highlight the influence of the numerical applied mass which strongly changes the frequency of the specimen.

All the specimens are modelled using 4 nodes multi-layered shell elements. The Gauss integration scheme is adopted with 4 Gauss integration points (S4); along the thickness each element is divided in 2 layers with 3 Simpson section integration points. Reinforcement is modelled using a smeared approach according to the PARC_CL 2.0 crack model prescriptions. In Figure 4.25 is reported a solid view of the meshes adopted for NLFEA.

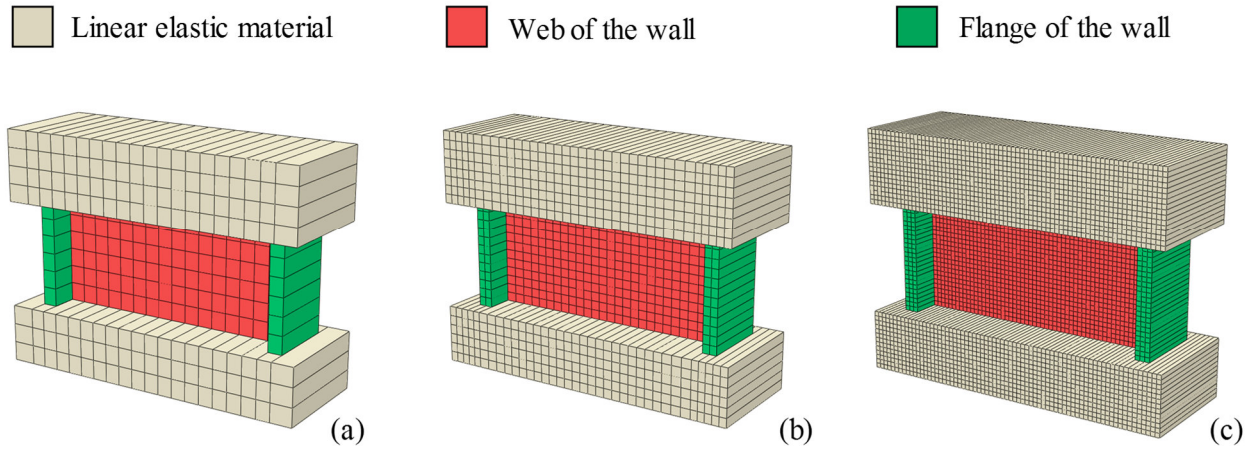

Figure 4.25 – Solid view of the adopted meshes: (a) coarse mesh, (b) medium mesh and (c) fine mesh.

The top and the bottom beams have been modelled using linear elastic material, while the web and the two flanges of the wall have been modelled using PARC_CL 2.0 crack model. Furthermore, due to the confining effect of stirrups, the flanges are modelled considering a confined concrete, calculated according to

the formulation proposed by [Mander et al., 1988], which leads to an increasing of both the compressive strength and the ultimate compressive strain.

The analyses have been carried out using the mean values of the material properties as reported in Table 4.2. In Table 4.2 the average crack spacing, a_m, is calculated on the basis of the length over which the slip between concrete and steel occurs, $l_{s,max}$, calculated as suggested in [*fib*-Model Code 2010]

The fracture energy in tension of plain concrete (G_F) is evaluated according to the formulation proposed in [*fib*-Model Code 1990]. Moreover, according to the formulation presented in §4.2.1.1, considering the presence of steel reinforcement, the fracture energy in tension is changed according to the following equation:

$$G_F^{RC} = G_F\left(1+\frac{h}{a_m}\right) \tag{4.76}$$

being h the equivalent element length, fixed equal to the square root of the average element area according to [Hendriks et al., 2012], and a_m the average crack spacing calculated on the base of the length over which the sleep between concrete and steel occurs, $l_{s,max}$, as define in [*fib*-Model Code 2010].

The fracture energy in compression (G_C) is set equal to 250 times the fracture energy in tension, according to Nakamura and Higai [Nakamura and Higai, 2001], for the unconfined concrete, while for the confined concrete the fracture energy in compression is derived in order to obtain the ultimate compressive strain in accordance to [Mander et al., 1988].

Table 4.2 – Mean mechanical properties used in NLFE model.

		Concrete (see §4.2.1.1)														Steel (see §4.2.1.2)		
								un-confined				confined						
Spec.	Mesh	h	a_m	Ec	f_t	$G^{RC}{}_F$	$\varepsilon_{t,u}$	f_c	G_C	$\varepsilon_{c,cr}$	$\varepsilon_{c,u}$	f_c	G_C	$\varepsilon_{c,cr}$	$\varepsilon_{c,u}$	E_s	$f_{y,vert}$	$f_{y,hor}$
		[mm]	[mm]	[Gpa]	[MPa]	[N/mm^3]	[-]	[MPa]	[N/mm^3]	[-]	[-]	[MPa]	[N/mm^3]	[-]	[-]	[GPa]	[MPa]	[MPa]
T6	Coarse	200	245	22.3	3.1	0.155	0.002	33.1	38.8	0.002	0.011	38.9	88.1	0.003	0.019	200	594	572
	Medim	100	245	22.3	3.1	0.120	0.003	33.1	30.0	0.002	0.016	38.9	56.6	0.003	0.025	200	594	572
	Fine	50	245	22.3	3.1	0.103	0.005	33.1	25.8	0.002	0.025	38.9	40.9	0.003	0.034	200	594	572
T7	Fine	50	245	23.0	3.3	0.103	0.005	36.4	25.8	0.002	0.023	39	38.3	0.003	0.032	200	594	572
T8	Coarse	200	288	21.3	2.8	0.131	0.002	28.6	32.8	0.002	0.011	34	74.4	0.003	0.019	200	594	594
	Medim	100	288	21.3	2.8	0.104	0.003	28.6	26.0	0.002	0.016	34	48.4	0.003	0.024	200	594	594
	Fine	50	288	21.3	2.8	0.091	0.005	28.6	22.8	0.002	0.026	34	35.4	0.003	0.035	200	594	594

The boundary and loading conditions applied for static pushover and static cyclic analyses are not reported in this section because they are widely explained in §3.4.1.2. The boundary and loading conditions applied for dynamic time history analysis are presented in Figure 4.26.

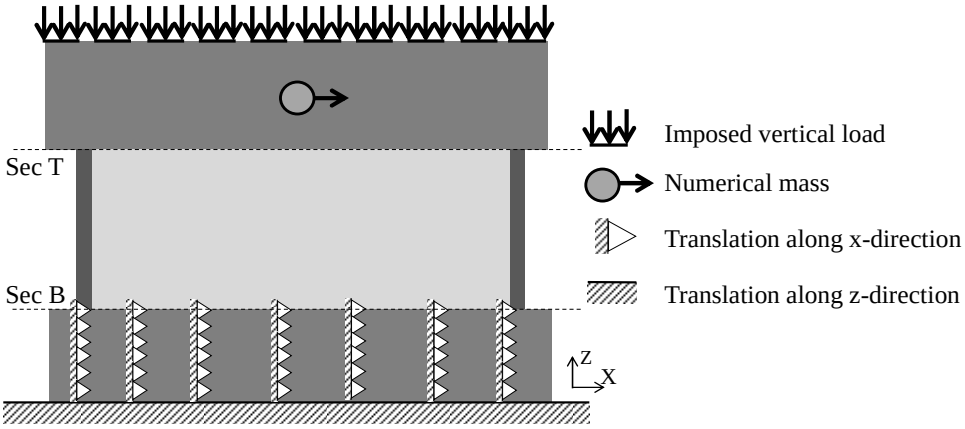

Figure 4.26 – Boundary and loading conditions for dynamic analyses.

The boundary conditions were the same for pushover and cyclic analyses while load is applied in different manner. An additional numerical mass, acting only along *x*-direction, defined as M_2 in Table 3.14, is added in the centroid of the top beam to simulate the numerical mass of the experimental tests.

As for static analyses the load is applied in two different steps: in a first step the self-weight and the vertical pressure is applied; in a second step the horizontal acceleration is imposed and the rotation of the top beam is prevented by applying a multi-point constraint, which imposes the same vertical displacements of the central node of "Sec T" to all the other nodes of "Sec T", Figure 4.26.

In dynamic analyses the structural damping was introduced according to Rayleigh's classical theory defined in Eq.(4.77):

$$\xi_n = \frac{\alpha}{2}\frac{1}{\omega_n} + \frac{\beta}{2}\omega_n \tag{4.77}$$

The mass proportional term (α) is introduced as an input value in the ABAQUS code [Abaqus 6.12, 2012], while the stiffness proportional term (β) was incorporated in the PARC_CL 2.0 crack model as explained in §4.2.2.2.

The α and β coefficients are calibrated in order to obtain a damping ratio of 2% for the frequencies of 0.5Hz and 35 Hz, according to the suggestion of the CASH benchmark organizer.

4.3.1.1.1 Pushover analysis

In Figure 4.27 is presented the comparison between the experimental results and the static pushover analysis, in terms of shear force vs top displacement, for T6 specimen. As just stated, in order to highlight the effect of the mesh dependency three different meshes are analysed: a coarse mesh with an average element size of 200 mm, a medium mesh with an average element size of 100 mm and a fine mesh with an average element size of 50 mm.

In Figure 4.27 the analyses are stopped when the failure occurred, due to crushing of concrete. Crushing of concrete is achieved when the compressive strain of concrete reaches the ultimate value, $\varepsilon_{c,u}$, Figure 4.28. The values of $\varepsilon_{c,u}$, for the different meshes analysed, are reported in Table 4.2.

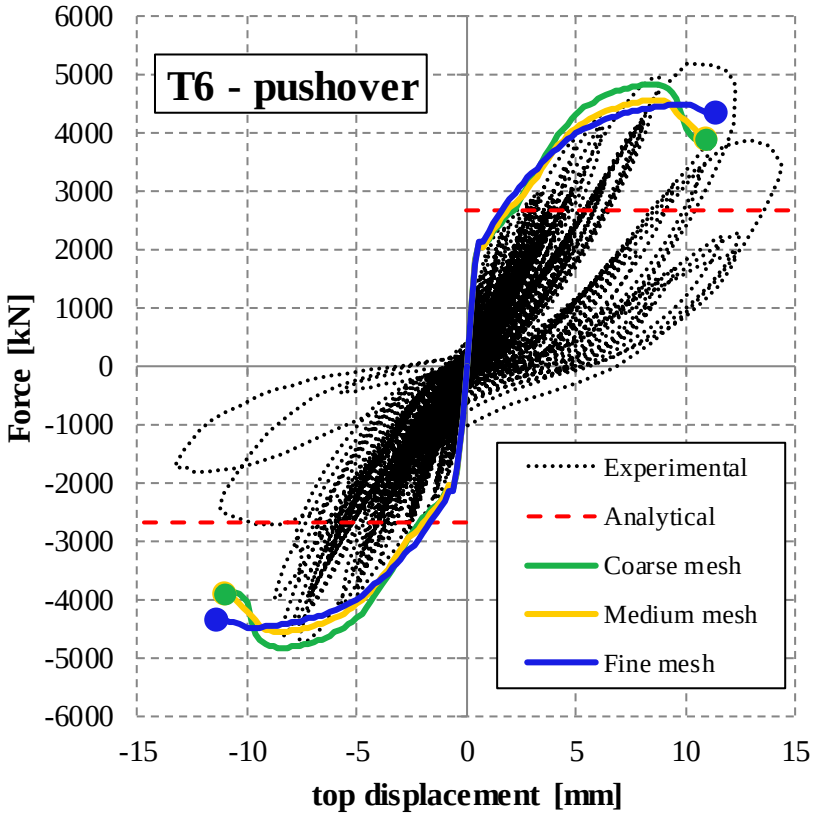

Figure 4.27 – Static pushover analysis, T6 wall: effect of using meshes with different average element size.

The results reported in Figure 4.27 showed that the results obtained analysing the same specimen with different meshes are quite similar; so, it can be assess that the idea to modify the fracture energy of concrete as a function of the element length and crack spacing can avoid the mesh dependency effects.

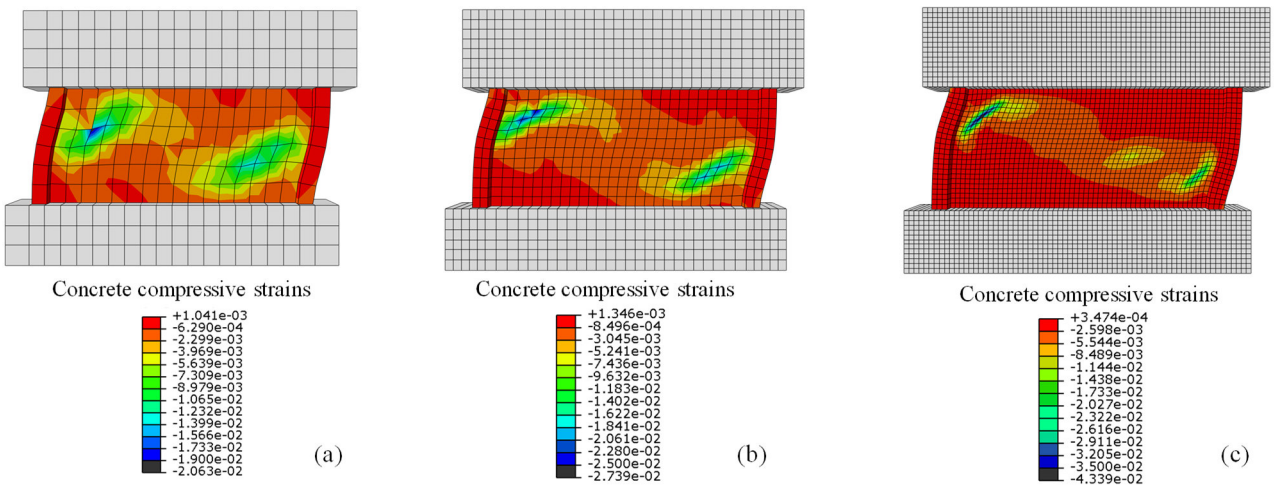

Figure 4.28 – Static pushover analysis of T6 wall, crushing of concrete for the different analysed meshes using PARC_CL 2.0 crack model: (a) coarse mesh, (b) medium mesh and (c) fine mesh.

Similar results can be obtained analysing the T8 specimen, as reported in Figure 4.29 where the comparison between experimental and NLFEA results are presented in term of Load-Displacement curve. As for the previous specimen the failure mode, characterized by crushing of compressive concrete is also highlighted in Figure 4.29. The strain in concrete in the failure condition for the different analysed meshes are reported in Figure 4.30; while in Table 4.2 are reported the values of the ultimate strain of compressive concrete, $\varepsilon_{c,u}$, which change for the different meshes.

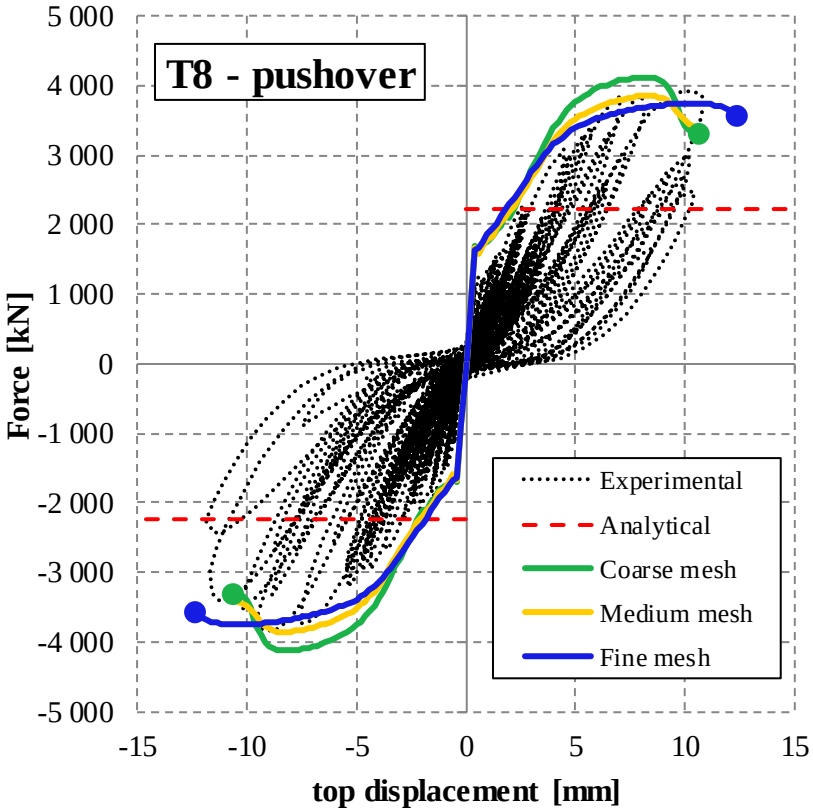

Figure 4.29 – Static pushover analysis, T8 wall: effect of using meshes with different average element size.

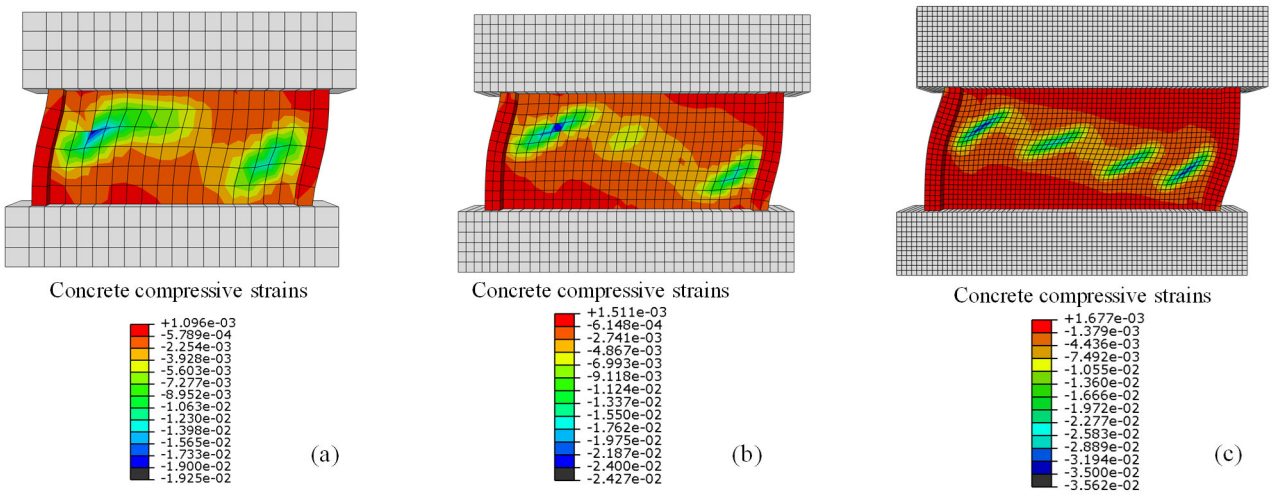

Figure 4.30 – Static pushover analysis of T8 wall, crushing of concrete for the different analysed meshes using PARC_CL 2.0 crack model: (a) coarse mesh, (b) medium mesh and (c) fine mesh.

The results reported in Figure 4.27 and Figure 4.29 highlighted that using different meshes it is possible to obtain similar results both in term of shear strength and failure mode. For the following cyclic and dynamic analyses, in order to have more consistent comparison with the PARC_CL 1.0 crack model, the same dimension of the element is adopted. So, the fine mesh, characterized by an average element size of 50 mm is chosen.

4.3.1.1.2 Cyclic analysis

As stated in the introduction of this chapter one of the main purpose of this section is to assess the capability of PARC_CL 2.0 crack model to predict the cyclic behaviour of RC structural members and in particular to underline the improvements made with respect to PARC_CL 1.0 crack model.

To do this in the following T6 and T8 specimen, just analysed using PARC_CL 1.0 crack model in §3.4.1.1.3, are analysed by means of PAC_CL 2.0.

In Figure 4.31 are presented the results of the static cyclic analysis obtained for T6 specimen with NLFEA using the PARC_CL 2.0 crack model together with the experimental outcomes and the results obtained using NLFEA associated with PARC_CL 1.0 crack model.

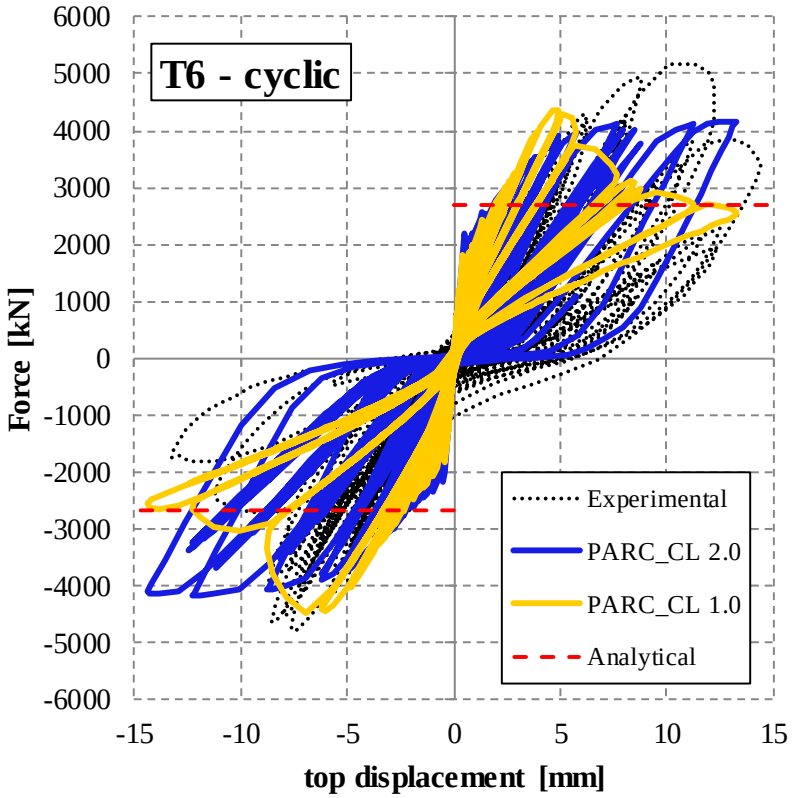

Figure 4.31 - Static cyclic analysis of T6 wall: comparison of experimental results with NLFEA using PARC_CL 2.0 and PARC_CL 1.0 crack models.

Figure 4.31 clearly shows the improvement in the prediction of the cyclic behaviour of a RC squat wall made by the PARC_CL 2.0 crack model with respect to the previous PARC_CL 1.0 crack model. As just

underlined in §3.4.1.3, from Figure 4.31 it can be highlight that the results obtained by means of NLFEA presented, as expected, a symmetric shape with respect to the origin, due to the fact that the specimen is perfectly symmetric in geometric and loading condition. On the other hand, the experimental results on the positive displacement side presents an higher strength value.

Another important difference, remarked in Figure 4.31, is the different envelope curve obtained in the post-peak behaviour of the NLFE curve. This difference can be explained with the different formulation adopted for the concrete fracture energy in tension, widely explained in §3.2.1 for PARC_CL 1.0 and in §4.2.1.1 for PARC_CL 2.0. In this context, it has to be remarked that the imposed cyclic displacement, derived by the measured displacement in the experimental PSD test, did not yield the specimen to failure. However, analysing the results of the pushover analysis, presented above, and of the dynamic analysis, presented in the following, it can be expected that a small increasing of the imposed displacement could bring the specimen up to crushing failure.

The comparison between PARC_CL 2.0 and PARC_CL 1.0 crack model is extended to the evaluation of the stability of the analysis. In Figure 4.32 is plotted the curve related to the number of iteration needed to obtain the convergence at each time increment. The red dotted line in Figure 4.32 represents the maximum number of iteration allowed for each time increment. The solution of a time increment is accepted after the maximum number of iteration allowed has been completed, even if the equilibrium tolerances are not satisfied.

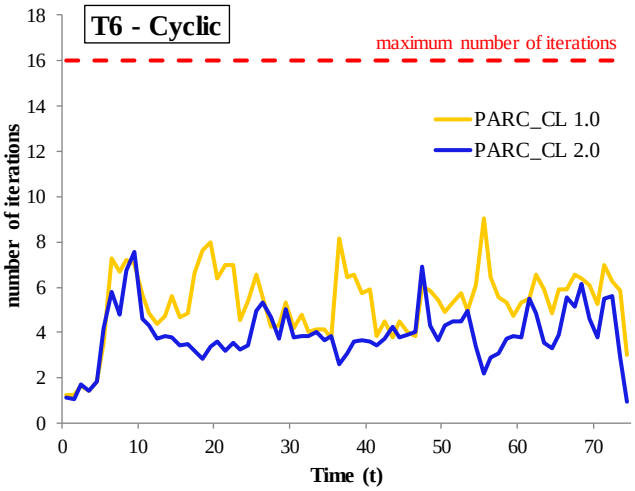

Figure 4.32 - Static cyclic analysis of T6 wall: number of iteration used to obtain the convergence of the implicit solution method for PARC_CL 2.0 and PARC_CL 1.0 crack models.

The results plotted in Figure 4.32 showed that the improvements made by the PARC_CL 2.0 crack model were not only in term of the prediction of the force vs displacement cyclic behaviour but also in term of stability of the analysis. This result is considered quite important because it influences not only the stability of the analysis but also the computational time.

Similar results can be obtained analysing T8 specimen as reported in Figure 4.33.

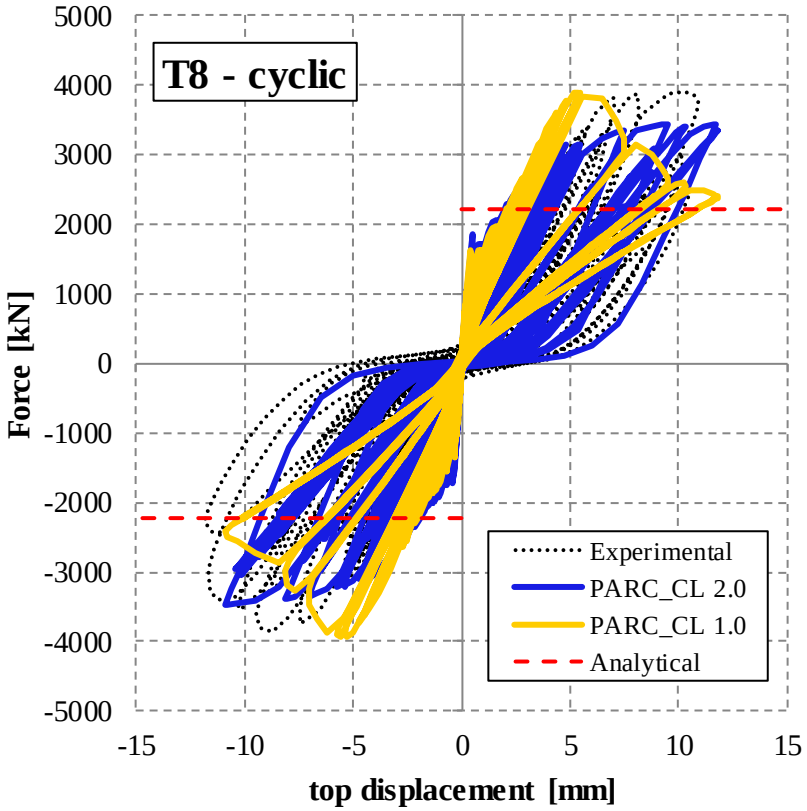

Figure 4.33 - Static cyclic analysis of T8 wall: comparison of experimental results with NLFEA using PARC_CL 2.0 and PARC_CL 1.0 crack models.

Also in this case the comparison between the numerical results obtained using PARC_CL 2.0 crack model are able to reproduce the experimental outcomes, especially in relation with the unloading behaviour, better that the PARC_CL 1.0 crack model. As for T6 specimen, also in this case the NLFEA carried out with PARC_CL 2.0 crack model did not reach the failure for the imposed cyclic displacement time history.

As showed for the T6 specimen also for the T8 specimen the PARC_CL 2.0 highlight good results in term of convergence of the analysis, as plotted in Figure 4.34.

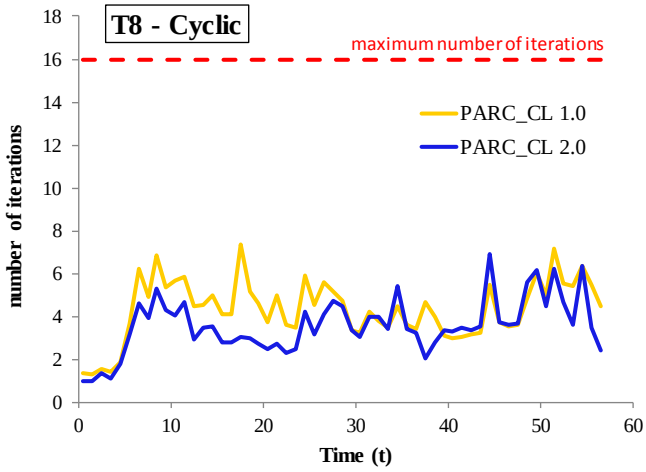

Figure 4.34 - Static cyclic analysis of T8 wall: number of iteration used to obtain the convergence of the implicit solution method for PARC_CL 2.0 and PARC_CL 1.0 crack models.

4.3.1.1.3 Dynamic analysis

In this section dynamic time history analyses of T6 and T7 specimens are carried out; these two specimens, neglecting the little differences in the concrete mechanical properties, differ only in the numerical mass applied in the Pseudo-Dynamic experimental test, as shown in Table 3.14. This difference can strongly influence the frequency of the system; for this reason, before running the full dynamic time history analyses, the frequency analyses have been carried out in order to calculate the natural frequency of each specimen and to compare it with the experimental results, Table 4.3.

Table 4.3 – Natural frequency and elastic stiffness: comparison between LFEA and experimental.

	NLFEA			Experimental		
	M [ton]	f_{NLFEA} [Hz]	K_{NLFEA} [MN/m]	f_{exp} [Hz]	K_{exp} [MN/m]	$\frac{K_{NLFEA}}{K_{exp}}$
T6	1252	9.6	4551	10.4	5341	0.85
T7	11272	3.4	5139	3.6	5761	0.89
				Average		0.87

From Table 4.3 it could be seen how the elastic stiffness derived from the natural frequency obtained by means of LFEA, K_{NLFEA}, is close to the experimental results. Indeed, the average value of the ratio between the elastic stiffness derived from LFEA and the experimental value is equal to 0.87.

Finally, in Figure 4.35 the results obtained with dynamic time history analyses are plotted and compared with the results of the experimental Pseudo-Dynamic tests.

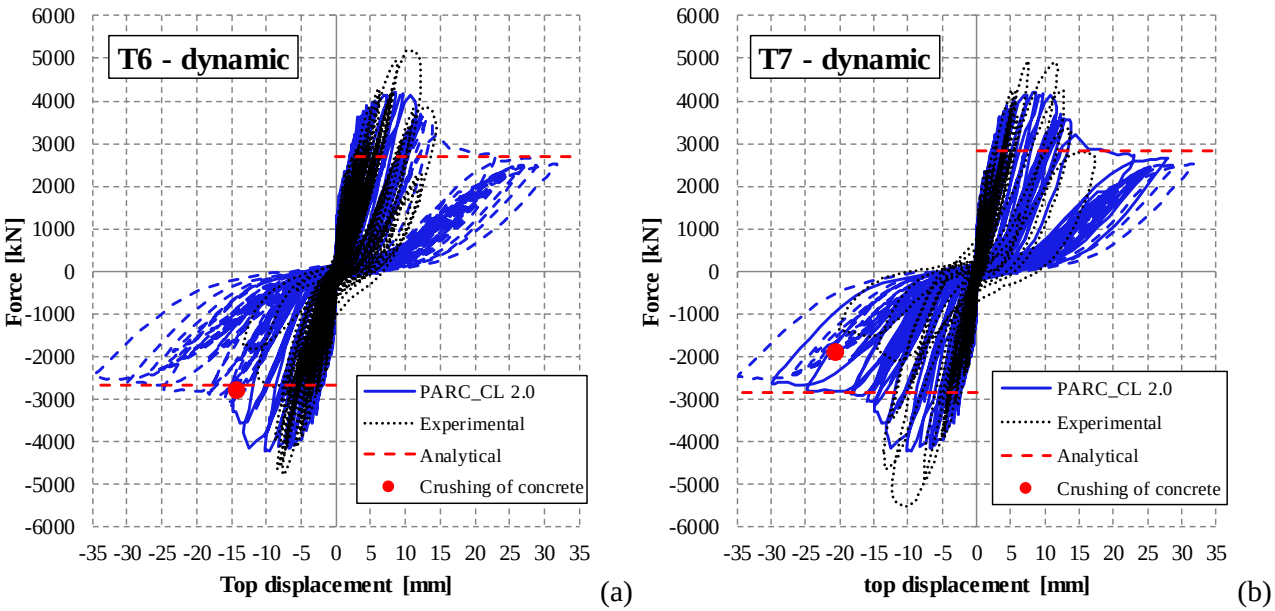

Figure 4.35 – Dynamic time histories analyses: comparison between experimental outcomes and NLFEA with PARC_CL 2.0 crack model for (a) T6 specimen and (b) T7 specimen.

In Figure 4.35 is also marked the point corresponding to the crushing of concrete, and so to the failure of the specimen; after the crushing of concrete is reached the NLFEA curve is presented with a dotted line. The crushing of concrete in NLFEA is considered as the point in which concrete reaches the ultimate strain, $\varepsilon_{c,u}$, reported in Table 4.2 (remember that for dynamic analysis the fine mesh is used).

Comparing Figure 4.35-a with Figure 4.35-b it appears that for T6 specimen the crushing of concrete occurs before than for the T7 specimen. Indeed, for T6 specimen the crushing of concrete occurs after 33.2 seconds out of the 74.4 seconds of the analysis, while for T7 specimen the crushing of concrete occurs after 64.5 seconds out of the 74.4 seconds of the analysis.

This difference can be related to the Rayleigh damping associated to the specimens. As stated in the introduction of this section (in the beginning of §4.3.1.1 where the NLFE model is described) the α and β Rayleigh's damping coefficients, according to the CASH benchmark organizer (that is the organizer of the project within which these analyses are carried out [Le Corvec et al., 2015]), are calibrated in order to obtain a damping ratio of 2% for the frequencies of 0.5Hz and 35 Hz, as shown in Figure 4.36. In the same graph is also reported the frequency of each specimen in the un-damaged phase (before to run the time history analysis) and in the damaged phase (at the end of the last run of the time history analysis), desumed by the experimental tests as reported in [Pegon et al., 1998[a]] and [Pegon et al., 1998[b]].

From Figure 4.36 it can be highlight that, especially considering the damaged frequencies of the two specimens, the adopted Rayleigh damping formulation leads to an higher damping ratio for the T7 specimen ($\xi_{damaged} \cong 2\%$) with respect to the T6 specimen ($\xi_{damaged} \cong 0.6\%$). This difference can lead to a premature failure of T6 specimen due to the fact that lower damping ratio is associated to higher forces on the specimen.

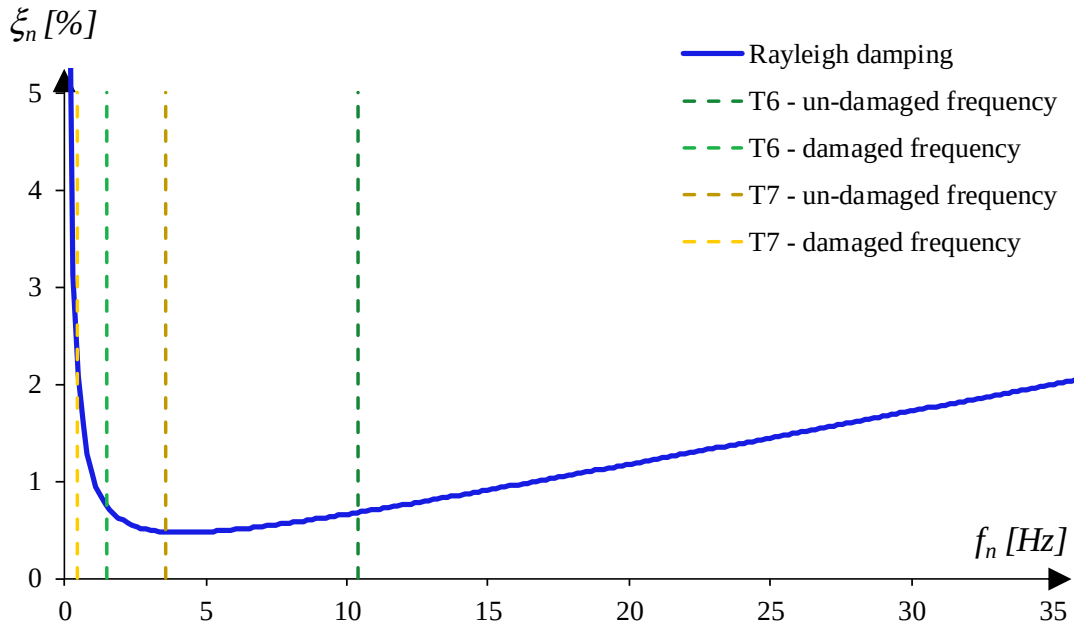

Figure 4.36 – Calibration of Rayleigh damping for T6 and T7 specimens.

In order to highlight the capability of the PARC_CL 2.0 crack model to predict the hysteretic behaviour of the specimens, neglecting the phenomenon explained above, in Figure 4.37 is reported the comparison

between NLFEA and experimental results, in which the NLFE curves are stopped when the crushing of concrete is reached.

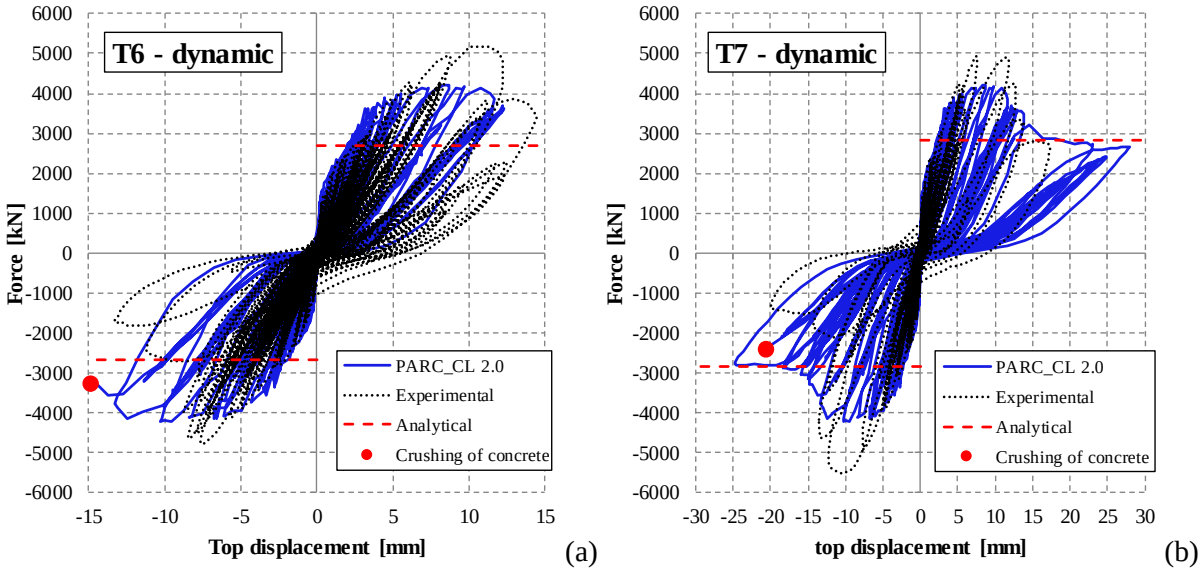

Figure 4.37 – Dynamic time histories analyses stopped after the crushing of concrete: comparison between experimental outcomes and NLFEA with PARC_CL 2.0 crack model for (a) T6 specimen and (b) T7 specimen.

From Figure 4.37 it can be remarked that the PARC_CL 2.0 crack model are able to reproduce the hysteretic behaviour of reinforced concrete squat walls subjected to dynamic loading.

4.3.2 Synopsis

In this section the monotonic, cyclic and dynamic behaviour of RC squat walls was investigated by means of NLFEA carried out using multi-layer shell elements and the implemented PARC_CL 2.0 crack model. The main conclusions can be remarked as follow:

- The definition of a fracture energy for reinforced concrete, G_F^{RC}, allows to avoid the mesh dependency effect; indeed, the pushover analyses carried out using three different meshing (coarse mesh, medium mesh and fine mesh) leads to comparable results;
- The PARC_CL 2.0 crack model seems to well reproduce the cyclic behaviour of a RC squat walls, in particular it was highlighted that a proper definition of the hysteretic behaviour of concrete and steel leads to better results than the ones obtained analysing the same specimens with the PARC_CL 1.0 crack model, which presents a behaviour secant to the origin in the unloading phase;
- The implementation, within the PARC_CL 2.0 crack model, of the stiffness proportional Rayleigh damping allows to run dynamic time history analyses. The results obtained using NLFEA underline the importance of a proper calibration of the Rayleigh's damping

coefficients. Nevertheless, dynamic analyses carried out using NLFEA and PARC_CL 2.0 are shown able to predict the cyclic behaviour of such kind of structural member.

4.4 Simulation of out-of-plane instability

Structural RC walls are one of the common lateral load resisting elements in buildings in seismic regions. They are commonly used both in civil and industrial buildings and in power plant buildings. As a matter of fact the walls, thanks to their dimensions and their in-plane disposition, give a high stiffness and a high resistance to the building, reducing the interstorey drift values at damage limit state and providing enough strength and ductility at collapse. Moreover, squat walls, characterized by a ratio of height to length less than or equal to two like the specimens analysed in the previous section, are widely used as main lateral force resisting structures in precast concrete blocks buildings and in power plant facilities. In fact, in nuclear facilities walls are supposed to be designed with few openings in order to prevent radiation leaks [Whyte and Stojadinovic, 2013]. On the other hand, slender structural RC walls, that can come in a variety of geometrical shapes, are commonly used in medium and high rise buildings as lateral force resisting systems, thanks to their capacity to provide strength and stiffness towards seismic actions and allowing a good displacement control [Riva et al., 2003]. In particular, in this section this latter case is analysed.

The studies presented in this section were triggered by the observation of the damage occurred in structural walls in recent earthquake in Chile (2010, M_w=8.8) and New Zealand (2011, M_w=7.2). These recent seismic events highlighted that many structural walls, in their failed configuration, where characterized by large out of plane displacement, as shown in Figure 4.38 and reported in [Wallace, 2012]. This underperformance of the ductile response of walls was highly influenced by the out-of-plane buckling (also defined as out-of-plane instability), which is triggered in the end region of the wall.

These seeming faults in the design of structural walls are emphasized also by analysing international code provisions. Indeed, the majority of standards, such as Eurocode 8 [CEN, 2004] and ACI Code [ACI Committee, 2011] treats the out-of-plane instability in a simplified way by imposing limits on the height to thickness ratio of the wall. Only the New Zealand code [NZS, 2006] includes more sophisticated models based on the studies presented in [Paulay and Priestley, 1993] and [Goodsir, 1985].

Prior to the Chile and New Zealand earthquakes this failure mechanism had only been observed in laboratory tests [Oesterle, 1979], [Vallenas et al., 1979] and [Thomsen IV & Wallace, 2004]. In the recent years the research on this topic has been continued by joining experimental test campaigns with advanced nonlinear finite element analysis (NLFEA).

On the experimental field the knowledge on this topic was surely developed due to the experimental campaigns carried out at EPFL in Lausanne, Switzerland. In particular, two different campaigns are carried out considering RC walls of different shape subjected both to uni-directional and bi-directional cyclic

horizontal loading; a “T-shaped” wall was tested in [Rosso et al., 2016] while a “U-shaped” wall was tested in [Constantin and Beyer, 2016].

Figure 4.38 – Out-of-plane buckling of walls after 2010 Chile earthquake [Wallace, 2012].

As just stated the research on this topic was extended to NLFEA. NLFEA are a widely validated numerical tool to simulate both the monotonic and cyclic behaviour of RC walls, as underlined for example in §4.3 or in [Belletti et al., 2013[b]]. Recently, this numerical tool was also used to simulate the out-of-plane instability of RC walls. In particular [Belletti et al., 2016], [Dashti et al., 2014] and [Dashti et al., 2015] studied by means of NLFEA the behaviour of RC walls subjected to horizontal cyclic loading, using the commercial solver code DIANA [Manie, 2015].

In this section, the implemented PARC_CL 2.0 crack model was used to simulate the cyclic behaviour of the experimental tests carried out at the EPFL in Lausanne. In particular, the two “T-shaped” walls tested in [Rosso et al., 2016], TW1 and TW4 subjected respectively to uni-directional and bi-directional loading, was analysed by means of NLFEA in §4.4.1. Moreover, the “U-shaped” RC wall investigated experimentally in [Constantin and Beyer, 2016] was studied using NLFEA in §4.4.2.

4.4.1 “T-shaped” slender RC walls

In this section two different “T-shaped” RC walls were analysed by means of NLFEA and the obtained results are compared with the results of an experimental campaign carried out at EPFL in Lausanne, Switzerland [Rosso et al., 2016].

4.4.1.1 Experimental campaign

The two walls, TW1 and TW4, were geometrically identical and represent a 2:3 scale model of a full dimension prototype wall. The walls were 2000 mm tall, 80 mm thick and 2700 mm long. At the north end (see Figure 4.39) the walls presented a flange 80 mm thick and 440 mm long. The foundation was 3600 mm

long, 700 mm thick and 400 mm tall, while the top RC beam was 3160 mm long, 440 mm thick and 420 mm tall, Figure 4.39.

In Figure 4.39 are also presented the reinforcement details, which are the same for the two specimens and follow the current design practices for residential buildings in Colombia. According to these detailing practices the reinforcement consisted of a single layer of grid reinforcement, characterized by a slight eccentricity with respect to the centreline of the section. The detail of the eccentricity of the rebar layer is shown in Figure 4.40.

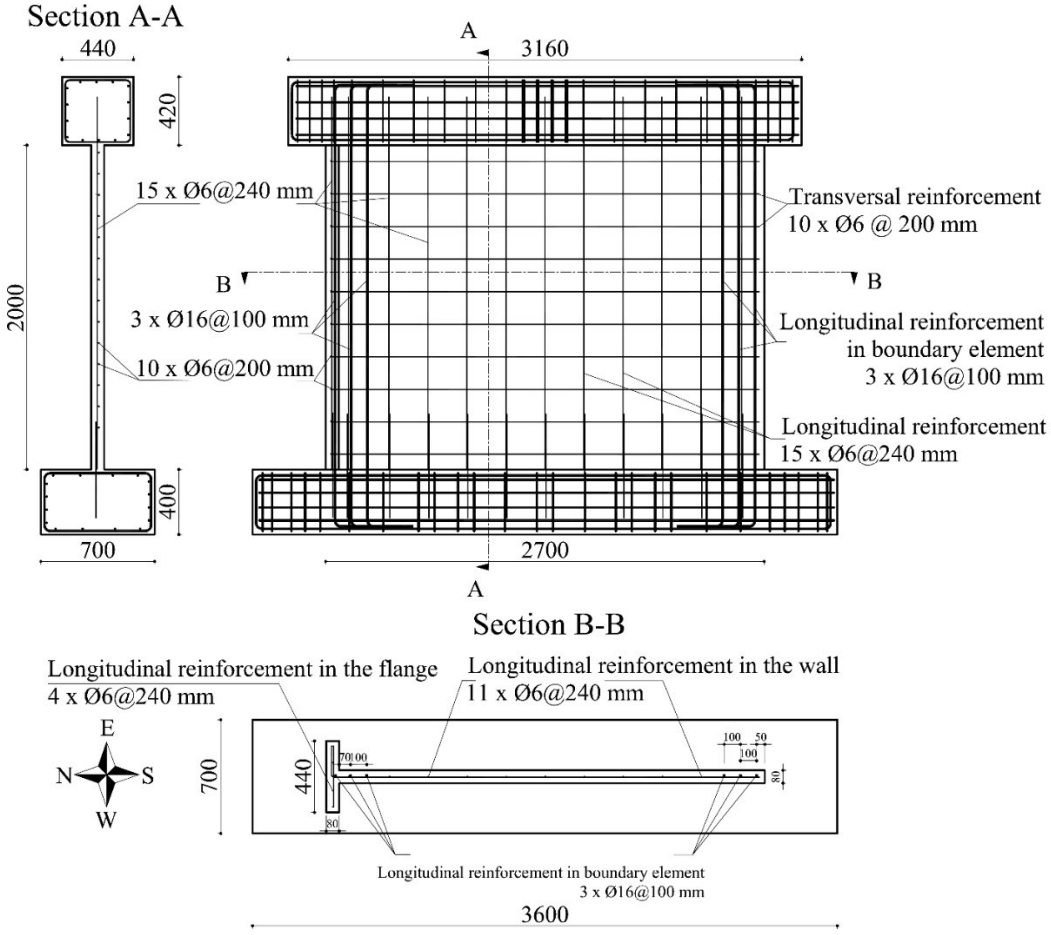

Figure 4.39 – Geometrical characterization and detailing of TW1 and TW4 experimental specimens (measure in mm).

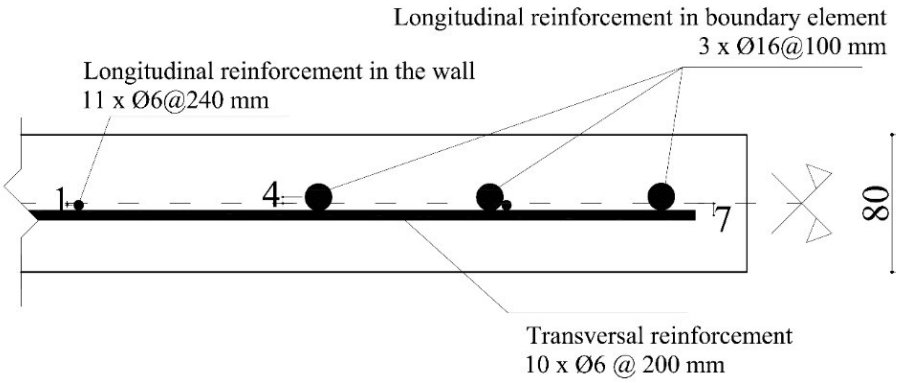

Figure 4.40 – Detail of the cross section of the south edge of the specimen, showing the eccentricity of the vertical reinforcement with respect to the centreline of the section (measure in mm).

The longitudinal reinforcement is characterized by ϕ6 bars spaced of 240 mm, moreover both the extremities of the wall (defined boundary elements in the following) were over reinforced with 3 longitudinal bars of 16 mm. The transverse reinforcement is constituted by ϕ6 bars spaced of 200 mm.

The main mechanical properties, derived from material tests, are resumed in Table 4.4.

Table 4.4 – Main mechanical properties derived from material tests for TW1and TW4 specimens

	concrete			transversal reinforcement						longitudinal reinforcement											
										web of the wall						boundary elements					
	E_c [Gpa]	f_c [MPa]	f_t [MPa]	f_y [MPa]	f_u [MPa]	E_s [Gpa]	ϕ [mm]	s [mm]	ρ [%]	f_y [MPa]	f_u [MPa]	E_s [Gpa]	ϕ [mm]	s [mm]	ρ [%]	f_y [MPa]	f_u [MPa]	E_s [Gpa]	ϕ [mm]	s [mm]	ρ [%]
TW1	25.3	28.8	2.2	460	625	183.5	6	200	0.17	460	625	183.5	6	240	0.15	565	650	208.0	16	100	2.5
TW4	29.2	31.2	1.5	460	625	183.5	6	200	0.17	460	625	183.5	6	240	0.15	565	650	208.0	16	100	2.5

During the test the axial load ratio was maintained constant and equal to 5% (equivalent to an applied constant axial force of 330 kN).

In Figure 4.41-a is reported a 3D scheme of the experimental set-up. A rigid steel beam was placed at the top of the RC beam in order to distribute the vertical load on the entire section of the wall. The vertical load is imposed by means of two vertical actuator connected to the steel beam close to the wall ends. The two vertical actuators are used to apply not only the axial load, but also the bending moment required to achieve the desired shear span of 10 m, which correspond to a shear span ratio equal to 3.7. This condition is obtained by coupling the control of the two vertical actuators with the horizontal actuator, connected to the top RC beam, which impose the in-plane loading on the specimen. In Figure 4.41-a two additional horizontal actuators are reported, coloured in green. They are used, as explained in the following, to impose the out-of-plane displacement at the top RC beam of TW4 specimen.

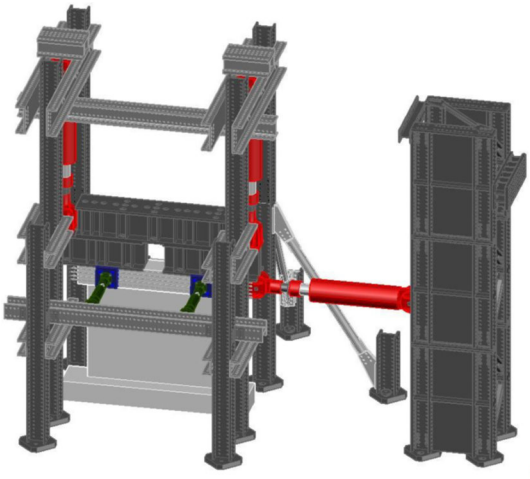

(a)

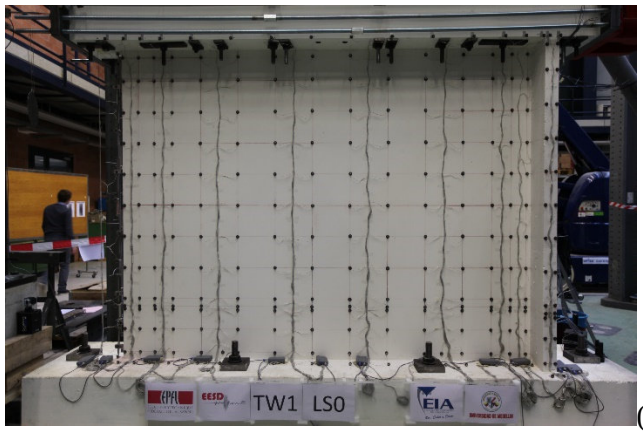

(b)

Figure 4.41 – Experimental tests: (a)3D representation of the test set-up [Rosso et al., 2016] and (b) view of TW1 specimen before running the test [Almeida et al. 2016]

The main difference between TW1 and TW4 specimens is related to the imposed horizontal loading. For TW1 specimen the loading protocol consisted in a reversed quasi-static cyclic in-plane history, as reported in Figure 4.42-a. As the in-plane horizontal loading is imposed the out-of-plane displacement at the top RC beam is prevented.

Regarding TW4 specimen, also the out-of-plane actuators are activated. The obtained loading protocol consisted in a quasi-static cyclic history, which combined the in-plane and the out-of-plane displacement as shown in Figure 4.42-b.

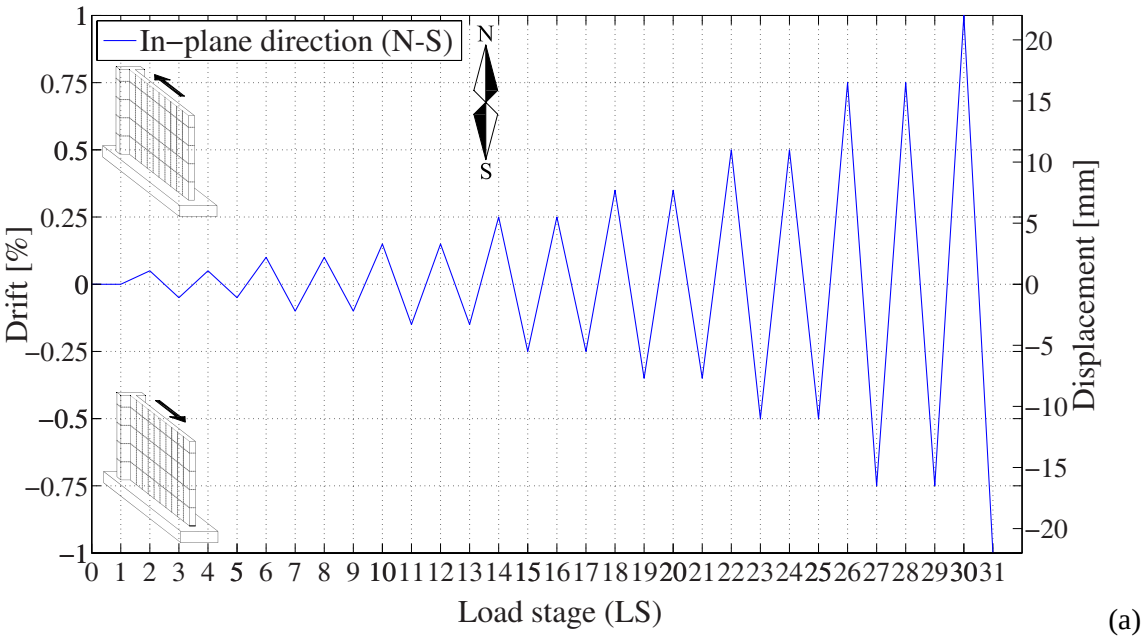

(a)

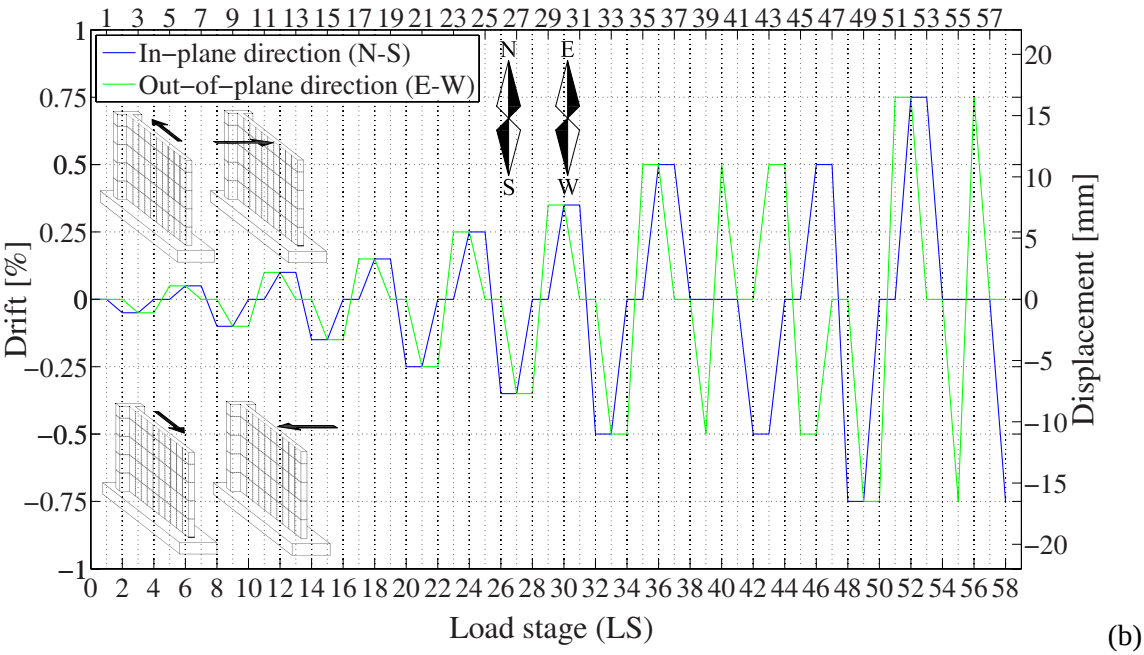

(b)

Figure 4.42 – Loading protocol of the quasi-static cyclic test: (a) TW1 specimen and (b) TW4 specimen [Rosso et al., 2016].

4.4.1.2 Nonlinear finite element modelling and results

In Figure 4.43-a is presented a sketch of the model used in NLFEA in which all the elements are presented with their thickness.

Both the specimens were modelled using 4-nodes elements with regular integration in plane (4 Gauss integration points). Moreover, each element was subdivided, along its thickness, into 4 different layers in order to properly set the exact position of the reinforcement layer, as shown in Figure 4.43-b; each layer is characterized by 3 Simpson integration points. The discretization of the thickness of the wall into different layers allows to consider the slightly eccentricity of reinforcing bars experimentally detected, shown in Figure 4.40.

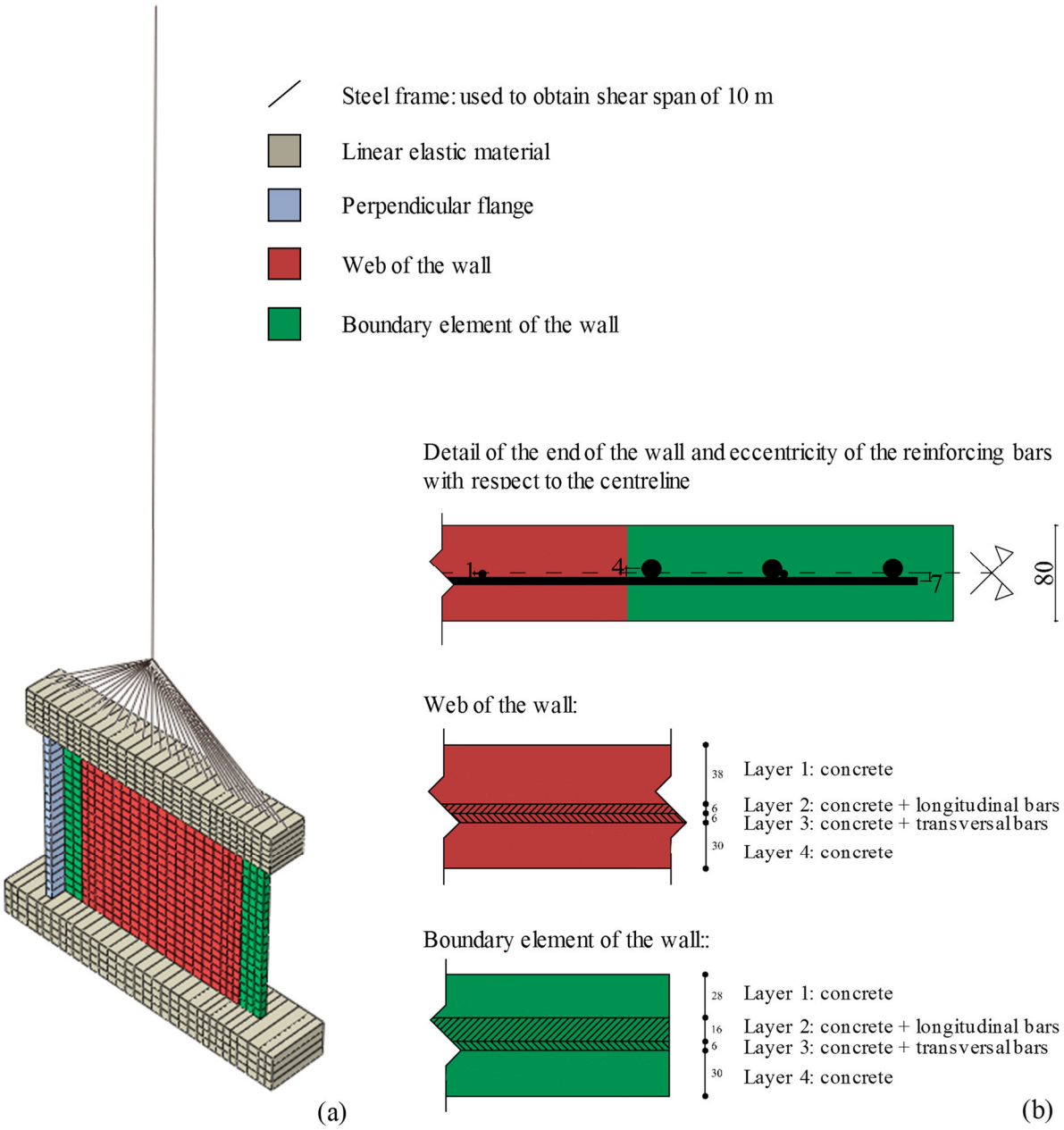

Figure 4.43 – Detail of the mesh used in NLFEA: (a) entire mesh and (b) discretization of the thickness into layers with different properties (measure in mm).

The steel frame indicated in Figure 4.43-a was adopted in the NLFEA to simulate the applied experimental shear span of 10 m. This frame is obtained using 2-node beam elements, with 2 Gauss integration points along the beam axis. Each beam was connected to the upper part of the top RC beam with a hinged connection. The legitimacy of this frame modelling approach was validated by verifying the ratio between shear and bending moment at the base of the wall.

Regarding the boundary conditions, both TW1 and TW4 specimens were fixed at the base of the linear elastic foundation. For TW1 specimen the cyclic in-plane loading history is applied at the top of the steel frame according to the loading protocol presented in Figure 4.42-a, while the out-of-plane displacement of the top beam was restrained as shown in Figure 4.44-a. On the other hand, for TW4 specimen a combination of in-plane loading, applied at the top of the steel frame, and out-of-plane loading, applied as displacement in correspondence of the top beam, was imposed as reported in Figure 4.44-b.

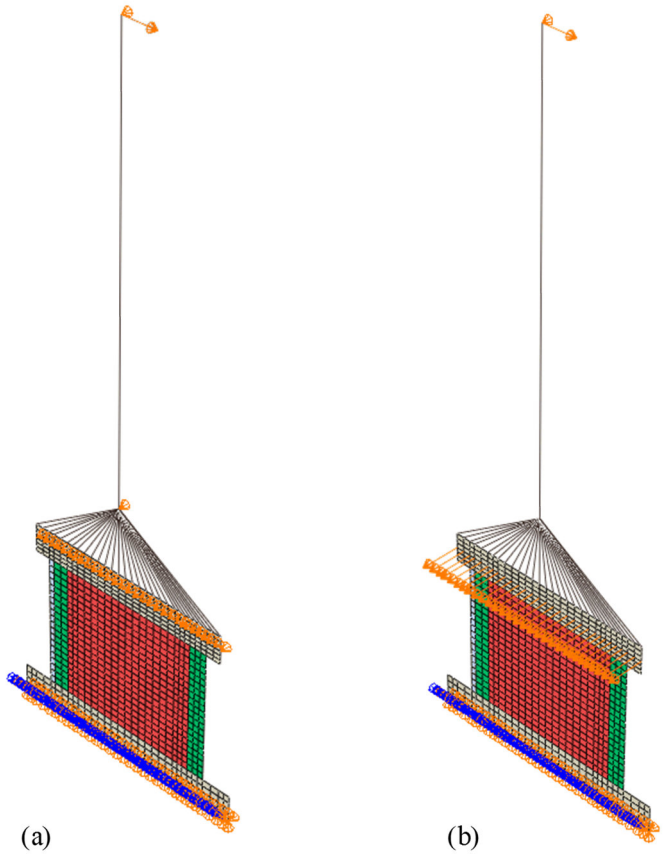

Figure 4.44 – Detail of boundary and loading conditions in NLFEA: (a) TW1 specimen and (b) TW4 specimen.

Regarding the material properties, The foundation and the top beam were modelled with concrete adopting a linear elastic behaviour while the wall was modelled with nonlinear behaviour for concrete and steel, applied by means of the implemented PARC_CL 2.0 crack model, as described in Table 4.5.

Table 4.5 – Main material properties adopted in NLFEA for TW1and TW4 specimens.

Spec.	Zone	Concrete (see §4.2.1.1)										Steel (see §4.2.1.2)					
		h	a_m	Ec	f_t	G^{RC}_F	$\varepsilon_{t,u}$	f_c	G_C	$\varepsilon_{c,cr}$	$\varepsilon_{c,u}$	E_s	$f_{y,\,long}$	ρ_{long}	E_s	$f_{y,\,trasv}$	ρ_{trasv}
		[mm]	[mm]	[Gpa]	[MPa]	[N/mm^3]	[-]	[MPa]	[N/mm^3]	[-]	[-]	[GPa]	[MPa]	[%]	[GPa]	[MPa]	[%]
TW1	Web	100	422	25.3	2.2	0.165	0.004	28.8	41.3	0.002	0.023	183.5	460	0.15	183.5	460	0.17
	Boundary element	100	176	25.3	2.2	0.210	0.003	28.8	52.4	0.002	0.029	208	565	2.5	183.5	460	0.17
TW4	Web	100	422	29.2	1.5	0.167	0.006	31.2	41.9	0.002	0.022	183.5	460	0.15	183.5	460	0.17
	Boundary element	100	176	29.2	1.5	0.213	0.007	31.2	53.1	0.002	0.027	208	565	2.5	183.5	460	0.17

NLFEA were run in displacement control using implicit solution method and Newton-Raphson convergence criterion, with force and displacement control tolerance limits respectively set equal to $5 \cdot 10^{-3}$ and 10^{-2}. The maximum number of iteration allowed for each time increment was set equal to 25. The solution of a time increment is accepted after the maximum number of iteration allowed has been completed, even if the equilibrium tolerances are not satisfied. However, this condition should be avoided because it could lead to a loss of stability and reliability of the results.

In the following the results obtained by means of NLFEA and PARC_CL 2.0 crack model are compared with the experimental outcomes.

In Figure 4.45 are presented the experimental and numerical global force-displacement response obtained for TW1 specimen (Figure 4.45-a) and TW4 specimen (Figure 4.45-b).

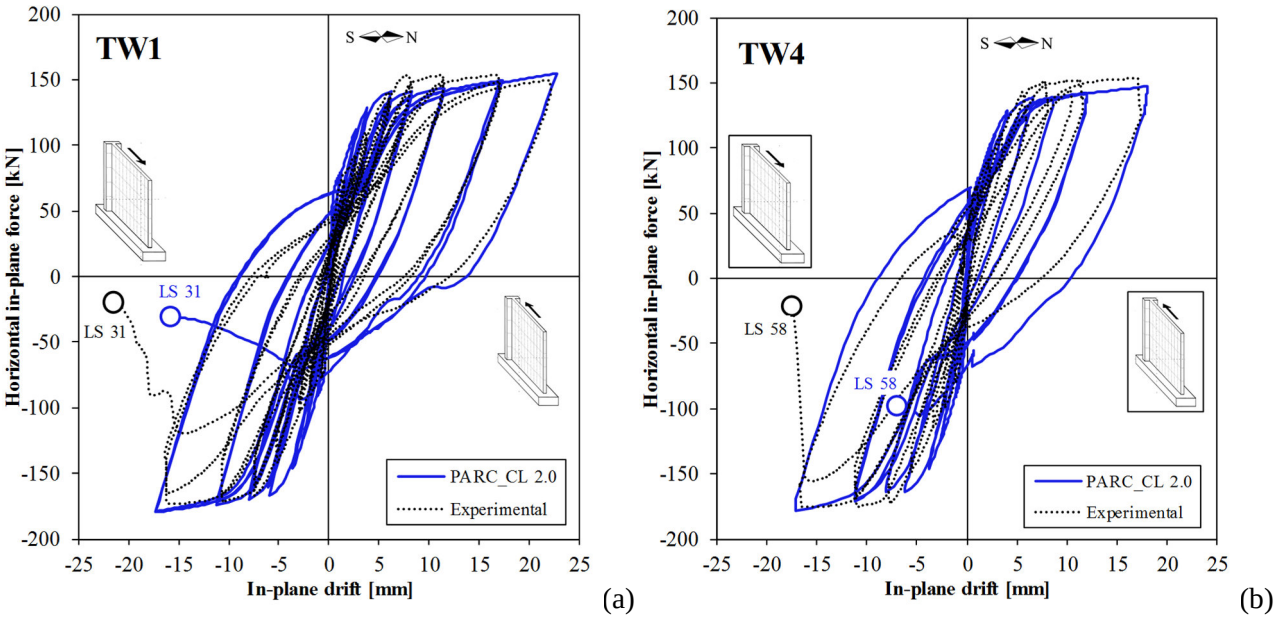

Figure 4.45 – In-plane force-displacement response, comparison between experimental and NLFEA results: (a) TW1 specimen and (b) TW4 specimen.

The results plotted in Figure 4.45 highlighted the capability of PARC_CL 2.0 crack model to capture the global response in term of both force-displacement hysteresis and failure mode. Indeed, for TW1 the failure obtained by means of NLFEA is characterized by crushing of concrete at the base of the specimen which has been triggered by damage induced by out of plane deformations, at Load Stage (LS) 31; this finding is in

accordance with the experimental outcomes as shown in Figure 4.46. To better understand the results plotted in Figure 4.46, please consider that the crushing of concrete in NLFEA is considered achieved when the compressive strain reaches the ultimate values, $\varepsilon_{c,u}$; the values of $\varepsilon_{c,u}$, for both web and boundary element, are reported in Table 4.5.

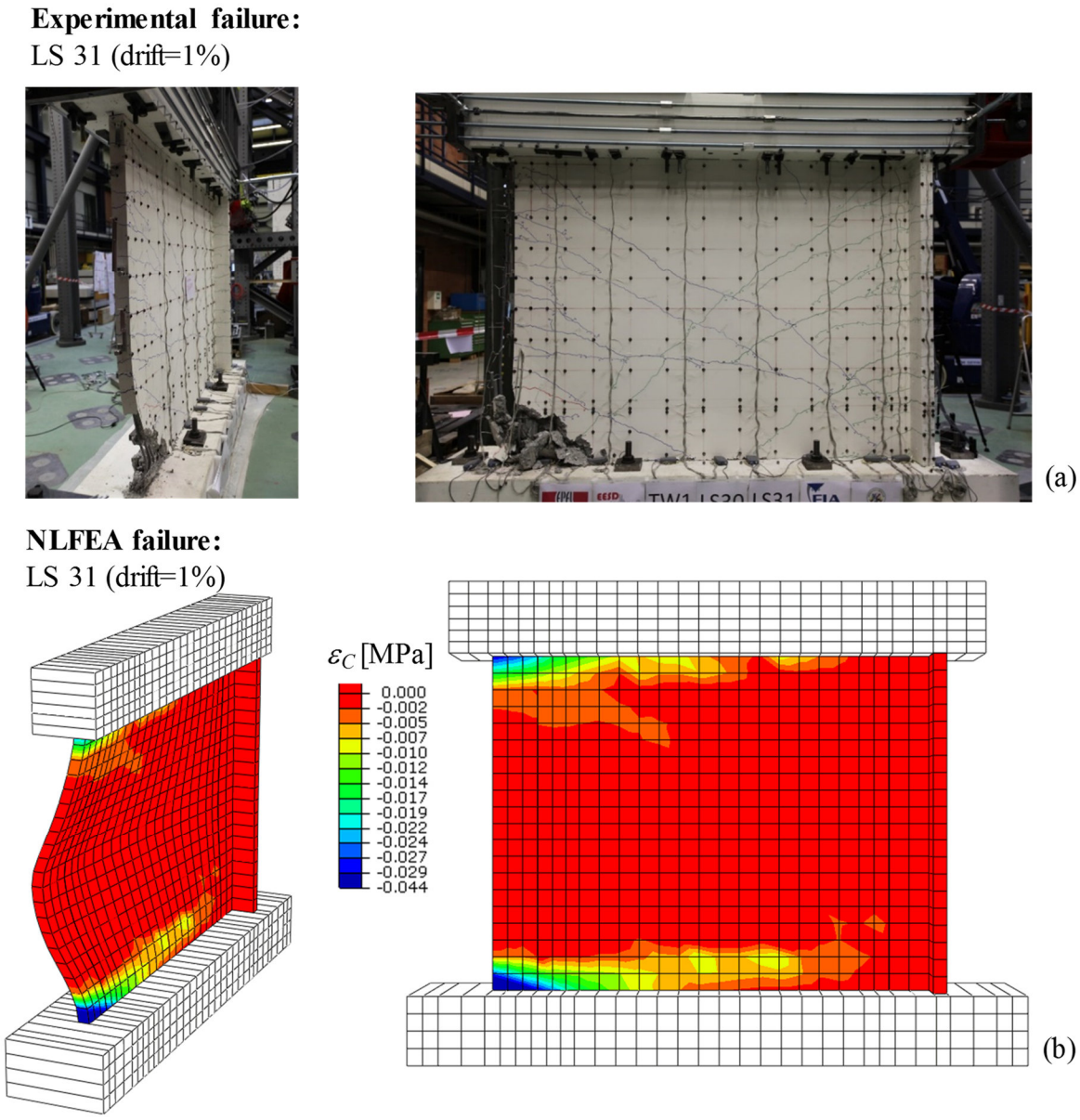

Figure 4.46 – TW1, crushing of concrete at LS 31: (a) experimental failure and (b) NLFEA failure.

A similar behavior was observed for TW4 specimen, as shown in Figure 4.47. when load is applied from the flange to the web edge, during the last imposed cycle (LS 58) the global force-displacement response presents a clear degradation of stiffness, due to the crushing of concrete at the base of the wall. Also in this case the failure mode detected by means of NLFEA are in good agreement with the experimental outcomes as reported in Figure 4.47, due to the fact that the compressive concrete strain reaches the ultimate value, $\varepsilon_{c,u}$, reported in Table 4.5.

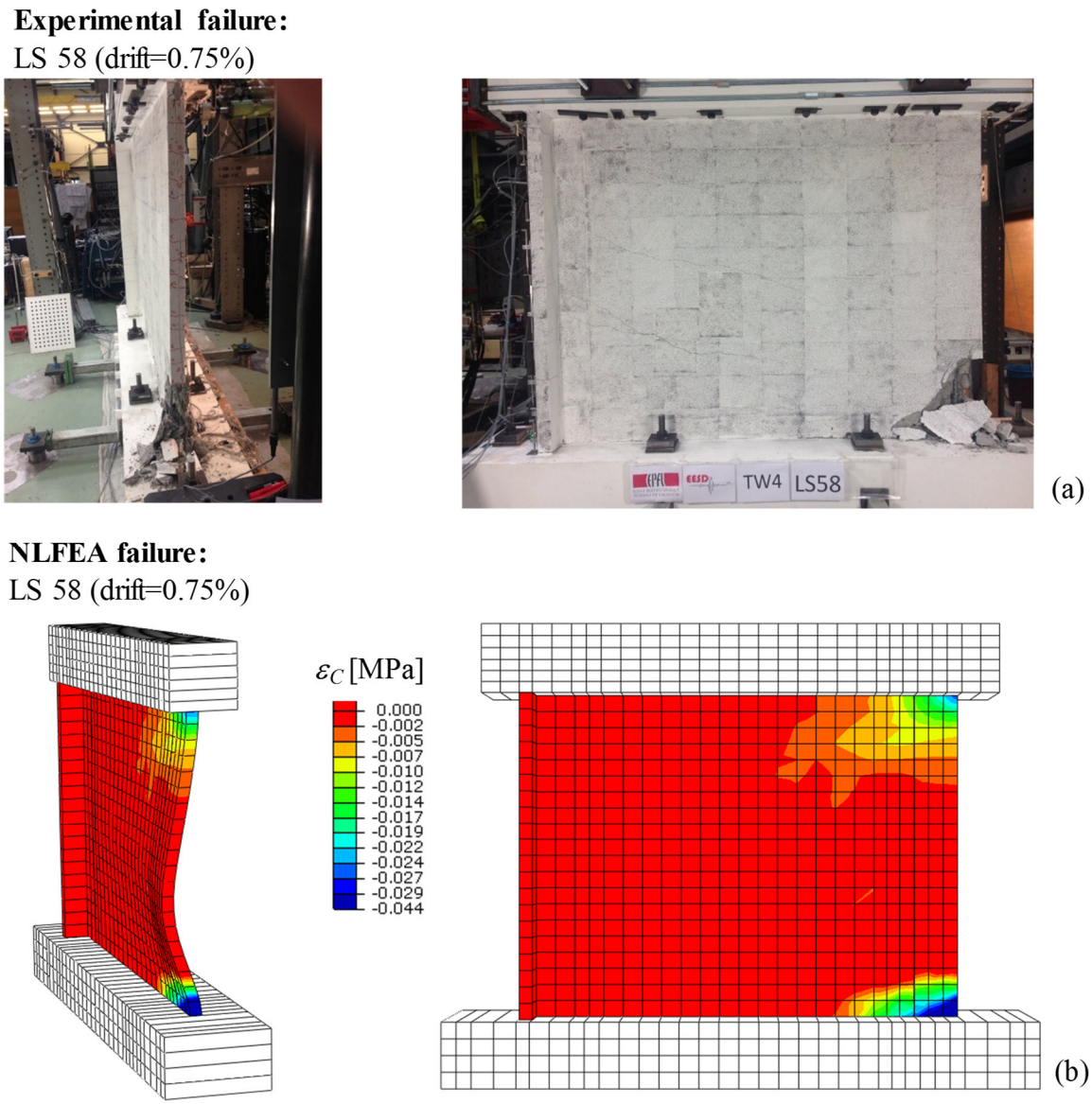

Figure 4.47 – TW4, crushing of concrete at LS 58: (a) experimental failure and (b) NLFEA failure.

The mechanism of out-of-plane instability, as analytically described by [Goodsir, 1985], which was demonstrated as one of the cause of the specimen failure, occurred after the development of large tensile strains in the boundary element; due to the cyclic load applied, when the boundary element is reloaded in compression and before cracks close, the compression force is supported only by the vertical reinforcement potentially leading to out-of-plane instability. For this reason, the comparison between NLFEA and experimental results is extended to the evaluation of the out-of-plane displacement. In Figure 4.48 is reported the comparison between experimental and NLFEA results in term of in-plane vs out-of-plane displacement for both the analysed specimens.

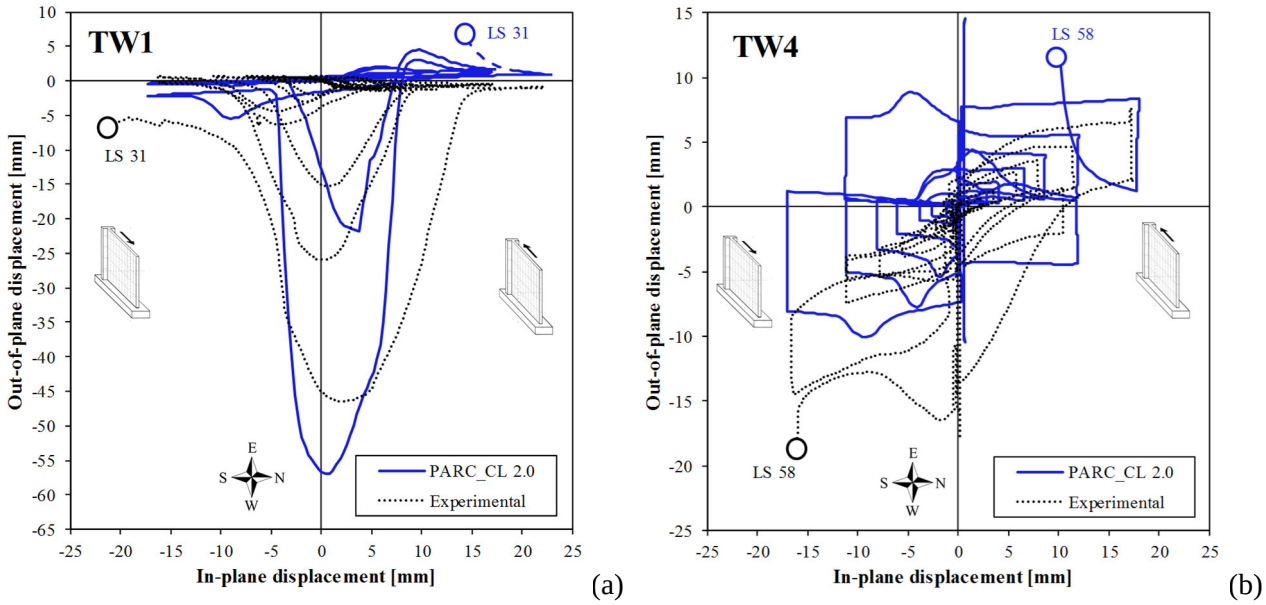

Figure 4.48 – In-plane displacement vs out-of-plane displacement at the height where maximum out of plane displacement was experimentally measured (h= 800 mm above foundation), comparison between experimental and NLFEA: (a) TW1 specimen and (b) TW4 specimen.

The mechanism of out-of-plane instability appears clear by analyzing Figure 4.48-a. Indeed, when load is applied from the flange towards the edge of the specimen (from positive to negative in-plane displacement), large out-of-plane displacement developed in the reference point, positioned at an height of 800 mm above foundation, when the in-plane displacements are close to zero. After the cracks closure this out-of-plane displacement was recovered. During the last cycle (LS30→LS31) permanent inelastic deformation occurred and the out-of-plane displacement was not recovered (see the experimentally detected residual out-of-plane displacement of approximately 5 mm in Figure 4.48-a). This damage cause a stiffness degradation which led to the in-plane failure of the specimen described above. The results obtained by means of NLFEA are in accordance with these, unless the fact that during the last cycle the out-of-plane displacement developed in the opposite direction till the failure of the specimen. The results of TW4 specimen are more difficult to understand, due to the fact that the external load was applied as a combination of in-plane and out-of-plane load. Nevertheless, analysing the last loading cycle (LS57→LS58) it can be highlight that, according to the tendency previously discussed for TW1 specimen, at around 0 mm in-plane displacement the out-of-plane displacement was close to the maximum obtained during the load history, both experimentally and numerically.

The evaluation of the out-of-plane behaviour was extended to the study of the out-of-plane displacement along the height of the wall for some selected load steps. According to the findings presented above the selected load steps was characterized by an in-plane displacement of 0 mm in order to have the maximum out of plane. In Figure 4.49 the comparison between experimental and NLFEA results are presented.

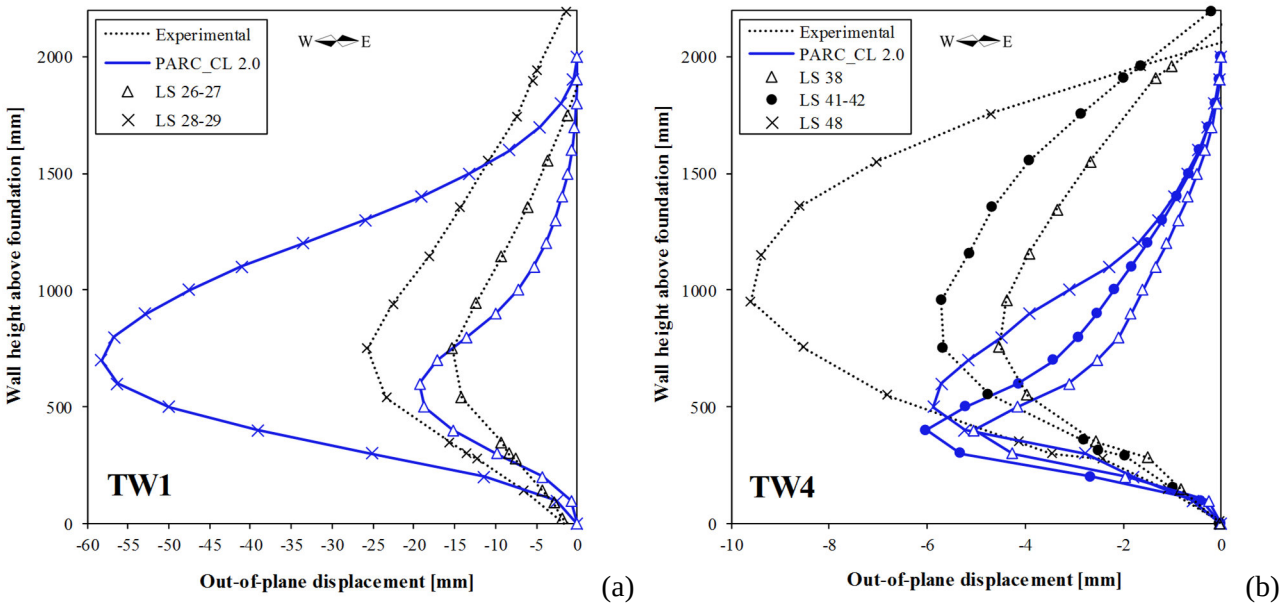

Figure 4.49 – Out-of-plane displacement along the height of the specimen, comparison between experimental and NLFEA results for some significant steps, characterized by an in-plane displacement around 0 mm: (a) TW1 specimen and (b) TW4 specimen.

From Figure 4.49 it can be noted that, for both the analysed specimens, the numerical model are able to satisfactory simulate the overall out-of-plane behaviour of the wall even if, especially for TW4 specimen (Figure 4.49-b) the maximum out-of-plane displacement was detected at a lower height.

The comparison between experimental and NLFEA was not only limited to the global behaviour but also extended to the evaluation of some local-level response quantities.

Figure 4.50 and Figure 4.51 show the crack patterns of TW1 and TW4 specimens, evaluated at the same level of drift (*0.75%* in-plane drift and *0%* out-of-plane drift) corresponding to Load Stages LS 26 and LS 53 respectively.

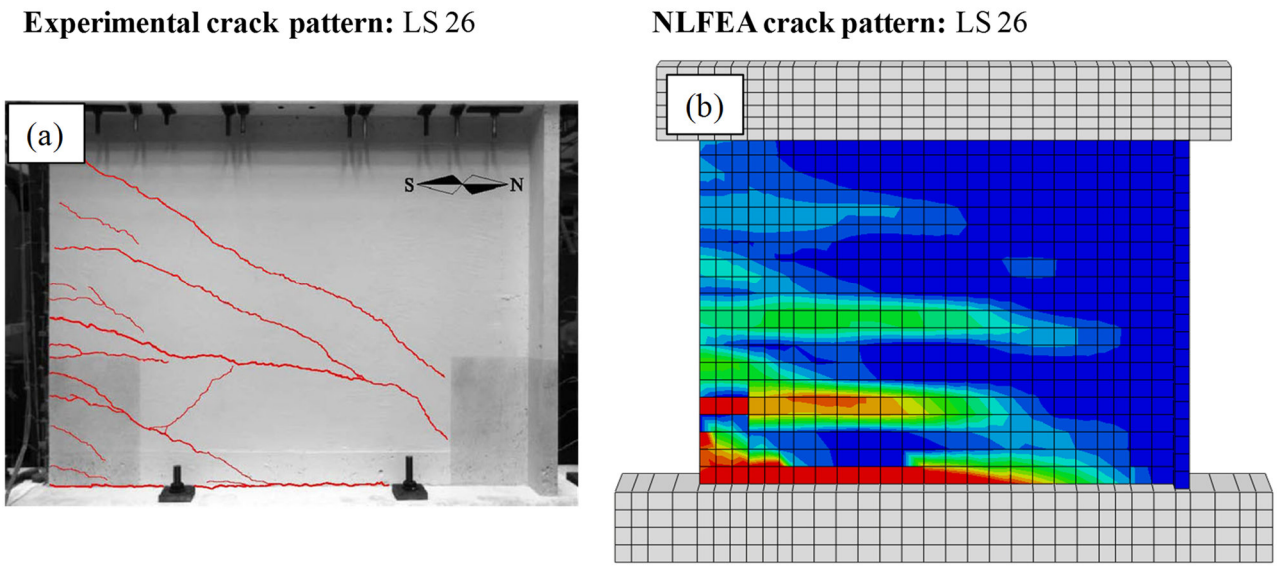

Figure 4.50 – Crack pattern on the West side of TW1 specimen at LS 26 corresponding to a drift of 0.75%: (a) experimental outcomes and (b) NLFEA results.

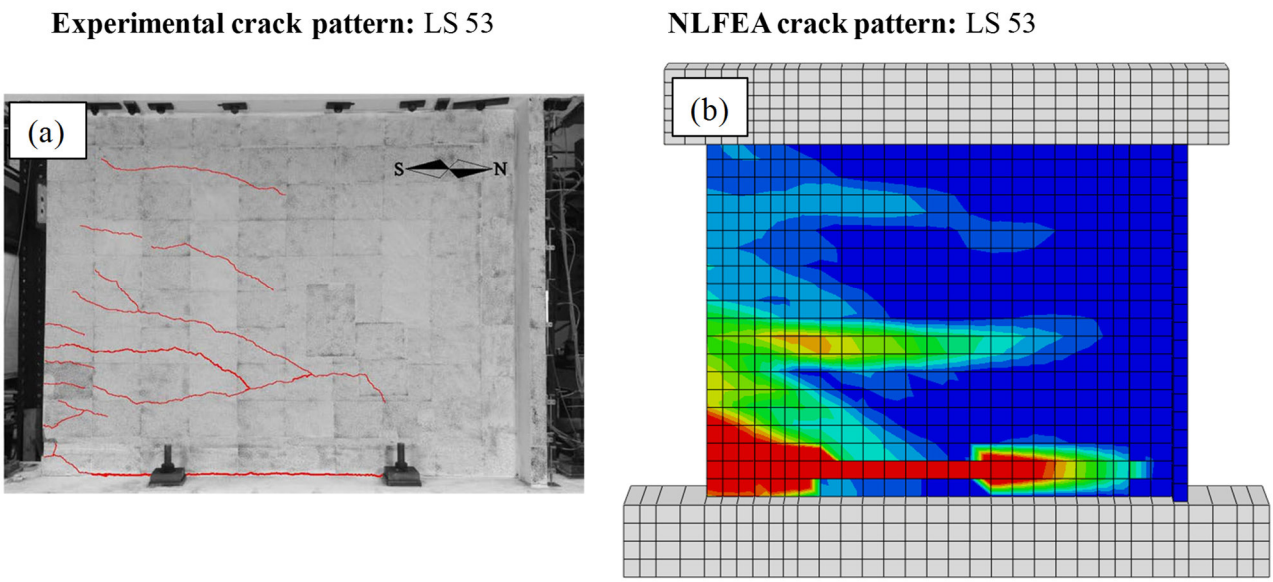

Figure 4.51 – Crack pattern on the West side of TW4 specimen at LS 53 corresponding to a drift of 0.75%: (a) experimental outcomes and (b) NLFEA results.

The results presented in Figure 4.50 and Figure 4.51 shows that NLFEA are in good agreement with the experimental outcomes also in term of crack pattern. Both in the experimental and the numerical crack pattern highlighted the typical flexural crack, characterized by an approximately horizontal inclination. Moreover, as the patterns of TW1 and TW4 specimens seem relatively similar, in TW1 (Figure 4.50) both the numerical and the experimental results highlighted larger crack at around mid-height with respect to TW4 (Figure 4.51). this difference can be explained with the larger out-of-plane displacement experienced by TW1 specimen with respect to TW4, as shown in Figure 4.48.

Finally, in the following are investigated the cyclic variation of strains in time for TW1 specimen. The experimental outcomes was derived from the LVDTs measurements. In particular along the height of the wall seven LVDTs with different displacement ranges were placed at the two sides of the specimen, as shown in Figure 4.52. LVDTs named from F1 to F7 were placed along the free edge of the wall, while LVDTs named from T1 to T7 were placed along the flanged edge. The comparison between experimental and NLFEA was limited to 4 out of the 7 LVDTs measurement (F1, F2, F3 and F4 for the free edge and T1, T2, T3 and T4 for the flanged edge) because, as showed above, this height was mainly involved by out-of-plane phenomenon. The LVDT presented different base lengths: for F1 and T1 the base length was equal to *50 mm*, for F2, T2, F3 and T3 the base length was equal to *200 mm* and for F4 and T4 the base length was equal to *400 mm*. The vertical strain experimentally evaluated was calculated by dividing the displacement measured by the LVDT by his base length.

In Figure 4.53 and Figure 4.54 the experimental vertical strains, derived as just explained, was compared with the vertical strains obtained from NLFEA at different heights along the free edge and the flanged edge respectively.

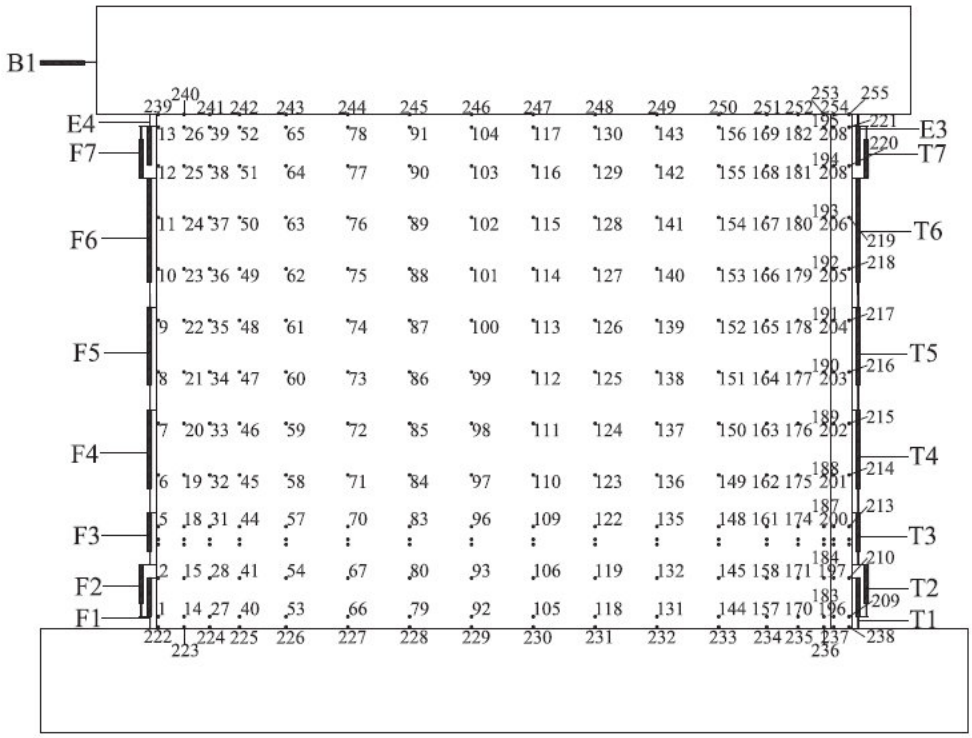

Figure 4.52 – TW1, labeling and position of LVDTs during the experimental test (East side view, the flange is on the right) [Almeida et al., 2016].

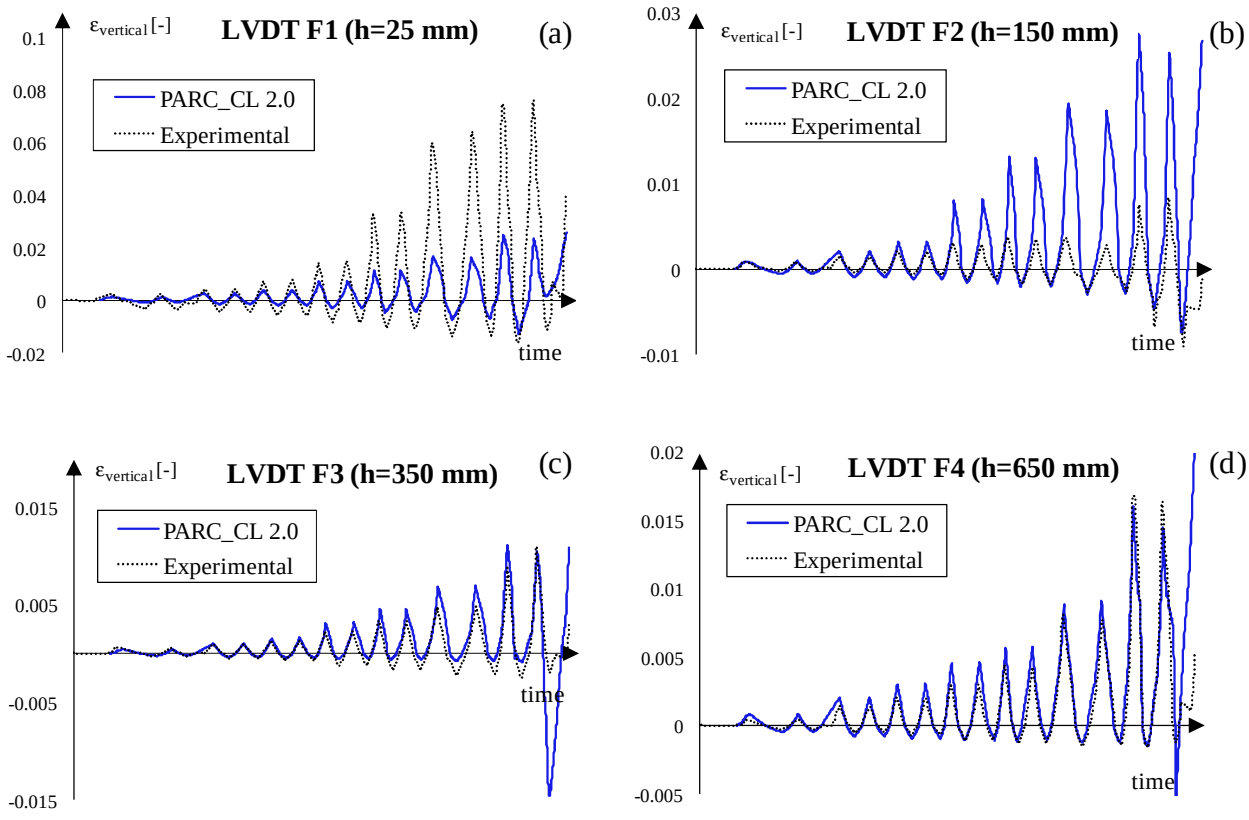

Figure 4.53 – TW1, comparison between experimental and NLFEA results in term of vertical strains measured along the edge of the specimen at different heights above foundation: (a) h= 25 mm, (b) h=150 mm, (c) h= 350 mm and (d) h=650 mm.

From Figure 4.53 it can be noted that for the two lower measured points (Figure 4.53-a and Figure 4.53-b) the results of NLFEA present high scatter with respect to the experimental ones. This scatter can be related to a different localization of the main crack at the base of the wall; indeed the experimental outcomes present the higher value for the lower measurement point (h=25 mm, Figure 4.53-a) while for NLFEA the higher strain values are obtained at the second measurement point (h=150 mm, Figure 4.53-b) . On the other hand, moving far from this contact zone, into the zone which was of mainly interest for the purpose of this document (due to the fact that this zone was involved by out-of-plane phenomenon), the comparison between experimental and NLFEA results are in good agreement, as shown in Figure 4.53-c and Figure 4.53-d.

In Figure 4.54 the same quantities are evaluated for the flanged end, derived from LVDTs named from T1 to T4 in Figure 4.52.

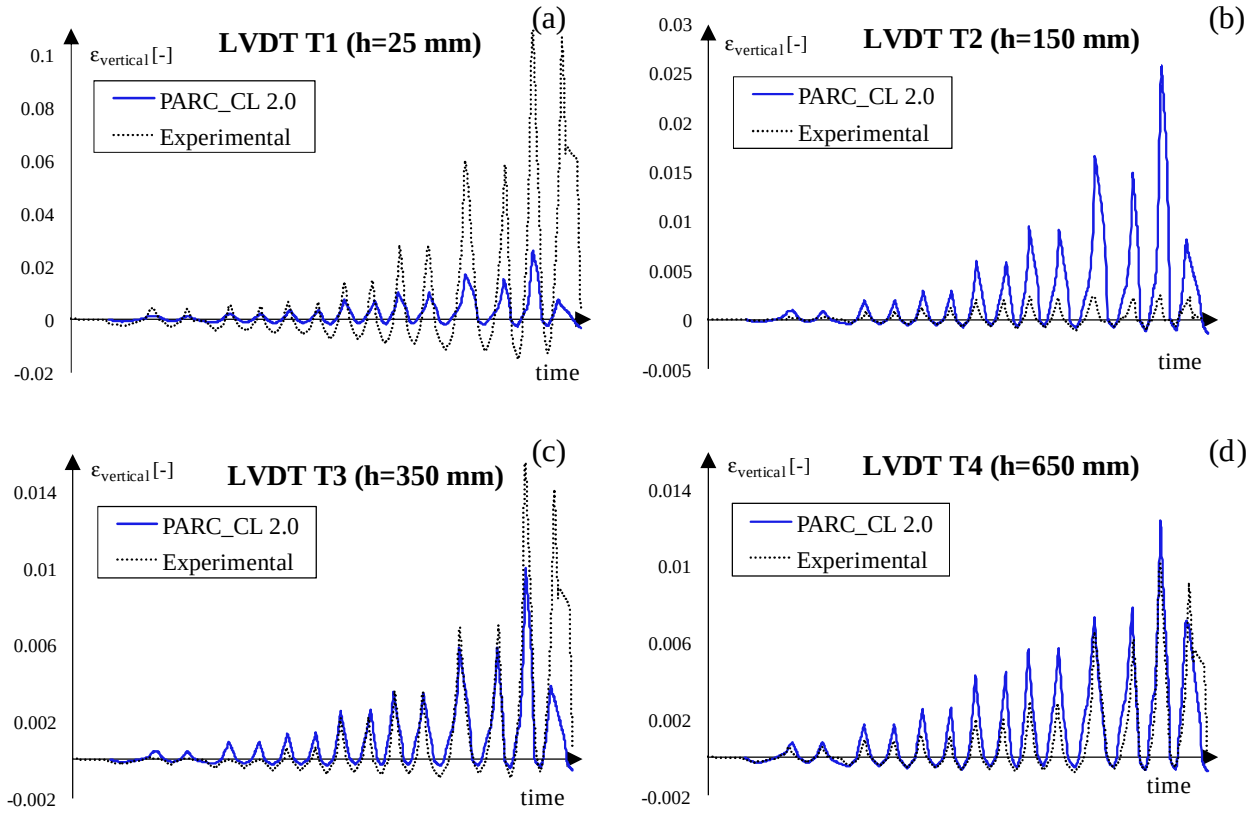

Figure 4.54 – TW1, comparison between experimental and NLFEA results in term of vertical strains measured along the flange of the specimen at different heights above foundation: (a) h= 25 mm, (b) h=150 mm, (c) h= 350 mm and (d) h=650 mm.

Analysing the variation of vertical strains in time in the flanged edge, reported in Figure 4.54, the same conclusions just underlined analysing the free edge (Figure 4.53) can be remarked. Indeed, in the two lower measurement points it can be highlighted some differences between experimental and NLFEA results, as shown in Figure 4.54-a and Figure 4.54-b. On the other hand, far from this zone the comparison between experimental and numerical vertical strains seems to be in good agreement, as reported in Figure 4.54-c and Figure 4.54-d.

4.4.1.3 Validation of PARC_CL 2.0 crack model by comparison with DIANA code

A further validation of the presented PARC_CL 2.0 crack model is carried out by analysing the same specimens using the software DIANA [Manie, 2015].

In Figure 4.55-a is reported a sketch of the adopted mesh. Concrete was modelled using 4 nodes curved shell elements (named Q20SH in DIANA) with 4 Gauss integration points over the element area and 5 Simpson integration points over the element thickness. Reinforcing bars were modelled using embedded reinforcement considering perfect bond between reinforcement and concrete, Figure 4.55-b. Each bar element is characterized by 2 Gauss integration points along the truss axis. This particular modelling of reinforcing bars constitutes one of the major differences from the PARC_CL 2.0 crack model, where reinforcements are modelled as smeared within the concrete elements.

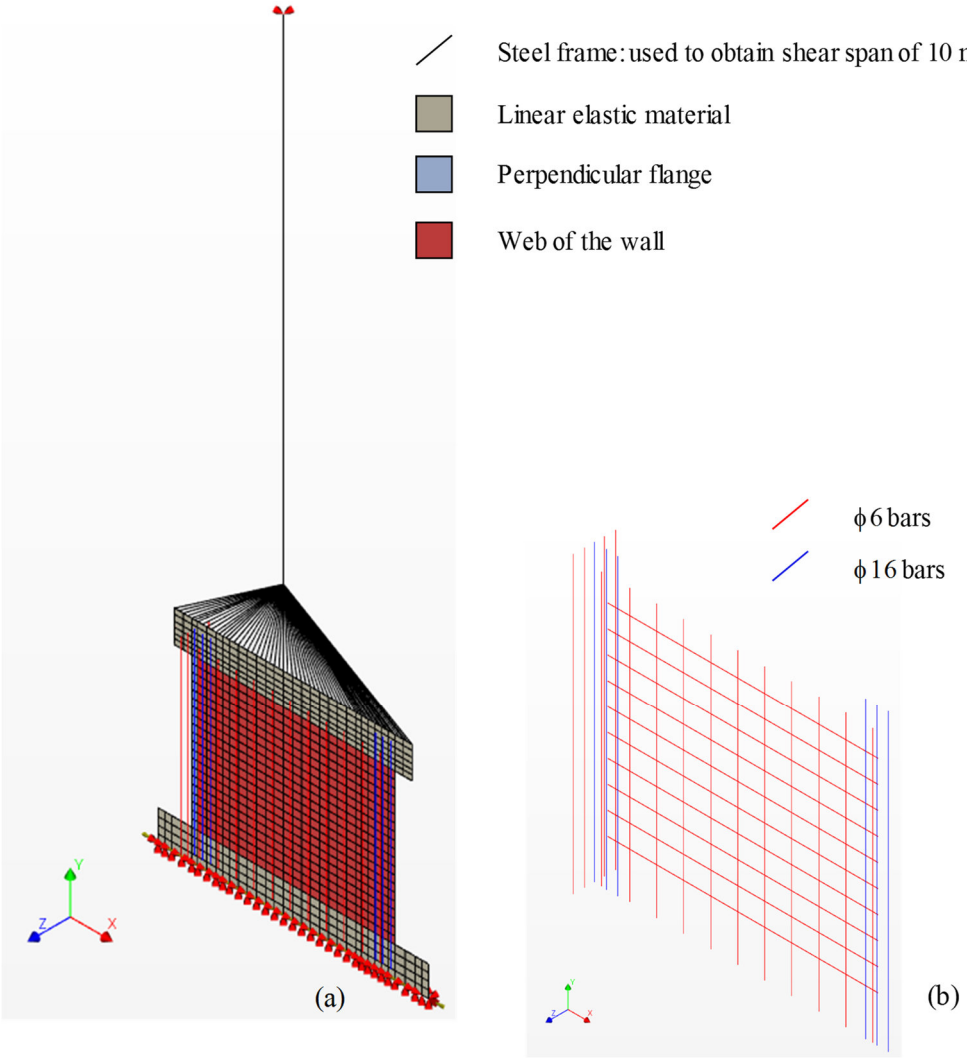

Figure 4.55 – TW specimens, NLFE model using DIANA code: (a) adopted mesh and (b) detail of reinforcement.

The total strain fixed crack model, available in DIANA [Manie, 2015], was used to model the concrete. For concrete in tension an exponential behaviour based on the definition of the fracture energy in tension, G_F, and of the crack bandwidth, h, have been adopted. G_F was calculated according to the proposal in [*fib*-Model

Code 2010] while *h* was assumed equal to the square root of the area of each element, as suggested by [Hendriks et al., 2012]. Concrete in compression has been modelled with a parabolic relationship, according to [Feenstra, 1993], based on the definition of the crack bandwidth, *h*, and of the fracture energy in compression, G_C, assumed equal to 450 times G_F, as done using PARC_CL 2.0 crack model. The reduction of the compressive strength of concrete, due to tensile strains perpendicular to the principal compressive direction, was taken into account according to [Vecchio and Collins, 1993]. The lower bound of this reduction curve is fixed at 0.6. The aggregate interlock phenomenon is considered by reducing the shear stiffness after cracking using a constant shear retention factor, equal to 0.03, that multiplies the elastic shear modulus of concrete.

The cyclic behaviour of steel was considered using the Monti-Nuti model [Monti and Nuti, 1992] available in DIANA. The parameters of the Monti-Nuti model was set equal to R_0=20, a_1=18.45 and a_2=0.001, based on a parametric study reported in [Belletti et al., 2016]. In Figure 4.56 are reported the adopted constitutive model for both concrete and steel.

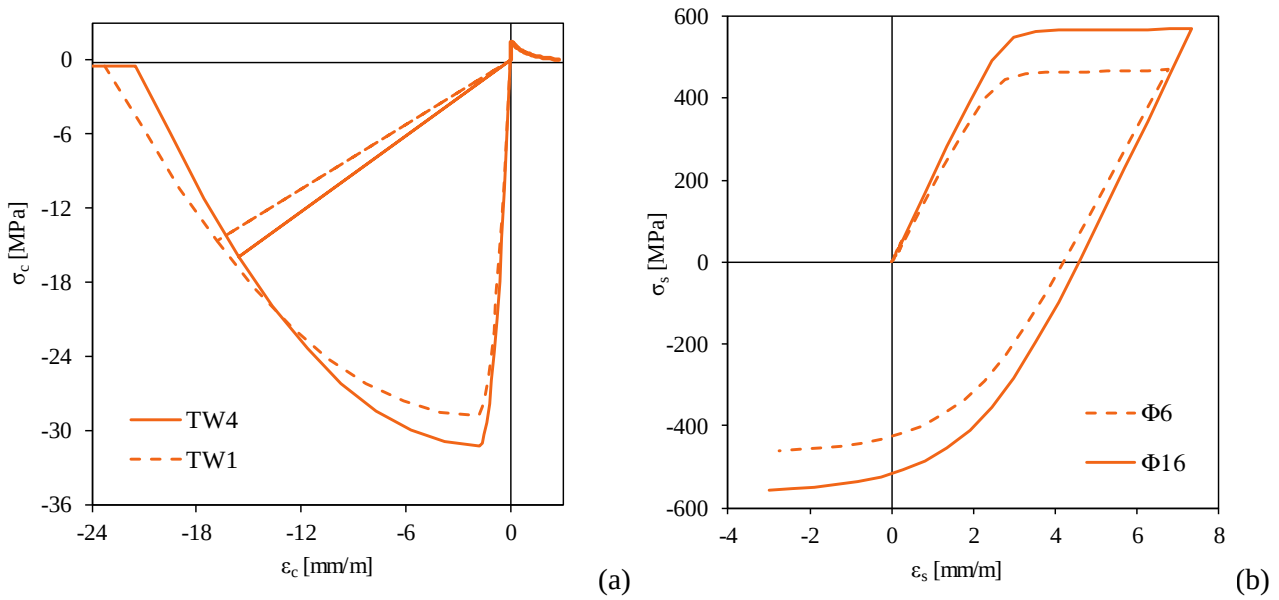

Figure 4.56 – TW specimens, adopted cyclic constitutive model with DIANA code: (a) concrete and (b) steel.

Figure 4.57 describes the comparison between experimental outcomes and NLFEA results. NLFEA are carried out using both the multi-layer shell element approach with PARC_CL 2.0 crack model (presented in the previous section) and the shell element approach with embedded reinforcement using DIANA code.

From Figure 4.57-a it can be highlighted that the global hysteretic behaviour is quite similar between the two numerical modelling approaches; moreover, also the failure mode, characterized by crushing of concrete at the base of the edge of the wall and marked with a circle in the graph, is the same.

Analysing Figure 4.57-b it can be assessed that also the out-of-plane instability of the specimen can be predicted with reasonable accuracy using both the numerical procedures.

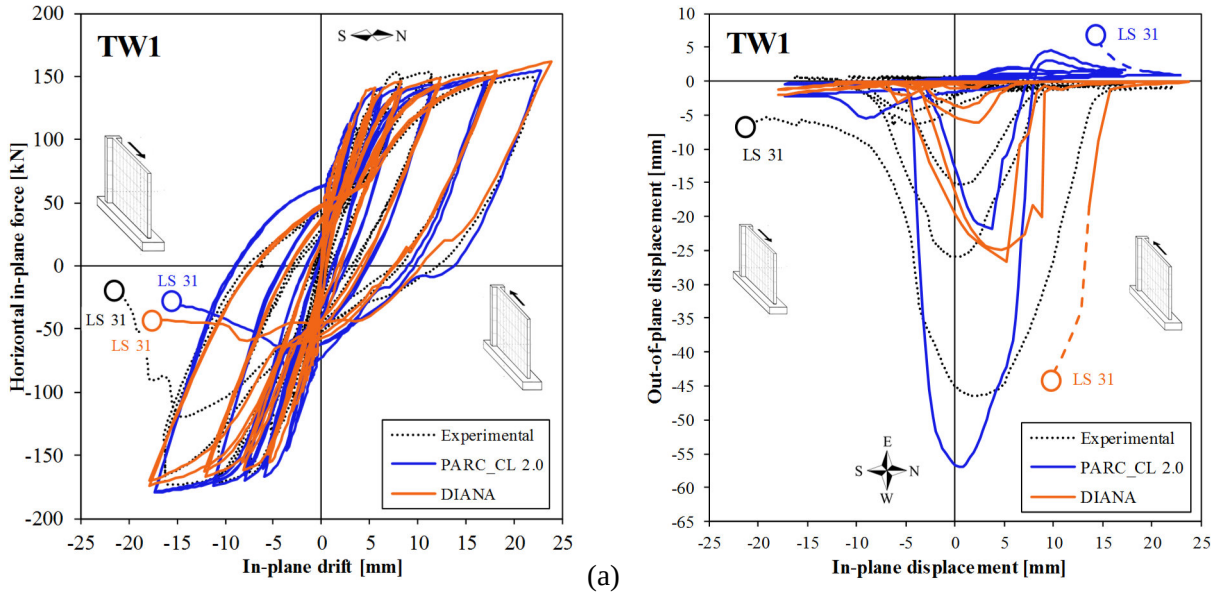

Figure 4.57 – TW1 specimen, comparison between experimental outcomes, PARC_CL 2.0 crack model and DIANA code: (a) in-plane force vs displacement and (b) in-plane displacement vs out-of-plane displacement at the height where maximum out of plane displacement was experimentally measured.

In Figure 4.58 the comparison between PARC_CL 2.0 crack model and DIANA commercial code is extended to the TW4 specimen. Figure 4.58-a highlight that PARC_CL 2..0 crack model is as able as DIANA code to predict the overall cyclic force-displacement behaviour. Also the failure mode, characterized by crushing of concrete is the same and it is detected at the same load stage. The out-of-plane behaviour, presented in Figure 4.58-b is quite similar for the lower load step (LS 38 – drift=0.5%) while for the higher one (LS 48 – drift=0.75%) the maximum out-of-plane displacement detected with DIANA code (≅10mm) is closer to the experimental maximum out-of-plane displacement with respect to the PARC_CL 2.0 crack model (≅6mm). However, this difference is considered negligible, because both the numerical models seem to predicted with reasonable accuracy the out-of-plane behaviour.

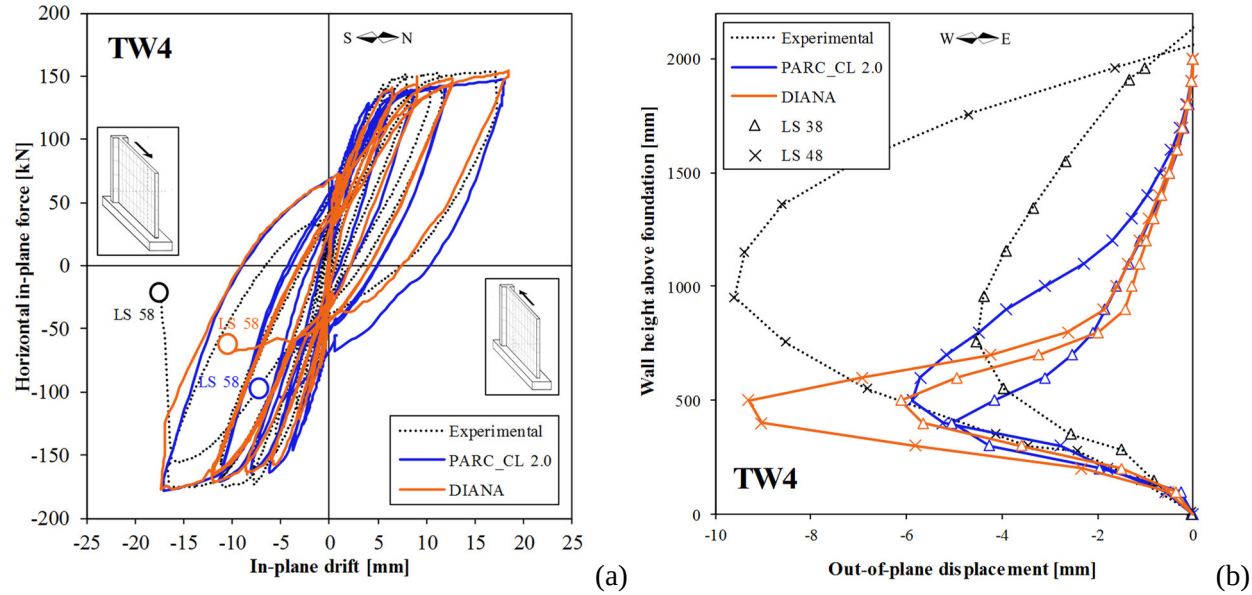

Figure 4.58 – TW4 specimen, comparison between experimental outcomes, PARC_CL 2.0 crack model and DIANA code: (a) in-plane force vs displacement and (b) out-of-plane displacement along the height of the wall.

4.4.2 "U-shaped" slender RC wall

In this section a "U-shaped" RC wall was analysed by means of NLFEA and the obtained results are compared with the results of an experimental campaign carried out at EPFL in Lausanne, Switzerland [Constantin and Beyer, 2016].

4.4.2.1 Experimental campaign

The experimental campaign carried out at EPFL by [Constantin and Beyer, 2016] consisted in two U-shaped walls, representing a half-scale model of the lower two storeys of a prototype elevator shaft, defined TUC and TUD which differed with respect to the applied axial load. For the purpose of this research one out of the two tested specimens was analysed, TUC wall, illustrated in Figure 4.59.

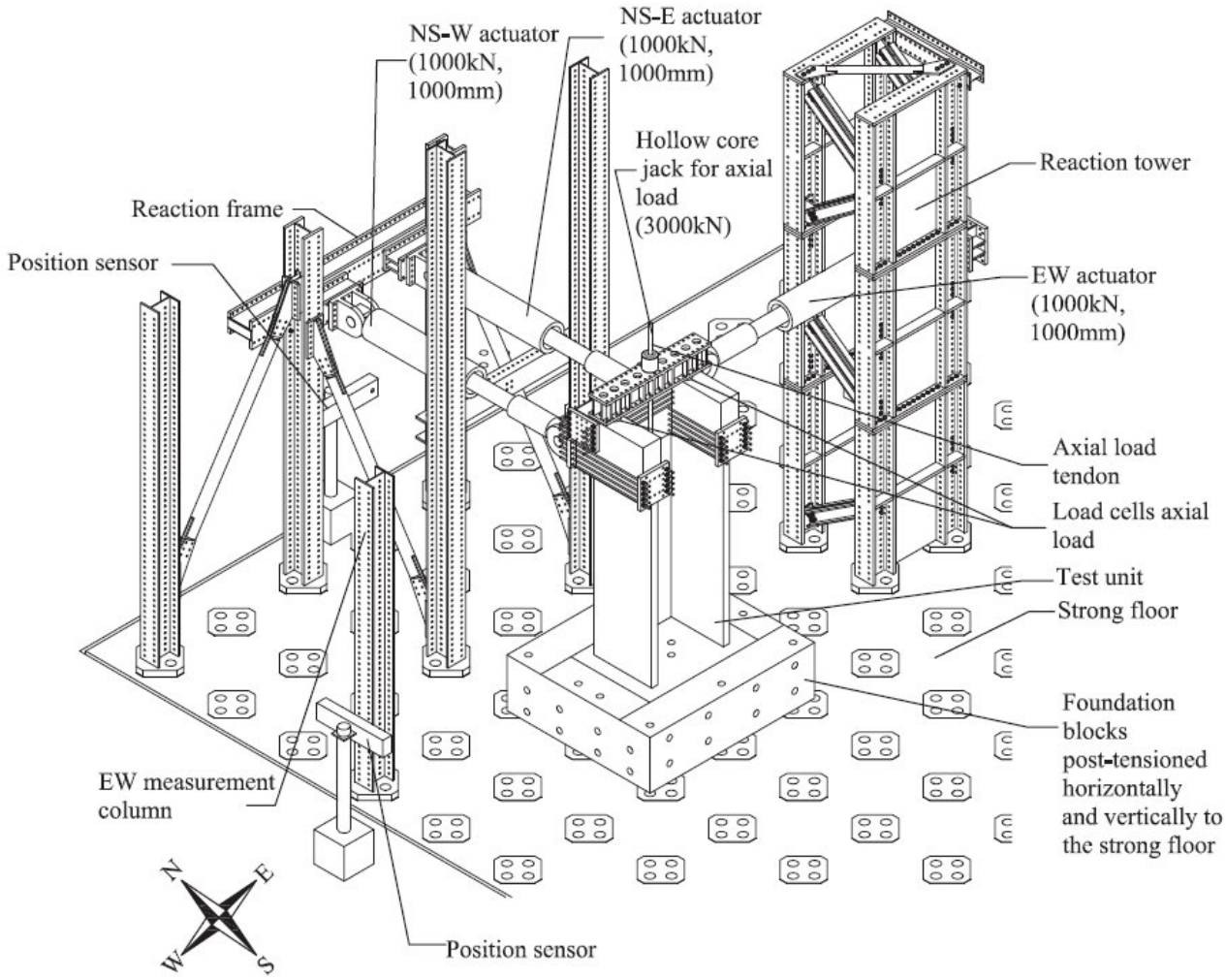

Figure 4.59 – 3D representation of TUC experimental set-up [Constantin and Beyer, 2016].

The geometrical properties of the specimen together with the reinforcement layout are presented in Figure 4.60.

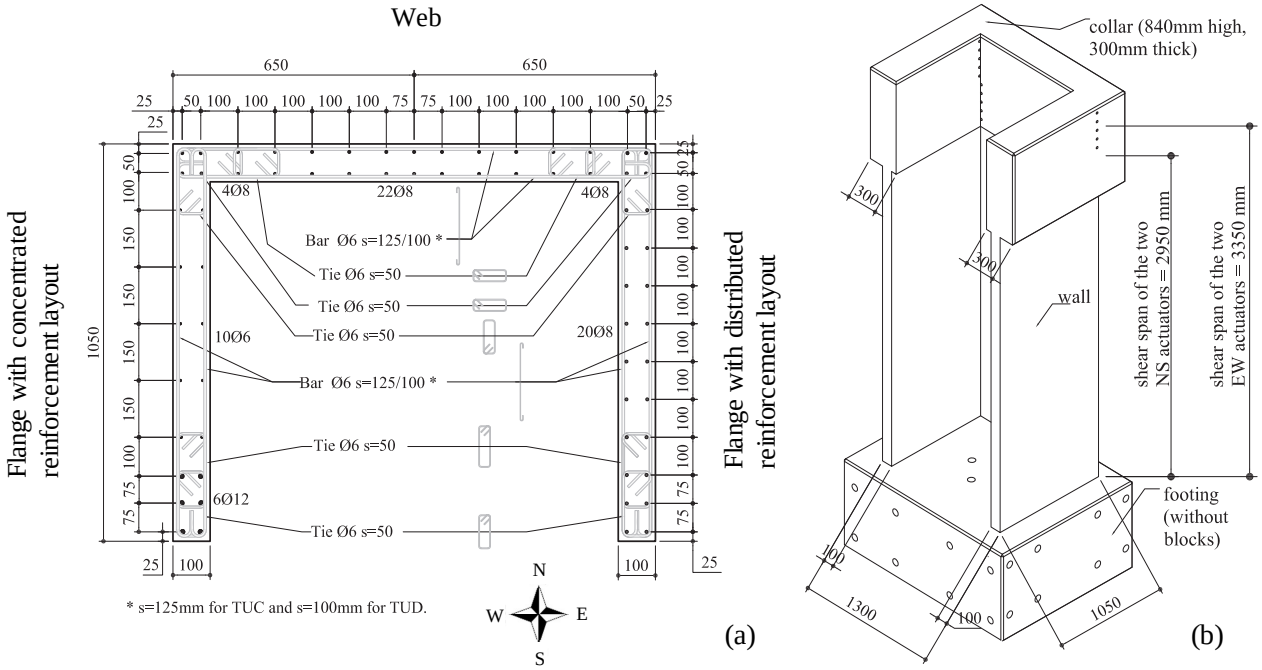

Figure 4.60 – TUC experimental test unit: (a) cross section and reinforcement layout and (b)elevation sketch (measure in mm) [Constantin and Beyer, 2016].

In Table 4.6 are resumed the concrete and reinforcement mechanical properties, derived from material test.

Table 4.6 – Main mechanical properties derived from material tests for TUC specimen.

	concrete			ϕ6 bars			ϕ8 bars			ϕ12 bars		
	Ec [Gpa]	f_c [MPa]	f_t [MPa]	f_y [MPa]	f_u [MPa]	Es [Gpa]	f_y [MPa]	f_u [MPa]	Es [Gpa]	f_y [MPa]	f_u [MPa]	Es [Gpa]
TUC	31.6	42	3.2	492	623	200	563	663	200	529	633	200

The transversal reinforcement is characterized by stirrups with a diameter of 6 mm spaced of 125 mm. Moreover, the extremities of the flanges, defined in the following as boundary elements, and the corners between the web and the flanges, are over reinforced with additional stirrups with a diameter of 6 mm spaced of 50 mm, Figure 4.60-a .

The longitudinal reinforcement was set different for the two flanges. The West flange was detailed with vertical reinforcement mainly concentrated in the boundary elements while in the East flange and in the web the vertical reinforcement was uniformly distributed. The total reinforcement percentage for the flanges is approximatively the same, as listed in Table 4.7.

Table 4.7 – Longitudinal reinforcement percentage for TUC specimen, detailed for the two flanges, the web and the entire wall section.

	$\rho_{l,\text{total}}$ [1]	$\rho_{l,\text{confined}}$	$\rho_{l,\text{unconfined}}$
Flange with distributed reinforcement (East)	1.06%	1.34%	0.91%
Flange with concentrated reinforcement (West)	1.01%	2.45%	0.31%
Web	1.16%	1.25/0.9% [2]	1.00%
Entire wall	1.09%		

[1] ρ_l was computed by counting the corners towards the web

[2] due to differencies in flange reinforcement, layouts reinforcement contents of confined corner regions differ slightly between the two corners

During the test the specimen was subjected to an axial load ratio of 6% (equivalent to an axial force of 806 kN).

The horizontal cyclic load is applied by means of three actuators: the EW actuator loaded the web at a height of h_{EW}=3.35 m while the two NS actuators loaded the flanges at a height of h_{NS}=2.95 m, see Figure 4.59 for the position of the actuators and Figure 4.60-b for them heights. The test was carried out in displacement control and the torsional effect on the specimen was prevented by applying equal displacement to the two NS actuators, NS-W and NS-E.

As the key objective of the experimental investigation was to understand the behaviour of the wall under diagonal loading, the main cycles were applied along the two geometric diagonals of the U-shaped section. The direction of the geometric diagonal joins the corner between web and flange with the edge of the flange (see direction E-F and H-G in Figure 4.61-a). The detail of the applied loading history is reported in Figure 4.61-b.

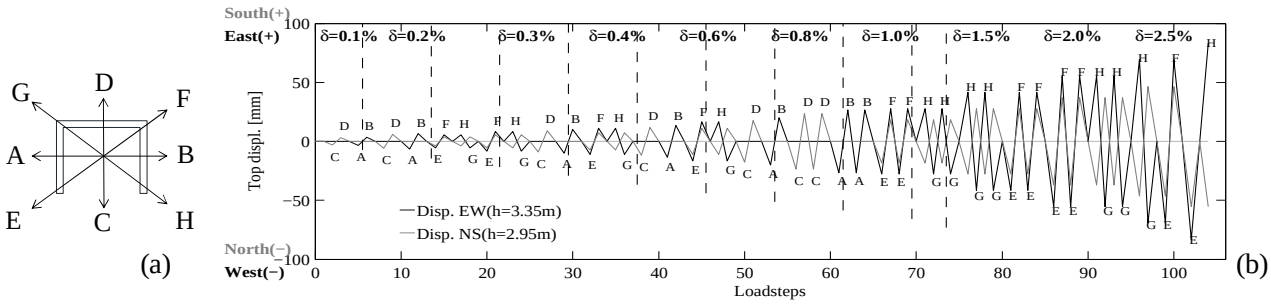

Figure 4.61 – (a) TUC loading positions and (b) loading protocol [Constantin and Beyer, 2016].

The loading protocol presented in Figure 4.61-b are described below:

- 0.1% drift: 0 → C → D → 0 → A → B → 0
- 0.2% drift: 0 → C → D → 0 → A → B → 0 → E → F → 0 → H → G → 0
- 0.3% drift: 0 → E → F → 0 → H → G → 0 → C → D → 0 → A → B → 0
- 0.4% drift: 0 → E → F → 0 → H → G → 0 → C → D → 0 → A → B → 0
- 0.6% drift: 0 → E → F → 0 → H → G → 0 → C → D → 0 → A → B → 0
- 0.8% drift: 0 → C → D → C → D → 0 → A → B → A → B → 0

- 1.0% drift: 0 → E → F → E → F → 0 → H → G → H → G → 0
- 1.5% drift: 0 → H → G → H → G → 0 → E → F → E → F → 0
- 2.0% drift: 0 → E → F → E → F → 0 → H → G → H → G → 0
- 2.5% drift: 0 → H → G → 0 → E → F → 0
- 3.0% drift: 0 → E → 0 → H → 0

4.4.2.2 Nonlinear finite element modelling and results

TUC specimen was modelled using 4-nodes elements with regular integration in plane (4 Gauss integration points). Moreover, each element is discretized, along its thickness, into 2 different layers in order to properly set the exact position of the two reinforcement layers; each layer is characterized by 5 Simpson integration points, Figure 4.62-a.

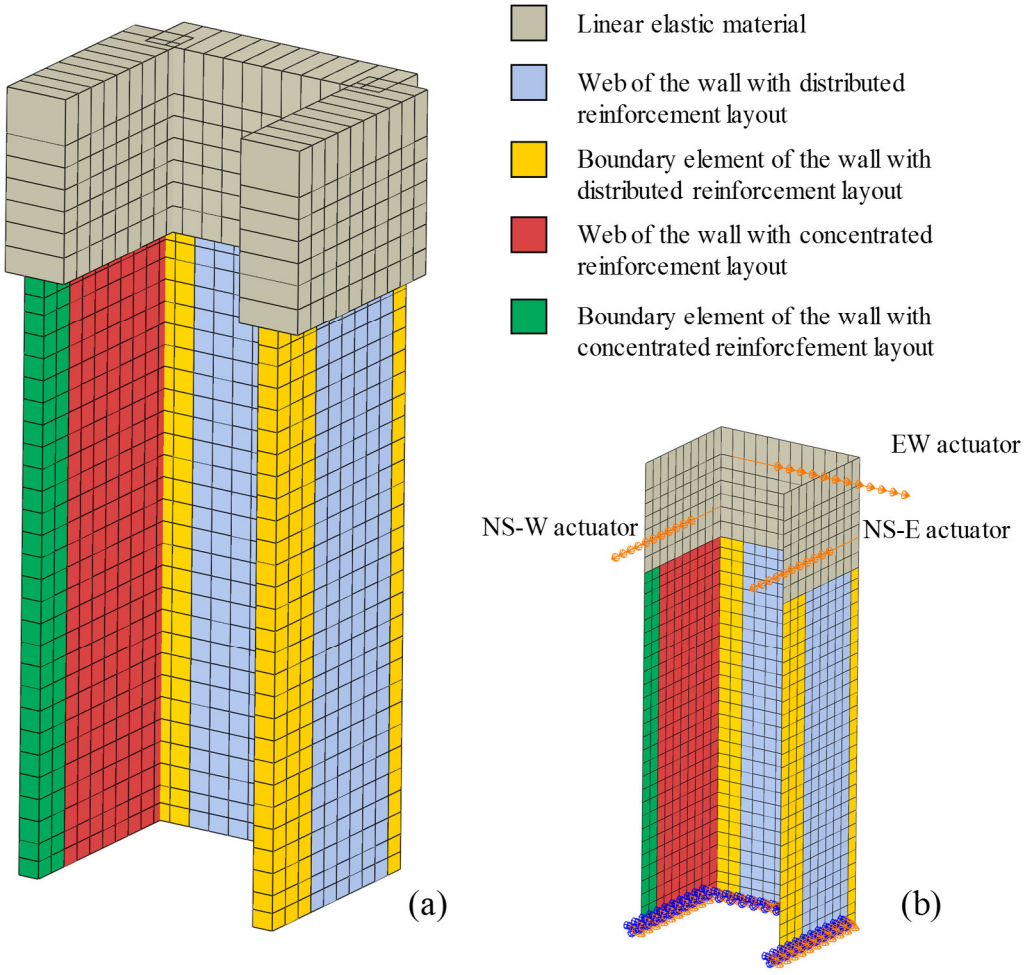

Figure 4.62 – TUC, detail of the mesh used in NLFEA.

As shown in Figure 4.62-a 5 different regions were considered in the model:

- the upper collar, used to distribute the external loading, is characterized by linear elastic material;

- the boundary elements, characterized by additional stirrups, are divided into two more regions in order to consider the differences in longitudinal reinforcement (green region represented the concentrated reinforcement layout while yellow region represented the distributed reinforcement layout);
- the webs of the walls, are characterized by two more regions which differ in the longitudinal reinforcement content, as shown in Table 4.7 (red region represented the concentrated reinforcement layout while light blue region represented the distributed reinforcement layout).

According to the mean mechanical properties reported in Table 4.6, the nonlinear material properties of the model was applied using the implemented PARC_CL 2.0 crack model as presented in Table 4.8. The confining effect, due to the increasing of stirrups in the boundary elements, are calculated according to the formulation proposed by [Mander et al. 1988], which leads to an increasing of both the compressive strength and the ultimate compressive strain. In Table 4.8 are presented the different mechanical properties for all the different regions shown in Figure 4.62.

Table 4.8 – Main material properties adopted in NLFEA for TW1and TW4 specimens.

color code	Region of the wall	Concrete (see §4.2.1.1)										Steel (see §4.2.1.2)				
		h	a_m	Ec	f_t	G^{RC}_F	$\varepsilon_{t,u}$	f_c	G_C	$\varepsilon_{c,cr}$	$\varepsilon_{c,u}$	E_s	$f_{y,\text{long}}$	ρ_{long}	$f_{y,\text{trasv}}$	ρ_{trasv}
		[mm]	[mm]	[Gpa]	[MPa]	[N/mm^3]	[-]	[MPa]	[N/mm^3]	[-]	[-]	[GPa]	[MPa]	[%]	[MPa]	[%]
	Web concentrated reinforcement	100	234	31.6	3.2	0.204	0.003	42	51.0	0.002	0.020	200	492	0.5	492	0.5
	Web distributed reinforcement	100	234	31.6	3.2	0.204	0.003	42	51.0	0.002	0.020	200	563	1.1	492	0.5
	Boundary concentrated reinfo.	100	123	31.6	3.2	0.268	0.003	50.7	118.0	0.003	0.038	200	529	3.4	492	1.1
	Boundary distributed reinfo.	100	123	31.6	3.2	0.268	0.003	50.7	118.0	0.003	0.038	200	563	1.1	492	1.1

Regarding boundary and loading conditions, the specimen was fixed at the base of the wall, so that the influence of the foundation was neglected. The cyclic loading history is applied at the top of the specimen, in the upper collar. The load was applied as a displacement loading history, according to the loading protocol of Figure 4.61, where for every actuator the same displacement was applied to all the nodes positioned on the same line, as shown in Figure 4.62-b

NLFEA were run in displacement control using implicit solution method and Newton-Raphson convergence criterion, with force and displacement control tolerance limits respectively set equal to $5 \cdot 10^{-3}$ and 10^{-2}. The maximum number of iteration allowed for each time increment was set equal to 25. The solution of a time increment is accepted after the maximum number of iteration allowed has been completed, even if the equilibrium tolerances are not satisfied. However, this condition should be avoided because it could lead to a loss of stability and reliability of the results.

In the following the results obtained by means of NLFEA and PARC_CL 2.0 crack model are compared with the experimental outcomes.

Due to the fact that, as stated above, the key objective of the experimental investigation was to understand the hysteretic behaviour of the wall under diagonal loading, in Figure 4.63 and Figure 4.64 are presented the global force-displacement hysteresis obtained when load is applied through diagonal E-F and H-G respectively.

The forces and the displacements obtained by each single actuator were combined using SRSS (Square Root of the Sum of Square) method, as shown in Figure 4.63-a and Figure 4.64-a, according to the following formulation:

$$F_{SRSS} = \sqrt{F_{EW}^2 + \left(F_{NS\_W} + F_{NS\_E}\right)^2} \cdot sign\left(\Delta_{NS}\right) \tag{4.78}$$

$$\Delta_{SRSS} = \sqrt{\Delta_{EW\ @\ 2.95}^2 + \Delta_{NS}^2} \cdot sign\left(\Delta_{NS}\right) \tag{4.79}$$

where F_{EW}, F_{NS_W} and F_{NS_E} represent the forces imposed by each actuator, while Δ_{EW} and Δ_{NS} represent the wall horizontal displacements in the EW and NS direction, measured both at an height equal to 2.95 m above foundation (the height of the NS actuators). The sign of NS displacement was added in the formulation in order to plot the SRSS hysteresis loops consistently.

In Figure 4.63 and Figure 4.64 are also plotted the force-displacement hysteresis obtained for each single actuator when load is applied through diagonal E-F and H-G respectively.

When load is applied along diagonal E-F, as shown in Figure 4.63, the experimental outcomes showed that the failure of the specimen occurred due to the out-of-plane buckling and compression failure, when the flange end was in compression at position E. During the last cycle (characterized by a drift equal to 3%, see Figure 4.61), the wall stiffness was significantly reduced when load is applied from zero towards position E, as compared to the previous cycles at the same loading position (Figure 4.63-a). This is due to the compression failure in the unconfined concrete of the West flange, as shown in Figure 4.65-a where is reported the crushing of concrete reached for a drift of 3%. The experimental evolution of failure can be summarised as follow: due to the large displacement imposed to the wall when load is applied towards position F (e.g. 3% of drift), large tensile strain developed in the West flange end resulting in wide horizontal cracks. When unloading from position F the longitudinal bars of the West flange ends could be subjected to compression before the cracks could close and this condition leads to out-of-plane buckling. Due to this out-of-plane buckling the West flange end lost his compressive carrying capacity and to compensate for this lack the compressed zone increased into the unconfined region, leading to compressive crushing of concrete.

Similar remarks can be done by analysing the experimental behaviour of the specimen when load is applied along diagonal H-G, as reported in Figure 4.64. After the failure occurred at position E, continuing loading along diagonal E-F would have led to the complete destruction of the West flange. For this reason, the specimen was unloaded and reloaded again along diagonal H-G, until the failure of the East flange. In this case the experimental outcomes highlight that the failure occurred due to crushing of concrete in the East flange, for the same reason expressed above, as reported in Figure 4.66-a.

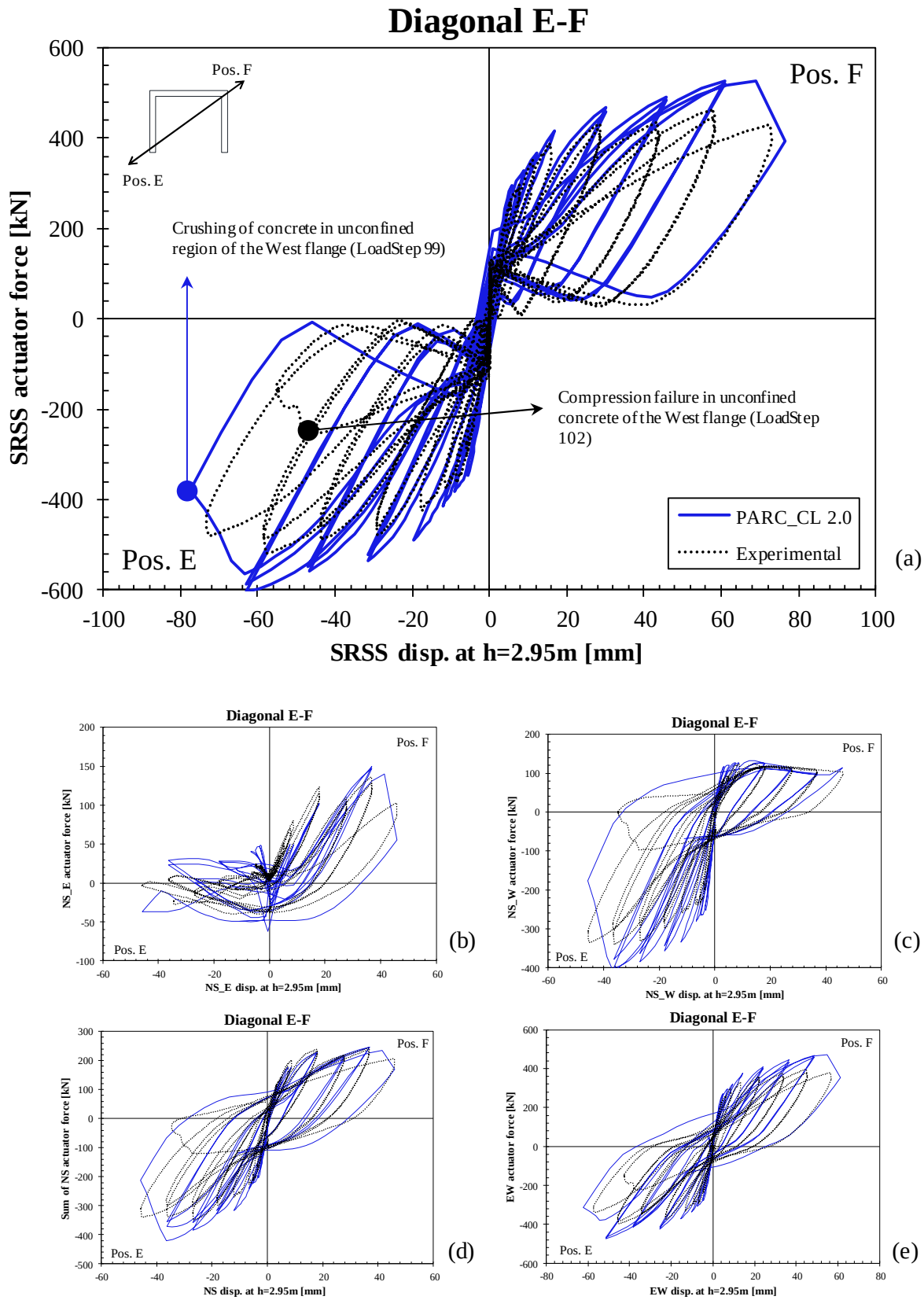

Figure 4.63 – TUC, comparison between experimental and NLFEA in terms of force-displacement hysteresis along diagonal E-F: (a) SRSS combination, (b and c) individual NS_E and NS_W actuator, (d) sum of NS actuators and (e) individual EW actuator.

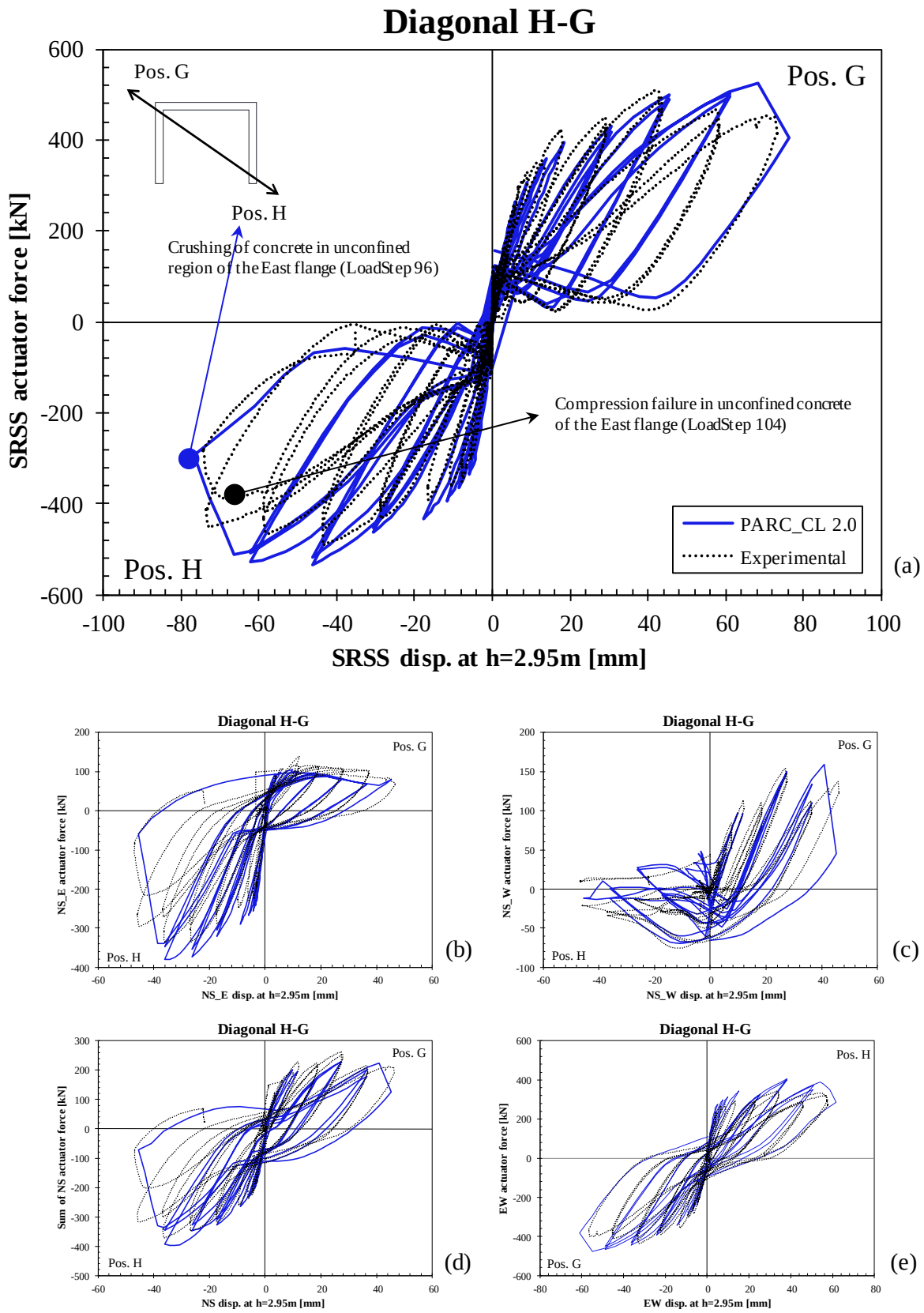

Figure 4.64 – TUC, comparison between experimental and NLFEA in terms of force-displacement hysteresis along diagonal H-G: (a) SRSS combination, (b and c) individual NS_E and NS_W actuator, (d) sum of NS actuators and (e) individual EW actuator.

As shown in Figure 4.63 and Figure 4.64, the results obtained by means of NLFEA and PARC_CL 2.0 crack model seems to well reproduce the global hysteretic behaviour of the specimen considering both the analysed direction of load (diagonal E-F and diagonal H-G).

The good agreement between experimental and numerical outcomes can be remarked also by comparing the experimental and the NLFEA failure mode. Indeed, when load is applied along diagonal E-F the failure in NLFEA is characterized by crushing of compressive concrete in the unconfined region of the West flange, as shown in Figure 4.65-b, according to the experimental test. The crushing of concrete in NLFEA is considered as the point in which the compressive strain reaches the ultimate strain, $\varepsilon_{c,u}$; the values of $\varepsilon_{c,u}$ for both confined and unconfined concrete are reported in Table 4.8.

The only difference between experimental and NLFEA results was related to the fact that the failure in NLFEA occurs a cycle before with respect to the experimental one.

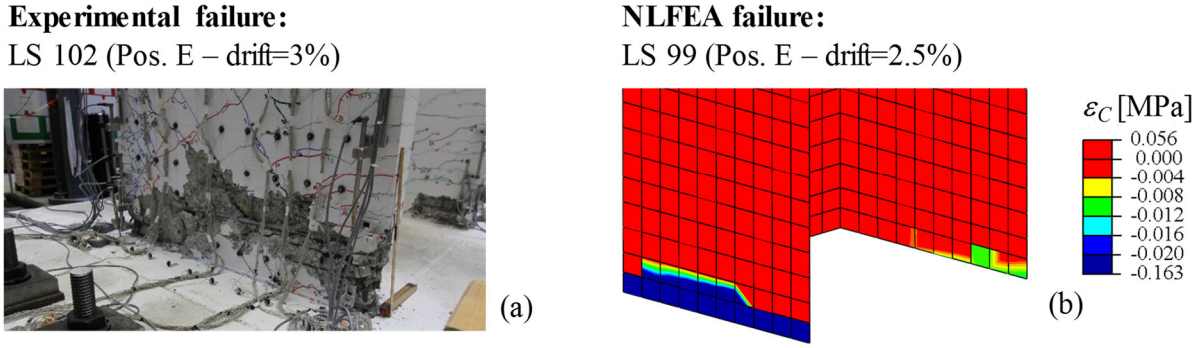

Figure 4.65 – TUC, crushing of concrete at Pos. E in the flange with concentrated reinforcement layout:(a) experimental failure due to crushing in the unconfined region at drift ≅3% and (b) experimental failure due to crushing in the unconfined region at drift ≅2.5%.

Similarly, when load is applied through diagonal H-G the failure mode detected by means of NLFEA was crushing of concrete in the unconfined region of the East flange, as reported in Figure 4.66-b, according to the experimental failure shown in Figure 4.66-a. As for the case when load was applied along diagonal E-F, also in this case the only difference between experimental and NLFEA results was related to the fact that the failure in NLFEA occurs a cycle before with respect to the experimental one.

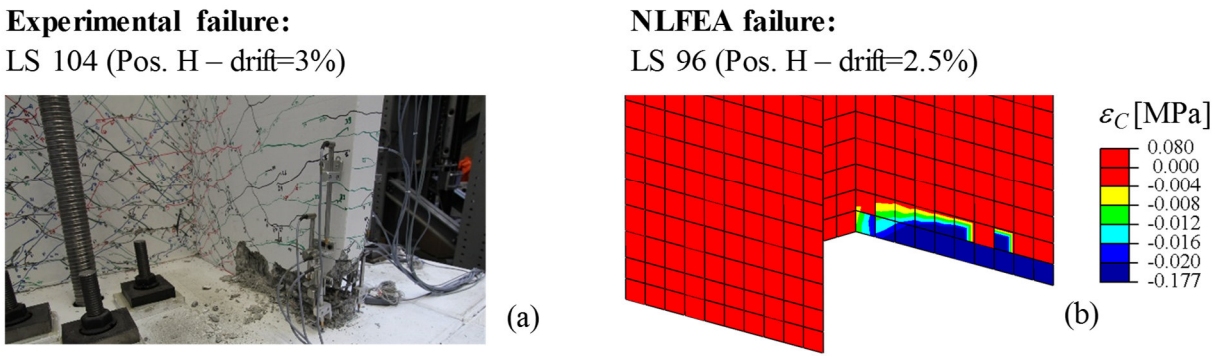

Figure 4.66 – TUC, crushing of concrete at Pos. H in the flange with distributed reinforcement layout:(a) experimental failure due to crushing in the unconfined region at drift ≅3% and (b) experimental failure due to crushing in the unconfined region at drift ≅2.5%.

Another important aspect that can be remarked by analysing NLFEA is related to the evolution of compressive concrete strain along the flange. In Figure 4.67 is reported the comparison between experimental and NLFEA in term of crushed concrete in the West flange when load is applied toward position E for different load levels.

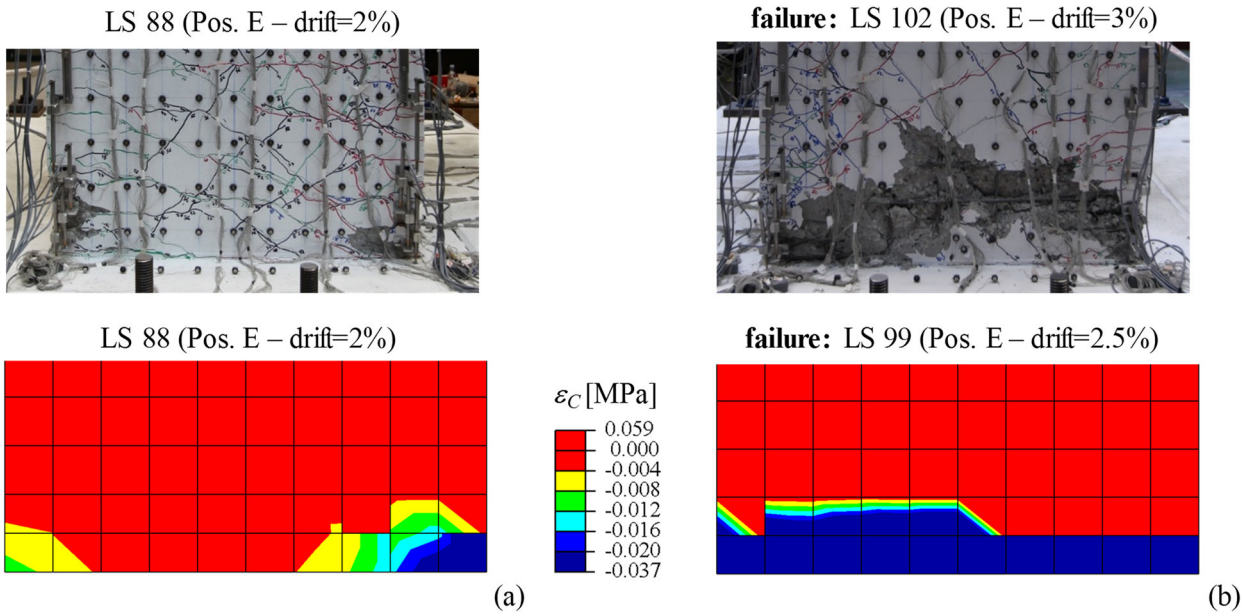

Figure 4.67 – TUC, comparison between experimental and NLFEA in term of crushed concrete in the West flange when load is applied along diagonal E-F: (a) Load Step 88 characterized by a drift=2% and (b) failure load

From Figure 4.67 it can be confirm that, as stated above, the failure of the specimen occurs when the highly compressed zone increased into the unconfined region. Until this moment, as shown in Figure 4.67-a the high compressive strains are concentrated in the boundary region at the end of the flange.

The comparison between experimental and NLFEA results are extended to the evaluation of the local deformation response of the specimen.

In Figure 4.68 is presented the vertical strain on the inside and outside of the West flange end, obtained when load is applied along diagonal E-F and for a drift of 0.4% (Figure 4.68-b and Figure 4.68-c) and 1% (Figure 4.68-d and Figure 4.68-e). The experimental results, derived from the LVDT measurements, and the NLFEA results are in good agreement and this is considered important for the aim of this research for the following reason. When the flange end is under compression (Pos. E) the compressive strains on the outer face of the flange are ≅2.5 times larger than on the inner face (Figure 4.68-b and Figure 4.68-d). On the other hand, when the flange end is under tension (Pos. F) the tensile strains on the outer face of the flange are as large as the tensile strains on the inner face. This large strain gradient, between the outside and the inside of the flange end when it is under compression promotes the instability of the wall and can lead to the out-of-plane buckling of the flange end which was observed in the experimental test.

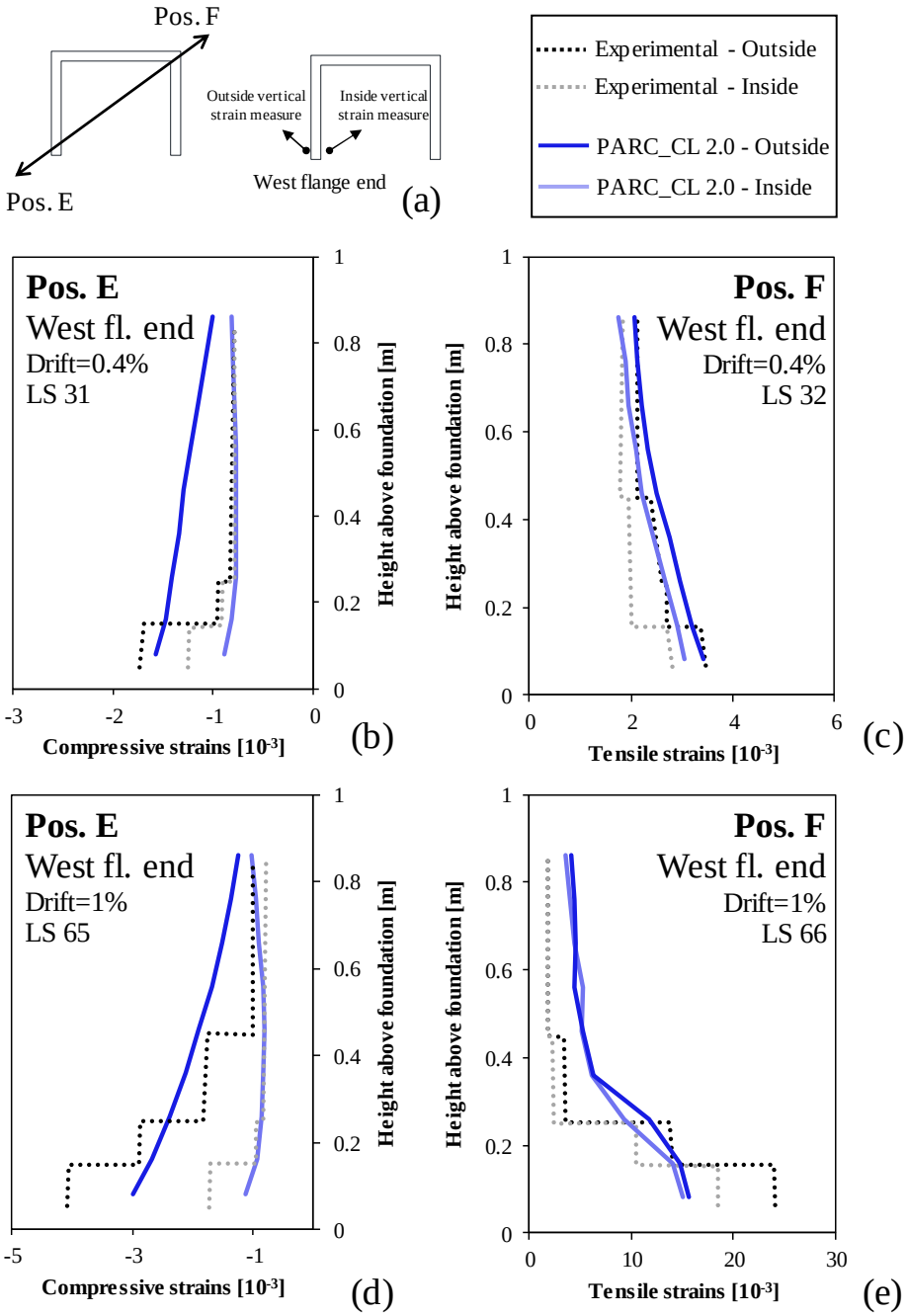

Figure 4.68 – TUC, vertical strain on the outside and inside of the West flange end when load is applied along diagonal E-F.

Similan conclusions can be obtained by comparing the same quantities in the outside and inside of the East flange end when load is applied through diagonal H-G for a drift of 0.4% (Figure 4.69-b and Figure 4.69-c) and 1% (Figure 4.69-d and Figure 4.69-e).

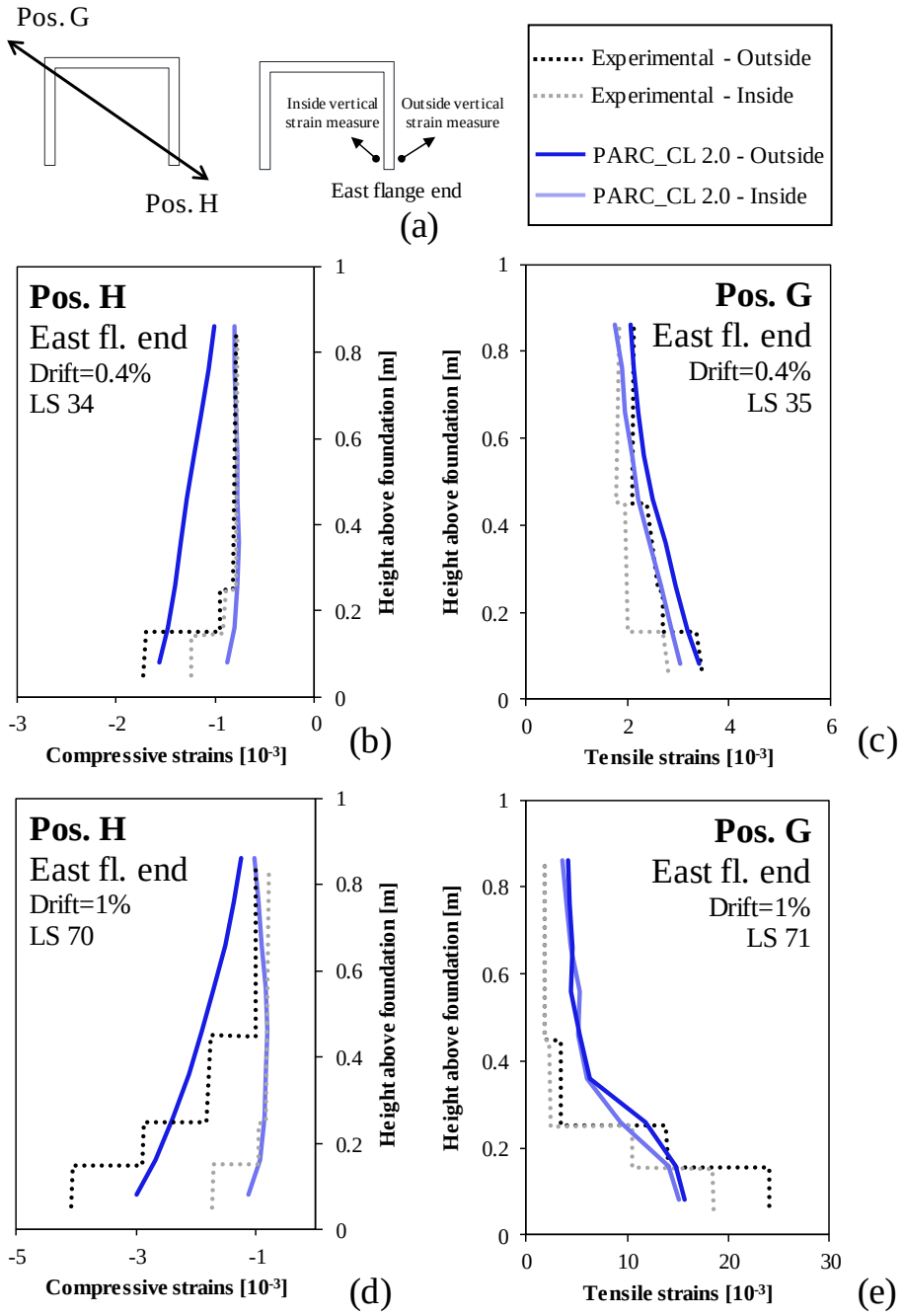

Figure 4.69 – TUC, vertical strain on the outside and inside of the East flange end when load is applied along diagonal H-G.

The good agreement obtained comparing NLFEA and experimental results in terms of vertical strains in the inner and outer sides of the flange (Figure 4.68 and Figure 4.69) is encouraging for the application of the current model in future parametric studies. Note that the large strain gradient under diagonal loading, exhibited when the flange ends are in compression, promotes the occurrence of local out-of-plane buckling of the wall, which was observed in the experimental test.

Another important comparison, in term of local deformation response, between experimental and numerical results is related to the vertical strains at the base of the wall. These quantities were experimentally derived from optical measurement data and so they were taken on the outer perimeter of the walls. The average vertical strains were measured in a height interval *h=0-75 mm* because this interval represents the relevant section for the force transfer mechanism from wall to foundation.

The evaluation of this quantity is considered quite important because the shear forces can be transferred from the wall to the foundation only through compression zone at the base of the wall, while small shear forces can be transferred through tension zone.

In [Constantin and Beyer, 2016] the authors of this experimental campaign compared the experimentally obtained vertical strain distribution along the base of the wall with the one obtained using plane section analysis, performed using zero-length fibre element in "Opensees" software [Mazzoni et al., 2009]. The result of this comparison, not reported herein, highlighted that, as stated by [Constantin and Beyer, 2016], "The plane section assumption, which is the basis of simple analysis tools for RC walls, does not hold for the U-shaped walls under diagonal loading since it fails to capture the presence of additional compression zones at the corners between web and flange."

In Figure 4.70 the experimentally determined vertical strain distribution along the base are compared with the results obtained by means of NLFEA using the implemented PARC_CL 2.0 crack model. The comparisons are plotted for the diagonal loading directions and for the same above mentioned drift levels, i.e. 0.4% and 1.0%.

The results reported in Figure 4.70 showed that NLFEA carried out using multi-layer shell elements combined with PARC_CL 2.0 crack model returns good results in terms of vertical strains at the base of the specimens. In particular, the numerical model allows to capture the presence of the compression zone in the corner between West flange and web when load is applied towards position E (Figure 4.70-a), which was one of the main lack highlighted in the use of plane section model, as explained above. Moreover, the implemented numerical model allows good representation of the depth of the wall subjected to tension or compression, as shown analysing the passage from tension to compression in the East flange when load is applied towards position F (Figure 4.70-b); this fact is considered quite important for the purpose of this research because, as stated above, only the compressed zones can transfer shear from the wall to the foundation and so a proper definition of the compressed zones is a fundamental issue for this kind of problem.

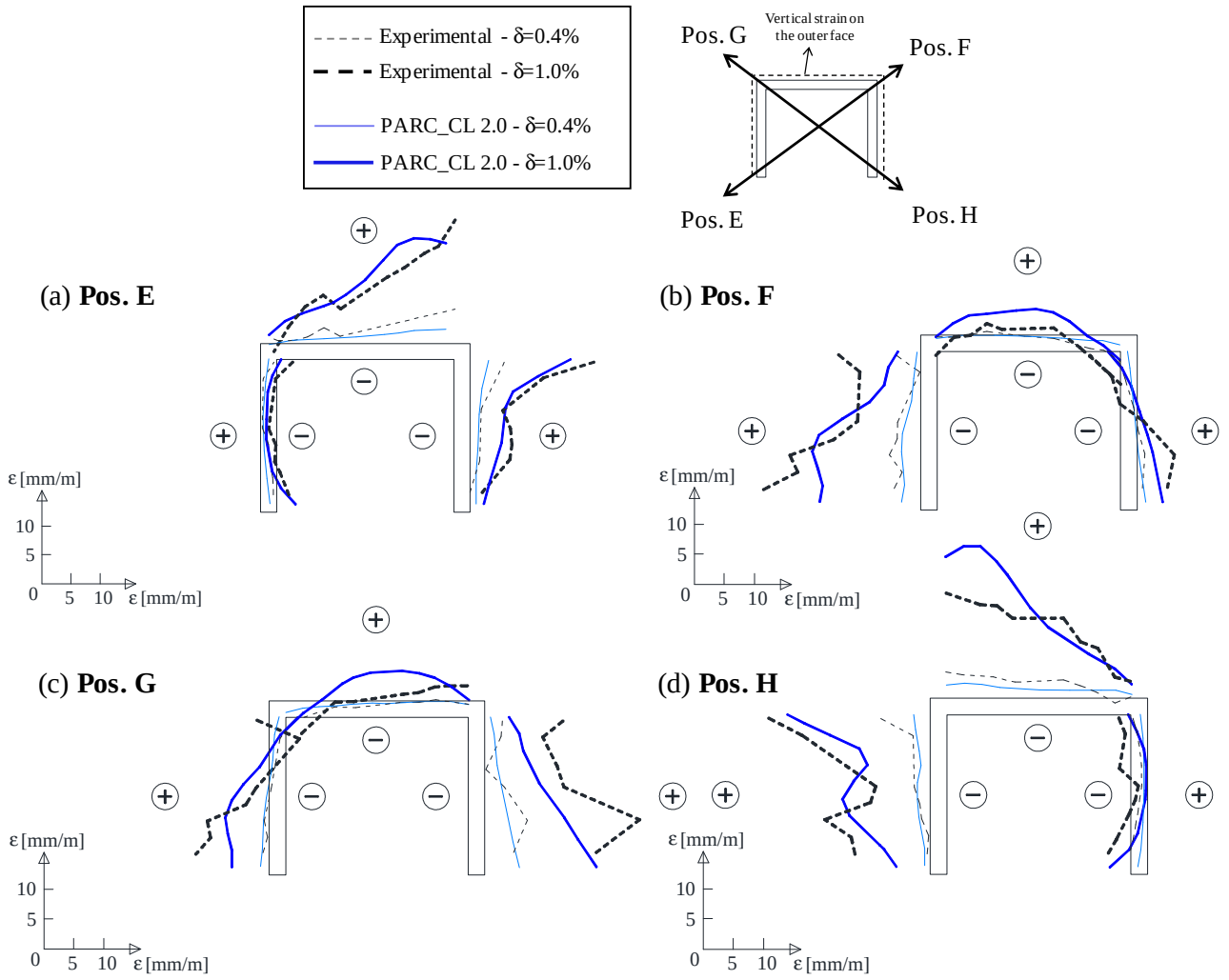

Figure 4.70 – TUC, comparison between experimental outcomes and NLFEA results in term of vertical strain at the base of the outer face of the wall, under diagonal loading: (a) Pos. E, (b)Pos. F, (c) Pos. G and (d) Pos. H Tensile strains are plotted on the outside of the U-shaped section (positive strains) while compressive strain on the inside (negative strains).

4.4.2.1 Validation by comparison with DIANA code

A further validation of the presented PARC_CL 2.0 crack model is carried out by analysing the same specimens using the software DIANA [Manie, 2015].

In Figure 4.71-a is reported a sketch of the adopted mesh. For the modelling of concrete 4 nodes curved shell elements (named Q20SH in DIANA) with 4 Gauss integration points over the element area and 5 Simpson integration points over the element thickness. Reinforcing bars were modelled using embedded reinforcement considering perfect bond between reinforcement and concrete, Figure 4.71-b. Each bar element is characterized by 2 Gauss integration points along the truss axis.

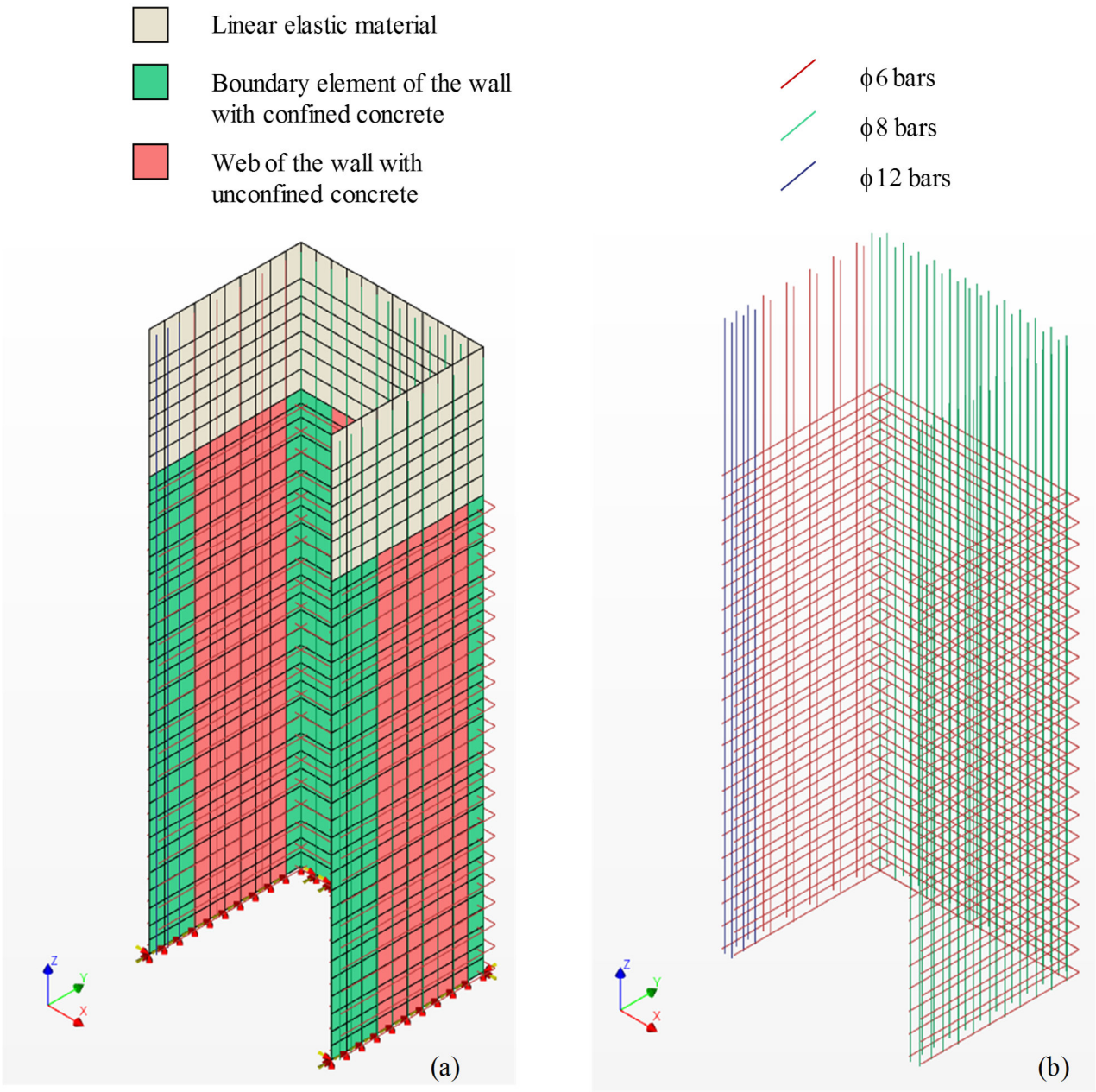

Figure 4.71 – TUC specimen, NLFE model using DIANA code: (a) adopted mesh and (b) detail of reinforcement.

In the NLFEA model, presented in Figure 4.71-a, three different regions are considered: the upper collar, made of linear elastic material, the boundary elements characterized by the presence of additional stirrups such as to confer to the concrete a confined behaviour, and the web of the wall, characterized by unconfined concrete, in the remaining zones. The influence of the foundation is neglected and hence the model restraints are located at the base nodes of the wall.

The Total Strain Fixed Crack Model, available in DIANA [Manie, 2015], was used to model the concrete. For concrete in tension an exponential behaviour based on the definition of the fracture energy in tension, G_F, and of the crack bandwidth, h, have been adopted. G_F was calculated according to the proposal in [*fib*-Model Code 2010] while h was assumed equal to the square root of the area of each element, as suggested by [Hendriks et al., 2012]. Concrete in compression has been modelled with a parabolic relationship, according

to [Feenstra, 1993], based on the definition of the crack bandwidth, *h*, and of the fracture energy in compression, G_C, assumed equal to 450 times G_F, as done using PARC_CL 2.0 crack model. The confinement effect due to the presence of stirrups in the boundary elements of the specimen was taken into account adopting the model proposed by [Mander et al., 1988], available in DIANA. Both the confined and unconfined cyclic stress-strain relationship for concrete are reported in Figure 4.72-a. Moreover, as for TW specimens, the reduction of the compressive strength of concrete, due to tensile strains perpendicular to the principal compressive direction, was taken into account according to [Vecchio and Collins, 1993]. The shear stiffness after cracking is reduced using a constant shear retention factor, equal to 0.03, that multiplies the elastic shear modulus of concrete.

The cyclic behaviour of steel was considered using the Monti-Nuti model [Monti and Nuti, 1992] available in DIANA. The parameters of the Monti-Nuti model was set equal to R_0=20, a_1=18.45 and a_2=0.001, based on a parametric study reported in [Belletti et al., 2016]. In Figure 4.72-b is reported the adopted cyclic constitutive model for steel reinforcement.

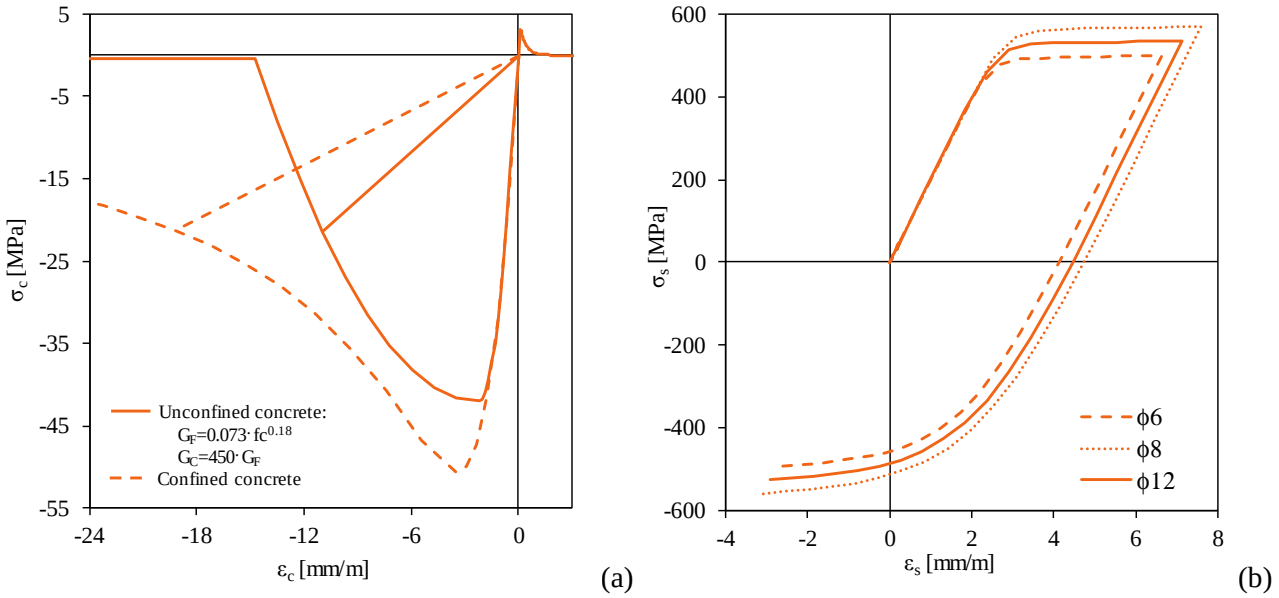

Figure 4.72 – TUC specimen, adopted cyclic constitutive model with DIANA code: (a) concrete and (b) steel.

Figure 4.73 describes the comparison between experimental outcomes and numerical results obtained using both PAC_CL 2.0 crack model within ABAQUS code and DIANA code. The results are presented in term of SRSS force *vs* displacement response when load is applied along the E-F diagonal (Figure 4.73-a) and H-G diagonal (Figure 4.73-b); the points in which the NLFEA failed due to crushing of compressive concrete in the unconfined region are also indicated. The SRSS values were multiplied by the sign of the NS displacement for plotting the hysteresis loop consistently.

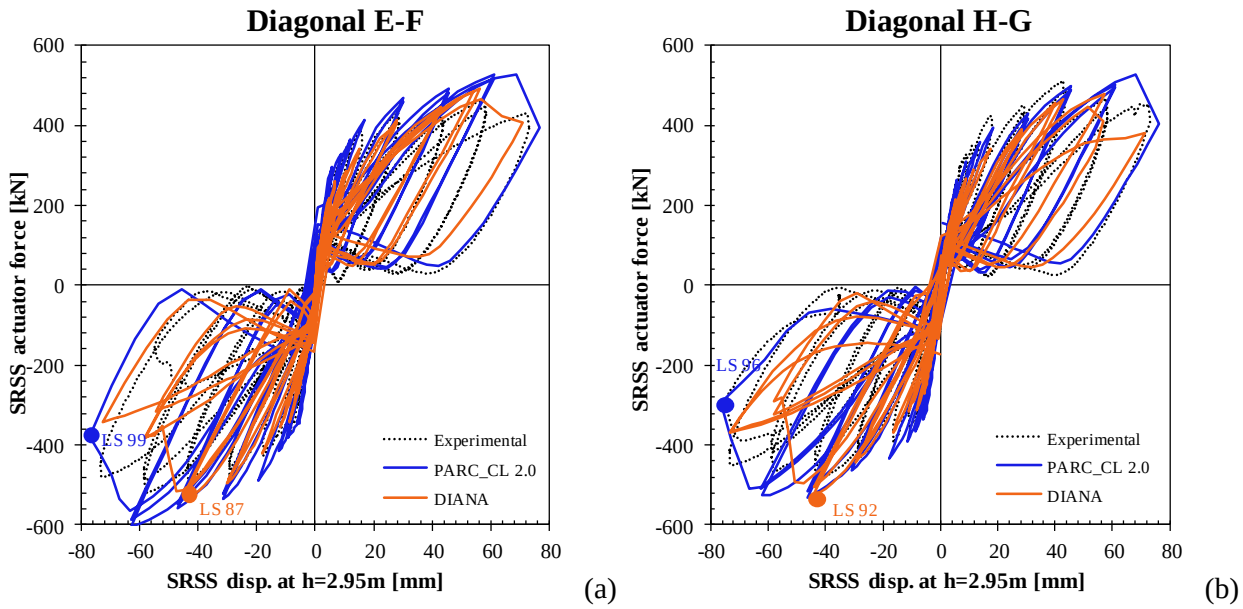

Figure 4.73 – TUC specimen, comparison between experimental outcomes and NLFEA results obtained with the proposed PARC_CL 2.0 crack model and the commercial DIANA code; SRSS in-plane force vs SRSS displacement when load is applied through (a) diagonal E-F and (b) diagonal H-G.

The results reported in Figure 4.73 show that both the numerical model are quite able to reproduce the experimental cyclic response. Moreover, considering both the analysed loading directions, the DIANA model fails for a lower drift with respect to the PARC_CL 2.0 crack model and also to experimental results. In Figure 4.73-a it can be seen that the numerical model developed in DIANA code fails at LS 87 (drift=2.0%) due to crushing of concrete in the unconfined region; on the other hand the numerical model developed in ABAQUS code using PARC_CL 2.0 crack model (widely described in the previous section) fails at LS 99 (drift=2.5%). Just to remind, the experimental specimen fails at LS 102, moving toward a drift of 3.0% as shown in Figure 4.65. Similar remarks can be done analysing diagonal H-G, reported in Figure 4.73-b. In this case the DIANA code model fails at LS 92 (drift=2.0%) due to crushing of concrete, while the ABAQUS code with PARC_CL 2.0 fails at LS 96 (drift=2.5%) and the experimental failure was detected at LS 104 (drift=3.0%) as shown in Figure 4.66.

In Figure 4.74 the comparison is extended to the vertical strains on the inner and outer side of the flange ends, along the height of the wall. These vertical strains are obtained when load is applied along H-G diagonal and for two different loading drifts (0.4% and 1.0%).

Figure 4.74 shows that both the DIANA model and the PARC_CL 2.0 crack model are in good agreement with the experimental outcomes. In particular, from Figure 4.74 it can be observed that when the flange end is in compression (Pos. H) the compressive strains at the base of the wall on the outer face are ~2 times larger than on the inner face, Figure 4.74-b and Figure 4.74-d. On the other end, when the flange end is in tension (Pos. G) the tensile strains in the outer face end are close to the tensile trains in the inner face end, Figure 4.74-c and Figure 4.74-e.

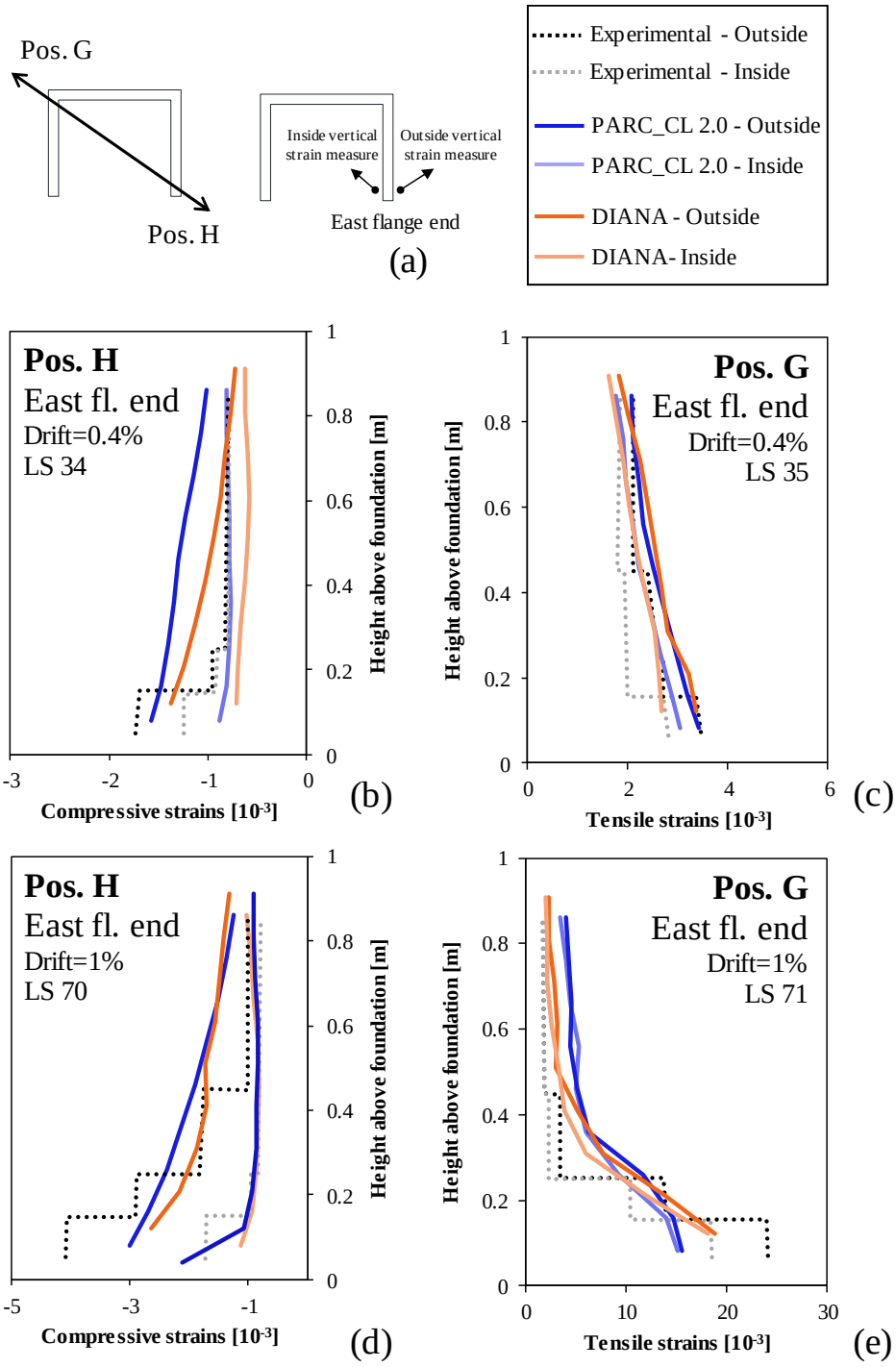

Figure 4.74 – TUC specimen, comparison between experimental outcomes and NLFEA results obtained with the proposed PARC_CL 2.0 crack model and the commercial DIANA code: vertical strains on the inner and outer side of the flange computed along the height when load is applied through H-G diagonal.

4.4.3 Synopsis

In this section the cyclic response of RC slender walls was investigated by means of NLFEA. In particular, the focus is pointed on the out-of-plane instability of such members triggered by horizontal cyclic reversal loading. The need for this research arises from the observed lack of numerical and experimental studies

on this topic. The aim of this section was to validate the capability of the multi-layer shell elements approach associated to the implemented PARC_CL 2.0 crack model to capture this particular phenomenon.

- The results demonstrated that NLFEA using multi-layer shell elements and PARC_CL 2.0 crack model are able to predict the global cyclic response both in loading and unloading phase;
- The comparison was extended to the evaluation of the local deformation response and also in this case NLFEA results are in good agreement with the experimental outcomes. Moreover, NLFE model seems to be able to capture some particular phenomena, such as the distribution of compressive strains along the base of the specimens which, with some simplified analyses (e.g. plane section analysis), it was not possible to capture;
- A further validation of the proposed approach is done by comparing the obtained results with the outcomes obtained using a common commercial code (DIANA code) for NLFEA. The modelling approach adopted in DIANA code was different from the proposed one; in particular, the specimens are modelled with curved shell elements and the reinforcing bars are considered as discrete truss elements embedded within the shells. These two different approaches lead to comparable results;
- It thus seems logical to use this advanced numerical tool to further study wall configurations that are able to optimize the response under bidirectional loading. In particular, the influence of the content and detailing of longitudinal reinforcing bars, the confining effect due to the increase of stirrups, and the width of confined zone in the boundary elements should be addressed.
- Once validated the implemented model by comparison with experimental outcomes, NLFEA offers the possibility to investigate several different conditions that would be impossible to analyse by means of experimental campaigns. Associated to this, further studies would investigate some crucial aspects related to real case studies such as: influence of slabs in the global response of the wall or influence of torsional effects.

5 Conclusion

"Il primo libro sarebbe meglio non averlo mai scritto. Finché il primo libro non è scritto, si possiede quella libertà di cominciare che si può usare una sola volta nella vita, il primo libro già ti definisce mentre tu in realtà sei ancora lontano dall'esser definito; e questa definizione poi dovrai portartela dietro per la vita, cercando di darne conferma o approfondimento o correzione o smentita, ma mai più riuscendo a prescinderne."

Italo Calvino – Il sentiero dei nidi di ragno

In the present thesis several applications of multi-layer shell (MS) elements are presented, in order to investigate both the in-plane and the out-of-plane behaviour of RC members by means of NLFEA. A special attention was payed to the evaluation of the cyclic and dynamic response of such members.

5.1 Summary and conclusions

The MS elements approach adopted in this thesis consists in discretizing the thickness of the element in several layers assuming a plane–stress hypothesis. Thus, they are able to consider the nonlinear out-of-plane flexural behaviour while they do not include the nonlinear behaviour due to shear along the thickness; it is, therefore, not possible to capture shear or punching shear out-of-plane failure.

To overcome this deficiency in this thesis a post-processing of NLFEA results is proposed, based on critical shear crack theory (CSCT). The CSCT, as reported by [Muttoni, 2008] and [Muttoni and Fernandez, 2008[a]], allows to evaluate both shear and punching shear failure modes based on few fundamental parameters, such as respectively the axial strain at mid-depth and the out-of-plane rotation of the element. The comparison between NLFEA and experimental outcomes, carried out on several RC slabs, allows to assess the capability of the proposed post-processing procedure to capture both the shear and the punching shear out-of-plane failure through the thickness of the elements. Moreover, the results obtained with NLFEA have allowed to underline that in case of real structures, characterized by complex boundary and loading conditions, it can lead to more accurate prediction of the structural response with respect to simplified analytical formulations. This is due to the fact that NLFEA allows to consider phenomena like redistribution of stresses and membrane effects which are usually neglected in the simplified formulations.

The main topic of this thesis was to investigate the capability of MS elements to predict the cyclic and dynamic response of RC members; for this reason, a cyclic crack model, for RC members, defined PARC_CL 2.0, was implemented as a user subroutine within the ABAQUS code. These studies are moved by the fact that researchers in the past have been successful in producing models that yield results of acceptable accuracy for conditions of monotonic loading while models that provide accurate simulations of behaviour under general loading conditions, and specifically under reversed cyclic loading, are less common. The PARC_CL 2.0 crack model allows considering plastic and irreversible deformation in the unloading phase and therefore to take into account the hysteretic cycles of both concrete and steel reinforcement. Moreover, in order to proper analyse the dynamic behaviour, the Rayleigh damping stiffness-proportional coefficient was developed within the model.

The implemented PARC_CL 2.0 crack model was primarily validated by means of comparison with experimental tests run on simple RC panels carried out at the University of Houston [Mansour and Hsu, 2005] and in a second phase it was applied to more complex structural members, such as RC walls. In order to evaluate the generalizability of the implemented model, different walls, characterized by different layouts were analysed: squat walls tested at ISPRA laboratory [Pegon, 1998] and slender walls with different cross sections tested at EPFL in Lausanne (two “T-shaped” walls [Rosso et al., 2016] and a “U-shaped” wall [Constantin and Beyer, 2016]). The obtained results highlighted the capability of the implemented PARC_CL 2.0 crack model associated to MS elements to capture not only cyclic in-plane behaviour but also phenomena associated to the out-of-plane instability. Moreover, the results presented in this thesis underlined that a proper constitutive law for reinforced concrete subjected to reversal cyclic loading allows to reproduce not only the global hysteretic response but also the local parameters, such as concrete and steel strains, crack openings etc. An appropriate evaluation of such local parameters is crucial in understanding the overall structural behaviour because they govern phenomena as the out-of-plane global buckling and the transfer of shear forces between a structural member and the foundation.

The importance of the obtained results is related to the fact that, once validated the model by means of comparisons with experimental tests, NLFEA allows to be applied to very complex case studies such as real scale buildings. Moreover, due to the recent increasing of computer power, which strongly reduced the computational time requires to the analysis, several parametric studies, that would be impossible to conduct experimentally, can be done.

The results presented in this thesis demonstrate that NLFEA using MS elements are suitable to model the nonlinear behaviour of several RC members subjected to different kinds of loading. Hence, it can be a useful tool for the design of new structures as well as for the assessment of existing ones. Moreover, it can be established that in case of assessment of existing structures, usually characterized by phenomena associated to the nonlinear behaviour (e.g. cracking, redistribution of stresses, compressive membrane action), it makes sense to invest in a more advanced and time-consuming calculation, as NLFEA, if this can show that an existing structure is reliable enough and does not need strengthening. This philosophy is in accordance with the level

of approximation approach (LoA) proposed by [*fib*-Model Code 2010], which proposed NLFEA as an alternative and more powerful method of verification with respect to the analytical formulation.

Related to the topic of the assessment of existing structures, and also to one of the argument covered in this thesis, a possible future application of NLFEA is associated to the study of the out-of-plane instability of walls triggered not by geometrical eccentricity, as the case studies analysed herein, but generated by different external conditions between inner and outer face of the wall (e.g. effect of corrosion on the outer face of a structural wall such that generate different condition through the cross section).

5.2 Future research

The implemented PARC_CL 2.0 crack model can be considered as the starting point for future researches. Indeed, a self-implemented model offers the possibility, with respect to the standard models available in the libraries of the commercial finite element software products, to account for several mechanical phenomena. These phenomena, after a thorough research conducted on the basis of literature studies, may be added to the model in order to achieve a more refined response of the structural member.

In particular, studies that are nowadays ongoing, and that will soon be added to the PARC_CL 2.0 model, are associated to phenomena as:

- Buckling of compressive steel reinforcement; this phenomenon can strongly influence the out-of-plane instability which, as widely discuss in this document, is strongly related to the compressive behaviour of steel;
- Tension stiffening effect, which can strongly influence specimens subject to phenomena such as the pull-out of reinforcing bars or, in general, the transmission of shear stresses between reinforcing bars and concrete;
- Shrinkage, which strongly influence the serviceability state of RC structures

References

Abaqus 6.12 (2012). User's and Theory Manuals 2012. http://www.3ds.com/.

ACI Committee 318 (2011) Building Code Requirements for Structural Concrete (ACI 318M-11) and Commentary. American Concrete Institute, Farmington Hills, U.S.

AFNOR (1992), Association Francaise de Normalisation, Regles techniques de conception et de calcul des ouvrages et constructions en beton arme suivant la methode des etats limites, DTU P18-702. (in French)

Almeida, J. P., Prodan O., Rosso A., Beyer K.. (2016). Tests on Thin Reinforced Concrete Walls Subjected to in-Plane and out-of-Plane Cyclic Loading. *Earthquake Spectra*.

Belletti, B., Cerioni R., and Iori I. (2001). Physical approach for reinforced-concrete (PARC) membrane elements. ASCE Journal of Structural Engineering, 127(12), pp. 1412-1426.

Belletti B., Esposito R., Walraven J. (2013[a]). Shear Capacity of Normal, Lightweight, and High-Strength Concrete Beams according to ModelCode 2010. II: Experimental Results versus Nonlinear Finite Element Program Results. ASCE Journal Of Structural Engineering, 139(9), pp. 1600-1607.

Belletti B., Damoni C., Gasperi A. (2013[b]) Modeling approaches suitable for pushover analyses of RC structural wall buildings. Engineering Structures, 57(12): 327-338;

Belletti B., Damoni C., Hendriks M.A.N., de Boer A. (2014) Analytical and numerical evaluation of the design shear resistance of reinforced concrete slabs. Structural Concrete 2014; 15(3): 317-330.

Belletti, B., Scolari, M., Muttoni, A., Cantone, R. (2015) Shear strength evaluation of RC bridge deck slabs according to CSCT with multi - Layered shell elements and PARC-CL Crack Model (2015) IABSE Conference, Geneva 2015: Structural Engineering: Providing Solutions to Global Challenges - Report, pp. 1158-1165.

Belletti B., Scolari M., Almeida João P., Beyer K. (2016) Validation of NLFEA of reinforced concrete walls under bidirectional loading. Italian Concrete Days – Giornate AICAP 2016 Congresso CTE, Roma, Italia, October 27-28.

Beyer, K., A. Dazio, and N. Priestley (2008[a]). "Inelastic Wide-Column Models for UShaped Reinforced Concrete Walls," Journal of Earthquake Engineering, 12(sup1), 1–33.

Beyer, K., Dazio, A., and Priestley, M.J.N. (2008[b]) "Quasi-static cyclic tests of two U-shaped reinforced concrete walls." *Journal of Earthquake Engineering*, 12(7), 1023-1053.

Bolander, J. E. and Saito, S. (1998). Fracture analysis using spring network with random geometry. Engineering Fracture Mechanics. 61.5-6, 569–591.

CEB (1996) Comité Euro-International du Béton - RC elements under cyclic loading, state of art report – CEB bulletin n. 230, 1996

CEN (2004) Eurocode 8: Design provisions for earthquake resistance of structures - Part 1: General rules, seismic actions and rules for buildings. European Committee for Standardization, Brussels, Belgium

Cervenka, J., Papanikolaou, V.K., (2008). Three dimensional combined fracture-plastic material model for concrete. International Journal of Plasticity 24, 2192‑2220.

Concrack2 (2011) 2nd Workshop on Control of Cracking in RC structures. 2011. CEOS.fr reserach programme, 2011, Paris, France.

Constantin R., Beyer K., (2016) Behaviour of U-shaped RC walls under quasi-static cyclic diagonal loading, Engineering structures, Vol. 106, pp 36-52.

Dashti F., Dhakal R.P., Pampanin S. (2014) Simulation of out-of-plane instability in rectangular RC structural walls. Second European Conference on Earthquake Engineering and Seismology. Istanbul, Turkey.

Dashti F., Dhakal R.P., Pampanin S. (2015) Development of out-of-plane instability in rectangular RC structural walls. 2015 NZSEE Conference.

Dazio, A., Beyer, K., Bachmann, H. (2009) "Quasi-static cyclic tests and plastic hinge analysis of RC structural walls." *Engineering Structures*, 31(7), 1556-1571.

Elmorsi M., Reza Kianoush M., Tso W.K. (1998). Nonlinear Analysis of Cyclically Loaded Reinforced Concrete Structures, ACI Structural Journal 95(6).

Feenstra P. H. (1993) "Computational Aspects of Biaxial Stress in Plain and Reinforced Concrete", PhD thesis, Delft Technische Universitelt Delft, 1993.

fib – International Federation for Structural Concrete. (2010) fib Model Code for Concrete Structures 2010. Berlin: Verlag Ernst & Sohn, 2013.

fib – International Federation for Structural Concrete (1993) fib-Model Code 1990. *(MC90),* Thomas Telford, London.

Fragiadakis M. , Pinho R. , Antoniou S. (2007) Modelling Inelastic Buckling of Reinforcing Bars under Earthquake Loading. ECCOMAS Thematic Conference on Computational Methods in Structural Dynamics and Earthquake Engineering. Rethymno, Crete, Greece, 13–16 June 2007.

Gambarova P. G., (1983) "Sulla trasmissione del taglio in elementi bidimensionali piani di C.A. fessurati", Proc., Giornate AICAP, 1983, pp141–156 (in Italian).

Giuriani E. (1981) "On the effective axial stiffness of a bar in cracked concrete", Bond in concrete, P. Bartos, ed., Dept. of Civ. Engrg., College of Technology, Paisley, Scotland, 1981, pp 107–126.

Goodsir W.J. (1985) The design of coupled frame-wall structures for seismic actions. University of Canterbury, Christchurch, New Zealand.

Grassl, P., Lundgren, K., Gylltoft, K., (2002). Concrete in compression: a plasticity theory with a novel hardening law. International Journal of Solids and Structures 39, 5205‑5223.

Grassl, P., Jirasek, M., (2006). Damage-plastic model for concrete failure. International Journal of Solids and Structures 43, 7166‑7196.

Greifenhagen, C., and Lestuzzi, P. (2005) "Static cyclic tests on lightly reinforced concrete shear walls." *Engineering Structures*, 27(11), 1703-1712.

Greifenhagen, C. (2006) "Seismic behavior of lightly reinforced concrete squat shear walls." *Ph.D.Thesis*, École Polythecnique Federal de Lousanne, Switzerland.

Guandalini, S.,(2005) "Symmetric Punching of Reinforced Concrete Slabs," Ph.D. thesis, École Polytechnique Fédérale de Lausanne, Lausanne, Switzerland, 2005, 289 pp. (in French)

Guadalini, S., Burdet, O. L., Muttoni, A. (2009): Punching Tests of Slabs with Low Reinforcement Ratios. ACI Structural Journal, 2009, 106(10), pp. 87–95.

Gulec, C.K, Whittaker, A.S. (2009) "Performance-Based Assessment and Design of Squat Reinforced Concrete Shear Walls." *Technical Report MCEER-09-0010*, University at Buffalo, State University of New York, New York, United States of America.

Hendriks, M.A.N., Uijl J.A, De Boer, A.,. Feenstra, P.H., Belletti, B., Damoni, C. (2012) "Guidelines for nonlinear finite element analyses of concrete structures", Rijkswaterstaat Technisch Document (RTD), Rijkswaterstaat Centre for Infrastructure, RTD:1016:2012.

Hidalgo, P.A., Ledezma, C.A., Jorden, R.M. (2002) "Seismic behavior of squat reinforced concrete shear walls." *Earthquake Spectra*, 18(2), 287-308.

Hilber H. M., Hughes T.J.R., Taylor R.L., (1977) Improved Numerical Dissipation for Time Integration Algorithms in Structural Dynamics. Earthquake Engineering and Structural Dynamics, vol. 5, pp. 283–292, 1977.

Hsu, T. T. C., Belarbi, A., and Pang, X. B. (1995[a]). "A universal panel tester." J. Test. Eval., 23(1), 41–49.

Hsu, T. T. C., Zhang, L. X., and Gomez, T. (1995[b]). "A servo-control system for universal panel tester." J. Test. Eval., 23(6), 424–430.

Hsu T.T.C., Mo Y.L. (2010), "Unified theory of concrete structures", Wiley (editor), 2010.

Hwang, S., Fang, W., Lee, H., and Yu, H. (2001). "Analytical Model for Predicting Shear Strength of Squat Walls." J. Struct. Eng., 10.1061/(ASCE)0733-9445(2001)127:1(43), 43-50.

Karsan, I. K., and Jirsa, J. O., (1969) "Behaviour of Concrete Under Compressive Loadings," ASCE, Journal of the Structural Division, Vol. 95, No. 12, 1969, pp. 2543-2563.

Kawai, T. (1977), New element models in discrete structural analysis, Journal of the Society of Naval Architects of Japan, 114, pp.1867–193

Kono, S., Tani, M., Mukai, T., Fukuyama, H., Taleb, R., Sakashita, M. (2014) "Seismic Behavior of Reinforced Concrete Walls for a performance based design." *Proceedings of Second European Conference on Earthquake Engineering and Seismology*, Istanbul, Turkey.

Le Corvec V., Petre-Lazar I., Lambert E., Gallitre E., Labbe P., Vezin J.M., Ghavamian S., (2015). CASH benchmark on the beyond design seismic capacity of reinforced concrete shear walls, Proceedings of SMiRT23 Conference, 10-14 August 2015, Manchester (United Kingdom).

Lefas, I., Kotsovos, M., Ambraseys, N. (1990) "Behavior of Reinforced Concrete Structural Walls: Strength, Deformation Characteristics, and Failure Mechanism." *ACI Structural Journal*, 87(1), 23-31.

Mander, J., Priestley, M., and Park, R. (1988). "Theoretical Stress-Strain Model for Confined Concrete." J. Struct. Eng., 10.1061/(ASCE)0733-9445(1988)114:8(1804), 1804-1826.

Manie J. (2015) DIANA User's manual, Release 10, TNO DIANA;

Mansour, M. and Hsu, T. (2005). "Behavior of Reinforced Concrete Elements under Cyclic Shear. I: Experiments." J. Struct. Eng., 10.1061/(ASCE)0733-9445(2005)131:1(44), 44-53.

Mazzoni S, McKenna F, Fenves GL, (2009). Opensees Command Language Manual, Opensees v. 2.0, Berkeley: University of California; May 2009.

Menegotto M., Pinto, P.E. (1973). "Method of analysis for cyclically loaded R.C. plane frames including changes in geometry and non-elastic behaviour of elements under combined normal force and bending, Symposium on the Resistance and Ultimate Deformability of Structures Acted on by Well Defined Repeated Loads", International Association for Bridge and Structural Engineering, (ABSE) Lisbon, Portugal.

Monti G. and Nuti C. (1992) Nonlinear cyclic behaviour of reinforcing bars including buckling. J. Struct. Eng., ASCE 118, 12 (1992), 3268-3284.

Muttoni A. & Fernàndez Ruiz M. (2008[a]), Shear strength of members without transverse reinforcement as function of critical shear crack width, *ACI Structural Journal*. 2008; **105**(2):163 – 72

Muttoni A. & Fernandez Ruiz M. (2008[b]), Tailor Made Concrete Structures – Walraven & Stoelhorst (eds) © 2008 Taylor & Francis Group, London, ISBN 978-0-415-47535-8

Muttoni, A. (2008) Punching Shear Strength of Reinforced Concrete Slabs without Transverse Reinforcement. ACI Structural Journal 2008; 105(4): 440-450.

Nakamura, H., and Higai, T. (2001). "Compressive fracture energy and fracture zone length of concrete." Modeling of inelastic behavior of RC structures under seismic loads, P. Benson Shing and T. Tanabe, eds., ASCE, Reston, VA, 471–487.

NZS (2006) New Zealand Standard. Concrete Structures Standard; Part 1: The Design of Concrete Structures. Standards Association of New Zealand, Wellington, New Zealand.

Natario F., Muttoni A. and Fernàndez Ruiz M. (2014) Shear strength of RC slabs under concentrated loads near clamped linear supports, *Engineering Structures*. 2014; **76**: 10 – 23

Newmark N. M. (1959) A method of computuation for structural dynamics, Journal of the engineering mechanics division, ASCE, pp. 676-694

Oesterle, R. (1979) Earthquake Resistant Structural Walls: Tests of Isolated Walls: Phase II, Construction Technology Laboratories, Portland Cement Association.

Oesterle, R. G, Fiorato, A. E., Johal, L.S., Carpenter, J.E., Russell, H.G., Corle, W.G. (1976) "Earthquake-resistant structural walls—Tests of isolated walls." Rep. National Science Foundation, Construction Technology Laboratories, Portland Cement Association, Skokie, Illinois.

Oesterle, R.G., Aristizabal-Ochoa, J.D., Shiu, K.N., and Corley, W.G. (1984). Web Crushing of Reinforced Concrete Structural Walls. ACI Journal 81:3, 231-241.

Okamura H., Maekawa K., (1991)Nonlinear analysis and constitutive models of reinforced concrete, Giho-do Press, University of Tokyo, Tokyo, 1991, 182pp.

Paulay, T., Priestley, M. J. N., 1992. Seismic design of reinforced concrete and masonry buildings. *Wiley, New York.*

Paulay T, Priestley M.J.N. (1993) Stability of ductile structural walls. ACI Struct J 90:385–392.

Pegon P. (1998). Programme SAFE: Présentation générale des essais, *JRC technical note.*

Pegon P., Magonette G., Molina F.J., Verzeletti G., Dyngeland T., Negro P., Tirelli D., Tognoli P., (1998[a]), 'Programme SAFE: rapport du test T6' JRC technical note.

Pegon P., Magonette G., Molina F.J., Verzeletti G., Dyngeland T., Negro P., Tirelli D., Tognoli P., (1998[b]), 'Programme SAFE: rapport du test T7' JRC technical note.

Pegon P., Magonette G., Molina F.J., Verzeletti G., Dyngeland T., Negro P., Tirelli D., Tognoli P., (1998[c]), 'Programme SAFE: rapport du test T8' JRC technical note.

Pegon P., Magonette G., Molina F.J., Verzeletti G., Dyngeland T., Negro P., Tirelli D., Tognoli P., (1998[d]), 'Programme SAFE: rapport du test T9' JRC technical note.

Richard B., Fontan M., Mazars J., (2014). Smart 2013: overview, synthesis and lessons learnt from the international benchmark. Ref: SEMT/EMSI/NT/14-037, Document émis dans le cadre de l'accord bipartite CEA-EDF.

Riva, P., Meda, A., Giuriani, E. (2003) "Cyclic behaviour of a full scale RC structural wall." *Engineering Structures*, 25, 835-845.

Rombach G. and Latte S. (2009) Shear resistance of bridge decks without transverse reinforcement. Beton Stahlbetonbau. 2009; **104**(10):642 – 56 [in German]

Rosso A., Almeida João P., Beyer K.. (2016) Stability of thin reinforced concrete walls under cyclic loads: State-of-the-art and new experimental findings, in Bulletin of Earthquake Engineering, vol. 14, num. 2, p. 455-484, 2016.

Sagaseta, J., Tassinari, L., Fernandez Ruiz, M., Muttoni, A. (2014) Punching of flat slabs supported on rectangular columns, Engineering Structures, 2014, 77 (2014), 17-33.

Sinha, B. P., Gerstle, K. H., and Tulin, L. G., (1964) "Stress-Strain Relations for Concrete Under Cyclic Loading," Journal of the American Concrete Institute, Vol. 61, No. 2, 1964, pp. 195-211.

Sozen M.A., Moehle J.P. (1993), Stiffness of Reinforced Concrete Walls Resisting In Plane Shear, Report No. EPRI TR-102731 Electric Power Research Inst., Palo Alto (CA).

Stevens N. J., (1987) Analytical modeling of reinforced concrete subjected to monotonic and reversal loading, Ph.D. thesis, Department of Civil Engineering, University of Toronto, Toronto, 1987

Taylor, S. E., Rankin, B., Cleland, D. J., Kirkpatrick, J.(2007): Serviceability of Bridge Deck Slabs with Arching Action. ACI Struct J., 2007, 104(1), pp. 39–48.

Thiele K. , Dazio A. , Bachmann H., (2001) Bewehrungsstahl unter zyklischer Beanspruchung. Institut für Baustatik und Konstruktion Eidgenössische Technische Hochschule Zürich. Mai 2001.

Thomsen IV, J.H. and Wallace, J.W. (2004) "Displacement-based design of slender reinforced concrete structural walls-experimental verification." *Journal of structural engineering*, 130(4), 618-630.

Vecchio F.J. (1999). Towards cyclic load modeling of reinforced concrete, ACI Structural Journal 96.

Vecchio F. J., Collins M. P., (1986) "The modified compression field theory for reinforced concrete elements subjected to shear" ACI Journal, 83(2), pp 219-231

Vecchio F. J., Collins M. P., (1993) "Compression response of cracked reinforced concrete", Journal of Structural Engineering, ASCE, 119 (12), 1993, pp. 3590-3610.

Vecchio F. J., Collins M. P., (1996) "The modified compression field theory for reinforced elements subjected to shear", ACI journal, 83(2), 219-231.

Wallace J. (2012) Behavior, design, and modeling of structural walls and coupling beams—Lessons from recent laboratory tests and earthquakes. International Journal of Concrete Structures and Materials, 6(1): 3-18.

Vallenas J.M., Bertero, V.V., Popov E.P. (1979) Hysteretic behaviour of reinforced concrete structural walls. Report no. UCB/EERC-79/20, Earthquake Engineering Research Center, University of California, Berkeley.

Whyte, C.A., Stojadinovic, B. (2013) "Hybrid Simulation of the Seismic Response of Squat Reinforced Concrete Shear Walls.", *PEER Report 2013/02*, Pacific Earthquake Engineering Research Center Headquarters at the University of California, Berkeley.

Wood, S.L. (1989) "Minimum tensile reinforcement requirements in walls." *ACI Structural Journal*, 86(5), 582- 591.

Yazgan, U., and A. Dazio (2011). "Simulating Maximum and Residual Displacements of RC Structures: I. Accuracy", Earthquake Spectra, 27(4), 1187–1202.

Zhang, Z.W., and Li, B. (2014) "Evaluation of seismic performance of slender L-shaped and T-shaped structural walls." *Proceedings of Second European Conference on Earthquake Engineering and Seismology*, Istanbul, Turkey.